

Superprotonic Solid Acids: Structure, Properties, and Applications

Thesis by
Dane Andrew Boysen

In Partial Fulfillment of the Requirements
for the Degree of
Doctor of Philosophy



California Institute of Technology
Pasadena, California

2004
(Defended January 9, 2004)

© 2004

Dane Andrew Boysen

All Rights Reserved

To my grandfather, Sydney J. Wallace.

*I am part of all that I have met;
Yet all experience is an arch wherethro'
Gleams the untravell'd world, whose margin fades
For ever and for ever when I move.
How dull it is to pause, to make an end,
To rust unburnish'd, not to shine in use!
As tho' to breath were life. Life piled on life
Were all too little and of one to me
Little remains: but every hour is saved
From that eternal silence, something more,
A bringer of new things;*

(excerpt from *Ulysses*, by Lord Tennyson)

Acknowledgements

First and foremost, I would like to thank my advisor and mentor, Professor Sossina Haile, for taking a chance on me. I am eternally grateful to Sossina for her patient and tireless support throughout the course of my thesis work, even when my work was resulting in perpetual failures. As a mentor, advisor, teacher, scientist, and mother—Sossina excels at all. My awe and appreciation for having had the opportunity to work with such an remarkable person can not be overstated.

Secondly, and for whose smiling face got me through the day, I have to thank my officemate, co-conspirator, and friend, Dr. Calum Chisholm. As my complete anti-thesis, Calum's pure optimism and happy nature made life and work in the laboratory a true joy. It has been my great pleasure to work with Calum.

Next, I would like thank Dr. Tetsuya Uda, whose timely addition to our research group has allowed significant progress to be made in using solid acids as electrolytes for fuel cells. I am fortunate to have had the opportunity to work with such an exceptional scientist.

In general, Caltech has provided me with the opportunity to meet and work with so many exceptional people from all over the world. Among these extraordinary scientists and coworkers, for whom I am thankful to have made their acquaintance are Jian Wu, Lisa Cowan, Kwang Ryu, Paul Asimow, Jed Mosenfelder, Geoff Staneff, Chris Bielawski, Steven Glade, Jörg Löffler, Boris Merinov, Lou Zaharopoulos, Carol Garland, Pam Albertson, and Mike Vondrus.

I am in debt to Professor Richard Secco and Hongjian Liu at the University of Western Ontario for their help with the high pressure measurements presented in this work.

Personally, I have to thank my parents for their steadfast support throughout my academic career, without which none of this work would have been possible. Also, I have to thank my friend and fellow Netzchian optimist Yasser Rathore for his support and friendship. Thanks also to Ashish Bardwaj for being brilliant, honest, and a great friend. Finally,

I would also like to thank the Peik and Escot families for giving me a home away from home.

Of course I must thank the California Institute and Technology, and specifically, the Materials Science Department, for giving me this great opportunity to study at such a remarkable institution. Caltech is like no other place, it is truly the ivory tower—a sanctuary for the noble pursuits of truth, knowledge, and understanding. In a society which continues to become increasingly anti-intellectual, Caltech is a last bastion for such high-minded endeavours—it has been a great honor to be a part of it. As caretakers of these high endeavours, I must give my humble thanks and appreciation to Professor Bill Johnson for inspiring me in his course on thermodynamics and statistical mechanics and to Professor Brent Fultz for taking the time to give me both professional and personal advice.

Lastly, I would like to thank the National Science Foundation, Office of Naval Research, and Caltech for funding this work.

Abstract

In this work, the structure and properties of superprotonic MH_nXO_4 -type solid acids (where M = monovalent cation, X = S, Se, P, As, and $n = 1, 2$) have been investigated and, for the first time, applied in fuel cell devices. Several MH_nXO_4 -type solid acids are known to undergo a “superprotonic” solid-state phase transition upon heating, in which the proton conductivity increases by several orders of magnitude and takes on values of $\sim 10^{-2} \Omega^{-1}\text{cm}^{-1}$. The presence of superprotonic conductivity in fully hydrogen bonded solid acids, such as CsH_2PO_4 , has long been disputed. In these investigations, through the use of pressure, the unequivocal identification of superprotonic behavior in both RbH_2PO_4 and CsH_2PO_4 has been demonstrated, whereas for chemically analogous compounds with smaller cations, such as KH_2PO_4 and NaH_2PO_4 , superprotonic conductivity was notably absent. Such observations have led to the adoption of radius ratio rules, in an attempt to identify a critical ion size effect on the presence of superprotonic conductivity in solid acids. It has been found that, while ionic size does play a prominent role in the presence of superprotonic behavior in solid acids, equally important are the effects of ionic and hydrogen bonding. Next, the properties of superprotonic phase transition have been investigated from a thermodynamic standpoint. With contributions from this work, a formulation has been developed that accounts for the entropy resulting from both the disordering of both hydrogen bonds and oxy-anion librations in the superprotonic phase of solid acids. This formulation, fundamentally derived from Linus Pauling’s entropy rules for ice, accurately accounts for the change in entropy through a superprotonic phase transition. Lastly, the first proof-of-principle fuel cells based upon solid acid electrolytes have been demonstrated. Initial results based upon a sulfate electrolyte, CsHSO_4 , demonstrated the viability of solid acids, but poor chemical stability under the highly reducing H_2 gas environment of the fuel cell anode. Later experiments employing a CsH_2PO_4 electrolyte proved quite successful. The results of these solid acid-based fuel cell measurements suggest solid acids could serve as an alternative to current state-of-the-art fuel cell electrolytes.

Contents

Acknowledgements	iv
Abstract	vi
1 Introduction	1
1.1 Solid Acids	1
1.2 Structure	2
1.2.1 Atomic Bonding ^{4,5,6}	3
1.2.2 Hydrogen Bonding ^{4,7}	4
1.2.3 Coordination ^{11,12}	9
1.2.4 Order–Disorder	11
1.3 Properties	14
1.3.1 Ionic Conductivity	15
1.3.1.1 Protonic Conductivity ^{18,19,20}	18
1.3.2 Phase Transitions	21
1.3.2.1 General Characterization ²⁴	21
1.3.2.2 Superprotonic Transitions	22
1.4 Applications: Fuel Cells	23
1.4.1 Fuel Cell Description	24
1.4.2 Types of Fuel Cells ²⁹	26
1.4.3 Fuel Cell Performance ²⁹	28
Bibliography	30
2 Experimental Methods	32
2.1 Synthesis	32
2.2 Structural Characterization	32

2.2.1	X-ray Diffraction	33
2.2.1.1	Single Crystal X-ray Diffraction	33
2.2.1.2	Powder X-ray Diffraction	33
2.2.1.3	Rietveld Method ^{2,3}	34
2.2.2	Nuclear Magnetic Resonance Spectroscopy	37
2.3	Properties Characterization	38
2.3.1	Impedance Spectroscopy ⁷	38
2.3.2	High-Pressure Impedance Spectroscopy	43
2.3.3	Thermal Analysis	45
2.3.4	Polarized Light Microscopy ¹²	46
	Bibliography	49
3	Structure of Superprotonic MH_nXO_4-type Solid Acids	50
3.1	Hydrogen Bonding	50
3.1.1	CsH_2PO_4 ⁵	52
3.1.1.1	Background	52
3.1.1.2	Ambient Pressure Behavior	57
3.1.1.3	High Pressure Behavior	66
3.1.2	RbH_2PO_4 ³²	70
3.1.2.1	Ambient Pressure Behavior	71
3.1.2.2	High Pressure Behavior	72
3.1.3	KH_2PO_4	75
3.1.3.1	Ambient Pressure Behavior	76
3.1.3.2	High Pressure Behavior	76
3.1.4	Summary	79
3.2	Cation and Oxy-Anion Size Effects	81
3.2.1	Radius Ratio Rules	82
3.2.2	Atomic Bonding	85
3.3	Conclusions	88
	Bibliography	90
4	Properties of Superprotonic MH_nXO_4-type Solid Acids	94
4.1	Pauling's Entropy Rules for Ice ³	95

4.2	Entropy of Superprotonic Phases ^{1,2}	98
4.2.1	Superprotonic Structures	99
4.2.2	Entropy Rules	106
4.2.3	Calculations	109
4.3	Entropy of Disordered Intra-Hydrogen Bond	110
4.4	Results	113
4.5	Conclusions	114
	Bibliography	116
5	Application of Superprotonic Solid Acids in Fuel Cells	119
5.1	State-of-the-Art Electrolytes ^{1,2,3}	119
5.1.1	Polymer Electrolytes	121
5.1.2	Solid Oxides	123
5.2	Solid Acid Electrolytes	125
5.2.1	CsHSO ₄	125
5.2.1.1	H ₂ /O ₂ Fuel Cell	126
5.2.1.2	Chemical Stability under H ₂	129
5.2.1.3	Chemical Stability under O ₂	135
5.2.1.4	O ₂ Concentration Cell	142
5.2.2	Sulfates and Selenates ¹⁹	145
5.2.3	CsH ₂ PO ₄ ¹⁷	146
5.2.3.1	Thermo-chemical Stability	146
5.2.3.2	H ₂ /O ₂ Fuel Cell	149
5.2.3.3	Direct Methanol Fuel Cell	150
5.3	Conclusions	151
	Bibliography	153
	Appendix	156
A.1	Solid Acid Synthesis Recipes	156
A.1.1	CsH ₂ PO ₄	156
A.1.2	CsHSO ₄	156
A.1.3	KHSeO ₄	157
A.1.4	RbH ₂ PO ₄	157

A.1.5	TiH_2PO_4	158
A.1.6	$(\text{NH}_4)_3\text{H}(\text{SO}_4)_2$	158
A.1.7	$\text{K}_3\text{H}(\text{SeO}_4)_2$	158
A.1.8	$\text{Rb}_3\text{H}(\text{SeO}_4)_2$	159
A.2	Thermal Analysis Results	160
A.2.1	RbH_2PO_4	160
A.2.2	TiH_2PO_4	161
A.2.3	NaH_2PO_4	162
A.2.4	LiH_2PO_4	163
A.3	High Pressure Conductivity Results	164
A.3.1	NaH_2PO_4	164
A.3.2	LiH_2PO_4	164
A.4	MH_nXO_4 -type Solid Acid Phase Behavior	165
A.4.1	MH_2XO_4 Phase Behavior	165
A.4.2	MHXO_4 Phase Behavior	166
A.5	Estimated Thermodynamic Values	167
A.5.1	CsHSO_4	167
A.5.1.1	$S_{298.15}^\circ$ and C_p	167
A.5.2	$\text{Cs}_2\text{S}_2\text{O}_7$	168
A.5.2.1	ΔH_f° , $S_{298.15}^\circ$, and C_p	168
	Bibliography	169

List of Figures

1.1	Symmetric and asymmetric hydrogen bonds	6
1.2	Hydrogen bond networks	8
1.3	Diagram of a coordinated atom	9
1.4	Hydrogen bond disorder in KH_2PO_4	12
1.5	Hydrogen bond disorder in CsH_2PO_4	13
1.6	Oxy-anion disorder in CsH_2PO_4	14
1.7	Arrhenius plot of CsHSO_4 conductivity	22
1.8	Schematic diagram of basic H_2/O_2 fuel cell	25
1.9	Fuel cell performance curves	29
2.1	Applied alternating electric field and current response	39
2.2	Nyquist plot of AC impedance spectrum	41
2.3	Equivalent RC circuit model	41
2.4	Nyquist plots of RC and RQ equivalent circuits	42
2.5	Large-volume 1000-ton cubic anvil hydraulic press	43
2.6	Schematic of high-pressure AC impedance cell	44
2.7	Schematic of high-pressure ball drop cell	45
2.8	Diagram of anisotropic crystal between cross-polarizers	47
3.1	Simple model for hydrogen bond disorder	52
3.2	Thermal analysis of CsH_2PO_4 from literature	54
3.3	Conductivity of CsH_2PO_4 from literature	55
3.4	Thermal analysis of CsH_2PO_4 with various particle sizes	58
3.5	Thermal analysis of CsH_2PO_4 at various heating rates	59
3.6	Onset temperature of thermal events in CsH_2PO_4	60
3.7	Polarized light microscopy of CsH_2PO_4	62

3.8	Conductivity of CsH_2PO_4 under ambient pressure	64
3.9	Nyquist plots of CsH_2PO_4 at ambient pressure	64
3.10	Nyquist plots of CsH_2PO_4 at 200 °C versus time	65
3.11	^1H -NMR of CsH_2PO_4	66
3.12	CsH_2PO_4 P - T phase diagram CsH_2PO_4	67
3.13	Conductivity of CsH_2PO_4 at 1 GPa	68
3.14	Nyquist plots of CsH_2PO_4 at 1 GPa	68
3.15	Powder X-ray diffraction patterns of CsH_2PO_4	69
3.16	Thermal analysis of RbH_2PO_4	72
3.17	RbH_2PO_4 P - T phase diagram	73
3.18	Conductivity of RbH_2PO_4 at 1 GPa	74
3.19	Nyquist plots of RbH_2PO_4 at 1 GPa	75
3.20	Thermal analysis of KH_2PO_4	77
3.21	KH_2PO_4 P - T phase diagram	78
3.22	Conductivity of KH_2PO_4 at 1 GPa	78
3.23	Nyquist plots of KH_2PO_4 at 1 GPa	79
3.24	MHSO_4 and MH_2PO_4 phase diagrams versus cation radius	82
3.25	Rotating oxy-anion coordinated cations	82
3.26	Effective tetrahedral radius of an oxy-anion	85
3.27	Radius ratios versus cation radius in MH_nXO_4 -type solid acids	86
3.28	Ionization potential and melting T versus cation size in MH_2PO_4	87
3.29	H-bond strength and superprotonic transition T versus oxy-anion size	88
4.1	Structure of ice phase Ih	95
4.2	Structure of paraelectric KH_2PO_4	97
4.3	Plakida's model for superprotonic phase transitions in CsHSO_4	99
4.4	Powder X-ray diffraction of RbHSeO_4 at 170 °C	100
4.5	Superprotonic structure of RbHSeO_4	102
4.6	Superprotonic structure of CsHSO_4	104
4.7	Proposed oxygen positions in superprotonic CsHSO_4	105
4.8	Superprotonic structure of CsH_2PO_4	107
4.9	Paraelectric structure of CsH_2PO_4	112

5.1	Conductivity of various fuel cell electrolytes	120
5.2	Polymer electrolyte structure	122
5.3	H ₂ /air fuel cell performance with Nafion [®] electrolyte	123
5.4	Solid oxide fuel cell configurations	124
5.5	Proof-of-principle H ₂ /O ₂ fuel cell with CsHSO ₄ electrolyte	126
5.6	Performance degradation in H ₂ /O ₂ fuel cell with CsHSO ₄ electrolyte	129
5.7	Thermal analysis of CsHSO ₄ with Pt under H ₂	130
5.8	Powder X-ray diffraction of CsHSO ₄ after heating in H ₂	131
5.9	Thermal analysis of CsHSO ₄ with different catalysts in H ₂	132
5.10	Reaction equilibrium constants for CsHSO ₄ in H ₂	136
5.11	Cs–H ₂ O–SO ₃ chemical potential diagrams	140
5.12	CsHSO ₄ –Cs ₂ S ₂ O ₇ and CsHSO ₄ –Cs ₂ SO ₄ co-existence curves	141
5.13	Schematic diagram of O ₂ concentration cell	143
5.14	Electric potential measurements of CsHSO ₄ in O ₂ concentration cell	144
5.15	Thermal analysis of sulfates and selenates in H ₂	145
5.16	Thermal analysis of CsH ₂ PO ₄ in H ₂ and O ₂	147
5.17	Dehydration of CsH ₂ PO ₄ versus $p_{\text{H}_2\text{O}}$	148
5.18	H ₂ /O ₂ fuel cell performance with CsH ₂ PO ₄ electrolyte	149
5.19	Direct methanol fuel cell performance with CsH ₂ PO ₄ electrolyte.	151
A.1	Thermal analysis of RbH ₂ PO ₄ , constant V	160
A.2	Thermal analysis of TlH ₂ PO ₄	161
A.3	Thermal analysis of NaH ₂ PO ₄	162
A.4	Thermal analysis of LiH ₂ PO ₄	163
A.5	Conductivity of NaH ₂ PO ₄ at 1 GPa	164
A.6	Conductivity of LiH ₂ PO ₄ at 1 GPa	164

List of Tables

1.1	Solid acid cations and oxy-anions	3
1.2	Hydrogen bond strengths between oxygen atoms	5
1.3	Atomic coordination based on radius ratio rules	10
1.4	Mechanisms of proton motion	20
1.5	Basic fuel cell components	25
1.6	Common types of fuel cells	26
3.1	Summary of onset temperatures of thermal events in CsH ₂ PO ₄	60
3.2	High <i>T</i> thermal and electrical results of MH ₂ PO ₄ at 1 atm and 1 GPa	81
3.3	Shannon ionic radii for MH _{<i>n</i>} XO ₄ -type solid acids	83
3.4	⟨X–O⟩ distance from MH _{<i>n</i>} XO ₄ -structures compared to Shannon radii	84
3.5	MH _{<i>n</i>} XO ₄ -type radius ratios	86
4.1	Rietveld refinement results of RbHSeO ₄ at 175 °C	101
4.2	Superprotonic RbHSeO ₄ atomic coordinates	102
4.3	Structural features of superprotonic MH _{<i>n</i>} XO ₄ solid acids	107
4.4	Calculated entropy of superprotonic MH _{<i>n</i>} XO ₄ -structures	110
4.5	Disordered hydrogen bond entropy in superprotonic MH _{<i>n</i>} XO ₄ solid acids	112
4.6	Calculated and measured entropy of MH _{<i>n</i>} XO ₄ superprotonic transitions	114
5.1	Charateristics of catalysts used in thermal analysis of CsHSO ₄ in H ₂	131
5.2	Thermodynamic data for the reduction of CsHSO ₄ in H ₂	135
5.3	Thermodynamic data for the decomposition of CsHSO ₄ in O ₂	137
A.1	Thermodynamic and structural data of MH ₂ XO ₄ -type solid acids	165
A.2	Thermodynamic and structural data of MHXO ₄ -type solid acids	166
A.3	Thermodynamic data for M ₂ S ₂ O ₇	168

Chapter 1

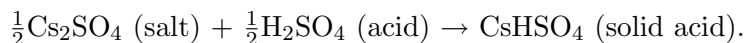
Introduction

The broad objective of this work is to develop a firm understanding of the correlation between the structure and the properties of superprotonic solid acid compounds, so as to allow the engineering of these compounds with the desired properties for the application in devices. In this introduction, a brief description of solid acids will be given, then an overview of the essential features governing the structure of solid acids, that is, the bonding or cohesive forces between atoms, the coordination or packing arrangement of atoms, and the concept of structural disorder. Moving then from structure to properties, the fundamental material properties of interest in this work will be reviewed—specifically, ionic (protonic) conductivity and phase transitions that lead to high protonic conductivity. Last of all, a general introduction to fuel cells, the primary application of interest for superprotonic solid acids, will be presented.

The overall structure of this work will be presented with the same basic outline as this introduction, that is, following a review of the experimental methods, the structure, properties, and finally application of superprotonic solid acids will be covered.

1.1 Solid Acids

Solid acids, or acid salts, are materials whose properties are intermediate those of a normal salt and those of a normal acid. For example,



Solid acids exhibit mechanical and electrical properties similar to a salt, *i.e.*, brittle and insulating. However, like acids, these compounds contain structural acid protons, which

can lead to high ionic conductivity ($\sim 10^{-2} \Omega^{-1}\text{cm}^{-1}$). In fact, it is precisely this structural acid proton in solid acids that is responsible for behavior such as ferroelectricity and superprotonic conductivity.

The first systematic investigations of solid acid compounds began after the discovery of ferroelectric behavior at low temperatures ($T < 120 \text{ K}$) in solid acid KH_2PO_4 ¹. Today, the low temperature properties ($T < 100 \text{ }^\circ\text{C}$), such as piezoelectric, ferroelectric, electro-optical, and non-linear optical properties of these materials, are well characterized and widely exploited in the construction of devices such as Kerr cells, high frequency light modulators, and optical frequency doublers.

Largely ignored in most early studies were the high temperature behavior ($T > 100 \text{ }^\circ\text{C}$) and ionic conducting properties of solid acids. In 1982, a unique order–disorder phase transition was observed in solid acid CsHSO_4 , in which upon heating the proton conductivity increased by $\sim 10^3 \Omega^{-1}\text{cm}^{-1}$ to a so called “superprotonic” phase². Despite unusually high proton conductivity the application of solid acids in electrochemical devices was thought to be impractical due to their solubility in water. However, as part of this work it was demonstrated that, by simply operating above the boiling point of water ($> 100 \text{ }^\circ\text{C}$), solid acids may well be applicable as an electrolyte in fuel cells³—it is to this end that I have investigated the nature of superprotonic behavior in solid acid compounds.

1.2 Structure

There are three essential concepts necessary to describe the structure of solid acids: (1) atomic bonding, (2) coordination, and (3) order-disorder. Here, the nature of atomic bonding or the cohesive force between atoms will be briefly described, with a more in depth characterization of hydrogen bonding, which plays a particularly prominent role in determining the structure and properties of solid acid compounds. Coordination, which describes how atoms arrange themselves based upon size, is also a factor in determining the structure of solid acids, and in particular *superprotonic* solid acids. Last of all, is the concept of structural disorder, which is not only fundamental to the structure of solid acids, but is also intimately related to their properties, such as ferroelectricity and superprotonic conductivity.

Solid acids can be represented by the general chemical formula: $\text{M}_a\text{H}_b(\text{XO}_4)_c$, where

M is a monovalent or divalent cation, XO_4 is a tetrahedral oxy-anion, and a, b, c are integers. The structure of solid acids are comprised of hydrogen-bonded tetrahedral oxy-anions charge balanced by a host lattice of cations. All possible tetrahedral oxy-anions and cations that are known to compose solid acids are listed in Table 1.1. Given the multitude of possible combinations of these tetrahedral oxy-anions and cations, solid acids represent a vast number of compounds with a wide-range of possible structures.

Table 1.1: Solid acid cations ($\text{M}^{+1,2}$) and tetrahedral oxy-anions ($\text{XO}_4^{-2,3,4}$).

Cations		Tetrahedral Oxyanions	
M^+	$\text{Li}^+, \text{Na}^+, \text{K}^+, \text{Tl}^+,$ $\text{Rb}^+, \text{NH}_4^+, \text{VO}^+, \text{Cs}^+$	XO_4^{-2}	$\text{SO}_4^{-2}, \text{SeO}_4^{-2}, \text{CrO}_4^{-2},$ $\text{TeO}_4^{-2}, \text{MoO}_4^{-2},$ WO_4^{-2}
M^{+2}	$\text{Be}^{+2}, \text{Mg}^{+2}, \text{Ca}^{+2},$ $\text{Sr}^{+2}, \text{Pb}^{+2}, \text{Ba}^{+2}$	XO_4^{-3}	$\text{PO}_4^{-3}, \text{AsO}_4^{-3}, \text{VO}_4^{-3},$ $\text{NbO}_4^{-3}, \text{MnO}_4^{-3},$ SbO_4^{-3}
		XO_4^{-4}	$\text{SiO}_4^{-4}, \text{GeO}_4^{-4}$

1.2.1 Atomic Bonding^{4,5,6}

The concept of atomic bonding is a useful construct for the characterization and prediction of the structure of solids. Solids are held together via cohesive forces, which are represented almost entirely by the electrostatic interaction between the negative charges of electrons and the positive charges of the nuclei⁵. Magnetic forces in solids only weakly contribute to the cohesion of crystals, and gravitational forces are negligible. As is conventional, we broadly term these cohesive forces between atoms as *chemical* or *atomic bonds*. Furthermore, chemical bonds of different character are broadly classified as *electrostatic bonds*, *covalent bonds*, and *metallic bonds*⁴. While bonding-type can exhibit character intermediate between these broad classifications, the convention is nonetheless a useful one.

The structure of solid acids is typically dominated by electrostatic bonding, more specifically *ionic bonding*. The ionic bond results from the electrostatic attraction between posi-

tively and negatively charged ions, the formation of which occurs when one or more electrons from one atom are transferred to another atom, forming a *cation* and *anion*, respectively. Other electrostatic forces, such as *Van der Waals interaction*, in which dipole interaction is caused by an induced polarization of the electronic charge distribution of an atom by a neighboring atom, play only a minor role.

1.2.2 Hydrogen Bonding^{4,7}

Prominent in the structure of solid acids is a fourth type of bond, known as the *hydrogen bond*. The hydrogen bond is defined as

an atom of hydrogen attracted by rather strong forces to two atoms, instead of one, so that it may be considered to be acting as a bond between them. - *Linus Pauling*

While relative to other types of bonds, the hydrogen bond is somewhat weak (2 to 10 kcal/mol)⁴, it nevertheless plays a significant role in determining the structure and properties of solid acids.

The hydrogen atom, containing only a single 1s electron, can form only one covalent bond, and therefore, the attraction observed between hydrogen-bonded atoms must be due largely to ionic forces. Especially relevant to solid acids are the hydrogen bonds between two oxygen atoms. In this case, the two oxygen atoms are labeled as the proton donor oxygen atom (O_d), in which the proton lies within the electron density of the oxygen atom and bond most closely resembles a covalent bond, and the proton acceptor oxygen atom (O_a), which is *hydrogen-bonded* to O_d via largely ionic forces.

For solid acid compounds, hydrogen bonds exhibit distinctive hydrogen bond geometries within the hydrogen bonds, *intra-hydrogen bonds*, as well as arranging themselves spatially within a crystalline lattice with a wide variety of geometries, *inter-hydrogen bonds*. Both intra- and inter-hydrogen bonding observed in solid acid compounds will be discussed in the following sections.

Intra-Hydrogen Bonds

Hydrogen bonds between oxygen atoms can be categorized according to their strength, which is related to the donor oxygen to hydrogen distance (d_{O_d-H}), and the donor to ac-

ceptor oxygen distance ($d_{O_d \dots O_a}$), Table 1.2^{8,7,9}. The strength of a hydrogen bond increases inversely with the covalency of the O_d -H bond, such that the hydrogen bond strength increases as the hydrogen bond character transitions from being largely ionic to mostly covalent.

Table 1.2: Categories of hydrogen bond types (strength) and the corresponding donor oxygen to hydrogen atom distances (d_{O_d-H}), donor to acceptor oxygen atom distances ($d_{O_d \dots O_a}$), Lewis notation, and bond character of the hydrogen bond^{8,7,9}.

Strength	$d_{O_d-H} / \text{Å}$	$d_{O_d \dots O_a} / \text{Å}$	Lewis Notation	Character
strong	1.30 – 1.02	2.4 – 2.6	$O_d \cdots H \cdots O_a$	covalent
medium	1.02 – 0.97	2.6 – 2.7	$O_d-H \cdots O_a$	polar covalent
weak	$\lesssim 1$	2.7 – 3	$O_d-H^+ \quad O_a^-$	ionic

Further distinction between types of hydrogen bonds between oxygen atoms in crystalline solids depends on the local symmetry of oxygen atoms participating in the hydrogen bond. If both oxygen atoms participating in a hydrogen bond occupy crystallographically equivalent positions, then the bond is *symmetric*, whereas, if the oxygen atoms occupy crystallographic distinct positions then the bond is *asymmetric*. In Figure 1.1 is a schematic representation of the hydrogen bond potential energies $E(\mathbf{r})$ (or potentials) as a function of interatomic distance between two oxygen atoms for strong, medium, and weak symmetric and asymmetric bonds⁹. For symmetric and asymmetric strong hydrogen bonds, at hydrogen bond distances less than 2.4 Å, there is no distinction between the donor and acceptor oxygen atoms and the hydrogen atom sits equidistant between the oxygen atoms in single-well potential. At medium bond strengths, with a hydrogen bond distance of ~ 2.6 Å, for symmetric and asymmetric bonds the hydrogen atom can reside near either oxygen atom, in one minimum of a double-well potential. At sufficiently high temperatures, thermal oscillations can allow the hydrogen atom to overcome the potential barrier between the minima in the double-well potential, partially occupying each position—this is known as *hydrogen bond disorder*. In Figure 1.1, for medium strength asymmetric hydrogen bonds both single-well potentials, case (1), which are not disordered, as well as, double-well potentials, case (2), which are disordered, are possible⁹. At hydrogen bond distances greater than 2.9 Å (weak hydrogen bonds), symmetric bonds are not generally observed and for

asymmetric bonds the hydrogen atom lies within the minimum of a single-well potential, close to the donor oxygen atom.

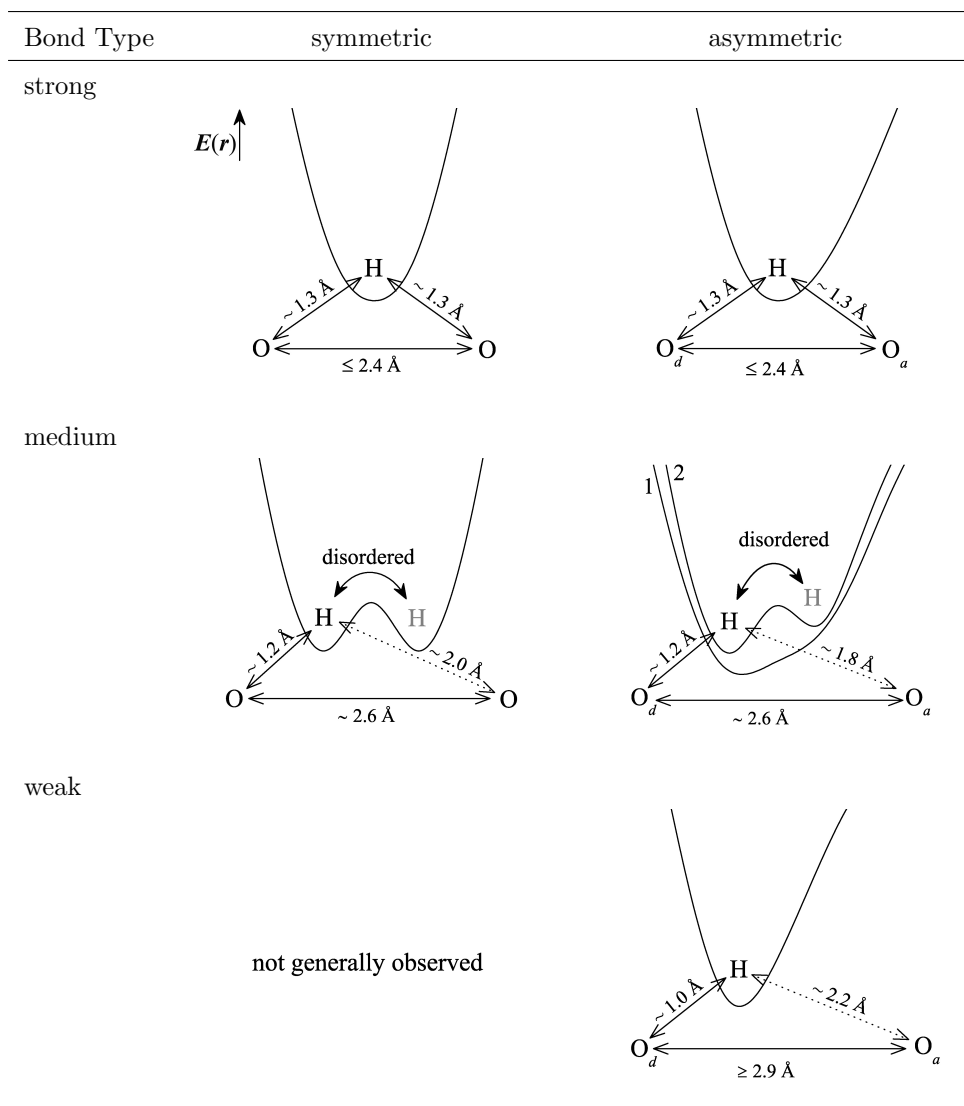


Figure 1.1: Schematic representation of symmetric and asymmetric strong, medium, and weak bond potentials as a function of inter-atomic distance $E(r)$ between hydrogen-bonded oxygen atoms⁹.

Inter-Hydrogen Bonds

Beyond *intra*-hydrogen bond geometry, the structure of solid acid compounds can also exhibit a wide variety of *inter*-hydrogen bond geometries, or networks, Figure 1.2¹⁰. The number of hydrogen bonds per tetrahedral oxy-anions (XO_4 s) can be as few as one hydrogen bond per XO_4 , as is the case for $K_3H(SO_4)_2$, or as many as four, in which all the oxygen

atoms of the oxy-anion are hydrogen-bonded, as in KH_2PO_4 . In general, the distribution of hydrogen bonds can exhibit zero-, one-, two-, and three-dimensional networks depending on the density of hydrogen bonds. As a general guide, the type of hydrogen bond network depends on the ratio of hydrogen to tetrahedral oxy-anions (H/XO_4). Zero-dimension hydrogen bond networks, in which there is only half a hydrogen atom per XO_4 can take the form of *dimers*. Solid acids that have one hydrogen atom per XO_4 , tend to exhibit one-dimensional networks in the form of *cyclic dimers*, *rings*, or *chains*. With one and a half hydrogen atoms per XO_4 , two-dimensional *planar layers* of hydrogen-bonded networks of XO_4 s are possible. Lastly, *three-dimensional networks* can be observed when all the oxygen atoms are hydrogen bonded.

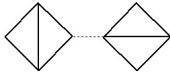

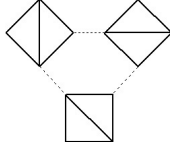
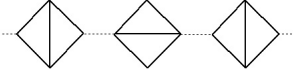
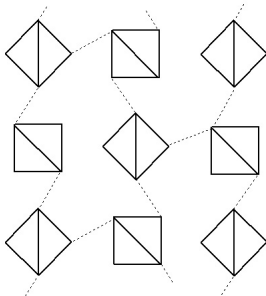
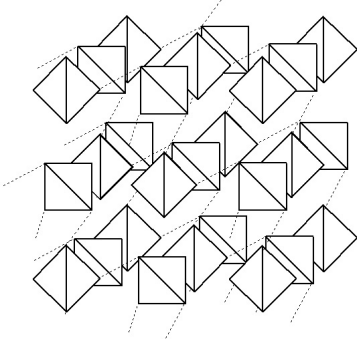
Dimensionality	Networks	H/XO ₄	Example
0-D	dimers 	0.5	K ₃ H(SO ₄) ₂
1-D	cyclic dimers  rings  chains 	1	KHSO ₄ Cs ₂ Na(HSO ₄) ₃ CsHSO ₄
2-D	planar layers 	1.5	Cs ₂ HSO ₄ H ₂ PO ₄
3-D	3-dimensional networks 	2	KH ₂ PO ₄

Figure 1.2: Diagrams of different inter-hydrogen bond networks exhibited by solid acids. Depending on the number of hydrogen bonds (...) per tetrahedral XO₄ oxy-anions (◊) different networks of varying dimensionality are possible¹⁰.

1.2.3 Coordination^{11,12}

The coordination of an atom is defined by the number of surrounding nearest neighbor atoms. Coordination plays a significant role in the arrangement of atoms in solids, and is influenced principally by the type of bonding and the relative size of atoms (or ions) in a solid. From simple geometric considerations and assuming a rigid sphere model for ions, the structure of ionic solids can often be inferred from the relative sizes of the constituent ions.

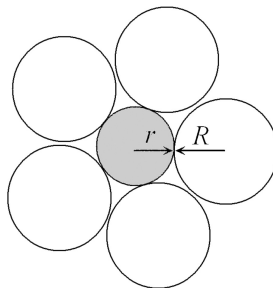


Figure 1.3: Two-dimensional depiction of an atom of radius r , coordinated by five other atoms of radius R .

Consider a compound containing two different ions of radii r and R , as depicted in two dimensions in Figure 1.3. Let r represent the radius of the smaller ion, usually the cation, and let R represent the radius of the larger ion, usually the anion. The relationship between the ratio of the radii r/R , and the resulting coordination number can be determined using the following constraints: (1) cations “touch” anions, (2) the number of anions surrounding a given cation will be as high as geometrically possible, and (3) the ions cannot overlap. As the relative size of r to R increases ($r/R \rightarrow 1$), the number of possible nearest neighbors increases (increasing coordination number) and the possible geometric arrangement of atoms change. The expected geometries based on these *radius ratio rules* are presented in Table 1.3, where for the geometries depicted, the vertices of the coordination polyhedron represent the positions of atoms of radius R , and the coordinated atom of radius r is positioned at the center of the polyhedron. Values of ionic radii obtained from diffraction data of ionic solids, such as those compiled by R.D. Shannon¹³, used in conjunction with these radius ratio rules are of considerable utility in determining the structural arrangement of ionic solids without any *a priori* knowledge of the structure.

Table 1.3: Coordination number of an atomic (ionic) species based on radius ratio (r/R) rules, where the radius of the the smaller atomic species (r) lies central to the depicted coordination polyhedron, and is coordinated by atomic species of larger radius (R) positioned at the vertices of the polyhedron (from reference¹¹).

Coordination Number	Minimum Radius Ratio		Coordination Polyhedron
4	0.225		Tetrahedron
6	0.414		Octahedron
	0.528		Trigonal prism
7	0.592		Capped octahedron
8	0.645		Square anti-prism
	0.668		Dodecahedron
	0.732		Cube
9	0.732		Tricapped trigonal prism
12	0.902		Icosahedron
	1.000		Cuboctahedron

1.2.4 Order–Disorder

Order–disorder in solid acid structures is a central feature in determining the properties of these compounds. There are many types of order–disorder phenomenon observed in solids. The two main types of order–disorder phenomenon which describe the arrangement of atoms are (1) *structural disorder*, in which a single atomic species partially occupies multiple crystallographic positions; and (2) *chemical disorder*, in which multiple atomic species occupy the same crystallographic position. Structural disorder can be broken into two general categories:

1. *Static disorder*, when a single atomic species is randomly distributed over multiple crystallographic positions.
2. *Dynamic disorder*, resulting from thermally activated atomic species moving between two or more crystallographic positions.

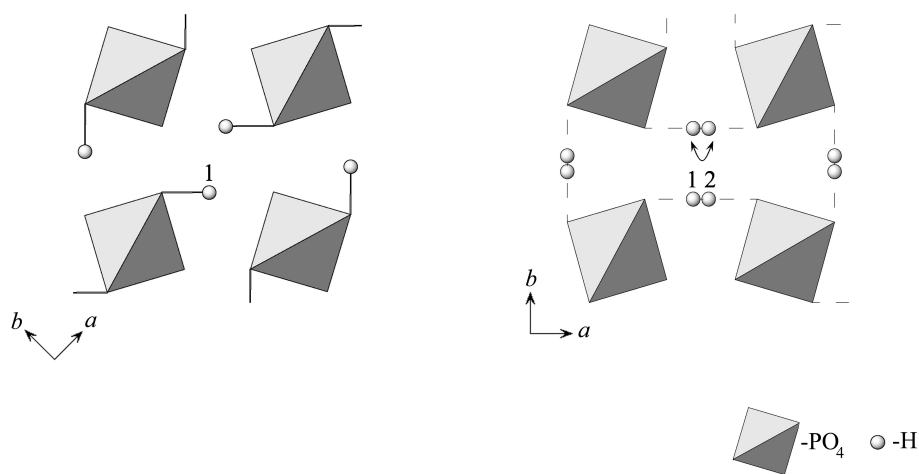
Of these types of structural disorder, dynamic disorder is the feature that is of greatest interest for the present investigations into the properties of solid acid compounds.

Dynamic Disorder

Dynamic disorder is responsible for some of the truly spectacular properties exhibited by solid acid compounds, such as ferroelectricity and superprotonic conductivity. The dynamic disorder exhibited in solid acids are as follows: (1) *Intra-hydrogen bond disorder*, (2) *Inter-hydrogen bond disorder*, and (3) *Oxy-anion disorder*. The first of these is responsible for ferroelectric transitions in solid acids, and the second and third, being intimately related to one another, are responsible for superprotonic behavior.

Intra-Hydrogen Bond Disorder As mentioned previously, intra-hydrogen bond disorder occurs in medium strength symmetric and asymmetric hydrogen bonds, in which there are two crystallographic positions separated by a potential barrier for a single hydrogen atom. At low temperatures there is insufficient thermal energy for the hydrogen atom to overcome the potential barrier, and the structure becomes ordered with respect to the intra-hydrogen bond—the hydrogen atom resides in just one crystallographic position. Upon heating, thermal oscillations of the hydrogen atom become sufficient to overcome the potential barrier between the two crystallographic positions and the crystallographic structure

becomes disordered with respect to the intra-hydrogen bond. In terms of properties, this transition from order to disorder in solid acids leads to a ferroelectric to paraelectric transition. The most well-known solid acid exhibiting this behavior is KH_2PO_4 , depicted in Figure 1.4 in both its (a) ferroelectric phase (ordered intra-hydrogen bond), and (b) paraelectric phase (disordered intra-hydrogen bond). Crystallographically, upon transforming from order to disorder, a center of symmetry is created between the two oxygens atoms participating in the hydrogen bond and a higher symmetry space group is formed, for example KH_2PO_4 transitions from orthorhombic ($Fdd2$)¹⁴ to tetragonal ($I\bar{4}2d$)¹⁵.



(a) Ordered intra-hydrogen bond (b) Disordered intra-hydrogen bond

Figure 1.4: Schematic representation of KH_2PO_4 crystal structures in (a) orthorhombic ($Fdd2$) ferroelectric phase¹⁴, in which a single hydrogen atom is located at crystallographic position 1—ordered intra-hydrogen bond, and (b) tetragonal ($I\bar{4}2d$) paraelectric phase¹⁵, in which a single hydrogen atom is disordered between crystallographic positions 1 and 2—disordered intra-hydrogen bond. Potassium atoms not shown for clarity.

Inter-hydrogen Bond Disorder Upon heating some solid acids the oxy-anions begin to librate between crystallographically equivalent positions, while simultaneously breaking and reforming new hydrogen bonds—a *superprotonic* phase transition. The hydrogen bond is thus distributed among several crystallographic positions, *i.e.*, the inter-hydrogen bonding becomes *disordered*. For example, in Figure 1.5 (a) the ordered inter-hydrogen bond, and (b) the disordered inter-hydrogen bond of CsH_2PO_4 are depicted. Here, in two-dimensions two hydrogen bonds (solid lines) per tetrahedral SO_4 group can be observed in the ordered

paraelectric (ferroelastic) phase and four hydrogen bonds (dashed lines) in the disordered superprotonic (paraelastic) phase (from a three-dimensional viewpoint, this would be four and six hydrogen bonds per tetrahedral PO_4 group, respectively). Clearly, there is an intimate relationship between this inter-hydrogen bond disorder and the oxy-anion disorder in solid acids, the former not occurring without the latter.

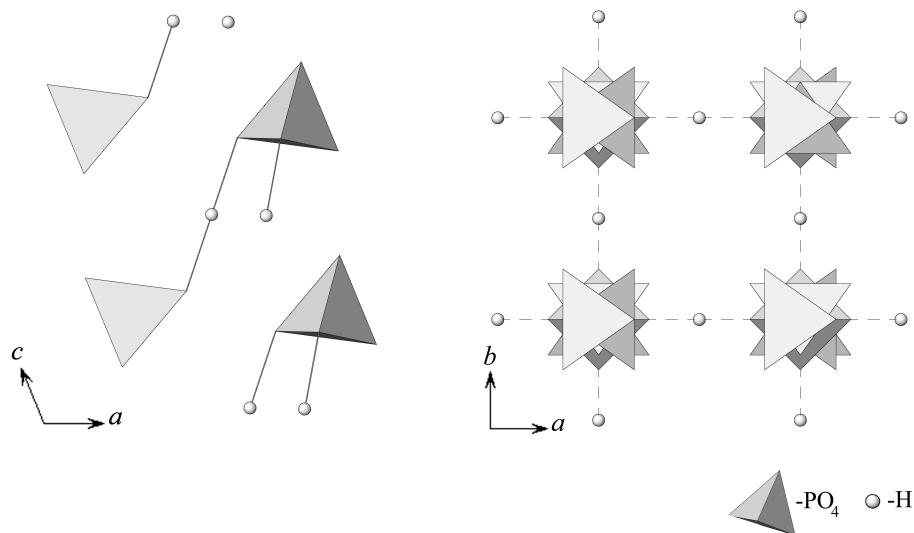
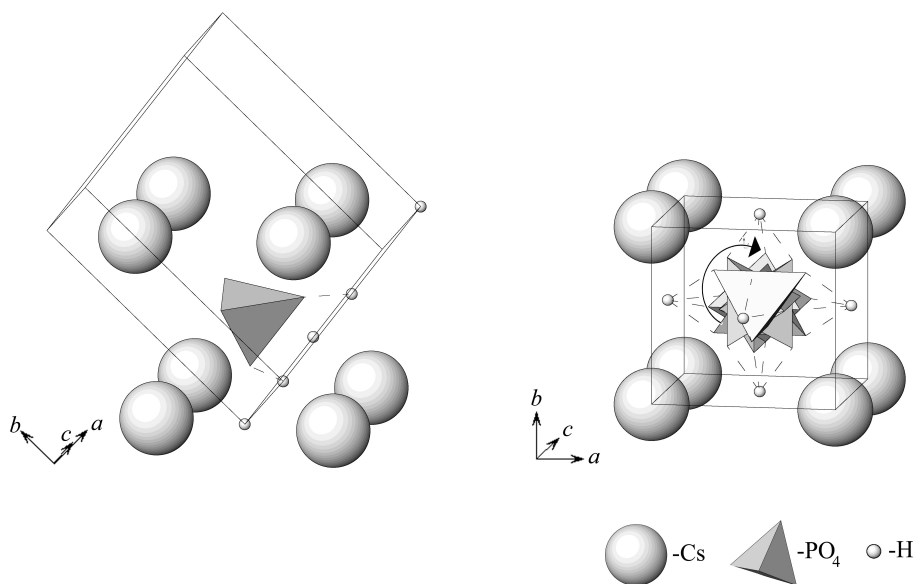


Figure 1.5: Schematic representation of CsH_2PO_4 crystal structures in (a) monoclinic ($P2_1/m$) phase¹⁶, in which the tetrahedral PO_4 oxy-anions and inter-hydrogen bonds (solid lines) are ordered, and (b) cubic ($Pm\bar{3}m$) superprotonic phase¹⁷, in which the tetrahedral PO_4 oxy-anions and inter-hydrogen bonds (dashed lines) are dynamically disordered. Cesium atoms are not shown for clarity.

Oxy-Anion Disorder Dynamic structural oxy-anion disorder occurs when the oxygen atoms of structural tetrahedral oxy-anions partially occupy crystallographically equivalent positions. Due to the strong bonding between the oxygen atoms and the central tetrahedral atom, the overall tetrahedral structure is maintained, leading to librations of the tetrahedron between these crystallographically equivalent positions, and manifesting in several possible orientations of the tetrahedron. In Figure 1.6, a three-dimensional depiction of ordered and disordered oxy-anion structures in CsH_2PO_4 are presented. In (a) the tetrahedral oxy-anion PO_4 exists in only one orientation—ordered phase, and in (b) the tetrahedron is rotationally disordered (as arrow indicates) among 6 possible orientations—disordered phase. This dynamic tetrahedral disorder corresponds to an oxygen atom dis-

ordered over 4 oxygen positions (= 24 oxygen positions per tetrahedron \div 6 tetrahedron positions). Given the appropriate structural prerequisites (cation to oxy-anion size), such a transition is expected, based on entropic considerations, even in the absence of hydrogen bonds. This expectation is, in part, confirmed by the observation of such phase transformations in salts such as Cs_2SO_4 , in which disordered tetrahedral PO_4 groups exist in absence of any hydrogen-bonding. Therefore, while dynamic inter-hydrogen bond disorder requires disordered oxy-anions, the reverse is not necessarily true.



(a) Ordered tetrahedral oxy-anions (b) Disordered tetrahedral oxy-anions

Figure 1.6: Schematic representation of CsH_2PO_4 crystal structures in (a) monoclinic ($P2_1/m$) paraelectric (or ferroelastic) phase¹⁶, in which the tetrahedral PO_4 oxy-anions resides in one position—ordered, and (b) cubic ($Pm\bar{3}m$) superprotonic (or paraelastic) phase¹⁷, in which the tetrahedral PO_4 oxy-anions are rotationally disordered (as arrow indicates) among six different tetrahedral orientations.

1.3 Properties

Electrolytes for application in fuel cells or batteries ideally have high ionic conductivity and little or no electronic conductivity. Therefore, the ionic conductivity and specifically protonic conductivity, is the principal material property of solid acids investigated here. Solid acids exhibiting high proton or *superprotonic* conductivity are of particular interest. To date, all known superprotonic behavior in solid acids is a result of a solid–solid order–disorder phase transition and for this reason, significant effort has been made in this work

to characterize these transitions, and the subsequent superprotonic behavior.

1.3.1 Ionic Conductivity

A phenomenological review of some of the basic underlying principles of ionic conduction is given here. Beginning with an isotropic solid the material property conductivity σ is a scalar quantityⁱ that relates the current density \vec{i} to an applied electric field $\vec{\mathcal{E}}$ according to Ohm's law

$$\vec{i} = \sigma \vec{\mathcal{E}}. \quad (1.1)$$

In an electrolyte with only one type of charge carrier, the current density \vec{i} for a concentration of charged carriers n each with charge q traveling with an average velocity of $\langle \vec{v} \rangle$ is

$$\vec{i} = nq \langle \vec{v} \rangle. \quad (1.2)$$

The charge carrier mobility u^{ii} , defined as

$$u \equiv \frac{\langle \vec{v} \rangle}{\vec{\mathcal{E}}}, \quad (1.3)$$

can be used to express the conductivity as

$$\sigma = nqu. \quad (1.4)$$

When the concentration of particles n and the electric field \mathcal{E} vary along the x -direction, the subsequent flux J (or number of charged carriers passing through an area per time) of charge carriers is equal to the product of the mean force on the particles $\langle F \rangle$, n number of particles per unit volume, charge q , and their mobility per charge u/q

$$J = \frac{-nu}{q} \langle F \rangle = \frac{-nu}{q} \left(\frac{\partial \mu}{\partial x} + q\mathcal{E} \right), \quad (1.5)$$

where μ ($= \partial G / \partial n$) is the chemical potential of the charge carriers. In the absence of an

ⁱFor anisotropic solids, the conductivity is a second rank tensor quantity.

ⁱⁱMobility is usually designated as μ , however in this case μ represents the chemical potential.

electric field ($\mathcal{E} = 0$) this reduces to

$$J = -nuq \left(\frac{\partial \mu}{\partial x} \right). \quad (1.6)$$

The flux of particles can also be expressed in terms of a charge carrier diffusion coefficient D according *Fick's first law*

$$J = -D \frac{\partial n}{\partial x}. \quad (1.7)$$

Then, from the definition of chemical potential in dilute solutions

$$\mu = \mu_0 + k_B T \ln n, \quad (1.8)$$

where k_B is the Boltzmann constant, and T is temperature, and differentiating with respect to x

$$\frac{\partial \mu}{\partial x} = \frac{k_B T}{n} \left(\frac{\partial n}{\partial x} \right). \quad (1.9)$$

Now equating Equations 1.6 and 1.7, and using the previous relationship the diffusion coefficient can be related to the mobility of the charge carriers according to the *Nernst-Einstein* equation,

$$u = \frac{qD}{k_B T}, \quad (1.10)$$

and substituting this into Equation 1.4 yields

$$\sigma = \frac{nq^2 D}{k_B T}. \quad (1.11)$$

Assuming uncorrelated motion of the charge carrying species a *random walk model* can be adopted to describe the diffusion coefficient, such that

$$D = \gamma a_0^2 \nu, \quad (1.12)$$

where γ is a geometric factor depending on the structure of the solid, a_0 is the distance the mobile charge carrier “jumps” between vacant crystallographic sites, and ν is the frequency at which the charge carrier jumps. The jumping of charge carriers between crystallographic sites is a thermally activated process, which is best described by an Arrhenius-type tem-

perature dependence,

$$\nu = \nu_0 \exp\left(\frac{-\Delta G_a}{k_B T}\right), \quad (1.13)$$

where ν_0 is the attempt frequency and ΔG_a is the Gibbs free energy for activation of this process. This leads to a diffusion coefficient that varies with an Arrhenius behaviour,

$$D = \gamma a_0^2 \nu_0 \exp\left(\frac{-\Delta G_a}{k_B T}\right) \quad (1.14)$$

$$= D_0 \exp\left(\frac{-\Delta G_a}{k_B T}\right), \quad (1.15)$$

where the pre-exponential factor $D_0 = \gamma a_0^2 \nu_0$. The Gibbs free energy of activation can be expressed in terms of an activation entropy ΔS_a and enthalpy ΔH_a

$$\Delta G_a = \Delta H_a - T \Delta S_a. \quad (1.16)$$

Similarly, the activation enthalpy can be expressed in terms of an activation energy ΔE_a and volume ΔV_a

$$\Delta H_a = \Delta E_a + P \Delta V_a, \quad (1.17)$$

where the activation volume is often neglected at ambient pressures. Using these thermodynamic relationships and combining Equations 1.4, 1.10, and 1.14 the Arrhenius relationship for the conductivity of a solid can be written as

$$\sigma T = A_0 \exp\left(\frac{-\Delta H_a}{k_B T}\right) = A_0 \exp\left(\frac{-\Delta E_a - P \Delta V_a}{k_B T}\right), \quad (1.18)$$

where the pre-exponential factor A_0 is

$$A_0 = \frac{D_0 n q^2}{k_B} \exp\left(\frac{\Delta S_a}{k_B}\right) \quad (1.19)$$

$$= \frac{\gamma a_0^2 \nu_0 n q^2}{k_B} \exp\left(\frac{\Delta S_a}{k_B}\right). \quad (1.20)$$

Thus, we have arrived at an expression for the ionic conductivity of an isotropic solid in terms of intrinsic material properties as a function of temperature that closely models the bulk behavior of real ionic solids.

1.3.1.1 Protonic Conductivity^{18,19,20}

The motion of protons in solids is unique among ionic species. The small size of protons relative to other ionic species allows for high mobility of these ions. However, the relatively small ratio of mass to charge leads to proton motion that is usually coupled with other phenomenon within a solid, such as molecular diffusion, phonons, and molecular dynamics. That is, unlike other ions, the proton rarely exists as a “bare” proton, preferring to lie within the electron density of other atoms, and its movements are usually assisted by these other phenomenon.

There are five basic mechanisms for proton motion in solids: (1) *atomic diffusion*, (2) *proton-displacement*, (3) *molecular reorientation*, (4) *vehicle mechanism*, and (5) *Grotthus mechanism*. A summary of these mechanisms, a brief description and depiction of each, and an example is given in Table 1.4.

Atomic diffusion This type of proton motion is simply coupled proton-electron diffusion, which is common in materials such as metal hydrides, like Li_3AlH_6 and Na_3AlH_6 . In such materials, the hydrogen can donate its electron density to the host matrix, accept electron density, or simply remain neutral. Due to the inherent electronic conductivity associated with these type of materials, they are of no practical interest for electrolyte studies.

Proton displacement This proton motion occurs when a proton “hops” along a hydrogen bond from one minima of a double-well potential to the other. As aforementioned, this type of proton motion is quite common in solid acid compounds, and is responsible for ferroelectric behavior in solid acids, such as KH_2PO_4 .

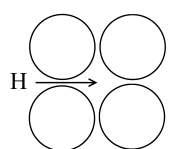
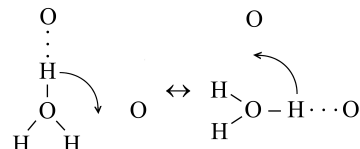
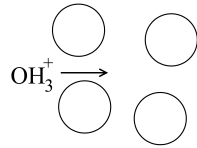
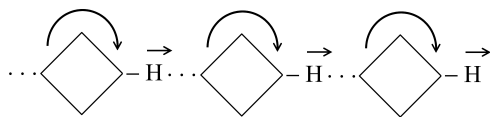
Molecular reorientation Also referred to as dipole reorientation, in this process a proton rides “piggy-back” a molecule undergoing a libration, rotation, or tumble. This motion was first proposed to describe proton transport in ice, but is also commonly observed in solid acid compounds, as well as liquid acids.

Vehicle mechanism In this mechanism, proton translation is associated with the diffusion of polyatomic species. In this type of proton motion, a proton rides “piggy-back”

on a mobile molecule, which may carry a positive charge (*e.g.* NH_4^+ , OH_3^+ , O_2H_5^+ , O_3H_7^+), a negative charge (*e.g.* NH^{-2} , OH^-), or be neutral (*e.g.* NH_3 , H_2O). The vehicle mechanism is, perhaps, the most common type of proton transport mechanism, and is exhibited by many fast-proton conductors, such as Nafion[®], in which H_3O^+ ions are transported along sulfonic acid functional groups ($-\text{SO}_3^-$), within a polymer host matrix.

Grotthus mechanism This mechanism is a cooperative process involving both a molecular (dipole) reorientation and proton-displacement. Superprotonic solid acids, such as CsHSO_4 , conduct protons via this process. In these superprotonic solid acids, the oxy-anion librates between crystallographically equivalent positions while carrying a proton with it, then the proton “hops” along a hydrogen bond to another oxy-anion, followed by another oxy-anion reorientation, and so on. Experimentally, it has been determined that the reorientation of these oxy-anions occurs at a rate of $\sim 10^{12}$ Hz, and the proton transfer (proton-displacement) rate at $\sim 10^9$ Hz, therefore, the rate limiting step in this mechanism for superprotonic solid acids is proton transfer^{21,22,23}.

Table 1.4: Basic mechanisms of proton motion, descriptions, depictions of mechanisms, and examples.

	Mechanism	Description	Example
(1)	Atomic diffusion	coupled proton-electron translation	NaAlH_6
			
(2)	Proton-displacement	intra-hydrogen bond translation	KH_2PO_4
		$\text{O} \cdots \overleftarrow{\text{H}} - \text{O} \leftrightarrow \text{O} - \overrightarrow{\text{H}} \cdots \text{O}$	
(3)	Molecular reorientation	piggy-back rotation, libration, or tumble	ice
			
(4)	Vehicle mechanism	piggy-back diffusion	Nafion [®]
			
(5)	Grotthus mechanism	proton diffusion via (2) + (3)	CsHSO_4
			

1.3.2 Phase Transitions

Phase transitions are of fundamental importance to this work as, to date, no superprotonic behavior has been observed in solid acid compounds that is not associated with a structural phase transition. Here, a general description of phase transitions will be given, as well as a specific description of superprotonic phase transitions.

1.3.2.1 General Characterization²⁴

A *phase* is a homogeneous solution of matter bounded by a surface so that it is mechanically separate from any other portion¹². Generally speaking, a *phase transition* is a transformation of matter induced by a change in a thermodynamic function, such as temperature T , pressure P , volume V , or entropy S , from one phase to another phase that is distinguishable from the first. For the purpose of this work phase transitions are identified by a discontinuous change in an extensive thermodynamic variable of a substance, such as volume V , entropy S , magnetization \mathcal{M} , polarization \mathcal{P} , or derivatives thereof, while varying an intensive variable, such as pressure P , temperature T , magnetic field \mathcal{B} , or electric field \mathcal{E} . Specifically, for transitions in which there is a discontinuous change in the entropy through the phase transition while varying temperature, there will also be a change in enthalpy ΔH or *latent heat* Q associated with the transition. This sort of phase transition is known as a *first order* phase transition. If the entropy is continuous, but its first derivative with respect to temperature, or heat capacity C_p is discontinuous,

$$C_p = T \left(\frac{\partial S}{\partial T} \right)_p, \quad (1.21)$$

the phase transition is said to be of *second order*, and if the entropy and heat capacity are continuous, and the derivative of the heat capacity $\frac{\partial C_p}{\partial T}$ is discontinuous, the transition is *third order*, and so on.

In this work, first order solid–solid phase transitions are of primary interest. For these transitions the change in extensive thermodynamic variables such as V and \mathcal{M} are negligible compared to the change in S . Therefore, the conjugate thermodynamic variables: entropy and temperature (which is the change in energy E with respect to entropy)

$$[S, T] = \left[S, \frac{\partial E}{\partial S} \right] \quad (1.22)$$

can be readily measured by calorimetry, and yield a complete thermodynamic description of such first order phase transitions.

1.3.2.2 Superprotonic Transitions

Superprotonic transitions are characterized by a discontinuous “jump” in protonic conductivity by several orders of magnitude to a superprotonic phase, which exhibit conductivity of $\sim 10^{-2} \Omega^{-1}\text{cm}^{-1}$. These solid–solid, order–disorder transitions have a latent heat associated with them, and therefore, are first order in nature. In Figure 1.7, the conductivity of the prototypical superprotonic solid acid, CsHSO_4 , is presented in an Arrhenius plot. At low temperatures, CsHSO_4 has a monoclinic ($P2_1/c$) crystal structure, and upon heating to the superprotonic phase, the structure transforms to a tetragonal ($I4_1/amd$) crystal structure of higher symmetry. Optical studies have shown that associated with this transition is a *ferroelastic* transition, in which a large spontaneous strain ($\sim 10^{-2}$) is associated with the low temperature (ferroelastic) phase²⁵.

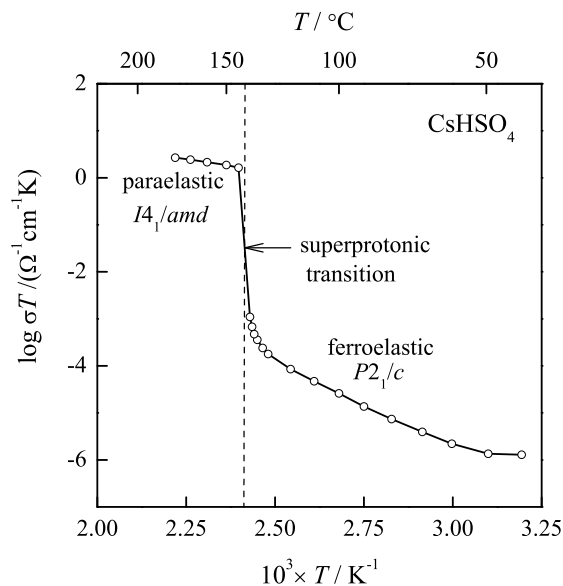


Figure 1.7: Arrhenius plot of the conductivity of CsHSO_4 measured through the superprotonic phase transition (this work), where the phase boundary is indicated by a dashed-line.

These superprotonic phase transitions exhibit properties not unlike those of solid–liquid transitions. For example, upon heating through the superprotonic phase transition temperature the sound velocity drops by nearly 50%, which is comparable to that of a solid–liquid transition²⁶. The “liquid-like” properties of these superprotonic solid acids are the result of

the highly disordered tetrahedral oxy-anions. Strictly speaking, these superprotonic compounds are solids, as they exhibit long range translational order. However, while there is no translation disorder, the rotation disorder of the oxy-anions in superprotonic solid acid is comparable to that observed in liquid H_nXO_4 acids. As one might expect, this rotational disordering through the superprotonic phase transition, also leads to dramatic changes in mechanical properties. For example, the superprotonic phase of $CsHSO_4$ has been described as having mechanical properties not unlike “clay or plasticine,”²⁷ whereas, at room temperature the mechanical properties are akin to conventional table salt. Ultimately, it is these highly disordered oxy-anions that allow for the high conductivity observed in superprotonic solid acids.

1.4 Applications: Fuel Cells

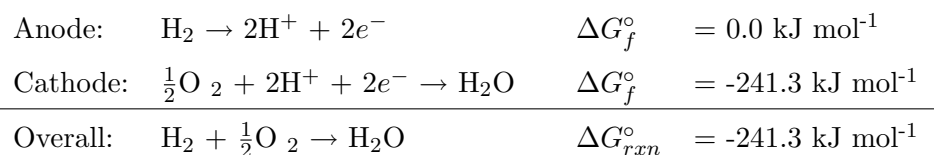
U.S. dependence on oil imports for energy is higher today than it was even during the “oil shock” of the 1970s. Passenger vehicles alone consume 6 million barrels of oil every single day, equivalent to 85% of oil imports. Fuel cell vehicles could dramatically affect these numbers. Utilization of fuel cells could reduce urban air pollution, decrease oil imports, reduce the trade deficit, and produce American jobs. The U.S. Department of Energy (DOE) projects that if a mere 10% of automobiles nationwide were powered by fuel cells, regulated air pollutants would be cut by one million tons per year and 60 million tons of the greenhouse gas carbon dioxide would be eliminated. DOE projects that the same number of fuel cell cars would cut oil imports by 800,000 barrels a day—about 13% of all oil imports²⁸. The application of solid acids in fuel cells is, therefore, motivated by this potential benefit to society.

A fuel cell can be thought of a device which has characteristics that are intermediate between those of an internal combustion engine and a battery. Like an internal combustion engine, a fuel cell uses *fuel* as a source of energy, and therefore has the potential for high energy densities, and does not need to be “charged up,” as with conventional batteries. However, like a battery *cell*, a fuel cell converts chemical potential energy directly into electricity, that is, it is an *electrochemical* device—thus, creating noiseless useful energy at very high efficiencies, as compared to internal combustion engines. Due to these advantages, fuel cells have captured the world’s attention and development is being aggressively pursued

by nearly every automobile manufacturer, as well as, manufacturers of power systems for portable electronic devices. In this section, a brief review of the basic internal workings of fuel cells, various types, and the characterization of a fuel cell's performance will be presented.

1.4.1 Fuel Cell Description

The basic internal workings of a fuel cell are best described by example. The simplest type of fuel cell is a hydrogen/oxygen fuel cell at 25°C and 1 atm (standard conditions). The thermodynamic driving force behind the operation of a fuel cell comes from the chemical reactions of the fuels. For this simple case, the Gibbs free energy for the reaction of hydrogen and oxygen can be described by two separate half cell reactions to yield the overall chemical reaction:



This chemical potential energy can be related to an electric potential or electromotive force \mathcal{E} using the *Nernst* Equation,

$$\Delta G_{rxn}^\circ = -nF\mathcal{E}_0^\circ, \quad (1.23)$$

where n is the stoichiometric number of charge carriers and F is Faraday's constant, the superscript 'o' refers to standard state conditions (25 °C, 1 atm), and the subscript '0' identifies this potential as the *theoretical open cell voltage (OCV)* or *Nernst potential*. For this reaction, the $\mathcal{E}_0^\circ = 1.25$ V. A schematic diagram of a hydrogen/oxygen fuel cell is shown in Figure 1.8. The overall process by which this fuel cell operates can be described in 7 steps: (1) hydrogen fuel is fed into the anode of the fuel cell, while (2) oxygen is fed into the cathode, (3) encouraged by a catalyst, the hydrogen atoms split into protons and electrons ($2\text{H}_2 \rightarrow 4\text{H}^+ + 4e^-$), (4) the protons are then transported through electrolyte, while (5) the electrons provide useful electricity that can provide power to a device (load), before finally (6) reuniting with the protons in the presence of oxygen gas and a catalyst, to (7) generate H_2O exhaust at the cathode ($2\text{H}_2 + \text{O}_2 \rightarrow 2\text{H}_2\text{O}$).

While the previous example is the simplest case of a fuel cell the basic mode of operation is the same for all fuel cells. However, the various types of fuel cells can differ significantly

in each of the separate components involved in the overall operation of the cell. These basic components that comprise a fuel cell are: the anode, cathode, electrolyte, catalyst, load, fuel, and oxidant. Fuel cell components can widely vary in the materials used, depending upon the type of fuel cell. In Table 1.5, a description of the essential components for the operation of a fuel cell and examples of each are given. Following is a general description of some of the most common types of fuels cells.

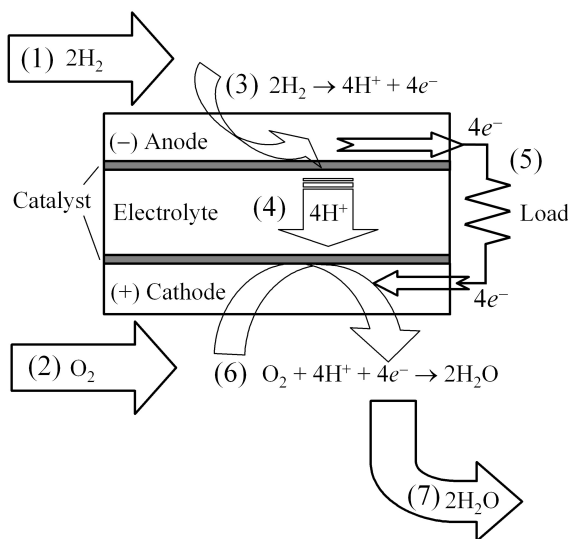


Figure 1.8: Schematic diagram of a basic H_2/O_2 fuel cell.

Table 1.5: The basic components essential to the operation of a fuel cell, and examples of each.

Component	Description	Examples
Fuel	source of chemical energy	H_2 , methanol, ethanol, methane
Oxidant	used to oxidize fuel	O_2 , air
Anode	porous electron conducting negative electrode	carbon paper, Ni
Cathode	porous electron conducting positive electrode	carbon paper
Electrocatalyst	catalyzes electrochemical reactions at anode and cathode	Pt, Pd, Ni
Electrolyte	ion conducting, electron insulating membrane, separating fuel and oxidant	Nafion [®] , ZrO_2 , CsH_2PO_4

1.4.2 Types of Fuel Cells²⁹

There are five common types of fuel cells, generally categorized according to the type of electrolyte used. Electrolytes operate optimally at different temperatures and transport different ion species depending on the type of electrolyte. An overview of these five fuel cell types is given in Table 1.6, and a brief description of each in the following sections.

Table 1.6: The most common types of fuel cells and their corresponding electrolyte, mobile ion species, operating temperatures, and fuels used.

Type	Electrolyte	Mobile Ion Species	Operating Temp.	Fuels
PEMFC polymer electrolyte membrane fuel cell	sulfonated polymer	H_3O^+	70–110°C	H_2 , CH_3OH
AFC alkali fuel cell	(Na,K)OH	OH^-	100–250°C	H_2
PAFC phosphoric acid fuel cell	H_3PO_4	H^+	150–220°C	H_2
MCFC molten carbonate fuel cell	$(\text{Na,K})_2\text{CO}_3$	CO_3^{2-}	500–700°C	hydrocarbons, CO
SOFC solid oxide fuel cell	$(\text{Zr,Y})\text{O}_{2-\delta}$	O^{2-}	500–700°C	hydrocarbons, CO

Polymer Exchange Membrane Fuel Cell (PEMFC) These cells operate at the relatively low temperatures of 80–110 °C. PEMFCs exhibit high power densities and are very reliable, as long as they remain humidified and free from catalyst poisoning gases (CO , H_2S , *etc.*). Most fuel cell systems now being developed for automotive and portable electronics are based on PEMFCs. Typical fuel cell stack outputs range from 50 W to 250 kW. The polymer exchange membrane (PEM) is a thin plastic sheet (giving it good mechanical properties) that allows hydrogen ions to pass through it when wet. The prototypical PEM, Nafion[®], developed by DuPont, is coated on both sides with highly dispersed metal alloy particles (usually Pt with loadings $\sim 0.4 \text{ mg cm}^{-2}$) that act to catalyze both the anode and cathode reactions. In the process of proton conduction, water molecules travel from the anode to the cathode resulting in the need for a water recirculation system. Due to

the limited operating temperatures and water balance issues, this type of fuel cell requires high catalyst loadings at both the anode and cathode and very pure gases (< 50 ppm of CO and S contaminants). These requirements ultimately lead to expensive gas purification systems, costly and inefficient waste heat management, and expensive water maintenance systems. Despite the drawbacks associated with PEMFCs, they continue to be the electrolyte of choice for the demonstration of automotive fuel cell power systems because of the combination of very high conductivity and adequate mechanical properties of these polymers.

Alkali Fuel Cell(AFC) Long used by NASA on space missions (*e.g.* on the Apollo spacecraft) to provide both electricity and drinking water, alkali fuel cells operate at temperatures of 100–250 °C. They use an aqueous solution of alkaline potassium hydroxide contained within an inert matrix as the electrolyte. They typically have a fuel cell stack output from 300 W to 5 kW. Alkali fuel cells, while providing extremely high power densities, are considered by most to be impractical because of the need to remove trace CO₂ from both the fuel and oxidant streams in order to prevent reaction of the electrolyte to form solid, non-conducting alkali carbonates. Nevertheless, some commercialization efforts are underway.

Phosphoric Acid Fuel Cell (PAFC) PAFCs are the most mature fuel cell technology and this type of fuel cell is commercially available today. Principal use of this type of fuel cell is for mid-to-large stationary power generation applications. Existing PAFCs have outputs of up to 11 MW. Operating temperatures are in the range of 150–220 °C. The electrolyte is 100% liquid phosphoric acid contained within an inert matrix, such as silicon carbide. PAFCs can withstand significant concentrations of the fuel cell catalyst poison carbon monoxide ($\approx 1.5\%$), a common by-product of reforming many hydrocarbon fuels. Disadvantages of PAFCs include (1) necessity for expensive platinum catalysts, (2) low current and power as compared to other types of fuel cells, (3) large in size and weight, and (4) the corrosive liquid electrolyte which requires complex system designs and negatively impacts operating life/costs. Although the leading fuel cell technology in the early 1990s, PAFCs have been largely abandoned because of the inability of developers to reach high power densities, and thus meet competitive cost targets on a per watt output basis.

Molten Carbonate Fuel Cell (MCFC) These fuel cells use an electrolyte composed of a liquid solution of lithium, sodium and/or potassium carbonates soaked in a matrix support. Typical operational temperatures are 500–700 °C. Because of these high operating temperatures which are needed to achieve sufficient electrolyte conductivity, noble metal catalysts are not required for the electrochemical oxidation and reduction processes of the fuel cell. However, these fuel cells suffer from the difficulties of containing a corrosive liquid electrolyte. In particular, dissolution of NiO at the cathode and its precipitation in the form of Ni at the anode can result in electrical shorts across the electrolyte—few U.S. researchers continue to pursue the development of this technology.

Solid Oxide Fuel Cell (SOFC) SOFCs are another highly promising type of fuel cell for high-power applications, such as industrial and large-scale central generators. Today's demonstration SOFCs utilize yttria stabilized zirconia (YSZ), containing typically 8 mol% Y, as the electrolyte, Ni-YSZ at the anode, and other electronically conducting ceramics at the cathode, which can withstand the operating temperatures of 700–1000 °C necessary for adequate ionic conduction. Solid oxide fuel cells have shown tremendous reliability when operated continuously. For example, a 100 kW system fabricated by Siemens-Westinghouse has successfully produced power for over 20,000 hrs without any measurable degradation in performance. In addition, such fuel cells offer good fuel flexibility, allowing a variety of hydrocarbon fuels to be utilized. However, SOFCs are still much too costly for widespread commercialization and they function poorly under intermittent operation. Furthermore, at such high operating temperatures, the peripheral fuel cell components can not be composed of inexpensive metals, and therefore costly ceramic components that are sensitive to thermal cycling and can lead to failure are employed.

1.4.3 Fuel Cell Performance²⁹

A perfect fuel cell would be able to deliver as much power as fuel delivered, but in practice the maximum power deliverable by a fuel cell is limited by several factors: (1) the electrolyte conductivity, (2) catalytic activity, (3) gas transport processes, and (4) inherent “leakages” across the electrolyte membrane. The performance of a fuel cell is generally characterized by measuring the electric potential, while drawing increasing amounts of current, which is then used to generate a performance “polarization” curve, such as that depicted by

the solid-line in Figure 1.9. Deviations from the theoretical open cell voltage, \mathcal{E}_0 , result from these aforementioned limitations. These “losses,” indicated in Figure 1.9, are termed *Ohmic polarization*, *activation polarization*, and *concentration polarization*. A significant limitation to the performance of a fuel cell is a result Ohmic losses, a direct consequence of slow ionic conduction in the electrolyte. A second significant source of losses, are the result of activation polarization, which is a consequence of sluggish reaction kinetics at the anode and cathode, and is directly affected by the activity of the fuel cell catalyst. Losses can also occur at high current densities, at which point concentration polarization losses result from the generation of fuel cell reaction products at a rate faster than they can be transported out of the cell—thereby diluting the fuel and lowering the overall chemical potential of the cell. The sum of these losses limits the overall performance of a fuel cell such that the measured power ($I \times \mathcal{E}$) output of a fuel cell, as a function of current, results in a characteristic peak power, indicated by the dotted-line in Figure 1.9. Last of all, inherent leakages across an electrolyte membrane can be the result of electronic conduction or fuel/oxidant cross-over through the electrolyte membrane, both of which lower the open cell voltage.

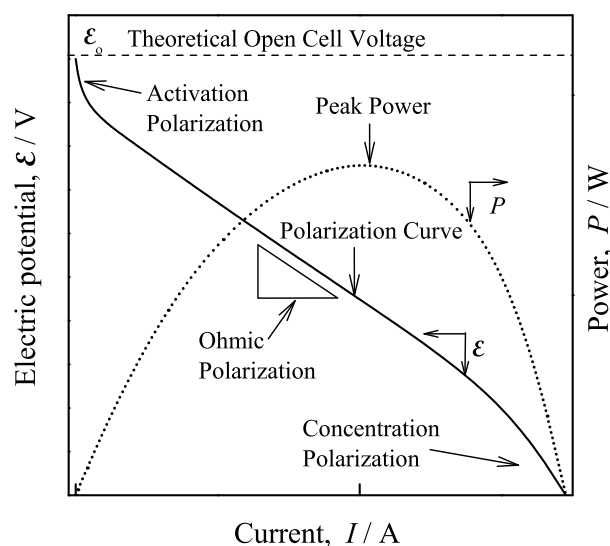


Figure 1.9: Diagram of a typical fuel cell performance characterization curves. Polarization curve, electric potential as a function of current—solid-line, and power as function of current—dotted-line.

Bibliography

1. G. Busch and P. Scherrer. Eine neue seignette-elektrische substanz. *Naturwissenschaften*, 23:737, 1935.
2. A.I. Baranov, L.A. Shuvalov, and N.M. Shchagina. Superior conductivity and phase-transitions in CsHSO₄ and CsHSeO₄ crystals. *JETP Letters*, 36(11):459–462, 1982.
3. S.M. Haile, D.A. Boysen, C.R.I. Chisholm, and R.B. Merle. Solid acids as fuel cell electrolytes. *Nature*, 410(6831):910–913, 2001.
4. Linus Pauling. *Nature of the Chemical Bond*. Cornell University Press, New York, 1960.
5. Charles Kittel. *Introduction to Solid State Physics*. John Wiley & Sons, Inc., New York, 6 edition, 1986.
6. John C. Slater. *Quantum Theory of Matter*. McGraw-Hill Book Company, Inc., New York, 1951.
7. P. Schuster, G. Zundel, and C. Sandorfy, editors. *The Hydrogen Bond: Recent Developments in Theory and Experiments*. Amsterdam: North-Holland Publishing Company, New York, 1976.
8. M. Ichikawa. O–H vs. O···O distance correlation, geometric isotope effect in OHO bonds, and its application to symmetric bonds. *Acta Crystallographica Section B–Structural Science*, 34(July):2074–2080, 1978.
9. S. M. Haile. Effect hydrogen bond symmetry. Private communications, January 1995.
10. S. M. Haile. Dimensionality of hydrogen bond networks. Private communications, February 1998.
11. A.F. Wells. *Structural Inorganic Chemistry*. Oxford University Press, London, Great Britain, 4th edition, 1975.
12. J.P. Schaffer, A. Saxena, S.D. Antolovich, T.H. Sanders, and S.B. Warner. *The Science and Design of Engineering Materials*. McGraw-Hill Companies, Inc., U.S.A., 2nd edition, 1999.
13. R.D. Shannon. Revised effective ionic-radii and systematic studies of interatomic distances in halides and chalcogenides. *Acta Crystallographica Section A*, 32(Sept 1):751–767, 1976.
14. B.C. Frazer and R. Pepinsky. X-ray analysis of the ferroelectric transition in KH₂PO₄. *Acta Crystallographica*, 6(3):273–285, 1953.
15. O. Hassel. Ueber die kristallstruktur des primaeren kaliumphosphats KH₂PO₄ und isomorpher salze. *Zeitschrift für Elektrochemie*, 31:523–529, 1925.
16. Y. Uesu and J. Kobayashi. Crystal-structure and ferroelectricity af cesium dihydrogen phosphate CsH₂PO₄. *Physica Status Solidi A–Applied Research*, 34(2):475–481, 1976.
17. A. Presinger, K. Mereiter, and W. Bronowska. The phase transition of CsH₂PO₄ (CDP) at 505 K. *Materials Science Forum*, 166:511–516, 1994.

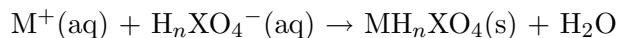
18. John B. Goodenough. *Solid State Microbatteries*, chapter Designing a Solid Electrolytes III. Proton Conduction and Composites, pages 195–212. Plenum Press, New York, 1990.
19. Philippe Colomban, editor. *Proton Conductors: Solids, Membranes, and Gels – Materials and Devices*. Chemistry of Solid State Materials. Cambridge University Press, Great Britain, 1992.
20. K.D. Kreuer. Proton conductivity: Materials and applications. *Chemistry of Materials*, 8(3):610–641, 1996.
21. A.V. Belushkin, C.J. Carlile, and L.A. Shuvalov. The diffusion of protons in the superionic conductor CsHSO₄ by quasi-elastic neutron-scattering. *Journal of Physics-Condensed Matter*, 4(2):389–398, 1992.
22. J.C. Badot and P. Colomban. RF-microwave dielectric relaxations and phase-transitions in superionic protonic acid sulfates (selenates). *Solid State Ionics*, 35(1-2):143–149, 1989.
23. M. Pham-Thi, P. Colomban, A. Novak, and R. Blinc. Phase-transitions in superionic protonic conductors CsHSO₄ and CsHSeO₄. *Solid State Communications*, 55(4):265–270, 1985.
24. D.L. Goodstein. *States of Matter*. Dover Publications, Inc., Mineola, NY, 1985.
25. A.I. Baranov, L.A. Shuvalov, and N.M. Shchagina. Superionic phase-transition in cesium deuteriosulfate and its ferroelastic properties. *Kristallografiya*, 29(6):1203–1205, 1984.
26. R. Mizeris, J. Grigas, V. Samulionis, V. Skritski, A.I. Baranov, and L.A. Shuvalov. Microwave and ultrasonic investigations of superionic phase-transitions in CsDSO₄ and CsDSeO₄. *Physica Status Solidi A-Applied Research*, 110(2):429–436, 1988.
27. L.F. Kirpichnikova, A.A. Urusovskaya, and V.I. Mozgovoi. Superplasticity of CsHSO₄ crystals in the superionic phase. *JETP Letters*, 62(8):638–641, 1995.
28. Fuel Cells 2000. Fuel Cell Basics – Benefits. <http://www.fuelcells.org/basics/benefits.html>, May 2004.
29. EG&G Services, Parsons, Inc. *Fuel Cell Handbook*. National Energy Technology Laboratory, Office of Fossil Energy, U.S. Department of Energy, P.O. Box 880, Morgantown, West Virginia 26507-0880, 5th edition, October 2000.

Chapter 2

Experimental Methods

2.1 Synthesis

One advantage to carrying out research on solid acids is the relatively easy synthesis of most compounds from aqueous solutions. In general, starting from the appropriate ions in aqueous solution in stoichiometric quantities yields the desired MH_nXO_4 -type solid acid,



where $\text{M} = \text{Li}, \text{Na}, \text{K}, \text{Rb}, \text{Tl}, \text{NH}_4$, and Cs ; $\text{X} = \text{S}, \text{Se}, \text{P}$, and As ; and $n = 1, 2$. Various methods are employed in precipitating solid acids compounds from solution: (1) heating to evaporate excess water, (2) freeze-drying to sublimate excess water, and (3) solvent introduction to exceed the solubility limit of the desired solid acid compound. The last method is preferred, as it is an inexpensive and expeditious synthesis method. For each solid acid some methods are more effective than others, and in the latter case some solvents are more productive than others. Other factors which have an effect on the synthesis of solid acid compounds are pH, synthesis temperature, and ion concentration. In the Appendix are recipes for the preparation of various solid acid compounds. In this work, single crystals were grown by slow evaporation of water at ambient temperature from aqueous solutions, where the solutions were prepared from re-dissolved powders of the desired solid acid compounds.

2.2 Structural Characterization

Two techniques were employed for the structural characterization of solid acids: (1) X-ray diffraction (XRD), and (2) nuclear magnetic resonance (NMR) spectroscopy. XRD was the principal method used for phase identification, structure determination, and crystal

orientation. Single crystal X-ray diffraction was used primarily for phase identification and crystal orientation. Phase identification and structure determination using the Rietveld method were carried out using powder X-ray diffraction (PXRD) data. Pulsed Fourier transform magic angle spinning (MAS) ^1H -NMR measurements were performed to identify the local proton environment of solid acid compounds.

2.2.1 X-ray Diffraction

Single crystal and powder X-ray diffraction are essential techniques for determining the atomic structure of crystalline solids. While single crystal X-ray diffraction techniques are preferred for the unambiguous determination of crystal structures, due to the difficulty in attaining single crystal samples and the polycrystallinity that is commonly induced by phase transitions, we often defer to PXRD. When crystal samples were available, single crystal X-ray diffraction was used primarily for phase identification and for the determination of crystal axis (crystal orientation), which would, in turn, be used to characterize other anisotropic properties of the crystal sample. In addition to routine phase identification, PXRD was also used to determine new crystal structures which were refined using the Rietveld method.

2.2.1.1 Single Crystal X-ray Diffraction

Single crystal diffraction data were collected using a Syntex four-circle diffractometer with Mo K_α radiation ($\lambda = 0.71073 \text{ \AA}$). For phase identification small ($\sim 0.15 \text{ mm}$ across) single crystals were cut from larger crystals, then attached to the end of a thin glass fiber using a common two-part epoxy. Next, the glass fiber was mounted into a cylindrical brass holder, which, in turn was placed in a goniometer. Finally, the crystal was aligned in the center of the X-ray beam. The crystal axis orientation of large crystals ($> 1 \text{ mm}$ across) was carried out by simply mounting the crystal on piece of clay attached to a goniometer head, and then aligning in the center of the X-ray beam.

2.2.1.2 Powder X-ray Diffraction

PXRD data obtained in this work were taken using either a Siemens D500 or a Philips X'Pert PRO diffractometer with Cu K_α radiation ($\lambda = 1.5418 \text{ \AA}$) and an applied voltage

and current of 45 kV and 40 mA, respectively. Data were collected at elevated temperatures using the Philips X'Pert PRO diffractometer fitted with an Anton Paar HTK 1200 high temperature furnace capable of temperatures up to 1200 °C and non-ambient atmospheres. For the identifications of phases, both ICSD (Inorganic Crystal Structure Database) and ICDD (International Centre for Diffraction Data) databases were used in conjunction with the commercial software package Philips X'Pert Highscore or the free software package PowderCell for Windows¹. When applicable, a silicon powder ground from single crystal silicon was used as an internal 2θ standard. Refinements of unknown crystal structures and the determination of lattice constants were carried out using the Rietveld method, see next section for details.

2.2.1.3 Rietveld Method^{2,3}

Rietveld analysis was carried out using the free software package Rietica⁴, as well as the commercially available software Philips X'Pert Plus. In principle the Rietveld method is based on the equation:

$$y_{ic} = y_{ib} + \sum_p \sum_{k=k_1^p}^{k_z^p} G_{ik}^p I_k, \quad (2.1)$$

where y_{ic} is the net intensity calculated at point i in the pattern, y_{ib} is the background intensity, G_{ik} is a normalised peak profile function, I_k is the intensity of the k th Bragg reflection, $k_1 \dots k_z$ are the reflections contributing intensity to point i , and the superscript p corresponds to the possible phases present in the sample. The intensity I_k is given by the expression:

$$I_k = SM_k L_k |F_k|^2 P_k, \quad (2.2)$$

where S is the scale factor, M_k is the multiplicity, L_k is the Lorentz polarization factor, and F_k is the structure factor defined by

$$F_k = \sum_{j=1}^n f_j \exp 2\pi i (\mathbf{h}_k^\top \mathbf{r}_j - \mathbf{h}_k^\top \mathbf{B}_j \mathbf{h}_k), \quad (2.3)$$

where f_j is the scattering factor or scattering length of atom j , and \mathbf{h}_k , \mathbf{r}_j and \mathbf{B}_j are matrices representing the Miller indices, atomic coordinates, and anisotropic thermal vibration parameters, respectively, and the superscript \top indicates matrix transposition. The factor

P_k is used to describe the effects of preferred orientation, where no preferred orientation is indicated $P_k = 1$.

The positions of the Bragg peaks from each phase are determined by their respective set of cell dimensions, in conjunction with a zero parameter and the wavelength provided. All of these parameters except the wavelength, may be refined simultaneously given a user defined peak profile function and crystal structure parameters.

Of the commonly employed peak profile functions (Gaussian, Lorentzian, Pseudo-Voigt, Pearson VII, and Voigt) Pseudo-Voigt was selected and used for all Rietveld refinements carried out in this work. The Pseudo-Voigt peak profile function (G_{ik}) is simply a linear combination of Gaussian (G_G) and Lorentzian (G_L) peak profile functions:

$$G_{ik} = \zeta \cdot G_G + (1 - \zeta) \cdot G_L \quad (2.4)$$

$$= \zeta \frac{c_0^{1/2}}{H_k \pi} (1 + c_0 X_{ik}^2) + (1 - \zeta) \frac{c_1^{1/2}}{H_k \pi^{1/2}} \exp(-c_1 X_{ik}^2), \quad (2.5)$$

$$(2.6)$$

where $c_0 = 4$, $c_1 = 4 \ln 2$, H_k is the full width at half maximum (FWHM) of the k th Bragg reflection, $X_{ik} = (2\theta_i - 2\theta_k)/H_k$, and ζ ($= 0$ to 1) is a refinable ‘‘mixing’’ parameter between pure Lorentzian and pure Gaussian peak profiles. The variation of the peak FWHM is described by the function:

$$H_k = \frac{1}{2}(U \tan 2\theta + V \tan \theta + W), \quad (2.7)$$

where U , V , and W are refinable peak shape parameters.

The background y_{ib} was obtained by a least square refinement of data obtained at positions where no peaks appear to contribute to the observed intensity using the function:

$$y_{ib} = \sum_{m=-1}^4 b_m (2\theta_i)^m, \quad (2.8)$$

where b_m is one of six refinable parameters.

The least-squares refinement procedure used here employs the Newton-Raphson algo-

rithm to minimize the quantity:

$$R = \sum_i w_i (y_{io} - y_{ic})^2, \quad (2.9)$$

where y_{io} is the set of observed diffraction intensities collected at each step across the pattern, y_{ic} is the set of corresponding calculated values obtained from equation 2.1, and w_i is the weight assigned to each observation (see below). The minimization of R is undertaken over all data points contributing to the peaks and the background.

Several values are used to determine the quality of a Reitveld refinement. They are defined as follows:

- The profile R -value (R_p)

$$R_p = \frac{\sum |y_{io} - y_{ic}|}{\sum y_{io}} \quad (2.10)$$

- The weighted profile R -value (R_{wp})

$$R_{wp} = \left(\frac{\sum w_i (y_{io} - y_{ic})^2}{\sum w_i y_{io}^2} \right)^{1/2} \quad (2.11)$$

- The Bragg R -value (R_B)

$$R_B = \frac{\sum |I_{ko} - I_{kc}|}{\sum I_{ko}} \quad (2.12)$$

- The expected R -value (R_{exp})

$$R_{exp} = \frac{N - P}{\sum w_i y_{io}^2} \quad (2.13)$$

- The goodness of fit (GOF)

$$\text{GOF} = \left(\frac{R_{wp}}{R_{exp}} \right)^2 \quad (2.14)$$

- Durbin-Watson statistic (d)

$$d = \frac{\sum_{i=2}^N (\Delta y_i - \Delta y_{i-1})^2}{\Delta \left(\prod_{i=1}^N y_i \right)^2},$$

where the parameters describing the values above are defined as follows:

y_{ic}	: calculated intensity at point i
y_{io}	: observed intensity at point i
w_i	: reciprocal of the variance at the i th step, $1/\sigma_i^2 = n/y_{ic} \approx n/y_{io}$
n	: number of detectors contributing to the step intensity average
I_{ko}	: observed intensity of reflection k
I_{kc}	: calculated intensity of reflection k
N	: number of observations
P	: number of adjusted parameters
Δy_i	: difference between observed and calculated intensity at a given step
i	

While, in theory, all parameters can be refined simultaneously in a Rietveld refinement, highly unstable parameters often require that parameters be systematically refined independently. For such cases, the parameter refinement strategy recommended by R.A Young³ was employed, where parameters were refined in the following order:

1. Scale of peak intensities
2. Specimen displacement
3. Zero point shift of instrument
4. First order background parameters
5. Lattice parameters: $a, b, c, \alpha, \beta, \gamma$
6. Higher order background parameters
7. Peak shape parameter: W
8. Atomic coordinates: x, y, z
9. Site occupancy and isotropic thermal parameters: N_j, B_j
10. Other peak shape parameters: U, V
11. Anisotropic thermal parameters: \mathbf{B}_j

2.2.2 Nuclear Magnetic Resonance Spectroscopy

Pulsed Fourier transform ¹H-NMR measurements were performed on finely ground samples to characterize the proton environment of selected compounds, specifically, the number of crystallographically distinct hydrogen atoms and their relative amounts. All measurements were taken on a Bruker DSX 500 MHz NMR spectrometer using tetramethylsilane (TMS) as a reference for measuring chemical shifts. Magic angle spinning (MAS) was employed

to reduce the proton-proton dipole broadening of the signal lines resulting from the local interactions of a proton's magnetic moment with the dipole fields generated by its neighbors. For most measurements, a 12 kHz spinning rate was used in conjunction with a 4 μ s, 90° pulse. The spin-lattice relaxation time t_1 was on the order of 1000 s for all compounds measured, revealing that the excited H⁺ nuclei in these solid acids interact weakly with their surrounding lattices⁵. The observed chemical shifts for the crystallographic protons were \sim 10–12 ppm, typical values for protons residing in medium strength hydrogen bonds⁵. Sharp peaks often observed at \sim 6 ppm were attributed to surface adsorbed water based upon similar phenomenon observed in calcium phosphates⁶.

2.3 Properties Characterization

Protonic conductivity was the principal property of interest in the materials examined here. For this, extensive use of alternating current (AC) impedance spectroscopy has been made to characterize the protonic conductivity of solid acid compounds as a function of temperature at both ambient and high pressures. Superprotonic behavior of solid acids compounds is (to date) always preceded by an order-disorder phase transition. Therefore, extensive effort has been made to characterize these phase transitions. Thermal analysis to measure the enthalpy and temperature of these transitions, as well as to evaluate decomposition behavior, has been an essential tool in these investigations. Furthermore, changes in optical properties resulting from these order-disorder transitions observed through optical polarized light microscopy were used to identify superprotonic phase transitions.

2.3.1 Impedance Spectroscopy⁷

The advantage of an AC method is that there is no *net* movement of ions, thereby eliminating the need for an ion source. This method is implemented by placing an ionic conducting material under an alternating electric field \mathcal{E} , with an angular frequency of ω and amplitude \mathcal{E}_0 , which can be described by the complex time (t) dependent wave function

$$\mathcal{E}(t) = \mathcal{E}_0 \cdot e^{i\omega t}. \quad (2.15)$$

The current response $I(t)$ generated by this electric field in the material being tested, as depicted in Figure 2.1, can be described by a similar time dependent wave function with some amplitude I_0 , plus some phase shift ϕ ,

$$I(t) = I_0 \cdot e^{i(\omega t + \phi)}. \quad (2.16)$$

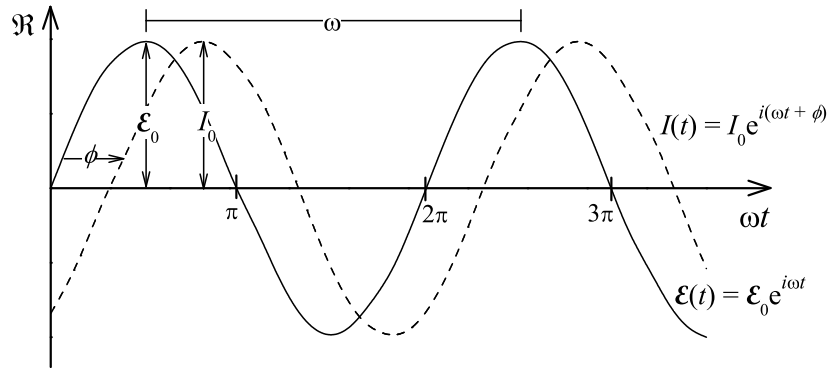


Figure 2.1: Depiction of the real (\Re) component of an alternating applied electric field $\mathcal{E}(t)$ with an amplitude \mathcal{E}_0 and angular frequency ω (solid line), and the real component of the induced current response $I(t)$ of a material with an amplitude I_0 and angular frequency ω phase shifted by some amount ϕ (dashed line).

From Ohm's law,

$$\mathcal{E}(t) = I(t) \cdot Z, \quad (2.17)$$

where Z is the complex impedance characterized by a real component Z' and an imaginary component Z'' ,

$$Z = Z' + iZ''. \quad (2.18)$$

It is convenient to define the reciprocal of impedance, or admittance Y , as

$$Y \equiv \frac{1}{Z} = Y' + iY''. \quad (2.19)$$

Rewriting Ohm's law using admittance

$$Y(\phi) = \frac{I(t)}{\mathcal{E}(t)} = \frac{I_0 e^{i(\omega t + \phi)}}{\mathcal{E}_0 e^{i\omega t}} = \frac{I_0}{\mathcal{E}_0} (\cos \phi + i \sin \phi). \quad (2.20)$$

When a material's current response is at frequency at which no phase shift occurs ($\phi = 0$),

then equation 2.20 becomes

$$Y(0) = \frac{I_0}{\mathcal{E}_0} = \frac{1}{R}, \quad (2.21)$$

where R is taken to be the real resistance of the material under test. As the frequency ω increases, the material's current response due to mobile charge carriers begins to lag behind the applied electric field by some phase shift ϕ . This, in turn, leads to a capacitive response from the material under test. This capacitive response is at a maximum at some characteristic frequency ω_0 , when the current response is exactly 90° out of phase with the applied electric field, or when $\phi = \frac{\pi}{2}$. Capacitance C , defined in terms of applied electric field and charge q ,

$$C \equiv \frac{q(t)}{\mathcal{E}(t)}, \quad (2.22)$$

can be used to evaluate the imaginary component of the admittance, by substituting in for $q(t)$ into the definition of current,

$$I(t) \equiv \frac{d}{dt}q(t) = C \frac{d}{dt}\mathcal{E}(t). \quad (2.23)$$

Now, substituting in for $\mathcal{E}(t)$, using equation 2.15, gives

$$I(t) = i\omega C \mathcal{E}(t). \quad (2.24)$$

From Ohm's law, equation 2.20, and the above result, the imaginary component of the admittance for $\phi = \frac{\pi}{2}$ is

$$Y\left(\frac{\pi}{2}\right) = \frac{I(t)}{\mathcal{E}(t)} = i\omega C. \quad (2.25)$$

With the real and imaginary components (at $\phi = 0$, and $\frac{\pi}{2}$, respectively) of the complex admittance the complete polar form can be written:

$$Y = Y' + iY'' = \frac{1}{R} + i\omega C. \quad (2.26)$$

Similarly, with some rearranging the complex impedance can be written:

$$Z = \frac{1/R}{(1/R)^2 + (\omega C)^2} - i \frac{\omega C}{(1/R)^2 + (\omega C)^2}. \quad (2.27)$$

It should be noted that a similar analysis could have been carried out using the impedance,

rather than the admittance; however, the result is an expression in which the real component of the impedance *increases* with frequency, which is not phenomenological.

In Figure 2.2, the complex impedance as a function of frequency ω or “Nyquist” plot of equation 2.27 is presented. Here the apex is defined by a characteristic frequency ω_0 in terms of the resistive and capacitive response of the material under test,

$$\omega_0 = \frac{1}{RC}, \quad (2.28)$$

and the diameter of the semi-circle is given by the real resistance of the material R . These results lead naturally to a phenomenological equivalent RC circuit model, depicted in Figure 2.3, which is commonly employed in the analysis of AC impedance results.

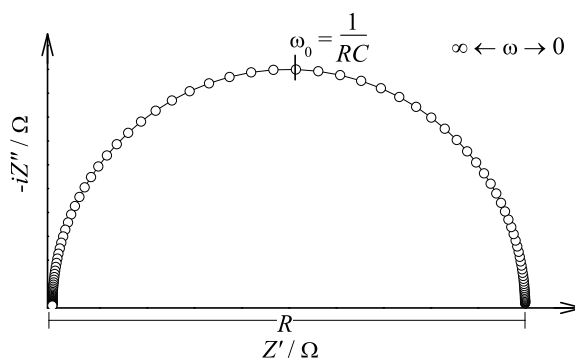


Figure 2.2: Nyquist plot (Z' versus $-iZ''$) of the AC impedance of a material as a function of frequency ω . The diameter of the the semi-circle yields the real resistance R of a material, whereas the apex occurs at a characteristic frequency ω_0 equal to $1/RC$.

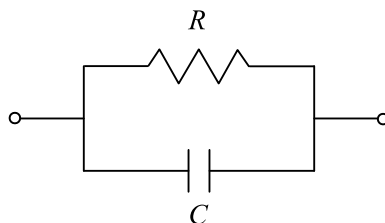


Figure 2.3: A resistor (R) in parallel with a capacitor (C) circuit used to model the AC impedance response of a material.

Real material impedance responses rarely exhibit perfect RC equivalent circuit behavior. The most prominent deviation observed in real material impedance spectra is a depression of the observed semi-circle in a Nyquist plot, shown in Figure 2.4. Phenomenologically,

this behavior is accounted for by introducing a new circuit element Q , or constant phase element (CPE), in place of the capacitor. Where Q is defined as

$$Q \equiv (i\omega)^n Y_0, \quad (2.29)$$

where n and Y_0 are parameters characterizing element Q . The admittance of an RQ circuit is

$$Y = \frac{1}{R} + Q = \frac{1}{R} + (i\omega)^n Y_0, \quad (2.30)$$

where in the limit as n goes to one, we get our previous RC circuit,

$$\lim_{n \rightarrow 1} \left(\frac{1}{R} + (i\omega)^n Y_0 \right) = \frac{1}{R} + i\omega C. \quad (2.31)$$

Unfortunately, no good physical description has yet been given for element Q , nevertheless it is of considerable utility in least square refinements of real data sets.

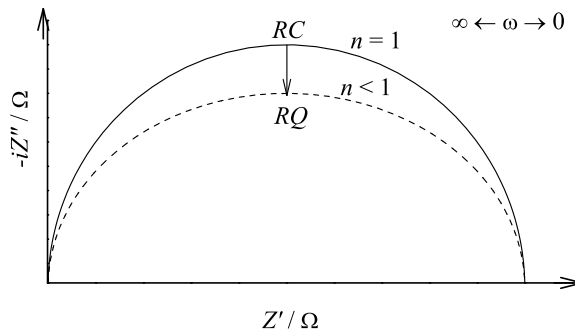


Figure 2.4: Nyquist plots of RC and RQ equivalent circuits, where R is a resistor, C a capacitor, and $Q (= (i\omega)^n Y_0)$ a constant phase element depicting the apex depression often observed in real AC impedance spectra.

The conductivity of materials was characterized by this method using an HP 4284A Precision LCR Meter, in the frequency range of 20 Hz to 1 MHz and an applied voltage of 1.0 V. Both single crystal samples and polycrystalline pellets were measured, with Ted Pella silver paint serving as the electrode material. Data were collected on samples upon heating and cooling in a tube furnace capable of temperatures up to 1200 °C under various atmospheres.

Least squares refinements using the previously described RQ equivalent circuit model were carried out using the commercially available software package, ZView (Scribner &

Associates). The refined material resistance R was then normalized by a geometric factor A/l , where A is the area of the sample and l is the thickness of the sample to obtain the conductivity σ ,

$$\sigma = \frac{1/R}{A/l}. \quad (2.32)$$

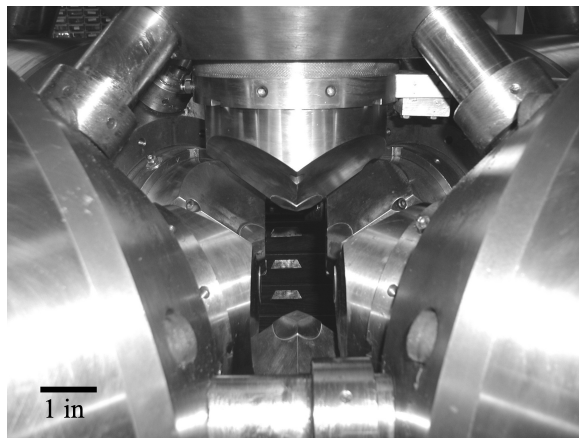
Then plotting the conductivity σ data as function of temperature T , in an Arrhenius plot ($\ln \sigma T$ versus $1/T$), the Arrhenius law:

$$\sigma(T) = \frac{A_0}{T} \exp\left(\frac{-\Delta H_a}{k_B T}\right), \quad (2.33)$$

where k_B is the Boltzmann constant, was used to extract the activation enthalpy ΔH_a and pre-exponential factor A_0 for protonic transport.

2.3.2 High-Pressure Impedance Spectroscopy

Though in principle high-pressure impedance measurements are no different than at ambient pressure, in reality these measurements are experimentally challenging to perform—appropriate equipment and careful sample preparation are essential. For these measurement a large-volume 1000-ton cubic anvil press (H.T. Hall Inc.) was employed, shown in Figure 2.5.



(a) Full view of experimental set-up

(b) Close-up view of anvils where cell is loaded

Figure 2.5: Photos of large-volume 1000-ton cubic anvil hydraulic press. (a) Full view of experimental setup, and (b) close-up view of anvils where high-pressure cell is loaded. (Photos courtesy of R.A. Secco⁸)

Powder samples, lightly ground from single crystals, were packed into a boron nitride

(BN) cup with platinum electrodes on top and bottom. The cup was then placed into an AC impedance high-pressure cell, a schematic of which is shown in Figure 2.6. The pressure cell assembly was in turn loaded into a large-volume press, Figure 2.5(b). Each anvil, in electrical isolation from the other, makes contact through the faces of the cube with the Pt electrodes, Pt/Pt10%Rh thermocouple, and Nb foil heater. In such a design, quasi-hydrostatic pressure is maintained by 12 gaskets formed by extrusion of the oversized pyrophyllite cube along its edges. Details of the experimental apparatus and pressure calibration are given elsewhere^{9,10}. Impedance measurements were performed from room temperature up to ~ 375 °C at 1.0 ± 0.2 GPa upon heating and cooling. A pressure-temperature correction was applied to the readings obtained from the Pt/Pt10%Rh thermocouple¹¹. AC impedance data were collected using a Solartron SI 1260 Impedance/Gain-Phase Analyzer over the frequency range 10 Hz to 1 MHz and with an applied voltage of 1.0 V. Data analysis was again performed using the commercial software package, ZView (Scribner & Associates).

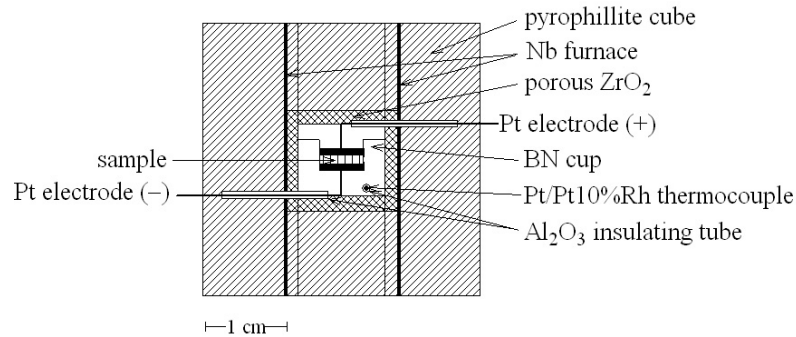


Figure 2.6: Cross-sectional schematic view of a high-pressure cell assembly used for AC impedance measurements.

Because the sample cannot be directly observed in the high-pressure cell, one must establish whether measured changes in conductivity are due to melting of the sample or to a true solid-solid transition. To achieve this, a second high-pressure ball drop experiment was performed. In this experiment, a 0.5 mm diameter ruby sphere and a 0.6 mm diameter tungsten carbide (WC) sphere, with 1 atm 22°C densities of 4.0 g cm^{-3} and 14.9 g cm^{-3} , respectively, were placed on top of a powder sample packed into a BN cup, as shown in the schematic in Figure 2.7. The pressure cell was loaded into the same large-volume press utilized in the previous high-pressure impedance measurements, the pressure and temperature raised to 1.0 ± 0.2 GPa and to the highest temperature attained for the high-

pressure impedance measurement, respectively, and held under these conditions for ~ 10 minutes. Observation of recovered samples, in which the ruby and WC spheres remained suspended over the sample indicated that melting had not occurred.

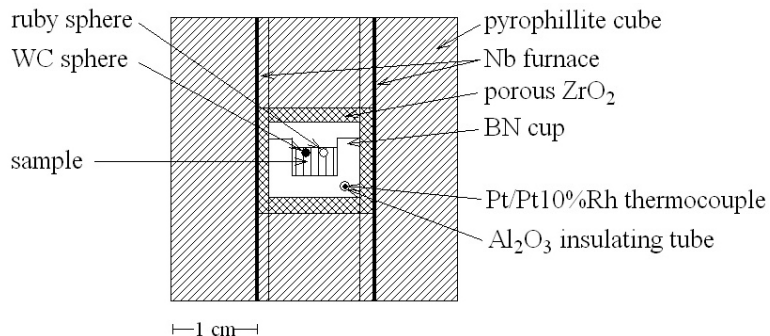


Figure 2.7: Cross-sectional schematic view of a high-pressure cell assembly used for ball drop experiments.

2.3.3 Thermal Analysis

Thermal analysis was utilized for the characterization of phase transitions and decomposition behavior of solid acids. Analysis was performed using Perkin Elmer DSC 7, as well as a Netzsch STA 449C thermal analyzer, capable of simultaneous differential scanning calorimetry (DSC) and thermal gravimetry (TG), equipped with a Pfeiffer Vacuum Thermal Star mass spectrometer for the analysis of evolved gasses under various flowing atmospheres and heating rates. Phase transitions were characterized by an endothermic or exothermic event observed by DSC upon heating or cooling samples, whereby the enthalpy (heat) of the transition ΔH_{tr} and transition temperature T_{tr} were measured to yield the changes in entropy at the transition ΔS_{tr} ,

$$\Delta S_{tr} = \frac{\Delta H_{tr}}{T_{tr}}, \quad (\Delta G_{tr} = 0). \quad (2.34)$$

Decomposition behavior was identified by weight-losses observed by TG and DTG (differential thermal gravimetry), and further aided by the analysis of evolved gasses by mass spectroscopy.

2.3.4 Polarized Light Microscopy¹²

Polarized light microscopy is an ideal tool for observing phase transitions in optically transparent anisotropic crystals. Isotropic materials, such as unstressed glasses and cubic crystals, demonstrate the same optical properties in all directions. They have only one refractive index, and therefore, no restriction on the vibration direction of light passing through them. Anisotropic materials, in contrast, have optical properties that vary with the orientation of incident light with respect to the crystallographic axes. They demonstrate a range of refractive indices depending both on the propagation direction of light through a substance and on the vibrational plane coordinates. By placing an anisotropic crystal with unique crystal axes, whose directions are represented by vectors \mathbf{a} ,

$$\mathbf{a} = a_x \hat{x} + a_y \hat{y}, \quad (2.35)$$

and \mathbf{b} ,

$$\mathbf{b} = b_x \hat{x} + b_y \hat{y}, \quad (2.36)$$

between two crossed-polarizers, where the polarizing direction of the first polarizer \mathbf{p}_1 is parallel to the x -axis,

$$\mathbf{p}_1 = \hat{x}, \quad (2.37)$$

and orthogonal to the second polarizer \mathbf{p}_2 , which is then parallel to the y -axis,

$$\mathbf{p}_2 = \hat{y}, \quad (2.38)$$

and then rotating the crystal, the optical axes of the crystal can be identified. To achieve this, we begin by describing how an anisotropic crystal behaves between cross-polarizers. First of all, when the incident beam, travels through the first polarizer, all vibrational directions, except those parallel to the x -axis are filtered out, Figure 2.8. The remaining “polarized” light beam then enters the crystal, which acts as beam splitter and divides light ray into two parts, such that the polarized light vector, \mathbf{v}_1 , can be written as a linear combination of the crystal vectors \mathbf{a} and \mathbf{b} ,

$$\mathbf{v}_1 = a_1 \mathbf{a} + b_1 \mathbf{b}, \quad (2.39)$$

to give two new light ray vectors \mathbf{v}_a and \mathbf{v}_b ,

$$\mathbf{v}_a = a_1(a_x\hat{x} + a_y\hat{y}), \quad (2.40)$$

$$\mathbf{v}_b = b_1(b_x\hat{x} + b_y\hat{y}). \quad (2.41)$$

After the light has passed through the crystal, it enters the second polarizer, which filters out all light, but that which is along the y -axis, such that

$$\mathbf{p}_2 \cdot \mathbf{v}_a = a_1a_y\hat{y} \quad (2.42)$$

$$\mathbf{p}_2 \cdot \mathbf{v}_b = b_1b_y\hat{y}, \quad (2.43)$$

and the final observable light ray \mathbf{v}_2 is

$$\mathbf{v}_2 = (a_1a_y + b_1b_y)\hat{y}. \quad (2.44)$$

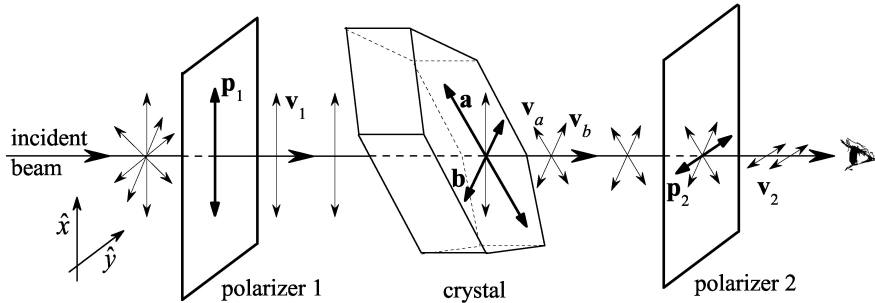


Figure 2.8: Diagram of an anisotropic crystal beam-splitting light between crossed-polarizers.

If, for example, the first polarizer is parallel to the \mathbf{a} direction of the crystal ($\mathbf{a} \parallel \mathbf{p}_1$), then all of the light passing through the crystal will be composed of \mathbf{a} , such that after passing through the second polarizer, no light will be observed

$$\mathbf{v}_2 = \mathbf{p}_2 \cdot \mathbf{v}_a = \hat{y} \cdot a_1a_x\hat{x} = 0. \quad (2.45)$$

This is known as the *extinction position* of the crystal, which can similarly be determined

for when \mathbf{b} is parallel to the either of the polarizing axes. Therefore, by simply rotation the crystal between the crossed-polarizers, the extinction positions, and thus, crystal axis can quickly be identified. However, when the crystal is isotropic, no distinction can be made between crystal axes, and therefore, the crystal is observed to be black if the crystal is not optically active, or of uniform illumination if optically active, when rotated between crossed-polarizers.

In this work, a transmission optical microscope, Leica DM LB polarized light microscope, was employed and fitted with an “in-house” built thermal stage capable of temperatures of ~ 270 °C under ambient atmospheres. Order-disorder phase transitions were identified upon heating crystals under the microscope, and observing whether the optical properties of the crystal became isotropic.

Bibliography

1. W. Kraus and G. Nolze. Powdercell for Windows, version 2.4. Federal Institute for Materials Research and Testing, Rudower Chaussee 5, 12487 Berlin, Germany, 2000.
2. J.E. Post and D.L. Bish. *Modern Powder Diffraction*, chapter 9. Rietveld Method Refinement of Crystal Structures Using Powder X-ray Diffraction Data, pages 277–308. Reviews in Mineralogy. Mineralogical Society of America, Washington, D.C., 1989.
3. R.A. Young, editor. *The Rietveld Method*, volume 5 of *International Union of Crystallography Monographs on Crystallography*. Oxford University Press, New York, 1995.
4. B.A. Hunter and C.J. Howard. Rietica: A Computer Program for Rietveld Analysis of X-Ray and Neutron Powder Diffraction Patterns. Australian Nuclear Science and Technology Organization, Lucas Heights Research Laboratories, Private Mailbag 1, Menai 2234 N.S.W., Australia, 2000.
5. R.J. Abraham. *Introduction to NMR Spectroscopy*. John Wiley & Sons, Chichester, New York, c1988.
6. J.P. Yesinowski and H. Eckert. Hydrogen environments in calcium phosphates – H-1 MAS NMR at high spinning speeds. *Journal of the American Chemical Society*, 109(21):6274–6282, 1987.
7. J. Ross Macdonald, editor. *Impedance Spectroscopy*. John Wiley & Sons, Inc., U.S.A., c1987.
8. R.A Secco, 2003. Department of Earth Sciences, University of Western Ontario, London, Ontario, N6A 5B7, Canada.
9. R.A. Secco. High- P,T physical property studies of earths interior – thermoelectric-power of solid and liquid Fe up to 6.4 GPa. *Canadian Journal of Physics*, 73(5-6):287–294, 1995.
10. R.A Secco. Proceedings of the Joint International Association for Research and Advancement of High Pressure Science and Technology and American Physical Society Topical Group on Shock Compression of Condensed Matter Conference, Colorado Springs, Colorado, June 28–July 2, 1993. In S.C. Schimdt, J.W. Shaner, G.A. Samara, and M. Ross, editors, *High Pressure Science and Technology*, New York, NY, USA, c1994. AIP Press.
11. F.P. Bundy. Effect of pressure on EMF of thermocouples. *Journal of Applied Physics*, 32(3):483, 1961.
12. Elizabeth A. Wood. *Crystals and Light*. Dover Publications, Inc., New York, NY, 2nd edition, 1977.

Chapter 3

Structure of Superprotonic MH_nXO_4 -type Solid Acids

This chapter will address some of the structural features affecting the presence of superprotonic behavior in solid acid compounds—specifically, hydrogen bonding and cation to oxy-anion size effects in MH_nXO_4 -type solid acid compounds (where M = monovalent cation, X = S, Se, P, As, and $n = 1, 2$). An effort has been made, in this chapter, to focus on the structural aspects of superprotonic solid acids, leaving inquiries relating to the properties of superprotonic phase transitions to be addressed in the next chapter. However, there is an intimate relationship between the structure and the properties of a material; that is, it is the observable properties of a material that give us insight into its structure, while it is the structure of a material that dictates its properties. This distinction between structure and properties is particularly vague in the case of superprotonic solid acids, in which such compounds exhibit a characteristic superprotonic transition to a highly disordered structure that is identified by its high protonic conductivity. As such, it will often be the case here that the structure of solid acids will be investigated by examining their properties, and vice versa.

3.1 Hydrogen Bonding

While it is well known that in solid acids containing partially hydrogen-bonded oxy-anions, such as CsHSO_4 ¹ and $\text{Rb}_3\text{H}(\text{SeO}_4)_2$ ², the existence of a superprotonic phase in *fully* hydrogen-bonded solid acids, such as CsH_2PO_4 , RbH_2PO_4 , and KH_2PO_4 , has been under dispute for quite some time. In this work, significant effort has been made to determine whether or not these fully hydrogen-bonded solid acids have superprotonic phase transi-

tions. Previous efforts to identify superprotonic conductivity in these compounds has been impeded by dehydration processes that often mask high temperature phase behavior, complicating the identification of a superprotonic phase. Here we set out to answer the question: *Can fully hydrogen-bonded solid acids exhibit superprotonic phase transitions?*

Because entropy drives all phase transitions, we began by looking at the entropic driving forces that encourage superprotonic phase transitions. The superprotonic phase in CsHSO_4 is known to exhibit hydrogen bond disorder³. In Figure 3.1, a simple two-dimensional model depicting hydrogen-bonded tetrahedral oxy-anions is presented. CsHSO_4 at room temperature, like Figure 3.1(a), exhibits two hydrogen bonds (solid circles) per tetrahedron, that is, 2 of the 4 possible hydrogen bond positions are occupied. Based upon this model, the configurational entropy S , as a function of the number of possible configurations Ω that would be gained by the hydrogen bonds being disordered is

$$S = R \ln \Omega = R \ln \binom{4}{2} = R \ln 6 = 14.9 \text{ J mol}^{-1}\text{K}^{-1}, \quad (3.1)$$

where R is the molar gas constant. This result is in close agreement with the reported experimental value of $14.8(6) \text{ J mol}^{-1}\text{K}^{-1}$ ⁴. Now, if we consider a fully hydrogen-bonded solid acid as depicted in Figure 3.1(b), such as CsH_2PO_4 , where there are 4 hydrogen bonds for 4 hydrogen bond positions. Then, the configuration entropy using this model would be

$$S = R \ln \binom{4}{4} = R \ln 1 = 0 \text{ J mol}^{-1}\text{K}^{-1}. \quad (3.2)$$

Therefore, based solely upon this simple model for hydrogen bond disorder, there would be *no entropic driving force* for a superprotonic phase transition in fully hydrogen-bonded solid acids, and thus, we *would not* expect such a transition.

In fact, this model is incomplete, as it does not account for oxy-anion disorder. In the following sections, background and experimental results of these investigations into the high temperature behavior of CsH_2PO_4 , RbH_2PO_4 , and KH_2PO_4 are presented. Evidence is given that demonstrates that CsH_2PO_4 and RbH_2PO_4 do, in fact, exhibit superprotonic transitions, while KH_2PO_4 does not.

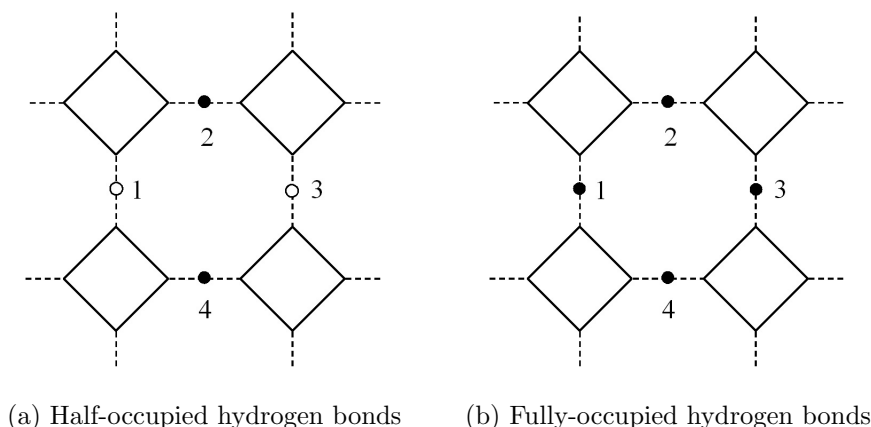


Figure 3.1: A simple model depicting hydrogen-bonded (dashed-lines) oxy-anions (squares) in solid acids, in which filled and empty circles represent occupied and unoccupied hydrogen bond positions, respectively. (a) Half-occupied hydrogen bonds, in which 2 of the 4 positions are occupied, *e.g.*, CsHSO_4 . (b) Fully occupied hydrogen bonds, in which 4 of the 4 positions are occupied, *e.g.*, CsH_2PO_4 .

3.1.1 CsH_2PO_4 ⁵

The objective of this section study is to demonstrate unequivocally whether or not CsH_2PO_4 undergoes a transition to a superprotonic phase prior to decomposition. In the first portion of this study, the dehydration and phase transition behavior, and the effect of surface water on conductivity at ambient pressures are presented. It is demonstrated that, even under ambient pressure conditions, a high temperature phase transition occurs that is independent of decomposition. The short-lived nature of this phase at ambient pressures, however, precludes accurate measurement of its electrical properties. To address this challenge, in the second portion, we employ high-pressure during conductivity measurements, with the aim of suppressing dehydration and enabling complete characterization of the high temperature phase. Before presenting the results of these sets of studies, a brief summary of the prior state of knowledge regarding the behavior of CsH_2PO_4 at elevated temperatures is given.

3.1.1.1 Background

Cesium dihydrogen phosphate, CsH_2PO_4 , has received attention because of both its high temperature proton transport properties and its low temperature ferroelectric properties. While there is wide agreement on the low-temperature behavior of this material—that it undergoes a ferroelectric phase transition at 154 K ($P2_1/m \rightarrow P2_1$)^{6,7}—there is significant discrepancy in the literature regarding its high temperature properties. It has been observed

that, upon heating, the conductivity of CsH_2PO_4 undergoes a sharp increase at $230\text{ }^\circ\text{C}$ ^{8,9,10}. Some, including Baranov *et al.*⁸, Romain and Novak¹¹, Preisinger *et al.*¹², and Luspín *et al.*¹³ attribute this behavior to a structural transition to a stable, high-temperature phase (a so-called superprotonic transition), whereas others, including Lee¹⁴ and Ortiz *et al.*⁹, attribute the increase in conductivity to an artifact of water loss due to thermal decomposition.

As aforementioned, whether or not CsH_2PO_4 undergoes a superprotonic transition is of particular relevance to understanding the role of hydrogen bonding in these phase transformations. Under ambient temperature and pressure conditions, this compound has a unique hydrogen bond network in which PO_4^{3-} oxy-anions are linked via $\text{O}-\text{H}\cdots\text{O}$ bonds at all corners of the phosphate tetrahedra, forming $[\text{H}_2(\text{PO}_4)^-]_\infty$ layers. Cesium cations reside at sites between these layers. Plakida has treated the superprotonic phase transition in the related solid acid compound, CsHSO_4 , in terms of a microscopic model that assumes an order-disorder relationship between the low and high temperature phases¹⁵. Although not stated explicitly, such a model rules out the possibility of a superprotonic transition in a compound such as CsH_2PO_4 , in which all oxygen atoms participate in hydrogen bond formation.

As an example of the controversy surrounding the high temperature behavior of CsH_2PO_4 , the thermal gravimetric and differential thermal analysis (TGA and DTA) data reported by Rashkovich *et al.*¹⁶, by Ortiz *et al.*⁹, and by Nirsha *et al.*¹⁷ are presented in Figure 3.2. It is immediately evident that there are significant discrepancies between these three sets of results. Rashkovich *et al.* have reported two structural (polymorphic) phase transitions, the onset of which occurs at 230 and $256\text{ }^\circ\text{C}$, prior to decomposition, which begins at $\sim 300\text{ }^\circ\text{C}$. Data were collected only for temperatures of $180\text{ }^\circ\text{C}$ and higher. In a later paper, Rashkovich and Meteva reported high temperature diffraction data and proposed that the formation of an intermediate phase of “symmetry no higher than monoclinic” was responsible for the transition at $230\text{ }^\circ\text{C}$ ¹⁸. In addition, they showed that the main peaks of cesium phosphite, CsPO_3 , appeared at temperatures as low as $100\text{ }^\circ\text{C}$, and that this phase was well-formed by $250\text{ }^\circ\text{C}$, although weight loss was not observed until higher temperatures were reached. Differential scanning calorimetry (DSC) measurements of Metcalfe and Clark (not shown in Figure 3.2) indicate the presence of two polymorphic transitions, one at $149\text{ }^\circ\text{C}$ (quasi-irreversible) and the latter at $230\text{ }^\circ\text{C}$ (reversible), with decomposition occurring

at temperatures above ~ 250 °C¹⁹, which is in relatively good agreement with Rashkovich *et al.* for the temperature regime of mutual examination.

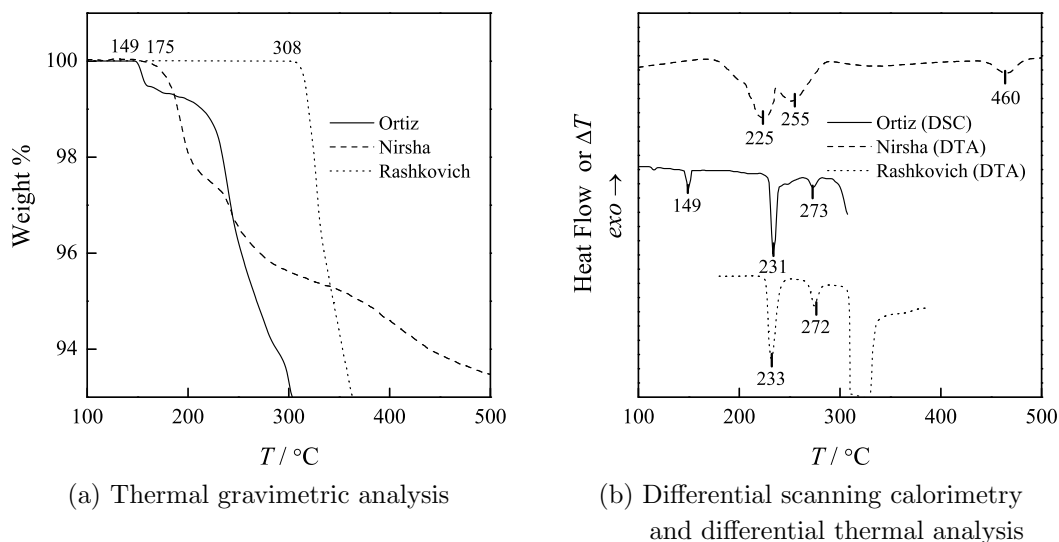


Figure 3.2: Prior thermal analysis results reported for CsH_2PO_4 by Ortiz *et al.*⁹, Nirsh *et al.*¹⁷, and Rashkovich *et al.*¹⁸; (a) thermal gravimetric analysis (TGA), and (b) differential scanning calorimetry (DSC) and differential thermal analysis (DTA) data.

In contrast, Nirsha *et al.* reported that thermal events occur at ~ 220 and 255 °C and are both due to thermal decomposition, with the compound dicesium dihydrogen pyrophosphate, $\text{Cs}_2\text{H}_2\text{P}_2\text{O}_7$, forming over the temperature range 175 – 225 °C and CsPO_3 over the range 235 – 285 °C¹⁷. This interpretation was supported by high temperature diffraction data and IR spectra. Thermal events evident in the DTA data at higher temperatures were ascribed to the crystallization of the initially amorphous CsPO_3 . The conclusions that Ortiz *et al.* draw from their results are in general agreement with the findings of Nirsha *et al.* although they differ in detail. Quite surprisingly, the DSC data of Ortiz *et al.* match the DTA data of Rashkovich *et al.*, but their TGA results differ significantly. Consistent with the results of Rashkovich *et al.*, Ortiz and coworkers observe thermal events at ~ 149 , 231 , and 273 °C, all of which coincide with peaks in their differential thermal analysis data. Accordingly, they ascribe all three, along with discontinuities in the conductivity of CsH_2PO_4 (see Figure 3.3, below) at 149 and 231 °C, to thermal dehydration and partial polymerization (*i.e.* polycondensation of phosphate groups).

A completely different interpretation of the high-temperature behavior of CsH_2PO_4 has been offered by a number of authors, specifically, that at ~ 230 °C the material transforms to

a phase of cubic symmetry with superprotonic conductivity. The conductivity of CsH_2PO_4 , as reported by several authors^{1,9,10}, is reproduced in Figure 3.3. It is evident that all authors are in agreement that the conductivity increases sharply at ~ 230 °C, while only Baranov *et al.* have attributed the increase to a transformation to a thermally stable, superprotonic phase¹. They report the activation energy for proton transport in this phase to be 0.32 eV, and the magnitude of the conductivity at 230 °C to be $2.3 \times 10^{-2} \Omega^{-1}\text{cm}^{-1}$, somewhat higher than others have observed. In contrast, Ortiz *et al.* flatly ruled out the possibility of a polymorphic phase transformation, as described above⁹. Haile *et al.* observed that the conductivity of CsH_2PO_4 immediately decreased after the transition at 230 °C, and concluded that if a superprotonic phase did indeed exist, it was a highly transient state, immediately followed by decomposition¹⁰. Prolonged examinations of the electrical properties of CsH_2PO_4 by Ortiz *et al.* showed a similar degradation in conductivity with time⁹.

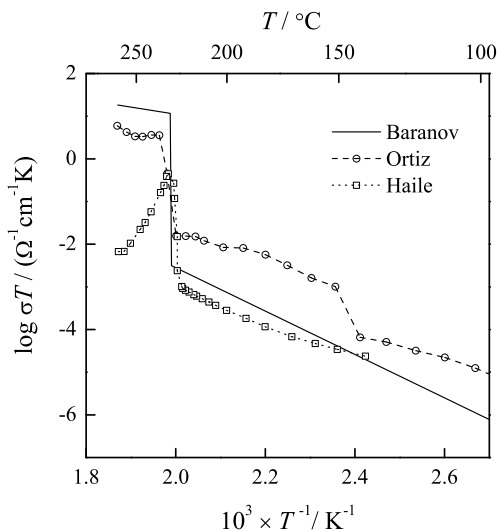


Figure 3.3: Prior conductivity data reported for CsH_2PO_4 by Baranov *et al.*⁸, Ortiz *et al.*⁹, and Haile *et al.*¹⁰, plotted in Arrhenius form.

Very convincing data for the presence of a cubic, high-temperature phase of CsH_2PO_4 has been presented by Preisinger *et al.* (see also reference²⁰), who performed diffraction experiments at elevated temperatures. Under dry atmospheres, dehydration and the formation of $\text{Cs}_2\text{H}_2\text{P}_2\text{O}_7$ was observed, but under humidified conditions, a stable cubic phase ($Pm\bar{3}m$, $a = 4.961$ Å) appeared at temperatures above 230 °C¹². Baranov *et al.* had earlier proposed that their superprotonic phase was cubic on the basis of optical microscopy

investigations, which showed the phase to be optically isotropic⁸. Further evidence for a polymorphic transition at 230 °C comes from the work of Romain and Novak, who showed by high temperature Raman spectroscopy that there is no evidence of Cs₂H₂P₂O₇ formation up to temperatures as high as 246 °C¹¹. In addition, in a comprehensive study of the high-temperature, high-pressure behavior of CsH₂PO₄, Rapoport *et al.* observed a stable, high-temperature phase, that transformed reversibly to and from the lower temperature monoclinic form at elevated pressures²¹.

In addition to the competing views as to whether the transition at 230 °C in CsH₂PO₄ corresponds to decomposition or a polymorphic transition, there is significant discrepancy regarding the behavior in the temperature regime 100–150 °C. As noted above, Ortiz *et al.* suggest that CsH₂PO₄ undergoes a thermal decomposition event at a temperature of 149 °C which, much like the transition at 230 °C, gives rise to an increase in conductivity⁹. Others have ascribed the transition at this temperature to a subtle, polymorphic, monoclinic → monoclinic transformation. Evidence for this interpretation is provided by Bronowska and Pietraszko, who observed a slight change in the thermal expansion coefficients at this temperature²⁰, and by Luspín *et al.*, who noted a small change in elastic constants¹³. Baranowski and coworkers²² observed a subtle transition, not at 149 °C, as most other groups have reported, but rather at 107 °C. What is quite clear from their work is that the thermal behavior of CsH₂PO₄ in this lower temperature regime is highly dependent on sample state and environment, that is, whether the material is subjected to mechanical grinding or has been freshly prepared, and whether the atmosphere is humid or dry. Moreover, in no case have these transitions at 107 and 149 °C been found to be reversible, nor are they associated with superprotonic conductivity. Given that the presence or absence of these transitions is not relevant to the question of whether or not a superprotonic phase can exist in a compound such as CsH₂PO₄, with its particular hydrogen bond network. Therefore, no effort was made in this work to obtain a detailed understanding of the behavior of CsH₂PO₄ in this lower-temperature regime.

3.1.1.2 Ambient Pressure Behavior

Thermal Analysis

Typical thermal analysis results for CsH_2PO_4 samples of different particle sizes and fixed heating rate ($5\text{ }^\circ\text{C min}^{-1}$) are presented in Figure 3.4. The thermal gravimetry (TG) and differential thermal gravimetry (DTG) results are shown in the top panel, differential scanning calorimetry (DSC) in the middle panel, and mass spectroscopy measurements of H_2O ($m18.00$) in the evolved gases in the bottom panel. For the complete dehydration of CsH_2PO_4 by the following reaction:



a weight loss of 7.83% is expected, as noted in the top panel. It is evident from these thermal measurements that surface area plays a significant role in the decomposition/dehydration of CsH_2PO_4 and may well explain the literature discrepancies noted above. For example, a weight loss of 7% was observed at $278\text{ }^\circ\text{C}$ for the fine powder, while for single crystals the same weight-loss was not observed until $352\text{ }^\circ\text{C}$. Quite significantly, regardless of sample surface area, in all cases a polymorphic transition, independent of decomposition, is clearly evident at $\sim 230\text{ }^\circ\text{C}$. Although the impact of this transition on conductivity cannot be assessed from thermal analysis alone, we identify this transformation as the superprotonic transition described earlier by Baranov *et al.*⁸ At temperatures just beyond this structural transformation, dehydration occurs via multiple steps. The superprotonic phase transition (SP) and what are defined here as the first (I), second (II), third (III), and fourth (IV) dehydration processes are indicated in Figure 3.4. For fine powders only dehydration processes I and II were observed, while the coarse powder and single crystals exhibited only slight or no dehydration at I and II, with the majority of dehydration taking place at high temperature processes III and IV.

The coincidence of the superprotonic phase transition with dehydration presents a challenge for the accurate measurements of the enthalpy ΔH_{SP} of the superprotonic phase transition. To address this challenge, the enthalpy of the transition was evaluated only from single crystals, in which dehydration processes I and II are minimized. A value of $49.0 \pm 2.5\text{ J g}^{-1}$ was obtained for a heating rate of $5\text{ }^\circ\text{C min}^{-1}$.

An inherent thermal lag in the thermal analysis can lead to systematic errors between true and measured transition and reaction temperatures as a function of heating rate.

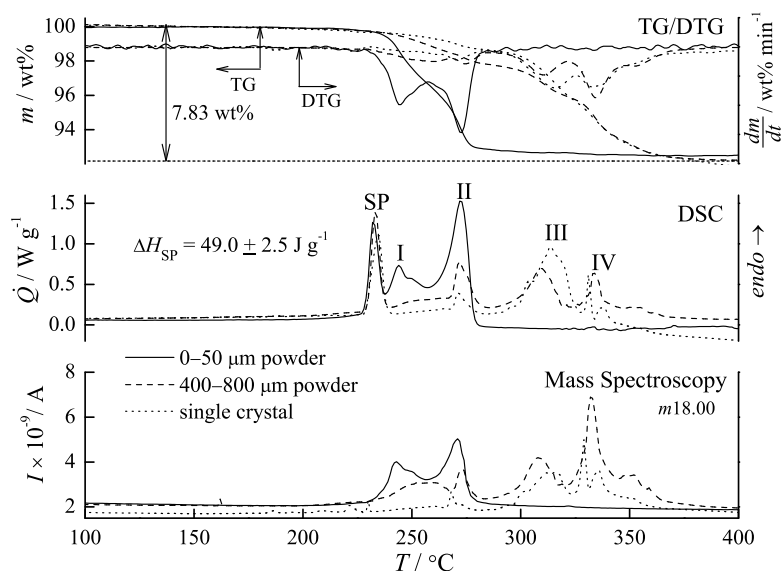


Figure 3.4: Thermal analysis of fine powder, coarse powder, and single crystals of CsH_2PO_4 heated at a rate of $5\text{ }^\circ\text{C min}^{-1}$ under flowing ($40\text{ cm}^3\text{min}^{-1}$) dry Ar. Analysis consisted of simultaneous thermal gravimetric (TG) and differential thermal gravimetric (DTG) analysis—top panel, differential scanning calorimetry (DSC)—middle panel, and mass spectroscopy of evolved H_2O vapor ($m18.00$)—bottom panel.

The temperature difference ΔT between the measured peak temperature T_{peak} and the equilibrium onset temperature T_{onset} of a transition or reaction of a pure compound is proportional to the heating rate ν , sample mass m , transition enthalpy ΔH , and the thermal resistance ρ ²³:

$$\Delta T = \sqrt{2m\nu\rho\Delta H}. \quad (3.3)$$

Assuming a constant ρ and utilizing samples of equal mass m , a linear relationship between ΔT and $\sqrt{\nu}$ can be obtained. As the heating rate $\nu \rightarrow 0$, the difference in temperature between the equilibrium onset and measured peak temperatures $\Delta T \rightarrow 0$, which implies that $T_{peak} \rightarrow T_{onset}$. Therefore, by carrying out thermal analysis at several different heating rates and extrapolating to a heating rate of zero, one can estimate the “true” onset temperature for any thermal event.

As an example of the heating-rate dependent thermal behavior of CsH_2PO_4 , a plot of the TG and DSC traces obtained at several different heating rates from a fine powder of CsH_2PO_4 is shown in Figure 3.5. Analogous results were obtained for coarse powders and single crystal samples. The T_{peak} values for each process, as measured by DSC, DTG, and mass spectroscopy, are plotted as a function of $\sqrt{\nu}$ for fine powders in Figure 3.6. The

results obtained from these three thermal analysis techniques are in good agreement. Moreover, a linear relationship between T_{peak} and \sqrt{v} is indeed evident. The true or equilibrium onset temperatures, T_{onset} , determined by extrapolation to zero heating rate for each process and for each of the three sample types are summarized in Table 3.1. As is apparent from these data, whereas T_{SP} is relatively independent of surface area, the temperature of the dehydration processes, I–IV, are not. Thus, for crystals of CsH_2PO_4 heated rapidly, the superprotonic phase transition will likely be observed before dehydration, however, if sufficiently slow heating rates ($< 0.3 \text{ }^\circ\text{C min}^{-1}$) and large surface area powders are utilized, dehydration can precede the superprotonic transition.

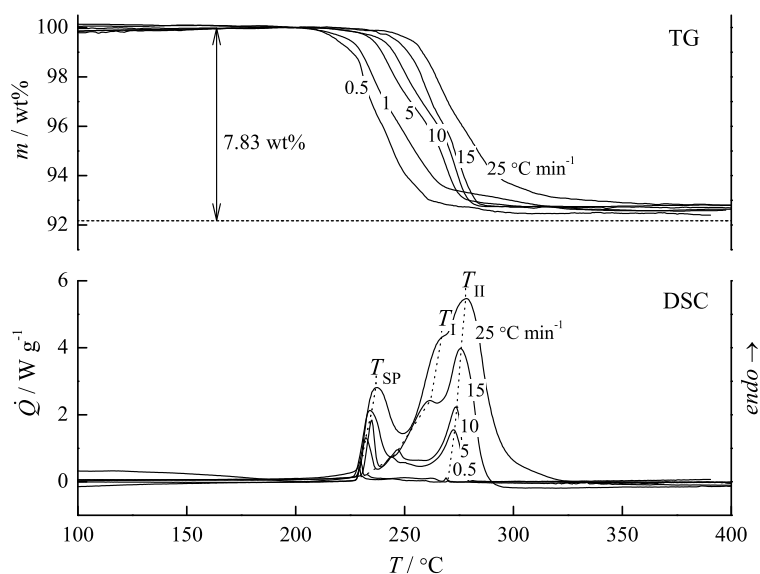


Figure 3.5: Thermal analysis of fine powders of CsH_2PO_4 heated at rates of 0.5, 1, 5, 10, 15, and 25 $^\circ\text{C min}^{-1}$ under flowing ($40 \text{ cm}^3\text{min}^{-1}$) dry Ar. Results of simultaneous thermal gravimetric (TG) analysis—top panel, and differential scanning calorimetry (DSC)—bottom panel.

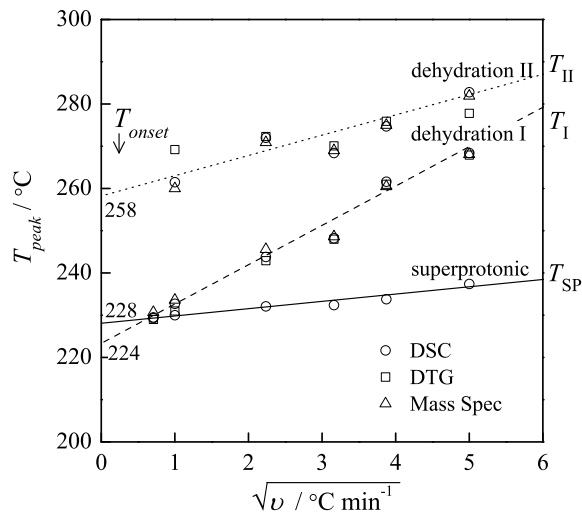


Figure 3.6: The peak temperature T_{peak} of thermal events in fine powders of CsH_2PO_4 as measured by differential scanning calorimetry (DSC), differential thermal gravimetric (DTG) analysis, and mass spectroscopy (Mass Spec) of evolved H_2O vapor ($m18.00$) plotted as function of \sqrt{v} , the square root of the heating rate employed for each measurement. Lines, calculated from a least squares fit of the data, identify the thermal events resulting from the superprotonic phase transition (SP), first dehydration process (I), and second dehydration process (II). The equilibrium onset temperature T_{onset} is indicated for each thermal event at $\sqrt{v} = 0$.

Table 3.1: Summary of measured onset temperatures for the superprotonic phase transition (T_{SP}), and the first (T_I), second (T_{II}), third (T_{III}), and fourth (T_{IV}) decomposition/dehydration processes in CsH_2PO_4 samples of various surface areas. Numbers in parentheses indicate the uncertainty in the final digit(s).

Sample Type	T_{SP}	T_I	T_{II}	T_{III}	T_{IV}	/ °C
fine powders	228(2)	224(3)	258(5)	—	—	
course powders	228(2)	230(4)	261(4)	292(5)	311(10)	
single crystals	228(2)	230(5)	261(6)	298(8)	325(12)	

Polarized Light Microscopy

Optical polarized light microscopy studies support the conclusion that single crystal CsH_2PO_4 undergoes a structural transition prior to decomposition. Typical images obtained under cross-polarizers are shown in Figure 3.7. At room temperature (prior to heating), the optically anisotropic, monoclinic form of CsH_2PO_4 was observed, Figure 3.7(a). Upon heating to ~ 245 °C, a rainbow-colored phase-front traveled from left to right across the crystal, leaving behind a new phase, which is optically isotropic (black) and presumably cubic, Figure 3.7(b) to (e). Upon cooling to room temperature, the crystal transformed back to an optically anisotropic phase, Figure 3.7(e) to (f), with some evidence of slight damage to the crystal quality. The reversible nature of this observed transformation is strong evidence for a polymorphic phase transition as opposed to decomposition.

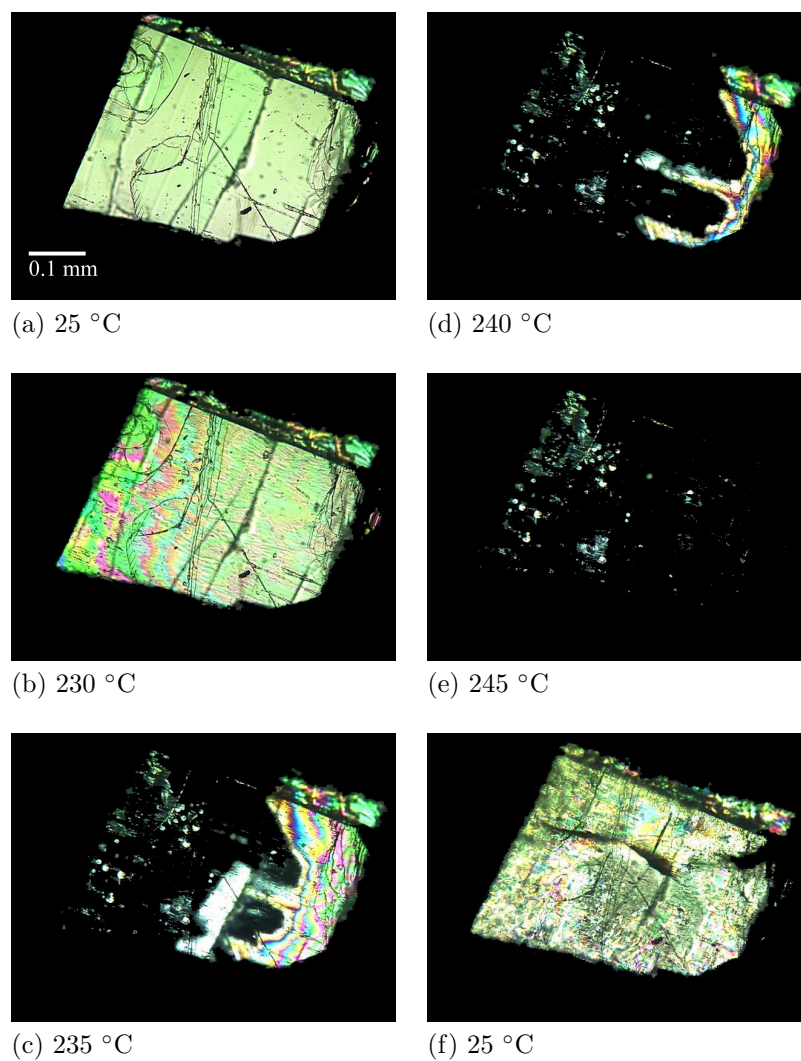


Figure 3.7: Polarized light microscopy images of a single crystal of CsH_2PO_4 taken in the sequence of temperatures: (a) 25 °C \rightarrow (b) 230 °C \rightarrow (c) 235 °C \rightarrow (d) 240 °C \rightarrow (e) 245 °C \rightarrow (f) 25 °C.

Impedance Spectroscopy

The results of AC impedance measurements for both single crystal and polycrystalline samples under ambient pressure conditions are presented in Figure 3.8 in an Arrhenius plot. Representative Nyquist plots obtained at temperatures above the superprotonic phase transition temperature T_{SP} are presented in Figure 3.9. The conductivity of both sample types increased sharply at the transition temperature, however, in neither case to the high value reported by Baranov *et al.*⁸. Moreover the jump in conductivity was significantly lower for the polycrystalline pellet than for the single crystal sample. Above T_{SP} , neither sample type exhibited a linear, Arrhenius region, as is typical for other superprotonic conductors. The polycrystalline pellet exhibited a monotonic decrease in conductivity, also evident in Figure 3.9(b), whereas the single crystal sample exhibited more erratic behavior, although the conductivity generally increased from 245 to 260 °C, Figure 3.9(a). As might be expected, the high-temperature behavior of CsH_2PO_4 was highly sample dependent, with polycrystalline samples and small single crystals typically exhibiting lower conductivity and lower stability above T_{SP} than large single crystals. These results are consistent with previous investigations, in which the electrical behavior of the superprotonic phase could be observed, such as by Baranov *et al.*,⁸ for sufficiently large crystals, whereas for smaller crystals, dehydration prevented such observations.¹⁰ In almost every case, samples measured upon cooling, either single crystals or polycrystalline pellets, did not exhibit conductivities as high as that obtained upon heating (not shown), indicating that the sample had undergone some degree of decomposition at elevated temperatures.

At temperatures below T_{SP} , a large difference between the conductivities of the single crystal (*b*-axis oriented) and polycrystalline samples is evident, Figure 3.8. Furthermore, both appear more conductive than the CsH_2PO_4 reported by Baranov *et al.*⁸ Fitting the conductivity σ of the CsH_2PO_4 single crystal to an Arrhenius law ($\sigma T = A_0 \exp \Delta H_a/k_B T$), yields a pre-exponential factor A_0 of $4.0(2) \times 10^6 \Omega^{-1}\text{cm}^{-1}\text{K}$ and activation enthalpy ΔH_a of 0.91(4) eV. Values of A_0 and ΔH_a for the polycrystalline samples are not reported here as they were highly dependent on sample history. Specifically, upon drying for long periods the conductivity of polycrystalline pellets gradually decreased.

The apparent discrepancy between the conductivities of the single crystal and polycrystalline samples of CsH_2PO_4 was further investigated by measuring the conductivity of a

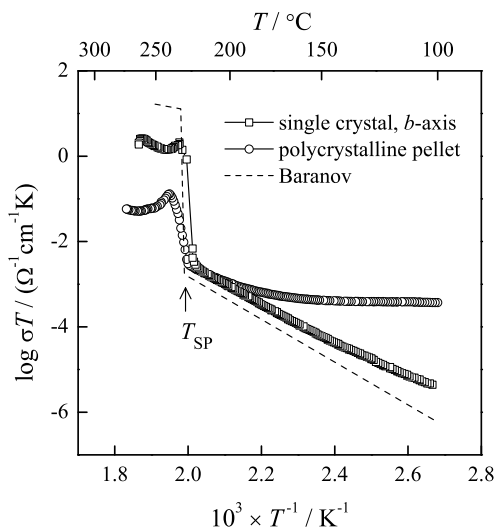


Figure 3.8: Arrhenius plot of the conductivity upon heating at $0.5 \text{ }^\circ\text{C min}^{-1}$ under flowing dry N_2 a CsH_2PO_4 single crystal and polycrystalline pellet, as compared to Baranov *et al.* results⁸. The temperature of the superprotonic transition is indicated by T_{SP} .

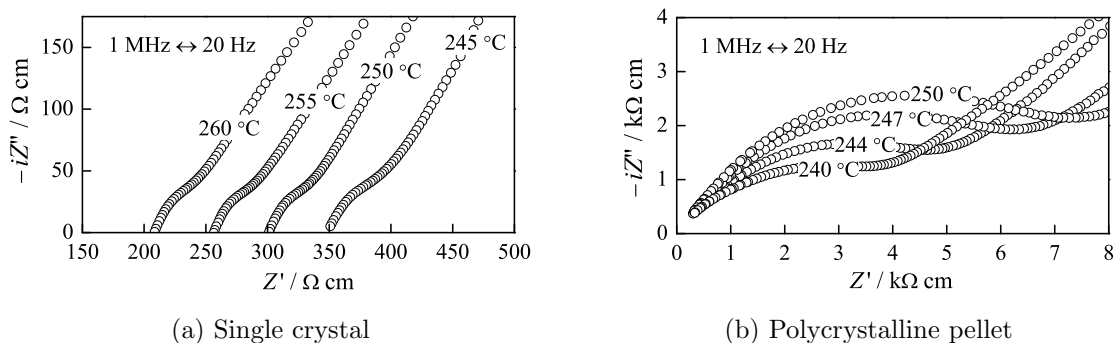


Figure 3.9: Nyquist plots at various temperatures of CsH_2PO_4 upon heating above the superprotonic transition temperature T_{SP} for (a) a single crystal, and (b) a polycrystalline pellet.

polycrystalline pellet as a function of time at $200 \text{ }^\circ\text{C}$ under flowing dry N_2 . The pellet was prepared from powders obtained by methanol-induced precipitation. The impedance data initially showed a single arc in the Nyquist representation, but after approximately 24 hours a second low-frequency arc became evident, Figure 3.10(a). This low-frequency arc was attributed to grain boundary conductivity (σ_{gb}), and the high-frequency arc to bulk conductivity (σ_{bulk}). With increasing time, both σ_{gb} and σ_{bulk} decreased, and σ_{bulk} approached that of the conductivity of a CsH_2PO_4 single crystal σ_{xtal} , Figure 3.10(b). These results suggest that the apparently high conductivity measured in polycrystalline samples is due to chemi-sorbed H_2O , which is very gradually desorbed at elevated temperatures. Materials such as $\text{Zr}(\text{HPO}_4)_2$, in both hydrated and anhydrous form, are known to show a

somewhat similar humidity dependence in their transport behavior due to adsorbed water between the layers of the highly layered crystal structure²⁴. However, retention of water to such high temperatures and for such long periods, as observed here, is unusual for a crystalline acid phosphate. Finally, we note that in this analysis, σ_{gb} has not been normalized to account for the grain boundary density, as would be necessary to compare samples with different grain sizes²⁵.

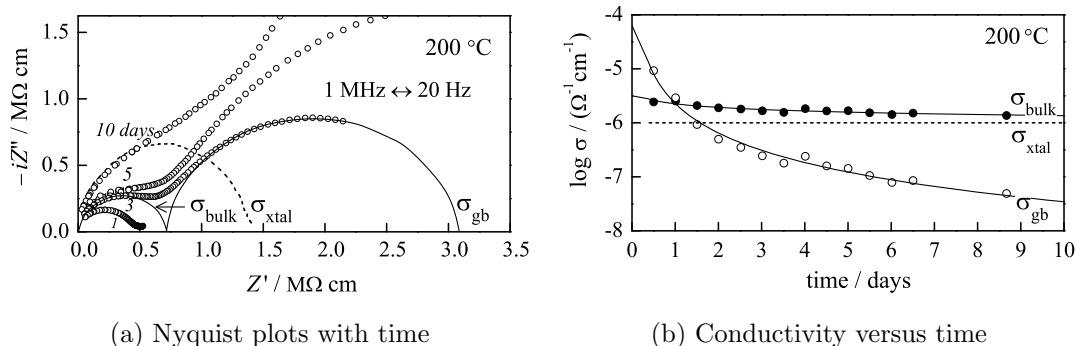


Figure 3.10: Impedance spectroscopy measurements on a polycrystalline pellet of CsH_2PO_4 carried out at $200\text{ }^\circ\text{C}$ under flowing dry N_2 gas over 10 days. (a) Nyquist plots at various times, in which two arcs are fit to the impedance data, the first, high frequency arc, attributed to the bulk conductivity (σ_{bulk}), and the second, low frequency arc to the grain boundary conductivity (σ_{gb}), as compared to the conductivity of a single crystal (σ_{xtal}). (b) Log plot of these conductivities as a function of time.

NMR Spectroscopy

Presented in Figure 3.11 are ^1H - NMR spectra of two CsH_2PO_4 powders: (1) produced by methanol-induced precipitation, and (2) by grinding a single crystal. The methanol-precipitated powder was dried at $200\text{ }^\circ\text{C}$ for 24 hours prior to measurement, whereas the ground single crystal was examined immediately after grinding. For both powders, peaks were observed at 14.5 and 10.9 ppm, which correspond to the two crystallographically distinct hydrogen atoms observed in the room temperature structure of CsH_2PO_4 ²⁶. However, for the methanol-precipitated powder an additional peak was observed at 6.6 ppm. On the basis of extensive studies of chemically similar calcium phosphates, in which chemical shifts of 5.5–6.2 ppm were observed for surface-adsorbed water,²⁷ it has been concluded that this third peak corresponds to chemically surface-adsorbed water. It is thus evident that chemi-sorbed surface water is particularly difficult to remove from CsH_2PO_4 , and that this water affects not only grain boundary conductivity, but also the AC impedance spectral

arc normally associated with bulk conductivity behavior. It is for this reason that well-dried single crystals were used (in crushed form) in the following high pressure conductivity experiments.

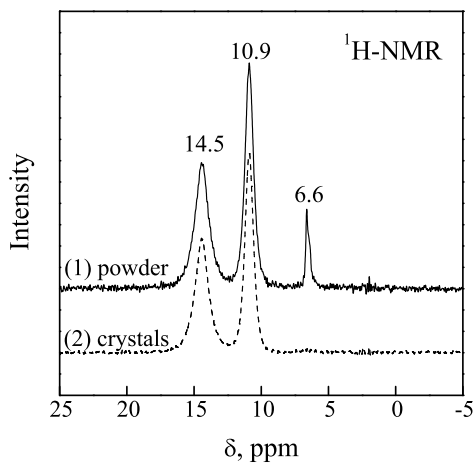


Figure 3.11: Solid-state $^1\text{H-NMR}$ spectra of CsH_2PO_4 powders obtained by (1) methanol induced precipitation and then dried for 24-hours at 200°C prior to measurement, and (2) from ground single crystals.

3.1.1.3 High Pressure Behavior

Impedance Spectroscopy

The pressure–temperature (P – T) conditions employed in these experiments can be compared to the phase diagram reported by Rapoport *et al.*²¹, as indicated in Figure 3.12. The dashed horizontal line at 149°C in this figure refers to a quasi-irreversible phase transition noted by those authors, from the room temperature phase III to an unidentified phase II. The results of the conductivity measurements, which would be expected to traverse both the III/II and II/I transitions, are presented in Figure 3.13. Upon heating for a first time (1), a sharp increase in conductivity was first observed at 150°C . In response to further heating, a second sharp increase in conductivity occurred at 260°C , beyond which Arrhenius behavior was exhibited up to 375°C . Upon cooling (2), the high temperature transition exhibited a large hysteresis, with the conductivity dropping by several orders of magnitude at about 240°C . A second heating revealed no anomalous behavior at 150°C , indicating the irreversible nature of this feature, consistent with earlier studies²¹. Upon further heating (3), the superprotonic transition at 260°C was reproduced. While cooling in this second thermal

cycle (4), a large hysteresis was again observed with a reverse transition at about 240 °C. In general, the magnitude of the conductivity at high temperature was highly reproducible upon multiple heating and cooling cycles, whereas in the low temperature regime (25–260 °C) it was not.

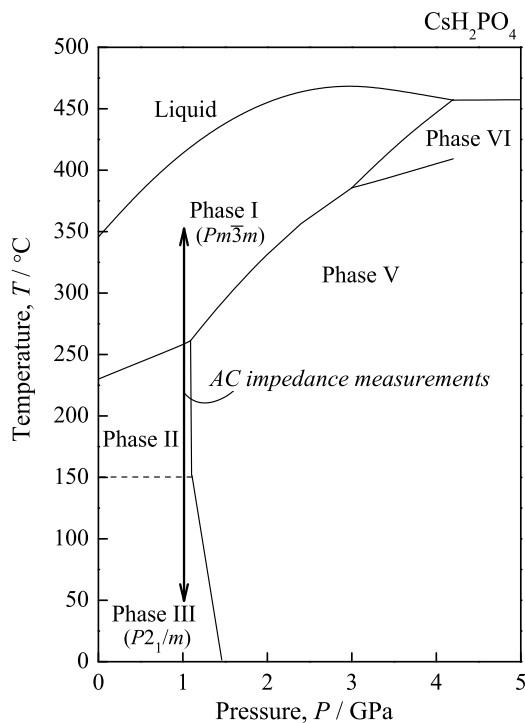


Figure 3.12: P - T phase diagram of CsH₂PO₄ from Rapoport *et al.*²¹ showing the path over which AC impedance measurements were performed in this work.

Representative Nyquist plots of the measured AC impedance spectra above and below the superprotonic phase transition are presented in Figure 3.14. Below the transition ($T < T_{\text{SP}}$), Figure 3.14(a), the intercept of the semi-circle with the real axis (Z') is interpreted as the resistivity of the sample, whereas above the transition ($T > T_{\text{SP}}$), Figure 3.14(b), the intercept of the electrode response with Z' is taken as the sample's resistivity. In both cases, the resistivity decreases with increasing temperature. This result differs markedly from the ambient pressure behavior, Figure 3.9, for which the resistivity of the sample increased with increasing temperature above the transition. With these data, we conclude that the observed high temperature electrical behavior while under pressure is due to the superprotonic phase of CsH₂PO₄, whereas at atmospheric pressure the electrical behavior is complicated by dehydration processes.

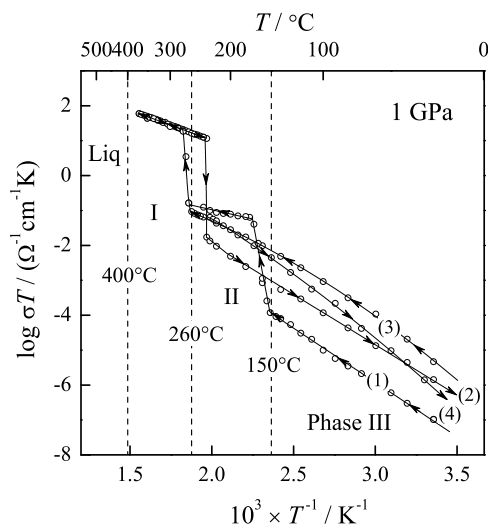


Figure 3.13: Conductivity results of impedance spectroscopy measurements at 1 GPa on polycrystalline CsH_2PO_4 upon a first heating (1) and cooling (2), and followed by a second heating (3) and cooling (4), plotted in Arrhenius form. Phase boundaries are indicated by dashed lines.

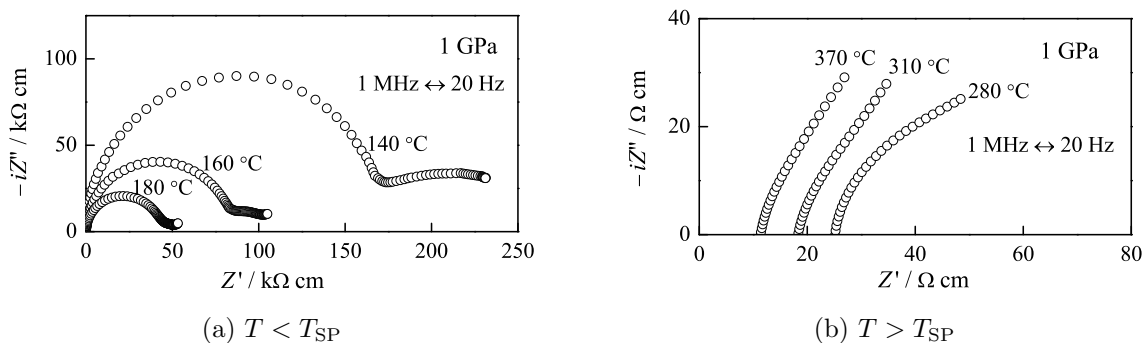


Figure 3.14: Nyquist representation of impedance data obtained from polycrystalline CsH_2PO_4 at 1 GPa and at temperatures (a) below and (b) above the superprotonic phase transition temperature T_{SP} .

Powder X-ray diffraction data collected from CsH_2PO_4 under ambient conditions after heating to 350 °C at 1 GPa, showed that the transformations undergone by CsH_2PO_4 under high-temperature, high-pressure conditions are reversible. Figure 3.15 shows the calculated X-ray powder diffraction pattern for the $P2_1/m$ paraelectric (ferroelastic) phase of CsH_2PO_4 ⁷ along with those of the experimental diffraction patterns of samples “as prepared” and “after recovery” from the high temperature, high pressure conditions. The similarity of the patterns demonstrates that the material did not undergo any kind of (irreversible) decomposition. Together with the results of the ball drop experiments described in Chapter 2, these data confirm that all of the effects evident in Figure 3.15 are due to

solid–solid transformations.

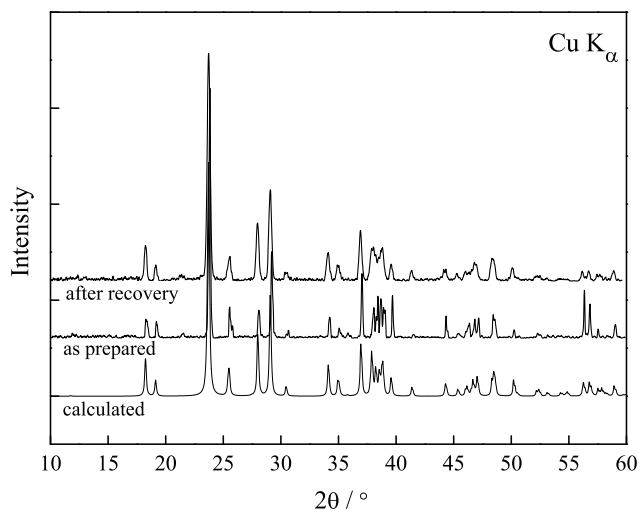


Figure 3.15: Powder X-ray diffraction patterns of CsH_2PO_4 : calculated⁷, as prepared, and after recovery from conditions of 350 °C and 1 GPa; backgrounds subtracted from experimental patterns.

The high temperature phase encountered in this work clearly corresponds to that identified as “phase I” by Rapoport *et al.*²¹ Those authors reported a transition to this phase at 258 °C under 1 GPa pressure, comparable to the transition temperature of 260 °C measured here. The dramatic increase in conductivity at the transition, along with the low activation enthalpy ΔH_a (see below), indicates phase I is ‘superprotonic’ in nature. These results thus support the findings of Baranov *et al.* that CsH_2PO_4 undergoes a solid–solid transformation that leads to high conductivity, independent of decomposition⁸. It can be further concluded that this superprotonic phase corresponds to the cubic ($Pm\bar{3}m$) phase reported by Preisinger *et al.* above 230 °C at atmospheric pressure¹². From their diffraction studies, Preisinger and coworkers reported a change in volume (ΔV) at the superprotonic transition of 3.6 Å³. Using the *Clausius-Clapeyron* equation, this value of ΔV , along with a ΔS of 22.4 J mol⁻¹K⁻¹, calculated from the enthalpy and transition temperature results in the previous section, we would expect a transition that occurs at ~ 330 °C at 1 GPa, much higher than observed here. One explanation for this could be the highly compressible nature of the superprotonic phase, which has been experimentally observed in superprotonic solid acid CsHSO_4 ²⁸.

In these measurements, an irreversible anomaly at ~ 150 °C was observed at 1 GPa upon an initial heating. The nature of this apparent transition and the phase to which CsH_2PO_4

transforms at this temperature, phase II, remain unclear; no signature of this phase was observed at ambient pressures. As stated above, there is significant ambiguity concerning this apparent transition, with researchers reporting transition temperatures ranging from 107 to 149 °C at ambient pressure, and 149 to 167 °C at 1 GPa²⁹, depending on the details of the sample preparation. Resolving these ambiguities is beyond the scope of this work.

Fitting the conductivity σ of superprotonic CsH₂PO₄ to an Arrhenius law yields values for A_0 and ΔH_a of $3.2 \times 10^4 \Omega^{-1}\text{cm}^{-1}\text{K}$ and 0.35 eV, respectively. In comparison, the values reported by Baranov *et al.*⁸ for superprotonic, single-crystal CsH₂PO₄ at ambient pressure are $A_0 = 2 \times 10^4 \Omega^{-1}\text{cm}^{-1}\text{K}$ and $\Delta H_a = 0.32$ eV. The difference between the two activation enthalpies indicates that pressure increases the barrier to proton transport. This increase in ΔH_a can be quantified in terms of the activation volume for proton conduction using the relationship:

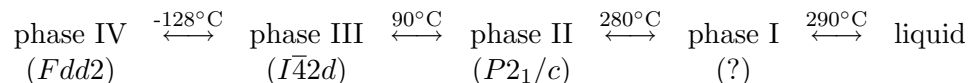
$$\Delta H_a = \Delta E_a + P\Delta V_a, \quad (3.4)$$

where P is pressure, ΔE_a the activation energy, and ΔV_a the activation volume. The result, $\Delta V_a = 2\text{--}3 \text{ cm}^3\text{mol}^{-1}$, corresponds to 3–4% of the unit cell volume. This value is comparable to those determined from high pressure studies of other superprotonic solid acids, such as CsHSO₄, Rb₃H(SeO₄)₂, and (NH₄)₃H(SO₄)₂^{30,31}. It is noteworthy, however, that in some cases, for example CsHSO₄ in its low temperature phase³⁰, the activation volume for proton conduction can be negative, reflecting the unique transport mechanism for this species as compared to other ions for which steric hindrances to motion are more relevant.

3.1.2 RbH₂PO₄³²

Rubidium dihydrogen phosphate, RbH₂PO₄, crystallizes in the tetragonal space group $I\bar{4}2d$ (referred to as phase III)³³. Cooling RbH₂PO₄ induces a well-documented transition at 145 K to an orthorhombic ($Fdd2$) ferroelectric phase (phase IV)^{34,33}. In contrast, heating produces a distinct series of transitions, which, like CsH₂PO₄, are of some debate in the literature. Upon heating, RbH₂PO₄ transforms quasi-irreversibly to a monoclinic phase (phase II) at a temperature of ~ 90 °C, depending on the details of the experimental conditions¹⁹. The transition has been observed by numerous authors using primarily thermal analysis methods^{19,22,35,36}, but also high temperature powder X-ray diffraction³⁵. The structure of phase II was determined from single-crystal X-ray studies to be monoclinic ($P2_1/c$)³⁷, in

which is in agreement with previous high temperature powder diffraction studies³⁵. Though not identical, the structure of RbH_2PO_4 in phase II, closely resembles that of phase II in CsH_2PO_4 ($P2_1/m$)⁷. There have been reports, based primarily on high pressure thermal analysis, that a second high temperature transition takes place at ~ 280 °C, to an as-of-yet unidentified phase I, just prior to melting at ~ 290 °C^{21,29,38}. To summarize, the reported transitions for RbH_2PO_4 take place as follows:



Despite the considerable evidence for high temperature phase transformations in RbH_2PO_4 , Park and coworkers have argued in a series of papers, that *none* within the MH_2PO_4 class of compounds undergoes a polymorphic phase transition prior to decomposition/polymerization^{39,40}, a position further supported by Ortiz and coworkers⁹. Both sets of authors conclude, primarily from thermal analysis measurements, that all anomalies in high temperature properties can be attributed to a decomposition process, which involves phosphate condensation and polymerization. In fact these thermal dehydration events at ambient atmosphere, which initiates at temperatures close to the $\text{II} \rightarrow \text{I}$ transition of RbH_2PO_4 , has prevented previous attempts to accurately characterization the electrical behavior of phase I⁴¹.

Ambient pressure thermal analysis results are presented here, confirming that dehydration processes readily masks any transition to phase I in RbH_2PO_4 . However, through the use of pressure, dehydration is suppressed, and the high temperature electrical behavior of RbH_2PO_4 phase I determined to be superprotonic in nature.

3.1.2.1 Ambient Pressure Behavior

Thermal analysis results obtained upon heating RbH_2PO_4 powder to 500 °C are presented in Figure 3.16. The DTG and mass spectroscopy results correspond well to one another and show at least two major dehydration events at 257 and 340 °C. On the otherhand, only one rather broad endothermic event at 261 °C is observed from the DSC measurements and is perhaps the result of the two overlapping dehydration events observed by DTG and mass spectroscopy. Analogous to CsH_2PO_4 , the existence of multiple dehydration events indicates a multi-step process, occurring via the formation of poly-phosphite intermediates. Nevertheless, the overall dehydration can be described by the following reaction:



This would result in a loss of mass of 9.9 wt%—precisely that observed by TG, Figure 3.16. Furthermore, samples recovered after thermal analysis, were identified by powder X-ray diffraction as RbPO_3 . No evidence of either polymorphic solid–solid or melting transitions was observed under ambient pressures. The use of finely ground powder samples thus results in high-temperature behavior that is dominated by thermal decomposition, as previously observed in CsH_2PO_4 .

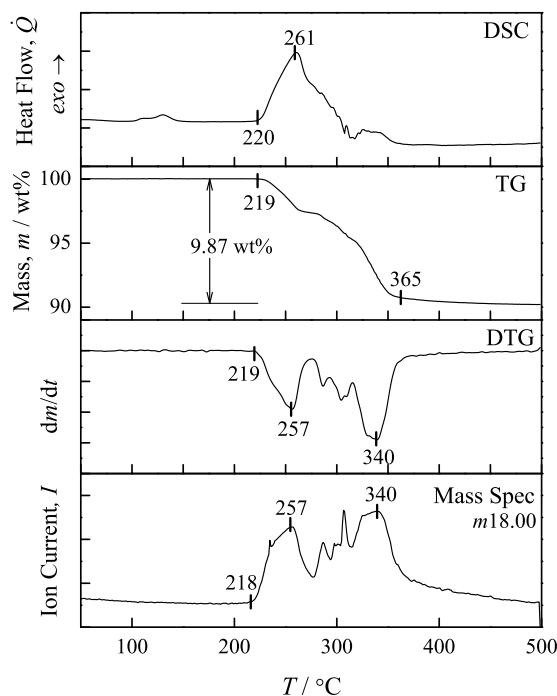


Figure 3.16: Simultaneous differential scanning calorimetry (DSC), thermal gravimetry (TG), and corresponding differential thermal gravimetry (DTG) of RbH_2PO_4 powder upon heating to 500 °C at 10 °C min⁻¹ under flowing 40 cm³min⁻¹ dry N₂ gas. H₂O in the evolved gas is identified by mass spectroscopy (Mass Spec), *m*18.00.

3.1.2.2 High Pressure Behavior

To characterize the high-temperature behavior of RbH_2PO_4 , and avoid the dehydration observed at ambient pressure, high pressure impedance spectroscopy was carried out on RbH_2PO_4 powder ground from single crystals just prior to the measurement. Presented in Figure 3.17 is a P – T phase diagram for RbH_2PO_4 , reproduced from Rapaport *et al.*²¹, which indicates the region over which AC impedance data were collected.

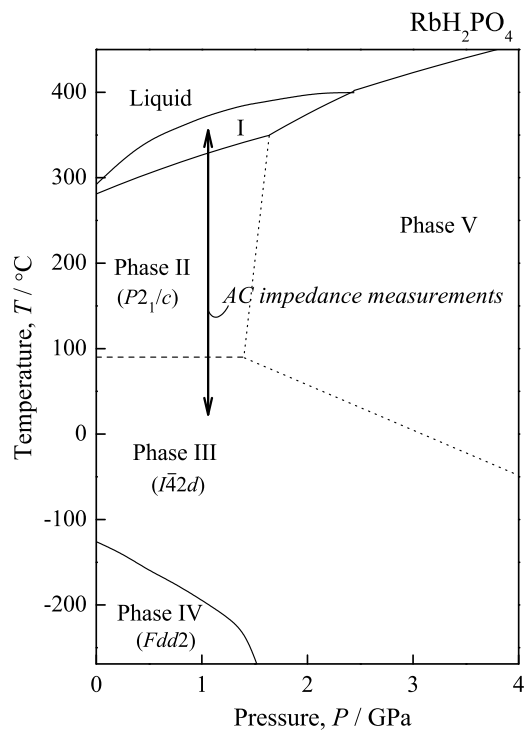


Figure 3.17: P - T phase diagram of RbH_2PO_4 from Rapoport *et al.*²¹ showing the path over which AC impedance measurements were performed in this work.

The conductivity results obtained from these high pressure impedance measurements are presented in an Arrhenius plot in Figure 3.18. The arrows indicate the direction of temperature change between data collections. The regions of phase stability expected from the P - T phase diagrams in Figure 3.17 are overlaid and indicated by dashed-lines. Prior to these measurements crystals of RbH_2PO_4 were stored at 100 °C, due to the hygroscopic nature of these compounds. In doing so, the quasi-irreversible III \rightarrow II transformation, which occurs at 90 °C, was induced. Therefore, the sample was in meta-stable (at room temperature) phase II prior to the initiation of the high pressure conductivity measurements. Upon heating RbH_2PO_4 above 327 °C, a II \rightarrow I phase transition is expected (see Figure 3.17). From the AC impedance results presented in Figure 3.18, a sharp “jump” in the conductivity to a value of $\sim 6.8 \times 10^{-2} \Omega^{-1}\text{cm}^{-1}$ at 340 °C is evident, and indicative of a superprotonic phase transition. The solid-solid nature of this transition was confirmed by a ball drop experiment (as described in Chapter 2). Reproducible Arrhenius behavior of the superprotonic phase I was observed, with $\Delta H_a = 0.232(8)$ eV and $A_0 = 3.4(6) \times 10^3 \Omega^{-1}\text{cm}^{-1}\text{K}$, values fairly typical of superprotonic conductors⁴². Upon cooling, there was

some hysteresis (~ 10 °C). Like that CsH_2PO_4 , the electrical behavior was somewhat irreproducible in the low temperature regime (phase II), between heating and cooling cycles, yielding rather large uncertainties when fit to an Arrhenius-type behavior, $\Delta H_a = 0.77(2)$ eV and $A_0 = 3(2) \times 10^5 \Omega^{-1}\text{cm}^{-1}\text{K}$.

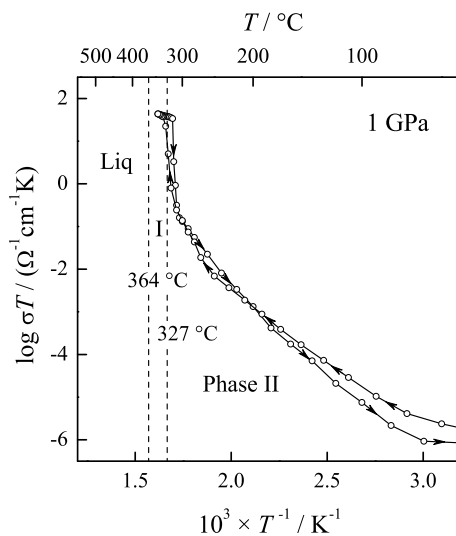


Figure 3.18: Arrhenius plot of conductivity results from AC impedance measurements performed on RbH_2PO_4 powder upon heating and cooling (as indicated by direction of arrows) from 25 to 350 °C under 1.0 GPa of pressure. Phase boundaries are indicated by dashed lines.

Typical Nyquist plots of AC impedance spectra from these conductivity measurements are presented in Figure 3.19 for selected temperatures. Below the superprotonic phase transition ($T < T_{\text{SP}}$), Figure 3.19(a), well-resolved semi-circles were obtained. The real resistance of the sample at low temperatures was identified by the intercept of the semi-circle with the real axis (Z'). In contrast, at $T > T_{\text{SP}}$, only an electrode response was observed, Figure 3.19(b), and the intercept with Z' was used as the estimated resistance of the sample.

With these data, we conclude that the observed high temperature electrical behavior while under pressure is due to the superprotonic phase of RbH_2PO_4 , whereas at atmospheric pressure the electrical behavior is complicated by dehydration processes. Furthermore, the proton transport properties of RbH_2PO_4 are quite comparable to those of CsH_2PO_4 , from which one would expect that phase I of RbH_2PO_4 shares the same cubic structure, in which phosphate groups are highly rotationally-disordered⁴³.

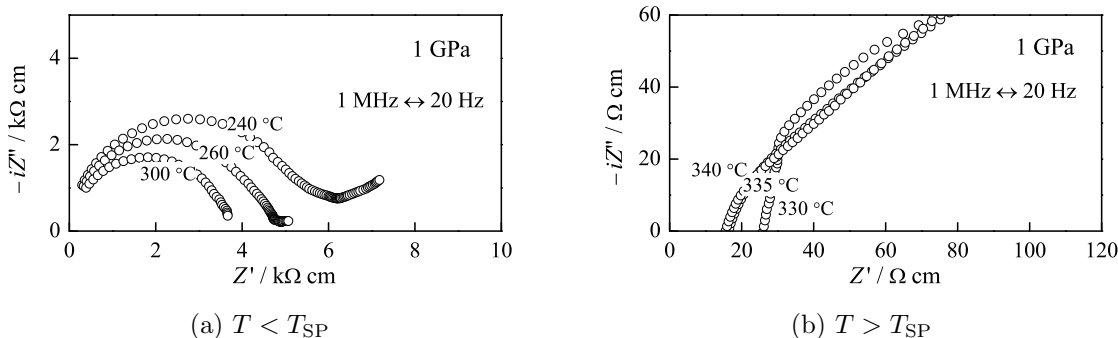


Figure 3.19: Nyquist representation of impedance data obtained from polycrystalline RbH_2PO_4 at 1 GPa and at temperatures (a) below and (b) above the superprotonic phase transition temperature T_{SP} .

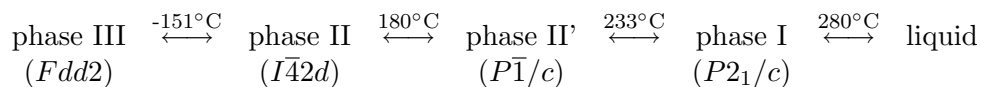
3.1.3 KH_2PO_4

Potassium dihydrogen phosphate, KH_2PO_4 , is isostructural with RbH_2PO_4 under ambient conditions, crystallizing in the tetragonal space group $I\bar{4}2d$ and commonly referred to as phase II⁴⁴. KH_2PO_4 is well known for its ferroelectric phase transition, in which, upon cooling below 123 K⁴⁵, it transforms to a ferroelectric phase with orthorhombic symmetry ($Fdd2$)⁴⁶ (phase III). However, like the other MH_2PO_4 compounds, the high-temperature behavior of KH_2PO_4 remains controversial.

Early studies of the high-temperature behavior of KH_2PO_4 indicated two polymorphic transitions, one at 180 °C, to phase II'⁴⁷, and a second at 233 °C⁴⁸, to phase I. More recent single crystal diffraction studies have confirmed the existence of both transitions and have shown phase II' to be triclinic ($P\bar{1}$), with entirely ordered phosphate groups, and phase I to be monoclinic ($P2_1/c$)⁴⁹. The existence of the II' \rightarrow I transition at 200–220 °C has been further confirmed by thermomechanical measurements, although little evidence for the transition at 180 °C was observed⁵⁰. The structures of additional polymorphs that exist under atmospheric conditions have also been reported^{49,51}.

Still, as with the previous compounds, CsH_2PO_4 and RbH_2PO_4 , recent arguments have been made claiming that the high-temperature behavior of this compound is dominated by decomposition and polymerization processes^{39,40,9}. Indeed, thermal dehydration, which initiates at temperatures close to the II' \rightarrow I transition of KH_2PO_4 and has prevented the accurate electrical characterization of phase I⁴¹.

To summarize, it has been suggested that KH_2PO_4 undergoes the following polymorphic changes at atmospheric pressure and in the absence of dehydraton:



In this section, the aim is to identify the high temperature electrical properties of KH_2PO_4 phase I. First, thermal analysis results at ambient pressure for KH_2PO_4 are presented, indicating that dehydration *does* mask any transition to phase I. Then results of high pressure AC impedance are presented, which suggest that KH_2PO_4 phase I is not superprotonic in nature, as might have been expected based on its monoclinic structure.

3.1.3.1 Ambient Pressure Behavior

Thermal analysis results obtained upon heating powder of KH_2PO_4 to $500\text{ }^{\circ}\text{C}$ are presented in Figure 3.20. The DTG and mass spectroscopy results correspond well to one another and show at least two major dehydration events at 233 and $320\text{ }^{\circ}\text{C}$. The single endothermic event at $241\text{ }^{\circ}\text{C}$ observed from the DSC measurements could be the result of the two overlapping dehydration events observed by DTG and mass spectroscopy. The absence of a transition for KH_2PO_4 at $\sim 180\text{ }^{\circ}\text{C}$, well before dehydration begins, cannot be readily explained, but suggests that the $\text{II} \rightarrow \text{II}'$ transformation is highly dependent on the details of sample preparation and experimental conditions. No clear step-wise dehydration process observed in the TG thermogram seems to suggest that dehydration must occur via a multi-step process, whereby poly-phosphite intermediates are formed. The complete dehydration of KH_2PO_4 by the reaction:



would result in a $13.2\text{ wt}\%$ loss of mass for KH_2PO_4 , which is in close agreement with the TG results, Figure 3.20. Recovered samples after thermal analysis, were identified by powder X-ray diffraction as KPO_3 . From these results, no evidence of either polymorphic solid–solid or melting transitions was observed under ambient pressures.

3.1.3.2 High Pressure Behavior

Given the difficulties in characterizing the electrical properties of KH_2PO_4 phase I associated with dehydration at ambient pressures, high pressure impedance spectroscopy was employed, the results of which are presented here. In Figure 3.21, a P – T phase diagram

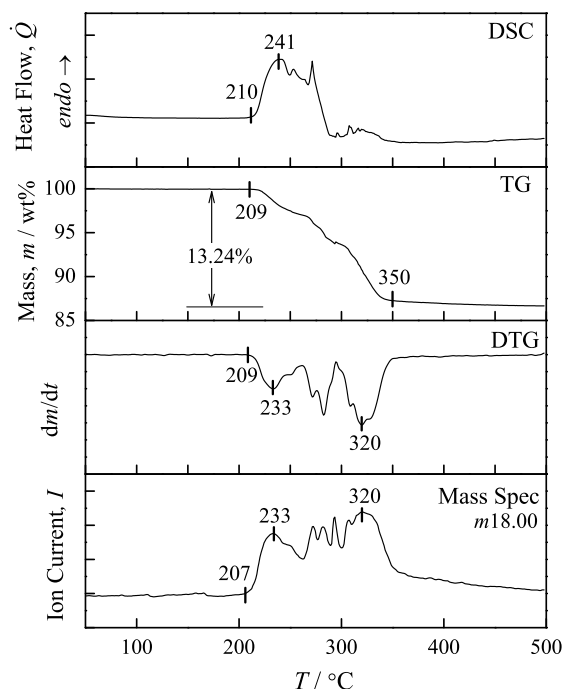


Figure 3.20: Simultaneous differential scanning calorimetry (DSC), thermal gravimetry (TG), and corresponding differential thermal gravimetry (DTG) of KH_2PO_4 powder upon heating to 500 °C at 10 °C min^{-1} under flowing 40 $\text{cm}^3\text{min}^{-1}$ dry N_2 gas. H_2O in the evolved gas is identified by mass spectroscopy (Mass Spec), $m18.00$.

for KH_2PO_4 , reproduced from Rapoport⁴⁸, indicates the region over which AC impedance data were collected. The conductivities obtained from the high pressure impedance measurements are presented in Arrhenius plots in Figure 3.22. The arrows indicate the direction of temperature change between data collections. The regions of phase stability expected from the P - T phase diagram in Figure 3.21 are overlaid and indicated by dashed-lines.

As synthesized KH_2PO_4 crystallizes in phase II (tetragonal, $I\bar{4}2d$). Application of pressure (at 25 °C) induces a transition to phase IV, however, the position of the II/IV phase boundary has not been determined and the exact phase present at the initiation of the high pressure conductivity measurements is thus not known. Regardless of this ambiguity, one expects KH_2PO_4 to transform to phase I at 250 °C upon heating under 1 GPa (Figure 3.21). The conductivity, Figure 3.22, increases smoothly through this temperature; there is no sharp increase that would be characteristic of a superprotonic phase transition. This behavior is entirely in agreement with the reported monoclinic structure of phase I. Upon further heating, one expects phase I to melt at 325 °C, and here the conductivity increases by more than two orders of magnitude to a value of $\sim 1.8 \times 10^{-2} \Omega^{-1}\text{cm}^{-1}$ at 345

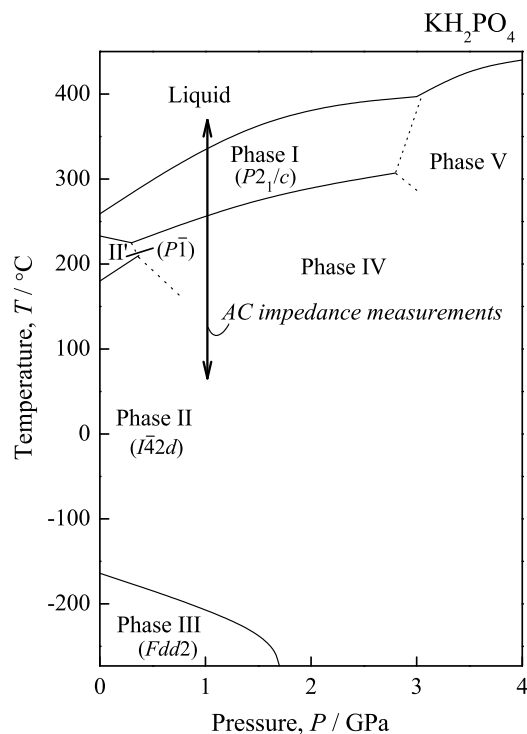


Figure 3.21: P - T phase diagram of KH_2PO_4 from Rapoport⁴⁸ showing the path over which AC impedance measurements were performed in this work.

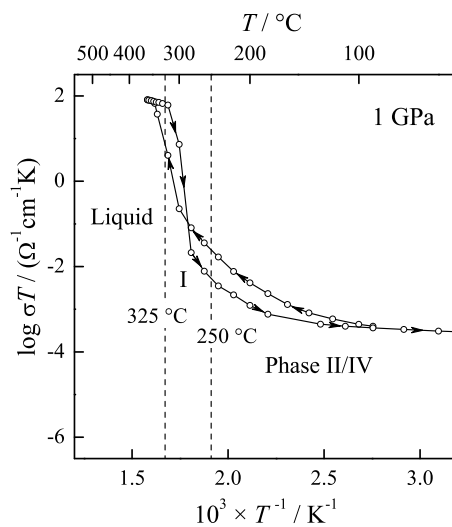


Figure 3.22: Arrhenius plot of conductivity results from AC impedance measurements performed on KH_2PO_4 powder upon heating and cooling (as indicated by direction of arrows) from 25 to 350 °C under 1.0 GPa of pressure. Phase boundaries are indicated by dashed lines.

°C. Recovery of the KH_2PO_4 sample from the ball drop experiment confirmed that this was a solid-liquid transition and not a solid-solid superprotonic transition.

Typical Nyquist plots of AC impedance spectra are presented in Figure 3.23 for selected

temperatures. At low temperatures ($T < T_m$), Figure 3.23(a), well-resolved semi-circles were obtained, in which the real resistance is determined from the intercept of the spectral arc with the real axis (Z'). In contrast, at high temperatures ($T > T_m$), only an electrode response was observed, Figure 3.23(b), and its intercept with Z' is the estimated resistance of the sample.

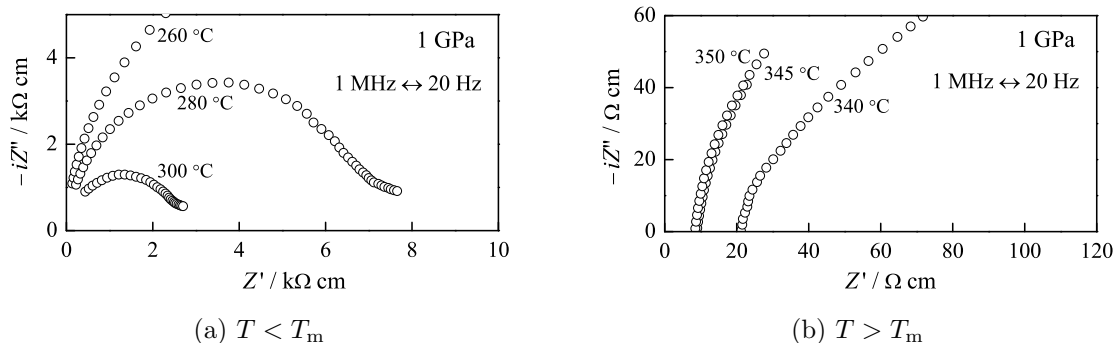


Figure 3.23: Nyquist representation of impedance data obtained from polycrystalline KH_2PO_4 at 1 GPa and at temperatures (a) below and (b) above the melting temperature T_m .

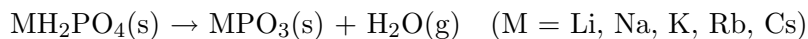
Fitting the conductivity data of the liquid phase to an Arrhenius relationship yields: $\Delta H_a = 0.227(4)$ eV and $A_0 = 5.2(5) \times 10^3 \Omega^{-1}\text{cm}^{-1}\text{K}$. Upon cooling KH_2PO_4 , some hysteresis (~ 20 °C) from the melt phase and rather irreproducible electrical behavior in the low conductivity solid phases was observed. It was not possible to distinguish between phases I, II, and IV from these electrical measurements, and the conductivity was highly non-Arrhenius in the low-temperature regime.

What is clear from these results is that none of the high temperature solid phases of KH_2PO_4 exhibit superprotonic conductivity. It is also noteworthy that the activation enthalpy of the liquid-phase of KH_2PO_4 is quite similar to that of the superprotonic phase I of RbH_2PO_4 and the overall difference in conductivity between the two is less than a factor of two. This points to similar mechanisms for ionic transport between liquid KH_2PO_4 and superprotonic RbH_2PO_4 .

3.1.4 Summary

At the onset of this work, the question was posed: *Can fully-hydrogen bonded solid acids exhibit superprotonic phase transitions?* Here it has been shown that, *yes*, fully-hydrogen bonded solid acids, such as CsH_2PO_4 and RbH_2PO_4 , can indeed exhibit superprotonic phase transitions.

A summary of the high temperature thermal and electrical behavior of MH_2PO_4 -type compounds at atmospheric and 1 GPa pressures characterized here is given in Table 3.2. Preliminary ambient pressure thermal analysis and high pressure impedance measurements of LiH_2PO_4 and NaH_2PO_4 have been carried out (see Appendix for details) and the results included in Table 3.2. From these results, it is clear that at atmospheric pressure, all MH_2PO_4 -type compounds dehydrate at elevated temperatures. In general, the overall dehydration reaction is:



Contrary to what previous authors have suggested, such a dehydration reaction *does not* preclude a superprotonic phase transition at higher temperatures. Thermodynamically speaking, the previous reaction is in equilibrium when the Gibbs free energy is zero ($\Delta G_{rxn} = 0$), which is a function of water partial pressure ($p_{\text{H}_2\text{O}}$),

$$\Delta G_{rxn} = \Delta G_{rxn}^\circ + RT \ln p_{\text{H}_2\text{O}}. \quad (3.5)$$

As such, thermal analysis in closed volume containers,ⁱ in which an equilibrium $p_{\text{H}_2\text{O}}$ is reached with only minimal sample degradation, has allowed the accurate characterization of the high temperature transition enthalpies of some of these compounds (see Appendix for details), also included in Table 3.2.

What *does* seem to preclude superprotonic transitions in some MH_2PO_4 -type compounds is the size of the cation. While large cation-sized MH_2PO_4 compounds (M = Rb, Cs) upon heating exhibit a superprotonic phase transition prior to melting, smaller cation-sized MH_2PO_4 compounds (M = K, Na, Li) simply melt. This effect has been observed in other MH_nXO_4 -systems as well⁴, and will be discussed in detail in the next section.

ⁱThe pressure rating of the closed volume containers was less than 1 MPa—resulting in a negligible pressure change.

Table 3.2: Summary of thermal and electrical characterization at atmospheric and 1 GPa pressures of MH_2PO_4 -type compounds. *Left*—thermal decomposition/dehydration (d), melting (m), and superprotonic phase transition (SP) temperatures (T) and enthalpies (ΔH) at 1 atm. *Right*—high temperature phase transition temperatures (T_{tr}) and electrical behavior (ΔH_a , σ_0) at 1 GPa.

	$P = 1 \text{ atm}$					$P = 1 \text{ GPa}$			
	T_d^\dagger	T_{SP}^\ddagger	$T_m^\ddagger / ^\circ\text{C}$	ΔH_{SP}	$\Delta H_m / \text{kJ mol}^{-1}$	Phase	$T_{tr} / ^\circ\text{C}$	$\Delta H_a / \text{eV}$	$A_0 / \Omega^{-1} \text{cm}^{-1} \text{K}$
CsH_2PO_4	225	228(2)	346(2)	11.3(6)	25.2(5)	SP	260	0.346(3)	$2.1(2) \times 10^4$
RbH_2PO_4	220	280(1)	290(2)	11.8(5)	22.7(8)	SP	327	0.323(8)	$3.4(6) \times 10^3$
KH_2PO_4	210	—	259(4)	—	—	m	325	0.227(4)	$5.2(5) \times 10^3$
NaH_2PO_4	200	—	—	—	—	m	350	—	—
LiH_2PO_4	195	—	—	—	—	m	255	—	—

[†]Approximate values—dehydration onset is dependent upon experimental conditions.

[‡]Values obtained by suppressing dehydration.

3.2 Cation and Oxy-Anion Size Effects

In this section, the effect of cation and oxy-anion size on the presence of superprotonic phase transitions in MH_nXO_4 -type solid acids will be examined. In the previous section, a clear cation size effect in MH_2PO_4 -type solid acids was observed. In Figure 3.24, phase diagrams of (a) MHSO_4 and (b) MH_2PO_4 compounds as function of cation radius are presented. From these diagrams, increasing cation size appears to increase the melting temperature, while at the same time, decrease the superprotonic phase transition temperature. From these observations, superprotonic phase transitions appear to be favored in solid acids composed of large cations. However, the effect of the oxy-anion size on phase transitions is somewhat less clear. In the following sections, both the effect of the cation and oxy-anion size will be considered. For the purpose of this study, the phase behavior of MH_nXO_4 -type compounds has been compiled from this and other published work into Tables A.2 and A.1 given in the Appendix, and these data are used throughout this section.

To begin with, radius ratio rules will be employed to examine the cation to oxy-anion size effect with the hope of developing a method for predicting the presence of superprotonic phase transitions in solid acids. Though moderately successful, cation to oxy-anion size effects alone do not give a complete picture of factors that govern the presence of superprotonic phase transitions. Notable exceptions to these radius ratio rules will then presented, and discussed in terms of bonding. From these investigations it will be shown that, while cation

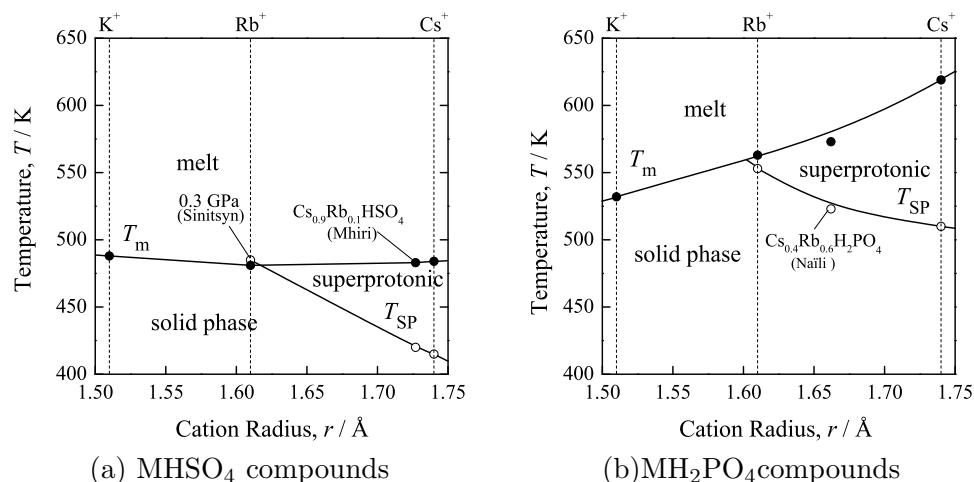


Figure 3.24: MHSO_4 and MH_2PO_4 phase diagrams as a function of cation radius, where $M = \text{K}$, Rb , and Cs . Cation radii were obtained from Shannon⁵² for values of M^+ with 8-fold coordination.

and oxy-anion size do play a significant role in the presence of superprotonic transitions, the role of both ionic and hydrogen bonding are equally important.

3.2.1 Radius Ratio Rules

Superprotonic phases of solid acids are composed of a rotationally disordered tetrahedral oxy-anion coordinated by cations, as depicted in Figure 3.25. We suppose that in order for the oxy-anions (XO_4^-) to become rotationally disordered, there must be sufficient space between cations (M^+) to be able to rotate freely, without the crystal falling apart (*i.e.*, melt). By such rationale, we expect superprotonic phase transitions to be favored by larger cation-cation distance (larger cations). But how large and what effect does the size of the oxy-anion have?

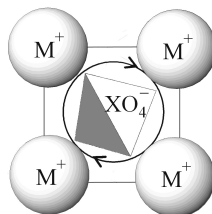


Figure 3.25: Schematic representation in two-dimensions of a rotationally disordered oxy-anion (XO_4^-), coordinated by cations (M^+).

Radius ratio rules have long been used to predict the likely structures of solids⁵³. Here,

Table 3.3: Shannon ionic radii (IR) for elements relevant to MH_nXO_4 -type solid acids, where CN is the ion coordination number⁵².

M	$IR / \text{\AA}$	CN	X	$IR / \text{\AA}$	CN	O/OH	$IR / \text{\AA}$	CN
Cs ⁺	1.74	8	S ⁺⁴	0.37	4	O ⁻²	1.38	4
Rb ⁺	1.61	8	Se ⁺⁴	0.50	4	OH ⁻	1.35	4
K ⁺	1.51	8	P ⁺⁵	0.17	4			
Na ⁺	1.18	8	As ⁺⁵	0.34	4			
Li ⁺	0.92	8						

radius ratios rules will be adopted in attempt to predict the likelihood of a superprotonic structure in MH_nXO_4 -type solid acids based upon cation and oxy-anion sizes alone. Technically speaking, the alkali cations in MH_nXO_4 -type solids acids are coordinated by oxygen atoms, however, we will treat the entire oxy-anion as the coordinating species. In general, the superprotonic structures of MH_nXO_4 -type solid acids are composed of oxy-anions, which are coordinated by 8 cations (except for $RbHSeO_4$, see Section 4.2.1). For such 8-fold coordination, the expected geometries based upon the minimum cation (r) to anion (R) radius ratios (r/R) rules are

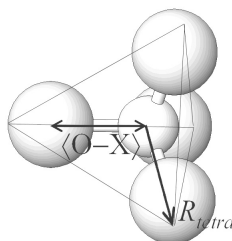
$$\begin{aligned}
 r/R &\geq 0.732 \rightarrow \text{cube} \\
 &\geq 0.668 \rightarrow \text{dodecahedron} \\
 &\geq 0.645 \rightarrow \text{square anti-prism}
 \end{aligned}$$

R.D. Shannon has compiled a comprehensive list of ionic radii that is based upon systematic structural studies of interatomic distances in halide and chalcogenide compounds⁵². These values of ionic radii are used throughout, and are reproduced in Table 3.3 for those relevant to these studies. To begin with, the validity of the Shannon ionic radii was established from a comparison of the tetrahedral oxy-anion distances $\langle X-O \rangle$ found in the room temperature structures of MH_nXO_4 -types solid acids, the results of which are given in Tables 3.4. These results show excellent agreement with Shannon's values for atomic radii.

Table 3.4: Average $\langle X-O \rangle$ distances in MH_nXO_4 -type solids acid room temperature structures compared to Shannon radii⁵².

$\langle X-O(H) \rangle / \text{\AA}$	MHSO ₄	MHSeO ₄	MH ₂ PO ₄	MH ₂ AsO ₄
Structures	1.540(4)	1.66(4)	1.47(9)	1.476(10)
Shannon	1.54	1.65	1.49	1.49

The first difficulty encountered in applying radius ratio rules to superprotonic solid acids is in assigning a radius to a non-spherical tetrahedral oxy-anion. We begin this task by defining the tetrahedral radius R_{tetra} as the distance from the center of the tetrahedral oxy-anion to the vertices,



such that

$$R_{tetra} = 2IR(O^{-2}) + IR(X^{+5,6}). \quad (3.6)$$

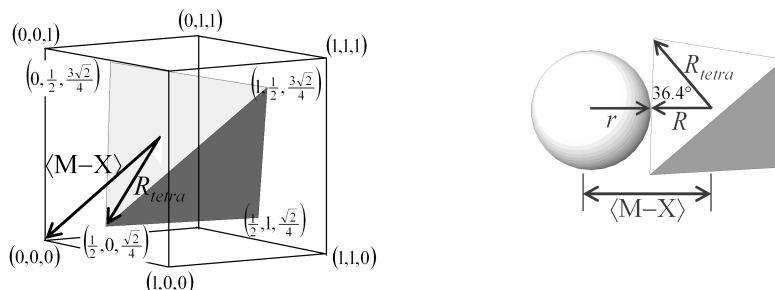
Radius ratio rules assume that the cation and anions are “just touching.” Using R_{tetra} as the anion radius, would result in the oxygen atom pointing directly into a cation—an unlikely scenario, and, in fact, not observed in any known room temperature or superprotonic solid acid structures^{54,12}. In the case of cubic superprotonic solid acids, the possible orientations of tetrahedral oxy-anion are very limited due to the symmetry of the cell, and therefore, can only be positioned as shown in Figure 3.26(a), plus the five symmetrically equivalent positions. In this orientation, the tetrahedral oxy-anion radius R_{tetra} is positioned 36.4° away from $\langle M-X \rangle$. By definition, the cation must “touch” the oxy-anion along $\langle M-X \rangle$, such that the “effective” oxy-anion radius R is

$$R = r - \langle M-X \rangle, \quad (3.7)$$

where r is the cation radius. Therefore, as depicted in Figure 3.26(b), the effective tetrahe-

dral radius can be related to the tetrahedral oxy-anion radius, such that

$$R = \cos(36.4^\circ)R_{tetra} = 0.805R_{tetra}. \quad (3.8)$$



(a) Orientation of tetrahedron in a cube (b) Effective tetrahedral radius

Figure 3.26: The effective tetrahedral radius (R) of an oxy-anion situated in a cubic cell. (a) The orientation of a tetrahedral oxy-anion in a cubic cell. (b) The effective tetrahedral radius of an oxy-anion based upon the cation and oxy-anion “just touching,” and in relationship to the actual tetrahedral radius R_{tetra} .

Using these results to calculate the radius ratios r/R for MH_nXO_4 -type compounds generates the values given in Table 3.5, which in Figure 3.27 are presented graphically and compared with known superprotonic (\circ) and non-superprotonic (\times) solid acid compounds. The 8-fold coordination assumed here and exhibited by most known MH_nXO_4 -type superprotonic solid acids does in fact appear to follow these radius ratio rules. In particular, the superprotonic structure of CsH_2PO_4 has cubic coordination geometry and $CsHSO_4$ has a geometry that closely resembles the square anti-prism coordination geometry (see Section 4.21 for more structural details).

3.2.2 Atomic Bonding

While the previous results may be quite convincing that the effect of cation and oxy-anion size are *the* key factors in identifying the presence of superprotonic conductivity in MH_nXO_4 -type solid acids, two examples will be presented here that will show this is clearly not the case.

Table 3.5: Cation to oxy-anion radius ratios (r/R) of MH_nXO_4 -type solid acids, where R is the “effective” tetrahedral $H_nXO_4^-$ radius and r is the M^+ radius.

$H_nXO_4^-$	$R / \text{\AA}$	Cation, M^+					
		$r / \text{\AA}$	r/R	r/R	r/R	r/R	r/R
$H_nXO_4^-$			1.74	1.61	1.515	1.18	0.92
HSO_4^-	2.31	r/R	0.755	0.698	0.655	0.512	0.399
$H_2PO_4^-$	2.33		0.746	0.690	0.647	0.506	0.394
$HSeO_4^-$	2.43		0.715	0.661	0.620	0.485	0.378
$H_2AsO_4^-$	2.47		0.705	0.653	0.612	0.478	0.373

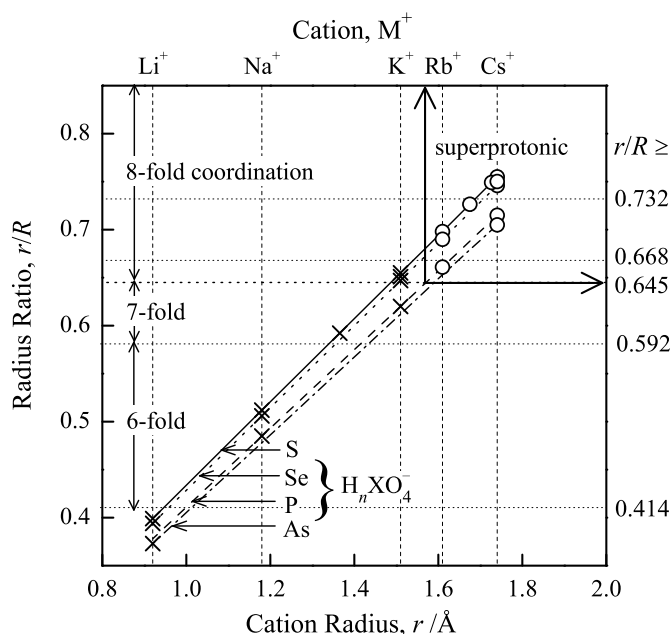


Figure 3.27: Radius ratios (r/R) as function of cation radius, as compared to known superprotonic— \circ , and non-superprotonic— \times conducting MH_nXO_4 -type solid acids.

Ionic Bonding

One may have noticed the conspicuous omission of other large cations such as NH_4^+ and Tl^+ in these studies. These cations were purposefully left out because their behavior often deviates substantially from alkali cations. However, at this point, using TlH_2PO_4 as example, will help to illustrate the shortcomings of radius ratio rules as a predictive measure for identifying superprotonic solid acids. The Shannon ionic radii of Tl^+ is 1.7 \AA , just slight larger than Rb^+ , therefore, since RbH_2PO_4 and CsH_2PO_4 both have superprotonic phase transitions, we would expect TlH_2PO_4 to follow suit. In fact, melting has been observed in this compound at 180 $^\circ\text{C}$ (see Appendix)—a melting temperature even lower than in

LiH_2PO_4 . The reason proposed for this behavior is that Tl^+ forms weak ionic bonds relative to the alkali ions. To verify the proposition, the ionization potential (IP) of the alkali ions as compared to Tl^+ are plotted as a function ionic radius in Figure 3.28. In the same figure, the melting temperature (T_m) of MH_2PO_4 -type compounds, where $M = \text{alkali}$ and Tl , is plotted above. The strong correlation between these data suggests that the large ionization potential of Tl , and therefore, weak overall ionic bonding, plays a much more significant role on melting than the cation size.

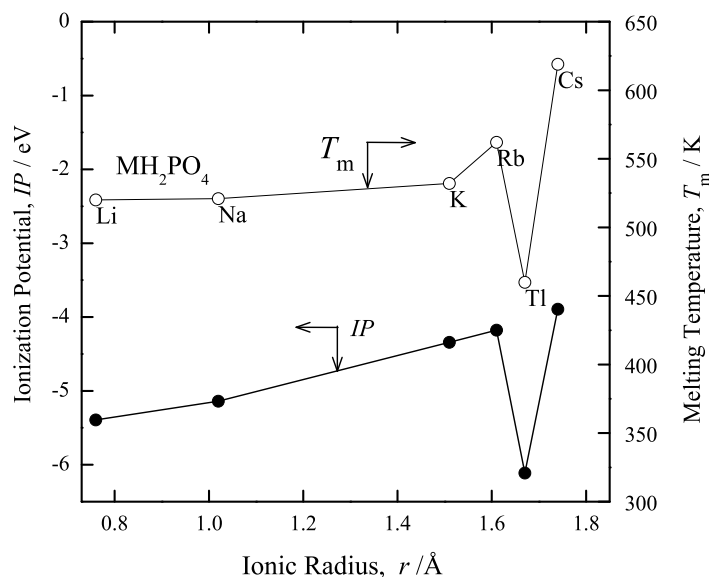
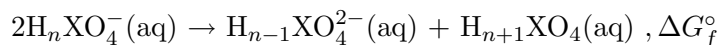


Figure 3.28: The ionization potential M and melting temperature of MH_2PO_4 (where $M = \text{Li, Na, K, Rb, Tl, Cs}$) as a function of M^+ ionic radius.

Hydrogen Bonding

A second observable phenomenon that deviates from these cation to oxy-anion ratio rules is the effect of the oxy-anion size on the superprotonic phase transition temperature (T_{SP}). From radius ratio rules one would expect small oxy-anions to have lower superprotonic transition temperatures, but in fact, this is opposite with what is observed. For example, CsH_2PO_4 has a high superprotonic transition temperature of 230°C , while CsH_2AsO_4 , with a much larger oxy-anion, transforms at only 155°C . A similar effect is observed between the sulfates and selenates. This effect is likely caused, not by oxy-anion size, but rather, by the difference in hydrogen bond strength between different oxy-anions. To consider this possibility, the difference in Gibbs free energies for the formation of ionic defects in aqueous

H_nXO_4 acids are considered,



where $X = S, Se, P, As$, and $n = 1, 2$. For the formation of such defects, acids exhibiting strong hydrogen bonding are expected to have large positive values of ΔG_f° . The ΔG_f° values calculated for the above defect formation are plotted as a function of oxy-anion size in Figure 3.29. In the same figure, the superprotonic transition temperature (T_{SP}) for CsH_nXO_4 compounds is similarly plotted as a function of oxy-anion size. The analogous trend between these two curves suggests that hydrogen bonding plays a prominent role in determining the superprotonic phase transition temperature, and furthermore, points out the relatively insignificant role oxy-anion size plays.

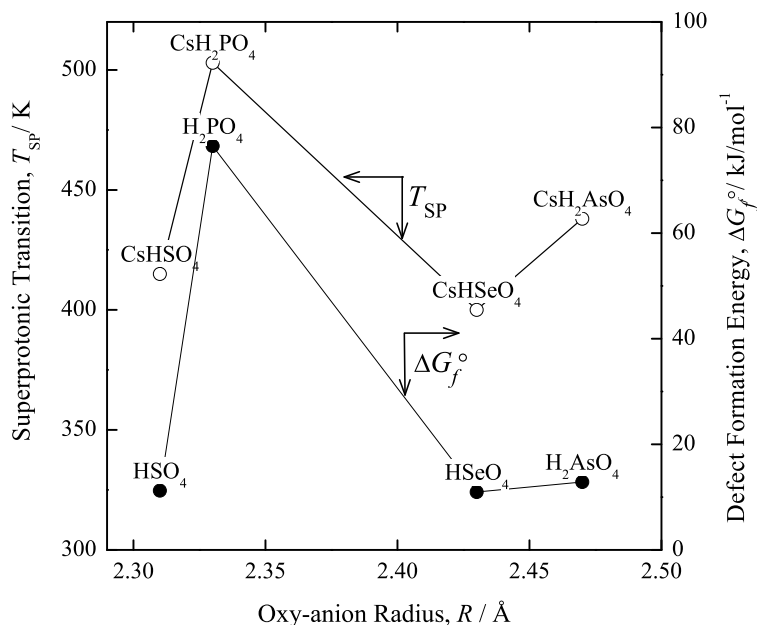


Figure 3.29: The superprotonic transition temperature in CsH_nXO_4 compounds and the Gibbs energy for ion defect formation in H_nXO_4 -acids plotted as a function of oxy-anion size (where $X = S, Se, P, As$).

3.3 Conclusions

The most substantial achievement presented in this chapter is the unequivocal identification of superprotonic behavior in fully hydrogen bonded solid acids, such as CsH_2PO_4 and RbH_2PO_4 . This single result has (1) allowed significant progress to be made in understanding the role of hydrogen bonding in superprotonic solid acids, and (2) provided illumination

to the effect of cation and oxy-anion size. Moreover, as will be seen in the following chapters, this result has (3) aided in the characterization of the entropic driving force behind superprotonic transitions, and (4) allowed for the successful application of solid acids in fuel cells.

Finally, a clear cation to oxy-anion size effect in MH_nXO_4 -type superprotonic solid acids has been explained in terms of radius ratio rules. However, while it has been observed that ion size does play a role in superprotonic transitions, ultimately, the effect of both hydrogen and ionic bonding are equally critical factors in allowing for superprotonic conductivity in a MH_nXO_4 -type solid acids.

Bibliography

1. A.I. Baranov, L.A. Shuvalov, and N.M. Shchagina. Superior conductivity and phase-transitions in CsHSO_4 and CsHSeO_4 crystals. *JETP Letters*, 36(11):459–462, 1982.
2. A.I. Baranov, I.P. Makarova, L.A. Muradyan, A.V. Tregubchenko, L.A. Shuvalov, and V.I. Simonov. Phase-transitions and proton conductivity in $\text{Rb}_3\text{H}(\text{SeO}_4)_2$ crystals. *Kristallografiya*, 32(3):682–694, 1987.
3. B.V. Merinov, A.I. Baranov, L.A. Shuvalov, and B.A. Maximov. Crystal-structure of the superionic phase of CsDSO_4 and phase-transitions in cesium hydrosulfates and deuteriosulfates (selenates). *Kristallografiya*, 32(1):86–92, 1987.
4. Calum R. I. Chisholm. *Superprotonic Phase Transitions in Solid Acids: Parameters affecting the presence and stability of superprotonic transitions in MH_nXO_4 family of compounds ($X = \text{S, Se, P, As}$; $M = \text{Li, Na, K, NH}_4, \text{Rb, Cs}$)*. PhD thesis, California Institute of Technology, 2002.
5. D.A. Boysen, S.M. Haile, H. Liu, and R.A. Secco. High-temperature behavior of CsH_2PO_4 under both ambient and high pressure conditions. *Chemistry of Materials*, 15:727–736, 2003.
6. A. Levstik, R. Blinc, P. Kadaba, S. Cizikov, I. Levstik, and C. Filipic. Dielectric properties of CsH_2PO_4 and CsD_2PO_4 . *Solid State Communications*, 16(12):1339–1341, 1975.
7. Y. Uesu and J. Kobayashi. Crystal-structure and ferroelectricity of cesium dihydrogen phosphate CsH_2PO_4 . *Physica Status Solidi A—Applied Research*, 34(2):475–481, 1976.
8. A.I. Baranov, V.P. Khiznichenko, V.A. Sandler, and L.A. Shuvalov. Frequency dielectric-dispersion in the ferroelectric and superionic phases of CsH_2PO_4 . *Ferroelectrics*, 81:1147–1150, 1988.
9. E. Ortiz, R.A. Vargas, and B.E. Mellander. On the high-temperature phase transitions of some KDP-family compounds: A structural phase transition? A transition to a bulk-high proton conducting phase? *Solid State Ionics*, 125(1-4):177–185, 1999.
10. S.M. Haile and D.A. Boysen. The high temperature behavior of CsH_2PO_4 . In *Material Research Society Symposium Proceedings*, volume 547, page 315, 1999.
11. F. Romain and A. Novak. Raman-study of the high-temperature phase-transition in CsH_2PO_4 . *Journal of Molecular Structure*, 263:69–74, 1991.
12. A. Presinger, K. Mereiter, and W. Bronowska. The phase transition of CsH_2PO_4 (CDP) at 505 K. *Materials Science Forum*, 166:511–516, 1994.
13. Y. Luspain, Y. Vaills, and G. Hauret. Discontinuities in elastic properties of CsH_2PO_4 at the superionic transition. *Journal de Physique I*, 7(6):785–796, 1997.
14. K.S. Lee. Hidden nature of the high-temperature phase transitions in crystals of KH_2PO_4 -type: Is it a physical change? *Journal of Physics and Chemistry of Solids*, 57(3):333–342, 1996.

15. N.M. Plakida. Superionic phase-transitions in hydrogen-bonded crystals. *Physica Status Solidi B—Basic Research*, 135(1):133–139, 1986.
16. L.N. Rashkovich, K.B. Meteva, Y.E. Shevchik, V.G. Hoffman, and A.V. Mishchenko. Growing of cesium dihydrophosphate single-crystals, and some of their properties. *Kristallografiya*, 22(5):1075–1081, 1977.
17. B.M. Nirsha, E.N. Gudinitza, A.A. Fakeev, V.A. Efremov, B.V. Zhadanov, and V.A. Olikova. Thermal dehydration process of CsH_2PO_4 . *Zhurnal Neorganicheskoi Khimii*, 27(6):1366–1369, 1982.
18. L.N. Rashkovich and K.B. Meteva. Properties of cesium dihydrophosphate. *Kristallografiya*, 23(4):796–800, 1978.
19. B. Metcalfe and J.B. Clark. Differential scanning calorimetry of RbH_2PO_4 and CsH_2PO_4 . *Thermochimica Acta*, 24(1):149–153, 1978.
20. W. Bronowska and A. Pietraszko. X-ray study of the high-temperature phase-transition of CsH_2PO_4 crystals. *Solid State Communications*, 76(3):293–298, 1990.
21. E. Rapoport, J.B. Clark, and P.W. Richter. High-pressure phase relations of RbH_2PO_4 , CsH_2PO_4 , and KD_2PO_4 . *Journal of Solid State Chemistry*, 24(3-4):423–433, 1978.
22. B. Baranowski, M. Friesel, and A. Lundén. New phase-transitions in CsHSeO_4 , CsH_2PO_4 , RbHSO_4 , RbHSeO_4 , and RbH_2PO_4 . *Zeitschrift für Naturforschung Section A—A Journal of Physical Sciences*, 41(7):981–982, 1986.
23. K.H. Illers. Determination of melting-point of crystal polymers by means of heat-flow calorimetry (DSC). *European Polymer Journal*, 10(10):911–916, 1974.
24. G. Alberti, M.G. Bernasconi, M. Casciola, and U. Costantino. Ion-exchange processes on the surface of micro-crystals of zirconium bis-(monohydrogen ortho-phosphate) monohydrate. *Annali Di Chimica*, 68(3-4):265–274, 1978.
25. S.M. Haile, D.L. West, and J. Campbell. The role of microstructure and processing on the proton conducting properties of gadolinium-doped barium cerate. *Journal of Materials Research*, 13(6):1576–1595, 1998.
26. R.J. Nelmes and R.N.P. Choudhary. Structural studies of monoclinic dihydrogen phosphates – neutron-diffraction study of paraelectric CsH_2PO_4 . *Solid State Communications*, 26(11):823–826, 1978.
27. J.P. Yesinowski and H. Eckert. Hydrogen environments in calcium phosphates – ^1H MAS NMR at high spinning speeds. *Journal of the American Chemical Society*, 109(21):6274–6282, 1987.
28. L.F. Kirpichnikova, A.A. Urusovskaya, and V.I. Mozgovi. Superplasticity of CsHSO_4 crystals in the superionic phase. *JETP Letters*, 62(8):638–641, 1995.
29. B. Baranowski, M. Friesel, and A. Lundén. Pressure-dependence of high-temperature phase – Transitions in solid CsH_2PO_4 and RbH_2PO_4 . *Physica Scripta*, 37(2):209–213, 1988.

30. V.V. Sinitsyn, E.G. Ponyatovskii, A.I. Baranov, A.V. Tregubchenko, and L.A. Shuvalov. The anisotropy of protonic conductivity in CsHSO_4 and CsDSO_4 crystals and the hydrostatic-pressure effect on it. *Zhurnal Eksperimentalnoi I Teoreticheskoi Fiziki*, 100(2):693–706, 1991.
31. V.V. Sinitsyn, A.I. Baranov, E.G. Ponyatovsky, and L.A. Shuvalov. Pressure effect on phase-transitions and protonic conductivity in $\text{Rb}_3\text{H}(\text{SeO}_4)_2$ and $(\text{NH}_4)_3\text{H}(\text{SO}_4)_2$. *Solid State Ionics*, 77:118–121, 1995.
32. D.A. Boysen, H. Liu, R.A. Secco, and S.M. Haile. Conductivity of potassium and rubidium dihydrogen phosphates at high temperature and pressure. *Chemistry of Materials*, 2003. in press.
33. N.S.J. Kennedy and R.J. Nelmes. Structural studies of RbH_2PO_4 in its paraelectric and ferroelectric phases. *Journal of Physics C—Solid State Physics*, 13(26):4841–4853, 1980.
34. P. Bärtschi, B. Matthias, W. Merz, and P. Scherrer. Eine neue, seignette-elektrische modifikation von rubidiumphosphat. *Helvetica Physica Acta*, 18(4):240–242, 1945.
35. R. Blinc, J.R. Ferraro, and C. Postmus. Effects of high pressure on far-infrared spectra of paraelectric KH_2PO_4 and RbH_2PO_4 . *Journal of Chemical Physics*, 51(2):732, 1969.
36. L. Erdey, G. Liptay, and S. Gal. Thermoanalytical properties of analytical-grade reagent—III Rubidium salts. *Talanta*, 12:883–892, 1965.
37. M.T. Averbuch-Pouchot and A. Durif. Structure of a new form of rubidium dihydrogenphosphate, RbH_2PO_4 . *Acta Crystallographica Section C—Crystal Structure Communications*, 41(May):665–667, 1985.
38. V.A. D'yakov, V.A. Koptsik, I.V. Lebedeva, A.V. Mishchen, and L.N. Rashkovi. High-temperature phase-transitions in crystals $\text{Rb}(\text{D}_x\text{H}_{1-x})_2\text{PO}_4$. *Kristallografiya*, 18(6):1227–1233, 1973.
39. J.H. Park, K.S. Lee, and J.N. Kim. Surface instability and possible polymerization in RbH_2PO_4 at high temperatures. *Journal of Physics—Condensed Matter*, 10(43):9593–9607, 1998.
40. J.H. Park, K.S. Lee, and B.C. Choi. High-temperature transformation in KH_2PO_4 and RbH_2PO_4 crystals. *Journal of Physics—Condensed Matter*, 13(42):9411–9419, 2001.
41. A.I. Baranov, V.P. Khiznichenko, and L.A. Shuvalov. High-temperature phase-transitions and proton conductivity in some KDP-family crystals. *Ferroelectrics*, 100:135–141, 1989.
42. V.V. Sinitsyn and A.I. Baranov. Compensation law for protonic conductors of the $\text{Me}_n\text{H}_m(\text{AO}_4)_p$ group. *Russian Journal of Electrochemistry*, 32(4):427–431, 1996.
43. W. Bronowska. Comment on “Does the structural superionic phase transition at 231 degrees C in CsH_2PO_4 really not exist?”. *Journal of Chemical Physics*, 114(1):611–612, 2001.

44. J. West. A quantitative X-ray analysis of potassium dihydrogen phosphate (KH_2PO_4). *Zeitschrift für Kristallographie*, 74:306–332, 1930.
45. G. Busch and P. Scherrer. Eine neue seignette-elektrische substanz. *Naturwissenschaften*, 23:737, 1935.
46. B.C. Frazer and R. Pepinsky. X-ray analysis of the ferroelectric transition in KH_2PO_4 . *Acta Crystallographica*, 6(3):273–285, 1953.
47. J. Grünberg, S. Levin, D. Gerlich, and I. Pelah. High-temperature phase-transitions and metastability in KDP type crystals. *Physica Status Solidi B–Basic Research*, 49(2):857–869, 1972.
48. E. Rapoport. Phase transformations and melting in KH_2PO_4 to 40 kbar. *Journal of Chemical Physics*, 53(1):311–314, 1970.
49. J.A. Subramony, S. Lovell, and B. Kahr. Polymorphism of potassium dihydrogen phosphate. *Chemistry Of Materials*, 10(8):2053–2057, 1998.
50. S. Vyazovkin and T.L. Ferrin. Thermomechanical study of the high temperature phase transition in KH_2PO_4 . *Solid State Communications*, 113(11):627–631, 2000.
51. M. Mathew and W. Wong-Ng. Crystal-structure of a new monoclinic form of potassium dihydrogen phosphate-containing orthophosphacidium ion, $[\text{H}_4\text{PO}_4]^+$. *Journal of Solid State Chemistry*, 114(1):219–223, 1995.
52. R.D. Shannon. Revised effective ionic-radii and systematic studies of interatomic distances in halides and chalcogenides. *Acta Crystallographica Section A*, 32(Sept 1):751–767, 1976.
53. Linus Pauling. *Nature of the Chemical Bond*. Cornell University Press, New York, 1960.
54. Z. Jirak, M. Dlouha, S. Vratislav, A.M. Balagurov, A.I. Beskrovnyi, V.I. Gordelii, I.D. Datt, and L.A. Shuvalov. A neutron-diffraction study of the superionic phase in CsHSO_4 . *Physica Status Solidi A–Applied Research*, 100(2):K117–K122, 1987.

Chapter 4

Properties of Superprotonic MH_nXO_4 -type Solid Acids

Superprotonic solid acids are known to undergo an order-disorder phase transition, upon which the ionic conductivity increases by several orders of magnitude. In this chapter, the thermodynamic driving force behind these phase transitions will be investigated. Phase transitions are, in general, driven by a systems tendency towards maximum entropy. Therefore, an effort will be made here to account for the change in entropy through a superprotonic phase transition. While there are many forms of entropy, a detailed account of the *configurational* entropy of superprotonic solid acids will be presented.

A methodology for calculating the configurational entropy of superprotonic solid acids will be presented here, much of which has been pioneered by coworker, Calum Chisholm^{1,2}. Nonetheless, the incontrovertible proof of superprotonic conductivity in fully hydrogen-bonded solid acids (presented in Chapter 3), was a key contribution to these developments. Overall, the approach employed here has been fundamentally derived from the work of Linus Pauling, and his landmark paper for evaluating the residual entropy in ice³.

This chapter will begin with a review of Pauling's entropy rules for ice. Then, based upon these entropy rules, a new set of entropy rules will be presented for superprotonic solid acids. In this section, the structural details of superprotonic phases and calculations of the configurational entropy of these phases will be presented. The section following will discuss the configurational entropy associated with the intra-hydrogen bond disorder, which results in ferro-paraelectric phase transitions in many of these solid acids. This is necessary to compare the calculated with the experimentally measured values of the change in entropy through the superprotonic transition ΔS_{SP} , which is the entropy of the superprotonic phase

S_{SP} , minus the entropy of the phase prior to the superprotonic transition, S_0 ,

$$\Delta S_{\text{SP}} = S_{\text{SP}} - S_0. \quad (4.1)$$

Lastly, a summary of these calculations and a comparison with experimental results will be presented.

4.1 Pauling's Entropy Rules for Ice³

Upon cooling H_2O to 0 K, it crystallizes in the hexagonal space group $P6_3/mmc$ ⁴, known as ice phase Ih, depicted in Figure 4.1. It was observed that a “residual” entropy persists in this phase to 0 K⁵. This residual entropy was explained by Pauling in terms of a configurational entropy associated with statically disordered hydrogen bonds between oxygen atoms, as indicated in Figure 4.1.

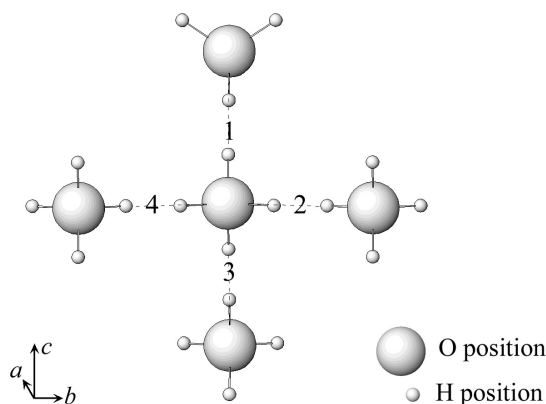


Figure 4.1: Depiction of the structure of hexagonal ice ($P6_3/mmc$), phase Ih⁴. Two hydrogen atoms are statically disordered among the four possible hydrogen positions, 1 through 4, as indicated.

From original observations of the structure of hexagonal ice, Bernal and Fowler concluded that the structure of individual H_2O molecules in ice was not unlike those in steam, and therefore, must follow these configuration rules⁴:

Rule 1 *Two and only two protons can be bonded to an oxygen atom.*

Rule 2 *One and only one proton is allowed per hydrogen bond.*

Later, Pauling added to these so-called ice rules, the following³:

Rule 3 *The hydrogen bonds must be directed approximately toward two of the four neighboring oxygen atoms.*

Rule 4 *The interaction of non-neighboring water molecules does not energetically favor one possible arrangement of protons with respect to other possible configurations so long as they all satisfy Rules 1–3.*

Using these four rules, Pauling estimated the number of configurations Ω per H_2O molecule to be

$$\begin{aligned}\Omega &= \binom{\text{number of proton}}{\text{configurations}} \times \binom{\text{probability a proton}}{\text{site is open}}^{\text{(number of protons)}} \\ &= \binom{4}{2} \times \left(\frac{2}{4}\right)^2 = \left(\frac{4!}{2 \cdot 2!}\right) \cdot \left(\frac{1}{4}\right) = \frac{3}{2}\end{aligned}\quad (4.2)$$

giving a residual configurational entropy S of

$$\begin{aligned}S &= R \ln \Omega = R \ln \left(\frac{3}{2}\right) \\ &= 0.405R \text{ or } 3.37 \text{ J mol}^{-1}\text{K}^{-1}.\end{aligned}\quad (4.3)$$

This result closely agrees with the experimentally determined residual entropy of $3.65 \text{ J mol}^{-1}\text{K}^{-1}$, calculated from the difference between the entropy of ice estimated from thermal data at very low temperature conditions ($185.16 \text{ J mol}^{-1}\text{K}^{-1}$)⁵ and the spectroscopic value of water vapor at standard conditions ($188.81 \text{ J mol}^{-1}\text{K}^{-1}$)⁶.

While the residual entropy in ice is due to *statically disordered* hydrogen bonds, others have extended these rules to account for the entropy of *dynamically disordered* hydrogen bonds in other H_2O -containing solids, such as ice-polymorphs, clathrate hydrates, $\text{SnCl}_2 \cdot \text{H}_2\text{O}$, $\text{Cu}(\text{HCO}_2)_2 \cdot \text{H}_2\text{O}$, and $(\text{H}_{31}\text{O}_{14})(\text{CdCu}_2(\text{CN})_7)$ ^{7,8,9,10}. The successful application of Pauling's Ice Rules to these dynamically disordered systems, which exhibit a wide variety of hydrogen bonding and dimensionality of hydrogen bonded networks, demonstrates the versatility of these rules.

While the aforementioned examples of the extension of Pauling's Ice Rules all dealt with the entropy associated with the disordering of hydrogen bonds between H_2O molecules, further extensions of these rules have been made by Slater to systems containing hydrogen bonded tetrahedral oxy-anions¹¹. Slater employed Pauling's Ice Rules to account for the

entropy associated with the ferroelectric transition in KH_2PO_4 , in which, upon cooling, disordered hydrogen bonds become ordered at the ferroelectric transition temperature T_{FE} ($-151\text{ }^\circ\text{C}$). The structure of KH_2PO_4 , depicted in Figure 4.2, is composed of PO_4 tetrahedra, each of which partake in four disordered hydrogen bonds in the paraelectric room temperature structure. Using the same formulation as used to determine the number of configurations in ice, Equation 4.2, Slater arrived at an entropy for the disordered paraelectric phase of KH_2PO_4 of $R \ln(3/2)$ or $3.37\text{ J mol}^{-1}\text{K}^{-1}$ (at $T \gg T_{\text{FE}}$). This value is not far the experimental value of $3.51(12)\text{ J mol}^{-1}\text{K}^{-1}$ from heat capacity measurements.^{12,i}

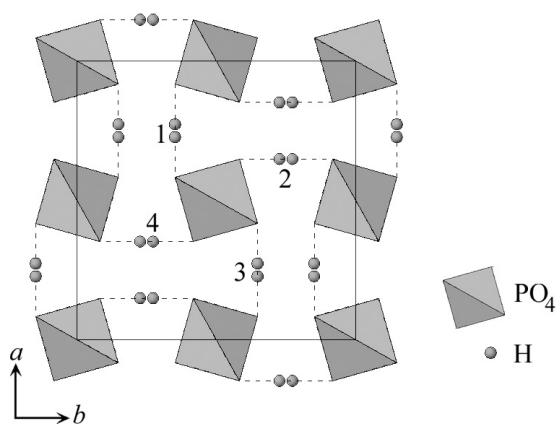


Figure 4.2: Depiction of the room temperature, paraelectric structure of KH_2PO_4 , tetragonal ($I4amd$)¹³. Disordered hydrogen bonds 1–4 of the central tetrahedral PO_4 are indicated. Potassium atoms not shown for clarity.

Pauling’s Ice Rules have, thus, successfully described the entropy changes of both disordered H_2O -containing systems and compounds containing tetrahedral oxy-anions. Further, extension of these ice rules have *even* been made to superprotonic solid acids for the purpose of distinguishing between the proton transport mechanisms of the ordered and disordered phases, as well as, to describe phenomenologically, the arrangement of protons in the superprotonic phases¹⁴. Therefore, the development of analogous rules to quantitatively account for the entropy associated with superprotonic solid acids, would seem a natural progression.

ⁱIt is the author’s experience that literature values of entropy based upon heat capacity measurements are highly variable—ultimately contingent upon the temperature range of the measurement and the baseline used.

4.2 Entropy of Superprotonic Phases^{1,2}

In this section, an adaption of Pauling’s entropy rules for ice, that accounts for *both* the disordered tetrahedral oxy-anions *and* hydrogen bond disorder in superprotonic MH_nXO_4 -type solid acids, will be presented.

Previous entropic models of superprotonic phase transitions have failed to (1) provide a general description of the entropic driving force for superprotonic phase transitions, and (2) accurately account for the experimentally measured entropy in such transitions. Most notable among these were the developments of Plakida, in which a Landau theory approach was adopted to describe the superprotonic phase transition in CsHSO_4 ^{15,16}. In this model, depicted in Figure 4.3, protons are (a) ordered at positions 2 and 4 at room temperature, and upon passing through the superprotonic transition, the protons become (b) disordered among positions 1–4. Assigning an order-parameter to proton positions 1 through 4 and incorporating the Silsbee-Jüling-Schmidt model¹⁷ to account for short-range proton correlations, Plakida obtains a first-order Slater type transition, identified by a discontinuous “jump” in the order parameter at the transition temperature T_{SP} . The calculated change in entropy, $\Delta S \sim 0.52R$, differed somewhat from the experimental value of the time, $\Delta S = 1.32R$, which, as Plakida explained, was on account of ignoring the disordering of SO_4 groups¹⁵. While this model does capture some aspects of the superprotonic phase transition, it falls short in accurately accounting for the entropy in the superprotonic phase, and moreover, would forbid superprotonic phase transitions in solid acids with fully hydrogen bonded tetrahedral oxy-anions.ⁱⁱ Furthermore, Plakida’s model relies upon a strict relationship between the low temperature and superprotonic structures, which is not necessarily obeyed by the real structures

In order to develop a more complete picture of the disordered superprotonic phases of MH_nXO_4 -type compounds, a new methodology for calculating the entropy of compounds with rotationally disordered oxy-anions, randomly linked by disordered hydrogen bonds, is presented.

ⁱⁱDiscussed in the Section 3.1

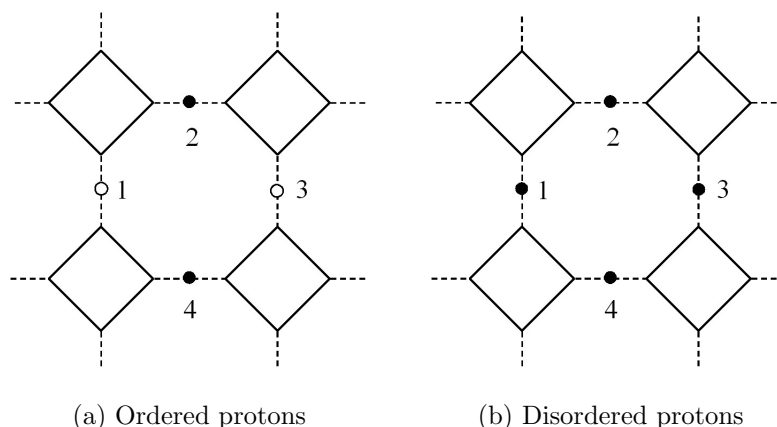
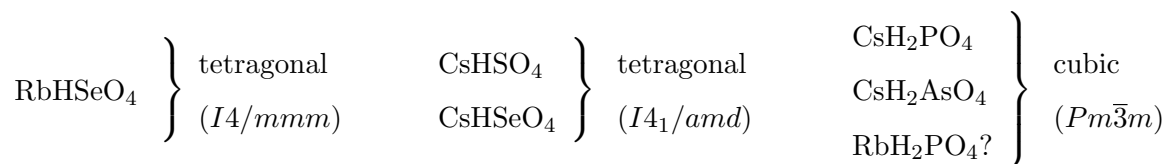


Figure 4.3: Model proposed for the superprotonic phase transitions in CsHSO_4 . Squares represent SO_4 groups and circles represent proton positions. (a) Ordered phase, in which positions 2 and 4 are occupied by protons. (b) Disordered superprotonic phase, in which, 2 protons are disordered among 4 positions^{15,16}.

4.2.1 Superprotonic Structures

In general, superprotonic MH_nXO_4 -type solid acids are known to exhibit one of two structures: tetragonal or cubic. Solid acids CsHSO_4 and CsHSeO_4 transform to an $I4_1/amd$ tetragonal structure^{18,19,20,21}, whereas CsH_2PO_4 , RbH_2PO_4 , and CsH_2AsO_4 transform to a $Pm\bar{3}m$ cubic structure^{22,23}. The structure of superprotonic RbHSeO_4 , determined here, also has a tetragonal structure ($I4/mmm$), however it differs significantly from the other two structures in its atomic arrangement. Before delving into calculating the entropy, details of these structures and controversies pertaining to them, as well as the refinement of the superprotonic structure of RbHSeO_4 , will be presented. To summarize, the structures of known superprotonic MH_nXO_4 -type solid acids are as follows.ⁱⁱⁱ



Tetragonal $I4/mmm$

The solid acid, rubidium hydrogen selenate (RbHSeO_4), is known to undergo a superprotonic transition at $173\text{ }^\circ\text{C}$ ²⁴, however, as-of-yet there are no reported structures for this superprotonic phase. Therefore, the structure of the superprotonic phase of RbHSeO_4 has

ⁱⁱⁱStructures *not* including mixed cation or oxy-anion compounds, such as $\text{Cs}_2(\text{HSO}_4)(\text{H}_2\text{PO}_4)$.

been investigated by high temperature powder X-ray diffraction, the results of which are presented here.

The data from powder X-ray diffraction performed on RbHSeO_4 with a Si-internal standard at 175°C is presented in Figure 4.4. With these data, a Rietveld refinement was carried out to determine the structure and atomic positions of the heavy atoms (Rb, Se). The structure was refined in the body-centered tetragonal cell $I/4mmm$, $a = 4.0309(2) \text{ \AA}$, $c = 7.0436(3) \text{ \AA}$, $Z = 2$, $V = 114.4 \text{ \AA}^3$. The structural results, measurement parameters, and refinement parameters of the Rietveld refinement are given in Table 4.1. In Figure 4.4, the calculated intensity (I_{calc}) of the refined structure is compared with the experimentally observed intensity (I_{obs}) and below is the difference between these two curves ($I_{\text{calc}} - I_{\text{obs}}$).

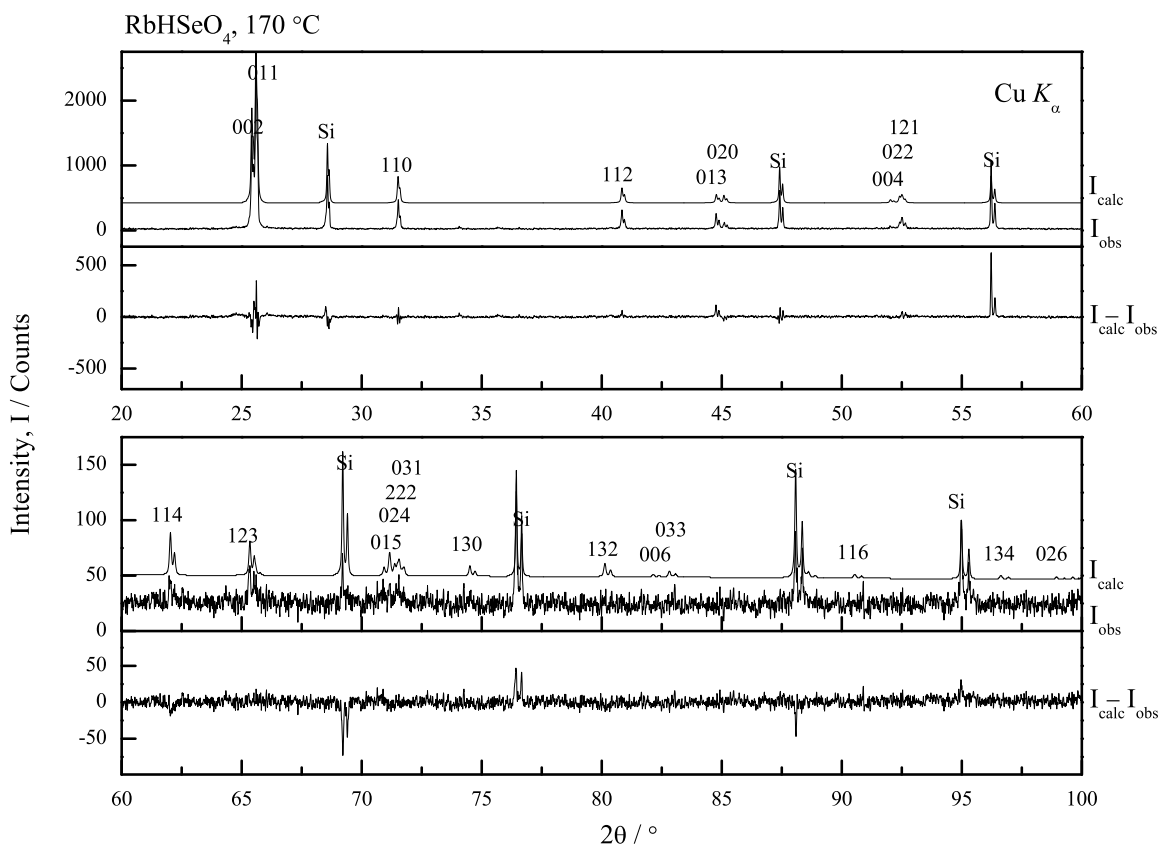


Figure 4.4: Powder X-ray diffraction pattern of RbHSeO_4 at 170°C with a Si-internal standard. The top-curve is the calculated intensities (I_{calc}) from the refined superprotonic structure ($I4/mmm$, $a = 4.031$, $b = 7.044 \text{ \AA}$) plus the Si-internal standard, the middle-curve the experimentally observed intensities (I_{obs}), and the bottom-curve the difference between the calculated and observed intensities ($I_{\text{calc}} - I_{\text{obs}}$).

The fractional atomic coordinates of the Rb and Se positions, determined from the

Table 4.1: Summary of structural data, measurement parameters, and refinement parameters of the Rietveld analysis of powder X-ray diffraction data taken from RbHSeO_4 with an Si-internal standard at 170 °C.

Structural Data	
Compound Name	Rubidium hydrogen selenate
Chemical Formula	RbHSeO_4
Molecular Weight/ $\text{g}\cdot\text{mol}^{-1}$	229.433
Weight Fraction/ %	23.9(2)
Space Group (No.)	$I4/mmm$ (139)
Lattice Parameters	
$a/ \text{Å}$	4.03149(9)
$b/ \text{Å}$	4.03149(9)
$c/ \text{Å}$	7.0457(2)
$\alpha/ ^\circ$	90
$\beta/ ^\circ$	90
$\gamma/ ^\circ$	90
Multiplicity, Z	2
Volume, $V/ \text{Å}^3$	114.513
Density, $\rho/ \text{g}\cdot\text{cm}^{-3}$	2.41
Measurement Parameters	
Generator Settings	45 kV, 40 mA
Divergence Slit/ $^\circ$	1.000
Scan-range, $2\theta/ ^\circ$	10.000–100.000
Step Size, $2\theta/ ^\circ$	0.008
Scan Time per Step/ s	3.15
Scan Type	continuous
Radiation	$\text{CuK}\alpha$
Temperature, $T/ ^\circ\text{C}$	170
Atmosphere	ambient
Refinement Parameters	
Number of Phases	2
Number of Variables	21
Displacement	0.1594(6)
Profile fit	Pseudo-Voigt
Background	refined
Coefficients for Peak FWHM	
U	0.000
V	0.012(1)
W	0.0017(3)
Preferred Orientation	1 0 0
Preferred Orientation Parameter	1.379(6)
Asymmetry Parameter	1.0(1)
Refinement Statistics	
$R_{\text{exp}}/ \%$	16.170
$R_{\text{p}}/ \%$	17.336
$R_{\text{wp}}/ \%$	22.929
$R_{\text{B}}/ \%$	6.233
GOF	2.011
d -statistic	0.057

Table 4.2: Atomic fractional coordinates, Wyckoff positions, and site occupancies of superprotonic RbHSeO_4 ($I4/mmm$). Rb and Se positions were determined from a Rietveld refinement. O positions estimated (*) from expected $\langle \text{Se-O} \rangle$ bond lengths (1.66 Å), $\angle \text{O-Se-O}$ bond angles (109.5°), expected 12-fold coordination of Rb by O atoms, and crystal symmetry requirements.

Atom	Wyckoff Position	Fractional Coordinates			Site Occupancy
		x	y	z	
Rb	$2a$	0	0	0	1
Se	$2b$	0	0	1/2	1
O(1)*	$32o$	0.125	0.348	0.116	1/8
O(2)*	$16n$	0.250	1/2	0.330	1/4

Rietveld refinement, are given in Table 4.2. From these, the structure of superprotonic RbHSeO_4 is depicted in Figure 4.5(a). In this structure, Rb atoms are positioned at the corners and body-center of the unit cell. The Se atoms are positioned in faces perpendicular to the c -axis, and on the edges of the unit cell parallel to the c -axis. The SeO_4 groups are coordinated by 6 Rb atoms, forming an octahedral coordination polyhedra, Figure 4.5(b).

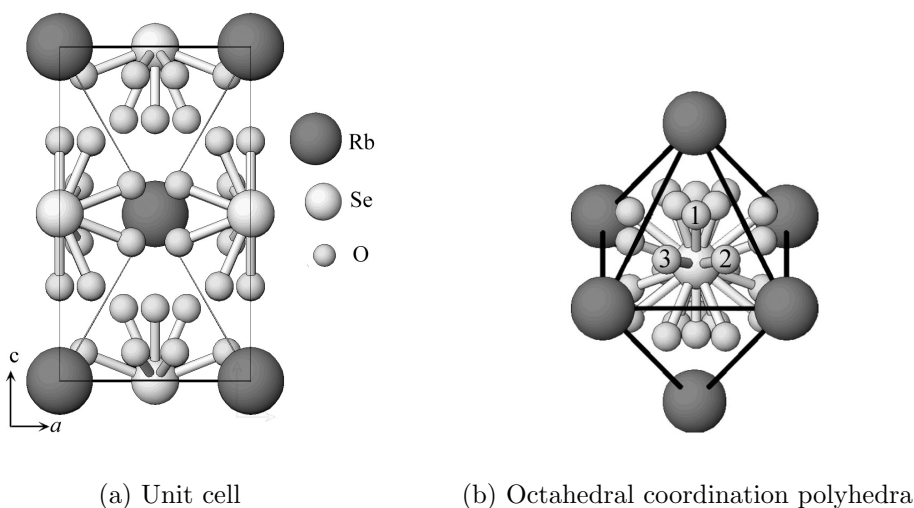


Figure 4.5: Depiction of the superprotonic structure of RbHSeO_4 , tetragonal space group $I4/mmm$. (a) The unit cell as viewed along the b -axis. (b) Octahedral coordination polyhedra of disordered SeO_4 groups by Rb cations, numbers 1–3 indicate disordered oxygen positions participating in hydrogen bonding through the faces of the octahedra.

Attempts at refining the oxygen positions using the Rietveld method proved unsuccessful. Probable causes for this could be the low atomic number of oxygen (*i.e.*, small scattering cross section), however, a more likely cause is the high degree of disorder associated with the rapid tetrahedral reorientations observed in superprotonic solid acids. Instead, the oxy-

gen positions are proposed based upon the optimization of four criteria: (1) the oxygen to selenium distances must be approximately equal those found in the room temperature structure of RbHSeO_4 , $\langle \text{Se-O} \rangle \approx 1.66 \text{ \AA}$, (2) the angles between two oxygen positions, with selenium positioned at the vertex, must form a complete set of six tetrahedral angles, $\angle \text{O-Se-O} \approx 109.5^\circ$, (3) at least 12 oxygen positions must coordinate a Rb atom—the preferred coordination of Rb^+ by O^{2-} ions²⁵, (4) the symmetry of the crystal must be preserved by the choice of any oxygen position. Based upon these criteria, approximate oxygen positions are proposed, given in Table 4.2.

The structure of RbHSeO_4 is unique among superprotonic MH_nXO_4 -type solid acids in that, unlike the characteristic 8-fold coordination of the oxy-anions by cations normally observed, superprotonic RbHSeO_4 exhibits 6-fold octahedral coordination, Figure 4.5(b). Disordered hydrogen bonds are expected to form through the faces of these octahedra, where intra-tetrahedral oxygen distances are $\sim 2.4 \text{ \AA}$ —suggestive of strong symmetric hydrogen bonds. Overall, 24 oxygen positions are suggested, resulting in 3 possible oxygen positions per octahedral face, numbered 1–3 in Figure 4.5(b), and, therefore, 3 unique tetrahedral orientations.

Tetragonal $I4_1/amd$

Both superprotonic CsHSO_4 and CsHSeO_4 structures belong to the tetragonal space group $I4_1/amd$ ^{20,21}. The tetragonal structure of superprotonic CsHSO_4 , depicted in Figure 4.6, is composed of Cs cations and SO_4 oxy-anions arranged in alternating pairs along the b -axis. Crystallographically equivalent and partially occupied oxygen positions result in the overall rotational disorder of the oxy-anion between crystallographically equivalent oxygen positions. These oxy-anions are coordinated by 8 Cs cations, forming a 6-sided polyhedra, in which two triangular prisms lie orthogonal to one another, termed here as a *triangular anti-prism*, Figure 4.6(b). The oxygen atoms of the rotationally disordered tetrahedra are likely to participate in disordered hydrogen bonds through the rectangular faces of the triangular anti-prism.

While reports of the superprotonic structure of both CsHSO_4 and isostructural CsHSeO_4 ^{18,19,20,21} more or less agree on the symmetry, lattice parameters, and heavy atom positions; they differ considerably in their assignment of oxygens positions, and consequently, tetrahedral orientations and direction of hydrogen bonds^{18,19,20}. This dissent is likely the result of highly

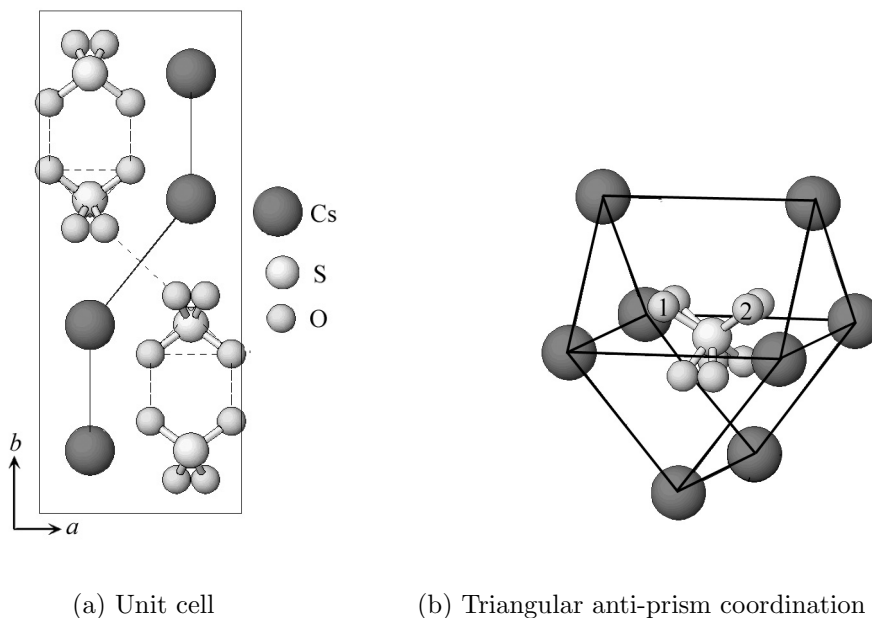


Figure 4.6: Depiction of the superprotonic structure of CsHSO_4 , tetragonal space group $I4/mmm$. (a) The unit cell as viewed along the c -axis. (b) Triangular anti-prism coordination polyhedra of disordered SO_4 groups by Cs cations, where numbers 1–2 indicate disordered oxygen positions according to structure proposed by Jirak²⁰. Disordered hydrogen bonds are like to occur through the rectangular faces of the coordination polyhedron.

rotationally-disordered tetrahedral oxy-anions in the superprotonic phase—ultimately, leading to a “smearing out” of the oxygen positions. Experimental difficulties have also been encountered in single crystal diffraction work of superprotonic CsHSO_4 due to the loss of structural integrity of the crystal while heating through the phase transition, resulting in polycrystallinity¹⁸.

Many structural descriptions have been given for the superprotonic structure of CsHSO_4 , each essentially differing in the assignment of oxygen positions. In Figure 4.7, three representative structures for the location of the tetrahedral oxygen positions are given, as proposed by (a) Jirak²⁰, (b) Merinov¹⁸, and (c) Belushkin¹⁹. In the structure suggested by Jirak, there are 8 oxygen positions, corresponding to 2 tetrahedral orientations. Similarly, Merinov has proposed a structure in which there are 8 oxygen positions and 2 tetrahedral orientations, except here the oxygen positions have been distinguished between oxygen donor (O_d) and acceptor (O_d) positions. Belushkin, on the otherhand, proposed a structure with 16 oxygen positions, and thus 4 tetrahedral positions, but like Merinov distinguished

between the donor and acceptor oxygen positions. Chisholm observed that by distinguishing between the donor and acceptor oxygen positions, the number of possible tetrahedral orientations is subject to the symmetry imposed by the crystal.² For example, in the structure proposed by Merinov, the oxygen positions lie on mirror planes, which will generate a second set of positions, resulting in a total of 4 tetrahedral configurations. Whereas, in the structure proposed by Belushkin, the oxygen positions do not lie on any special positions, and therefore, each oxygen is associated with only one tetrahedral orientation—again, totaling 4 tetrahedral configurations. Consequently, both the structures of Merinov and Belushkin yield a total of 4 tetrahedral configurations, to give a configuration entropy of $R \ln(4)$ or $11.52 \text{ J mol}^{-1}\text{K}^{-1}$ —a value much lower than the $14.8 \text{ J mol}^{-1}\text{K}^{-1}$ measured experimentally¹. In contrast, the structure given by Jirak does not distinguish between O_d and O_a , hence, each oxygen position can partake in any of the possible tetrahedral orientations, regardless of the placement of the hydrogen bond. In order to account for such a structure, a more general entropic model is needed, which includes both tetrahedral reorientation and hydrogen bond disorder.

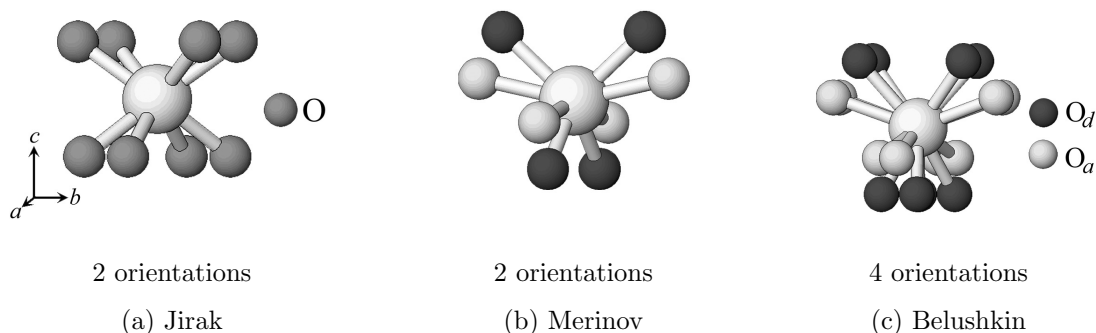


Figure 4.7: Proposed oxygen positions for the superprotonic phase of CsHSO_4 ($I4_1amd$). (a) Jirak—two tetrahedral orientations and does not distinguish between oxygen atoms²⁰. (b) Merinov—two tetrahedral orientations and distinguishes between oxygen donor O_d and acceptor O_a atoms.¹⁸ (c) Belushkin—four tetrahedral positions and distinguishes between O_d and O_a .¹⁹

Based upon the previous discussion, the structure proposed by Jirak is adopted in the following entropy calculations of tetragonal $I4_1/amd$ superprotonic MH_nXO_4 -type solid acids. It will be seen that this structure, in fact, can be used to accurately account for the entropy of the superprotonic phase. Beyond this self-consistent account of the entropy, Chisholm has carried out molecular dynamic simulations of the superprotonic phase transition in CsHSO_4 , the results of which, also favor the structure of Jirak¹.

Cubic $Pm\bar{3}m$

Superprotonic CsH_2PO_4 has a CsCl-type structure, belonging to the cubic space group $Pm\bar{3}m$ ²². There has been only one structural study of this compound in its superprotonic phase. While no explicit structural data exist for the superprotonic phases of CsH_2AsO_4 or RbH_2PO_4 , they are likely to be isostructural with superprotonic CsH_2PO_4 . Observed optical isotropy in superprotonic CsH_2AsO_4 by polarized light investigations do, in fact, suggest cubic symmetry in this crystal²³. Likewise, comparable superprotonic transition entropies between RbH_2PO_4 and CsH_2PO_4 , $\Delta S_{\text{SP}} = 21.3$ and $22.2 \text{ J mol}^{-1}\text{K}^{-1}$, respectively, suggest these compounds have identical superprotonic structures.

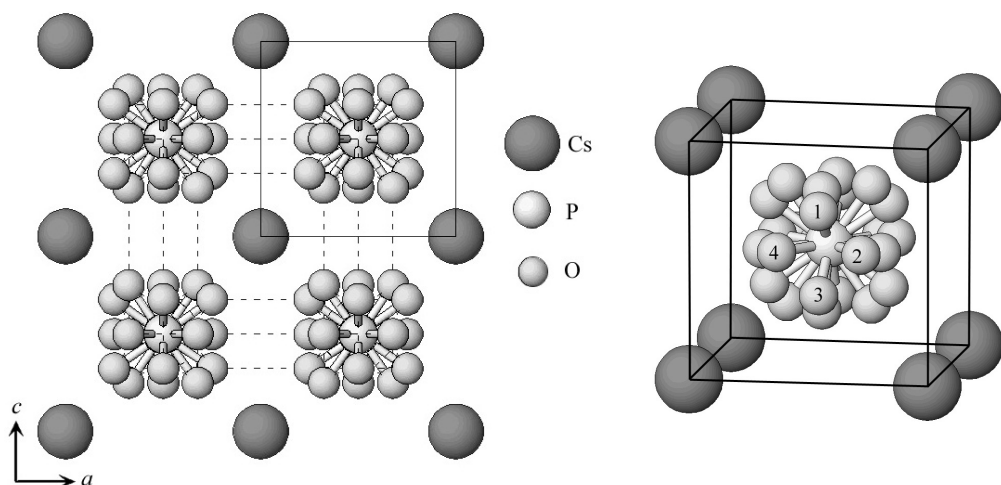
The structure of superprotonic CsH_2PO_4 is composed of disordered tetrahedral oxy-anions positioned at the body centers of cubic coordination polyhedra composed of Cs cations, depicted in Figure 4.8. Based upon inter-tetrahedral oxygen to oxygen bond distances, strong symmetric disordered hydrogen bonds ($\langle \text{O-O} \rangle \approx 2.48 \text{ \AA}$) are expected to form through each of the six faces of the cube. A total of 24 oxygen positions per cell result in 6 tetrahedral orientations, and 4 disordered oxygen positions per hydrogen bond direction, as indicated in Figure 4.8(b). Each Cs position is coordinated by a total of 12 O positions—precisely that expected from radius ratio rules²⁵.

Summary of Superprotonic Structures

A summary of some of the key structural features of these superprotonic MH_nXO_4 -type solid acids is presented in Table 4.3. Since entropy is fundamentally a measure of the number of configurational states ($S = R \ln \Omega$), particularly important to the following the entropy calculations are the *number of hydrogen bonds* per polyhedra and the *number of oxygen positions* per hydrogen bond direction. These two values represent both the hydrogen bond and tetrahedral disorder, which should account for most of the entropy of the superprotonic phase.

4.2.2 Entropy Rules

To generate a set of entropy rules for the superprotonic phases of MH_nXO_4 -type solid acids we begin by modifying Pauling’s entropy rules for ice. First of all, in solid acids the number of hydrogen atoms associated with each tetrahedral oxy-anion (H:XO_4) can be 1 *or* 2,



(a) Four unit cells

(b) Cubic coordination polyhedra

Figure 4.8: Depiction of the superprotonic structure of CsH_2PO_4 , cubic space group $Pm\bar{3}m$ ²². (a) Four unit cells, where dashed lines represent possible hydrogen bonds based upon intra-tetrahedral oxygen to oxygen distances ($\langle \text{O}-\text{O} \rangle < 2.5 \text{ \AA}$), and (b) cubic coordination polyhedra of disordered PO_4 groups by Cs cations, numbers 1–4 indicate disordered oxygen positions participating in hydrogen bonds through the faces of the cube.

Table 4.3: Summary of key structural features observed in superprotonic MH_nXO_4 -type solid acids.

Superprotonic Structure	Tetragonal $I4/mmm$	Tetragonal I_1/amd	Cubic $Pm\bar{3}m$
Solid Acids	RbHSeO_4	CsHSO_4 CsHSeO_4	RbH_2PO_4 CsH_2PO_4 CsH_2AsO_4
Oxy-Anion Coordination Polyhedra	Octahedron	Triangular Anti-Prism	Cube
Oxy-Anion/Cation Coordination	6	8	8
Number of H-Bonds /Polyhedra	6	4	6
Number of Tetrahedral Orientations/Polyhedra	3	2	6
Number of Oxygen Positions /H-bond Direction	3	2	6

whereas, in ice the number of hydrogen atoms per oxygen atom (H:O) is fixed at 2. Thus, we modify Pauling's Ice Rule 1 to read as follows:

Rule 1 *One or two protons can be associated with a tetrahedral oxy-anion.*

Since the nature of a hydrogen bond, itself, is essentially the same for all hydrogen bonded materials, Ice Rules 2 and 3 remain effectively unchanged, adding only that the oxygen atoms are associated with tetrahedral oxy-anions:

Rule 2 *One and only one proton is allowed per hydrogen bond.*

Rule 3 *The hydrogen bonds must be directed approximately toward the oxygen atoms of a neighboring tetrahedral oxy-anion.*

Ice Rule 4 is essentially a statement that hydrogen bond configurations are *only* affected by nearest-neighbor interactions. Here, we follow suit by assuming only nearest-neighbor interactions between tetrahedral oxy-anions. However, one may ask, to what extent is the proton and tetrahedral oxy-anion motion correlated? Here, we assume the independence of the tetrahedral orientation between crystallographically equivalent positions from the direction of the hydrogen bond. This is, perhaps, a reasonable assumption, considering the relatively high degree of rotational disorder exhibited by the tetrahedral oxy-anions as compared to the proton motion (~ 100 times faster). Therefore, we modify Ice Rule 4 to include the independent motion of the tetrahedral oxy-anions and its protons:

Rule 4 *The interactions of non-adjacent tetrahedral oxy-anions do not affect the possible configurations of a tetrahedral oxy-anion and its protons, so long as they all satisfy Rules 1–3.*

Carrying out these rules lead to a formulation for the number of configurational states that accounts for both the tetrahedral oxy-anion disorder and the hydrogen bond disorder in superprotonic solid acids:

$$\Omega = \underbrace{\left(\text{number of proton configurations} \right) \times \left(\text{probability a proton site is open} \right)^{\left(\text{number of protons} \right)}}_{\text{Pauling's Ice Rules}} \times \underbrace{\left(\text{number of oxygen positions} \right)}_{\text{New Term}} \quad (4.4)$$

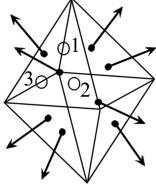
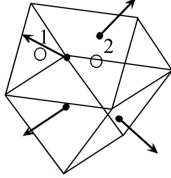
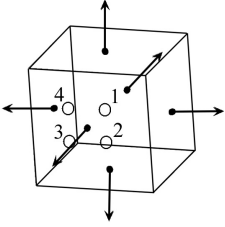
Clearly, the first term is identical to Pauling’s formulation for ice (Equation 4.2), except the total number of hydrogen positions around a tetrahedral oxy-anion need to be limited to four, as is the case for the oxygen atoms in ice. The new term accounts for the reorientations of the tetrahedral oxy-anions, or rotational disorder, which results in multiple oxygen positions for each hydrogen bond direction. With this formulation, which now accounts for both hydrogen bond disorder and oxy-anion disorder, the number of configurational states, and therefore, entropy of the superprotonic phase of MH_nXO_4 -type compounds can be calculated.

4.2.3 Calculations

Utilizing Equation 4.4 and the necessary structural details from Table 4.3 the configuration entropy of the superprotonic phase, S_{SP} , can be calculated for each of the known superprotonic MH_nXO_4 -type structures. These calculations are summarized in Table 4.4.

Before the total change entropy through the superprotonic phase transition, ΔS_{SP} can be determined, the initial entropy before the superprotonic transition, S_0 , must be established. The most significant source of configurational entropy prior to the superprotonic phase transition is the result of intra-hydrogen bond disorder.

Table 4.4: Calculations of the configuration entropies, S_{SP} , in superprotonic MH_nXO_4 -type solid acids, from the number of configurational states Ω .

Structure Space Group	Tetragonal $I4/mmm$	Tetragonal $I4_1/amd$	Cubic $Pm\bar{3}m$
Compounds	RbHSeO ₄	CsHSO ₄ CsHSeO ₄	RbH ₂ PO ₄ CsH ₂ PO ₄
			
Polyhedra	Octahedron	Triangular Anti-prism	Cube
Coordination	6-fold	8-fold	8-fold
Hydrogen Bond Directions	8	4	6
Oxygen Positions	3	2	4
Number of Protons	1	1	2
$\Omega = \binom{\text{number of proton configurations}}{1} \times \binom{\text{probability a proton site is open}}{3}^{\binom{\text{number of protons}}{1}} \times \binom{\text{number of oxygen positions}}{4}$			
$\Omega =$	$\binom{8}{1} \left(\frac{7}{8}\right)^1 (3) = 21$	$\binom{4}{1} \left(\frac{3}{4}\right)^1 (2) = 6$	$\binom{6}{2} \left(\frac{4}{6}\right)^2 (4) = 26.\bar{6}$
$S_{SP} = R \ln \Omega$			
$S_{SP} =$	$3.04R$ $25.3 \text{ J mol}^{-1}\text{K}^{-1}$	$1.79R$ $14.9 \text{ J mol}^{-1}\text{K}^{-1}$	$3.28R$ $27.3 \text{ J mol}^{-1}\text{K}^{-1}$

4.3 Entropy of Disordered Intra-Hydrogen Bond

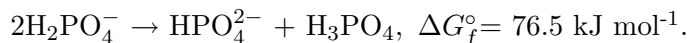
Many solid acids are known to undergo a ferroelectric transition upon cooling, in which a disordered proton within a hydrogen bond double-well potential becomes ordered. This disordered hydrogen bond can contribute significantly to the entropy of a solid acid prior to

the superprotonic phase transition. Classically, the entropy associated with the disordering of a hydrogen bond (S_H) between the two positions in a double-well potential, is simply

$$\begin{aligned} S_H &= R \ln \Omega = R \ln 2 \\ &= 0.69R \text{ or } 5.76 \text{ J mol}^{-1}\text{K}^{-1}. \end{aligned} \quad (4.5)$$

The structures of RbHSeO_4 , RbH_2PO_4 , CsH_2PO_4 , and CsH_2AsO_4 all exhibit one disordered hydrogen bond per XO_4 group, just prior to heating through the superprotonic phase transition.^{26,27,28,29,iv} Solid acids CsHSO_4 and CsHSeO_4 do not exhibit any disordered hydrogen bonds prior the superprotonic phase transition, therefore, $S_H = 0$ for these compounds.

The structure of the paraelectric phase of CsH_2PO_4 is depicted in Figure 4.9. Here, zig-zag chains of PO_4 groups are connected via a disordered hydrogen bond along the b -axis. In CsH_2PO_4 , the classical configurational entropy of a disordered hydrogen bond of $5.76 \text{ J mol}^{-1}\text{K}^{-1}$, differs substantially from the measured ferroelectric transition entropy value of $1.05 \text{ J mol}^{-1}\text{K}^{-1}$ ³⁰. This discrepancy can be explained by the formation of domains, in which the motion of the disordered protons are likely to be correlated with the oxy-anions on some small length scale λ . Take, for example, if the correlation length is limited to two tetrahedral oxy-anions, λ_2 in Figure 4.9, then the configurational entropy would be reduced by half or $2.88 \text{ J mol}^{-1}\text{K}^{-1}$ ($\frac{1}{2}R \ln 2$). Such local ordering effects, would yield erroneously small transition entropies, if heat capacity measurements were performed over an insufficient temperature range. In other words, the correlation length above the ferroelectric transition temperature would be a function of temperature ($\lambda = \lambda(T)$). This proposition is further supported by the rather high energy associated with the formation of oxy-anion defects, which would favor correlations between the proton and oxy-anion. For example,



Such a large Gibbs free energy of formation, ΔG_f° , would certainly favor local ordering at low temperatures, where the thermal energy per hydrogen bond would be too small to form such ionic defects. Upon heating to higher temperatures, such defects would become increasingly more likely, the correlation length would gradually approach the distance between hydrogen

^{iv}It should be noted that the ferroelectric transition of RbH_2PO_4 and CsH_2AsO_4 involve the disordering of *two* hydrogen bonds per XO_4 , but both compounds undergo structural modifications at intermediate temperatures, in which only one disordered hydrogen bond remain up to T_{SP}

bonded oxygens, and the disordering of the hydrogen bond would become eventually become independent of (uncorrelated with) the oxy-anions.

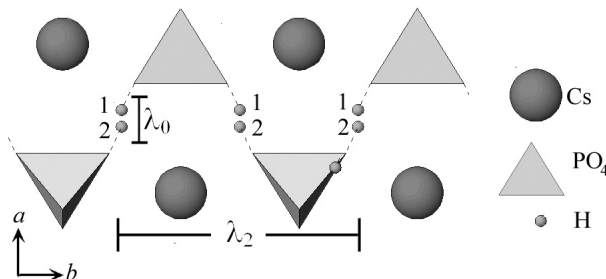


Figure 4.9: Paraelectric phase of CsH_2PO_4 depicting disordered hydrogen bond positions 1 and 2. The correlation length of the disordered hydrogen bond if correlated with 2 oxy-anions— λ_2 , or uncorrelated— λ_0 , as indicated.

In these calculations, we have adopted the classical configurational entropy of a disordered hydrogen bond. In doing so we implicitly make the following assumption:

As $T \rightarrow T_{SP}$, the correlation length λ of the disordered hydrogen bond with tetrahedral oxy-anions approaches λ_0 , the distance between the hydrogen bonded oxygen atoms ($\lambda \rightarrow \lambda_0$), such that the disordering of the hydrogen bond becomes independent of the tetrahedral oxy-anions.

That is, as a solid acid is heated to the superprotonic transition temperature, the formation of oxy-anion defects, like those just mentioned, become more and more likely, and therefore, the disordering of the hydrogen bond becomes independent of the oxy-anion—ultimately attaining the full entropy of a classically disordered hydrogen bond. Therefore, the entropy associated with disordered intra-hydrogen bonds employed here, are derived from the entropy of a classically disordered hydrogen bond, Table 4.5.

Table 4.5: The entropy due to disordered intra-hydrogen bonds (S_H) in MH_nXO_4 -type solid acids derived from the classical disorder of a hydrogen bond ($R \ln 2$).

Solid Acid	CsHSO_4	CsHSeO_4	RbHSeO_4	RbH_2PO_4	CsH_2PO_4	CsH_2AsO_4
$S_H / \text{J mol}^{-1}\text{K}^{-1}$	0	0	5.76	5.76	5.76	5.76

4.4 Results

In superprotonic MH_nXO_4 -type solid acids, the entropy of a superprotonic transition, ΔS_{SP} , is the entropy of the superprotonic phase, S_{SP} , minus the (configurational) entropy before the phase transition, S_0 . While several structural modifications exist in these compounds prior to the superprotonic phase transition, none substantially increase the overall entropy ($< 1 \text{ J mol}^{-1}\text{K}^{-1}$)—with one exception, the ferroelectric transition. The entropy associated with the ferro–paraelectric transition, is simply a result of intra-hydrogen bond disorder, S_{H} . Therefore, the approximate entropy prior to the superprotonic transition is

$$S_0 \approx S_{\text{H}}. \quad (4.6)$$

Using the configuration entropy values of the superprotonic phases (S_{SP}) calculated in Table 4.4, and the intra-hydrogen bond disorder (S_{H}) values given in Table 4.5 the change in entropy of the superprotonic phase transition can be calculated,

$$\Delta S_{\text{SP}} = S_{\text{SP}} - S_0. \quad (4.7)$$

The results of these calculations are compared with experimentally measured superprotonic phase transition entropies in Table 4.6. In all cases, except CsHSeO_4 , the calculated values of the superprotonic phase transition entropies are within experimental error of the measured values. It is probable that the discrepancy observed, in the case of CsHSeO_4 , is related to inaccurate measurements, as this is the only value reported here that was obtained from an outside source. Similarly, previous experimental measurements of CsHSO_4 ranged between 10.9 and $13.3 \text{ J mol}^{-1}\text{K}^{-1}$ ^{31,32}, before efforts were made by Chisholm¹ to obtain an accurate measurement, resulting in a value of $14.8(6) \text{ J mol}^{-1}\text{K}^{-1}$. Regardless, the general agreement between the calculated and experimental values presented here demonstrate that this new formulation can accurately account for the entropy of superprotonic phase transitions.

Table 4.6: A comparison of calculated with measured values of the superprotonic phase transition entropy (ΔS_{SP}) in MH_nXO_4 -type solid acids, where S_{SP} and S_0 are the calculated values of configurational entropy of the superprotonic phase and the intra-hydrogen bond disorder prior the superprotonic transition, respectively. † Represents the values obtained in this work.

Solid Acid	S_{SP}	S_0	ΔS_{SP}	ΔS_{SP}	Reference
	/J mol ⁻¹ K ⁻¹	/J mol ⁻¹ K ⁻¹	calculated	/J mol ⁻¹ K ⁻¹ measured	
RbHSeO ₄	25.3	5.76	19.5	19.2(4)	†
CsHSO ₄	14.9	0	14.9	14.8(6)	Chisholm ¹
CsHSeO ₄	14.9	0	14.9	16.0(5)	Hilczler ³³
RbH ₂ PO ₄	27.3	5.76	21.5	21.3(9)	†
CsH ₂ PO ₄	27.3	5.76	21.5	22.2(12)	†
CsH ₂ AsO ₄	27.3	5.76	21.5	21.0(8)	†

4.5 Conclusions

A model that successfully accounts for the entropy of a superprotonic phase in MH_nXO_4 -type solid acids has been developed, in collaboration with coworker Calum Chisholm. This formulation is fundamentally based upon Pauling’s entropy rules for ice, and adapted to account for the rotational disorder of tetrahedral oxy-anions. Based upon the excellent agreement of these calculations with experiment, the previous assumption that intra-hydrogen bond disorder is independent of the oxy-anion, appears to be valid.

These calculations have only been applied here to MH_nXO_4 -type solid acids, however Chisholm¹ has extended their application, with some modification, to mixed sulfate-phosphate systems. Furthermore, this formulation, given sufficient structural knowledge, should be broadly applicable to all superprotonic solid acids.

The limitations of these calculations are rooted in the necessity for an accurate structural description of the superprotonic phase. Therefore, they cannot not serve as a tool for predicting the presence of superprotonic phase transitions *a priori*. However, for a known superprotonic solid acid, these calculations can be used as an effective tool in identifying likely superprotonic structures. For example, in the case of CsHSO₄, of the structural models presented, the structure which contains only two tetrahedral configurations is preferred by this formulation. Similarly, for superprotonic RbHSeO₄, the entropy of the superprotonic transition had long been known, but not the structure. Though chemically, one might expect this superprotonic phase of this compound to be isostructural with CsHSeO₄, the

relatively high experimental value of superprotonic transition entropy led us to believe that it was not—which, in fact, turned out to be the case.

Overall, the development of these entropy rules have led to a better understanding of the thermodynamic driving force behind superprotonic phase transitions in solid acids. These results also suggest that changes in entropy through superprotonic transition are primarily due to changes in configurational entropy, and that other sources of entropy (such as vibrational entropy) are the same in the low and high temperature phases. With the characterization of parameters effecting superprotonic phase transition temperatures, *i.e.*, bonding and ionic size, both the conjugate thermodynamic variables, entropy and temperature, $[S, \frac{dE}{dS}]$, can ultimately lead to a complete thermodynamic description of these superprotonic phase transitions.

Bibliography

1. Calum R. I. Chisholm. *Superprotonic Phase Transitions in Solid Acids: Parameters affecting the presence and stability of superprotonic transitions in MH_nXO_4 family of compounds ($X = S, Se, P, As$; $M = Li, Na, K, NH_4, Rb, Cs$)*. PhD thesis, California Institute of Technology, 2002.
2. C.R.I. Chisholm, D.A. Boysen, and S.M. Haile. Entropy calculations for the superprotonic phase of $CsHSO_4$: Pauling's Ice Rules adjusted for systems containing disordered hydrogen-bonded tetrahedra. *in preparation*.
3. L. Pauling. The structure and entropy of ice and of other crystals with some randomness of atomic arrangement. *Journal of American Chemical Society*, 57:2680–2684, 1935.
4. J.D. Bernal and R.H. Fowler. A theory of water and ionic solution, with particular reference to hydrogen and hydroxyl ion. *Journal of Chemical Physics*, 1:515–548, 1933.
5. W.F. Giauque and M.F. Ashley. Molecular rotation in ice at 10 K. Free energy of formation and entropy of water. *Physical Review*, 42:81–82, 1933.
6. A.R. Gordon. The calculation of thermodynamic quantities from spectroscopic data for polyatomic molecules; the free energy, entropy, and heat capacity of steam. *Journal of Chemical Physics*, 2:65–68, 1934.
7. H. Suga, T. Matsuo, and O. Yamamuro. Thermodynamic study of ice and clathrate hydrates. *Pure and Applied Chemistry*, 64(1):17–26, 1992.
8. T. Matsuo, H. Suga, S. Seki, and M. Oguni. Glassy crystalline state in 2-dimensional hydrogen-bonded network in stannous chloride dihydrate and dideuterate crystals. *Proceedings of the Japanese Academy*, 48(4):237, 1972.
9. T. Matsuo, Y. Kume, H. Suga, and S. Seki. Heat-capacities of copper(II) formate tetrahydrate and tetradeuterate – comparative-study of phase-transitions in layer hydrate crystals. *Journal of Physics and Chemistry of Solids*, 37(5):499–506, 1976.
10. K. Okishiro, O. Yamamuro, T. Matsuo, S. Nishikiori, and T. Iwamoto. Calorimetric and dielectric studies on an order-disorder transition in the hydrogen-bond system formed by water molecules in the $(H_{31}O_{14})(CdCu_2(CN)_7)$ crystal. *Journal of Physical Chemistry*, 100(47):18546–18549, 1996.
11. J.C. Slater. Theory of the transition in KH_2PO_4 . *Journal of Chemical Physics*, 9:16–33, 1941.
12. W. Reese and L.F. May. Critical phenomenon in order-disorder ferroelectrics. I. Calorimetric studies of KH_2PO_4 . *Physical Review*, 162(2):510–518, 1967.
13. J. West. A quantitative X-ray analysis of potassium dihydrogen phosphate (KH_2PO_4). *Zeitschrift für Kristallographie*, 74:306–332, 1930.
14. A.I. Baranov. Proton-conduction anomalies in phase transitions in hydrogen-bonded crystals. *Investiya Akademii Nauk SSSR. Seriya Fizicheskaya*, 51(12):2146–2155, 1987.

15. N.M. Plakida. Theory of the superionic phase-transition in CsHSO_4 . *JETP Letters*, 41(3):114–116, 1985.
16. N.M. Plakida. Superionic phase-transitions in hydrogen-bonded crystals. *Physica Status Solidi B–Basic Research*, 135(1):133–139, 1986.
17. H.B. Silsbee, E.A. Uehling, and V.H. Schmidt. Deuteron intrabond motion + ferroelectricity in KD_2PO_4 . *Physical Review A-General Physics*, 133(1a):A165, 1964.
18. B.V. Merinov, A.I. Baranov, L.A. Shuvalov, and B.A. Maximov. Crystal-structure of the superionic phase of CsDSO_4 and phase-transitions in cesium hydrosulfates and deuteriosulfates (selenates). *Kristallografiya*, 32(1):86–92, 1987.
19. A.V. Belushkin, W.I.F. David, R.M. Ibberson, and L.A. Shuvalov. High-resolution neutron powder diffraction studies of the structure of CsDSO_4 . *Acta Crystallographica Section B–Structural Science*, 47(2):161–166, 1991.
20. Z. Jirak, M. Dlouha, S. Vratislav, A.M. Balagurov, A.I. Beskrovnyi, V.I. Gordelii, I.D. Datt, and L.A. Shuvalov. A neutron-diffraction study of the superionic phase in CsHSO_4 . *Physica Status Solidi A–Applied Research*, 100(2):K117–K122, 1987.
21. M.A. Zakharov, S.I. Troyanov, and E. Kemnitz. Superprotonic high temperature phase and refinement of the low temperature structure of CsHSeO_4 . *Zeitschrift für Kristallographie*, 216(3):172–175, 2001.
22. A. Presinger, K. Mereiter, and W. Bronowska. The phase transition of CsH_2PO_4 (CDP) at 505 K. *Materials Science Forum*, 166:511–516, 1994.
23. A.I. Baranov, V.P. Khiznichenko, and L.A. Shuvalov. High-temperature phase-transitions and proton conductivity in some KDP-family crystals. *Ferroelectrics*, 100:135–141, 1989.
24. Y.M. Moskvich, A.A. Sukhovskii, and O.V. Rozanov. Ion motion and high-temperature phase-transition in NH_4HSeO_4 and RbHSeO_4 crystals. *Fizika Tverdogo Tela*, 26(1):38–44, 1984.
25. Linus Pauling. *Nature of the Chemical Bond*. Cornell University Press, New York, 1960.
26. I.P. Makarova, L.A. Muradyan, E.E. Rider, V.A. Sarin, I.P. Alexandrova, and V.I. Simonov. Neutron-diffraction study of RbHSeO_4 and NH_4HSeO_4 single-crystals. *Ferroelectrics*, 107:281–286, 1990.
27. H. Matsunaga, K. Itoh, and E. Nakamura. X-ray structural study of ferroelectric cesium dihydrogen phosphate at room-temperature. *Journal of the Physical Society of Japan*, 48(6):2011–2014, 1980.
28. M.T. Averbuch-Pouchot and A. Durif. Structure of a new form of rubidium dihydrogenphosphate, RbH_2PO_4 . *Acta Crystallographica Section C–Crystal Structure Communications*, 41(May):665–667, 1985.
29. S. Hart, P.W. Richter, J.B. Clark, and E. Rapoport. Phase-transitions in CsH_2AsO_4 at high-pressures and temperatures. *Journal of Solid State Chemistry*, 37(3):302–307, 1981.

30. E. Kanda, M. Yoshizawa, T. Yamakami, and T. Fujimura. Specific-heat study of ferroelectric CsH_2PO_4 and CsD_2PO_4 . *Journal of Physics C-Solid State Physics*, 15(33):6823–6831, 1982.
31. B. Baranowski, J. Lipkowski, and A. Lunden. On the phase-transitions of cesium hydrogen sulfate (CsHSO_4). *Journal of Solid State Chemistry*, 117(2):412–413, 1995.
32. B. Baranowski, M. Friesel, and A. Lunden. Pressure-dependence of phase-transitions in CsHSO_4 studied with differential scanning calorimetry. *Physica A*, 156(1):353–363, 1989.
33. B. Hilczer, C. Pawlaczyk, and F.E. Salman. Superionic phase-transition in CsHSeO_4 and CsDSeO_4 single-crystal. *Ferroelectrics*, 81:1157–1160, 1988.

Chapter 5

Application of Superprotonic Solid Acids in Fuel Cells

Perhaps the most exciting potential application of superprotonic solid acids is as fuel cell electrolytes. The high proton conductivity and intermediate temperature range (100–350 °C) of these compounds make them specifically well-suited for this application. To fully appreciate how solid acids are uniquely qualified as potential alternatives to current fuel cell electrolytes, a brief review of some of the current state-of-art fuel cell electrolytes is presented. Then the first “proof-of-principle” solid acid-based fuel cell, utilizing a CsHSO₄ electrolyte is demonstrated, along with the unfortunate findings that CsHSO₄ decomposes under fuel cell conditions. This is followed by a detailed thermodynamic characterization of CsHSO₄ under oxidizing and reducing atmospheres. As a result of the chemical instability encountered in CsHSO₄, a search for a stable solid acid was undertaken. Next, thermal analysis results confirming the chemical instability examined solid acid sulfates and selenates under fuel cell conditions are presented. Finally, the potential of solid acid phosphates as electrolytes is established through the demonstration of long-term stability and high performance in both H₂/O₂ and direct-methanol fuel cells based on a CsH₂PO₄ electrolyte.

5.1 State-of-the-Art Electrolytes^{1,2,3}

There are many types of fuel cells broadly characterized according to the electrolyte used. Among these are (1) polymeric electrolyte membrane fuel cells (PEMFCs), (2) phosphoric acid fuel cells (PAFCs), (3) alkaline fuel cells (AFCs), (4) molten carbonate fuel cells (MCFCs), and (5) solid oxide fuel cells (SOFCs). Over the last few years PEMFCs and SOFCs have undergone the most intense research and development efforts, and significant

progress has been made in both performance and long-term stability of these types of fuel cells. The results of this progress has been primarily through the development and engineering of existing materials. However, the physical limitations of currently employed electrolytes have inhibited the further progress of fuel cell development.

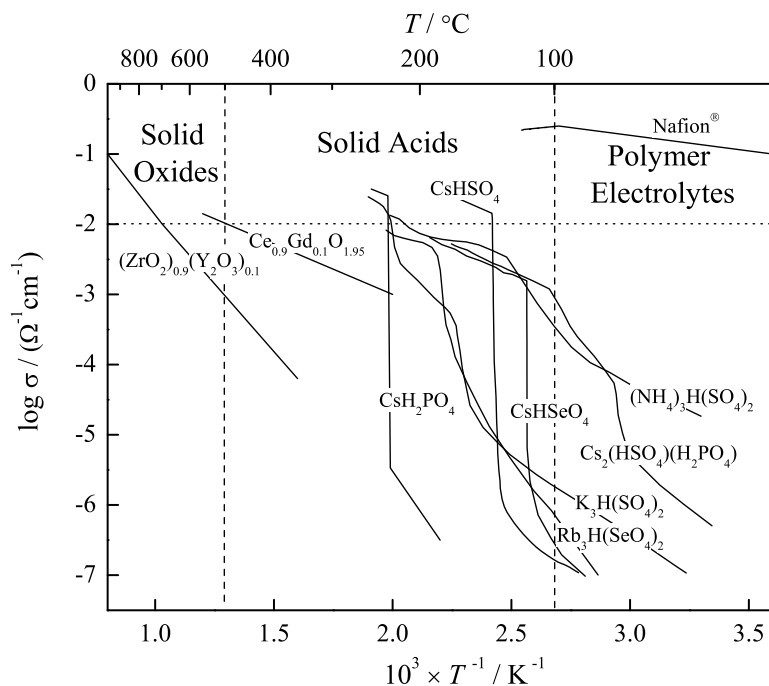


Figure 5.1: Arrhenius plot of the conductivity of various fuel cell electrolytes as compared to solid acids. The dotted-line indicates the minimum value of conductivity, $10^{-2} \Omega^{-1}\text{cm}^{-1}$, at which electrolytes are considered useful as fuel cell electrolytes. Solid oxides,^{ref3} $(\text{ZrO}_2)_{0.9}(\text{Y}_2\text{O}_3)_{0.1}$ and $\text{Ce}_{0.9}\text{Gd}_{0.1}\text{O}_{1.95}$ are only applicable at temperatures above 500°C —indicated by a dashed-line; where as, polymer electrolytes, such as Nafion[®],^{ref3} due to dehydration, are only useful below 100°C —also indicated by a dashed-line. Superprotonic solid acids, CsH_2PO_4 ,^{ref4} CsHSO_4 ,^{ref5} CsHSeO_4 ,^{ref5} $\text{Rb}_3\text{H}(\text{SeO}_4)_2$,^{ref6} $\text{K}_3\text{H}(\text{SO}_4)_2$,^{ref7} $\text{Cs}_2(\text{HSO}_4)(\text{H}_2\text{PO}_4)$,^{ref8} and $(\text{NH}_4)_3\text{H}(\text{SO}_4)_2$ ^{ref9} have potential application in the temperature range between 100 and 350°C .

A pre-requisite for consideration of an electrolyte for fuel cell applications is high ionic conductivity. A typical area specific resistance (resistance \times thickness) for a fuel cell with competitive performance is $\sim 0.15 \Omega \text{ cm}^2$. Through fairly routine processing techniques $\sim 20 \mu\text{m}$ thick membranes can be achieved. Then, for reasonable fuel cell performance, an electrolyte must have ionic conductivities on the order of $10^{-2} \Omega^{-1}\text{cm}^{-1}$. In Figure 5.1, the conductivity is plotted on log scale versus the reciprocal of temperature for Nafion[®], the industrial standard for PEMFCs; two common solid oxide electrolytes, $(\text{ZrO}_2)_{0.9}(\text{Y}_2\text{O}_3)_{0.1}$ or yttria-stabilized zirconia (YSZ) and $\text{Ce}_{0.9}\text{Gd}_{0.1}\text{O}_{1.95}$ or gadolinium-

doped cerate (CGO); and several superprotonic solid acid compounds— CsH_2PO_4 , CsHSO_4 , CsHSeO_4 , $\text{Rb}_3\text{H}(\text{SeO}_4)_2$, $\text{K}_3\text{H}(\text{SO}_4)_2$, $\text{Cs}_2(\text{HSO}_4)(\text{H}_2\text{PO}_4)$, $(\text{NH}_4)_3\text{H}(\text{SO}_4)_2$. A dotted-line, at a conductivity of $10^{-2} \text{ } \Omega^{-1}\text{cm}^{-1}$, indicates the minimum ionic conductivity needed for a fuel cell electrolyte. Up to 100°C , Nafion[®] has spectacular ionic conductivity, while, the solid oxides are only applicable at temperatures greater than 500°C . The operating temperatures of these two leading fuel cell technologies, leaves a temperature gap between 100 and 500°C , indicated by dashed-lines in Figure 5.1. Operating at such intermediate temperatures would have significant advantages, such as increased catalytic performance, as compared to PEMFCs, and wider availability of materials for cost-effective fuel cell components, as compared to SOFCs. Solid acids, with high proton conductivities in the range of 100 to 350°C , could potentially bridge this temperature gap and dramatically help to advance fuel cell technology.

5.1.1 Polymer Electrolytes

Progress in fuel cells based upon polymer electrolytes has been possibly the most rapid over the last decade. Most notable and prevalent among these are fuel cells based on a polymer electrolyte known as Nafion[®] made by DuPont. Polymeric membranes, such as Nafion[®], are composed of a hydrophobic perfluorinated polymer backbone with covalently bonded hydrophilic sulfonic acid functional groups. Upon hydration of these polymers, protons are transported through the polymer matrix via a vehicle transport mechanism, in which H_3O^+ ions are the carriers. These H_3O^+ ions travel through polymer via a network of inter-connected nano-domains of hydrophilic sulfonic groups (SO_3^-), depicted in Figure 5.2. Due to the inherent need for water in polymer electrolytes, they might, in fact, be more correctly termed as “polymer-*water* composite electrolytes.”

The performance of a H_2 /air fuel cell using a Nafion[®] polymer electrolyte membrane is shown in Figure 5.3¹⁰. For pure H_2 fuel at the anode the performance is quite impressive, with a peak power density of 0.5 W cm^{-2} at 0.5 V and maximum current density of almost 2 A cm^{-2} . However, competitive fuel cells must be able to withstand modest amounts of CO, which is a by-product of hydrocarbon fuel reforming. In Figure 5.3, at just 100 ppm of CO in the fuel stream, the fuel cell performance drops below 0.1 W cm^{-2} at 0.2 V and has a maximum current density of less than 0.4 A cm^{-2} . This effect is not directly due to the membrane itself, but a result of CO adsorbing to the surface of the Pt-catalyst, thereby

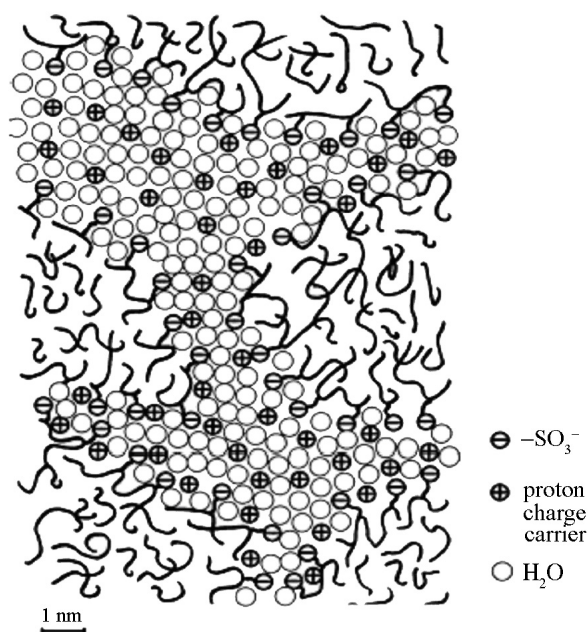


Figure 5.2: Structure of perfluorinated sulfonated polymers (*i.e.* Nafion[®] and its close relatives) depicting the nanoscale phase separated microstructure as determined by SAXS (small angle X-ray scattering).

inhibiting the catalyst performance—this is commonly referred to as “catalyst poisoning.” CO-tolerance of catalysts is strongly temperature dependent, for example at ~ 200 °C, CO-tolerance of Pt-catalysts is expected to increase to 2–3%¹¹. Circumventing this problem is non-trivial for fuel cells employing polymer electrolytes, due to their hydrated nature and corresponding temperature limitations. Several approaches have been adopted to overcome this problem, such as the use of CO-fuel scrubbers and utilizing pressure to access higher temperatures, both of which effectively reduce the overall efficiency of the fuel cell. A third approach has been through the replacement of water by an acid within a basic polymer matrix, such as phosphoric acid (H_3PO_4) into polybenzimidazole (PBI), however these membranes suffer from issues similar to those encountered by PAFCs, such as acid leaching out from the polymer matrix and large over potentials at the cathodes¹².

Though polymer electrolytes exhibit excellent proton conductivity, the necessity for hydration, places severe limitations on them. For practical applications, some of the most problematic of these are (1) limited operating temperature (0–100 °C), (2) necessity for complex and expensive hydration systems, (3) poor catalyst performance, (4) permeability

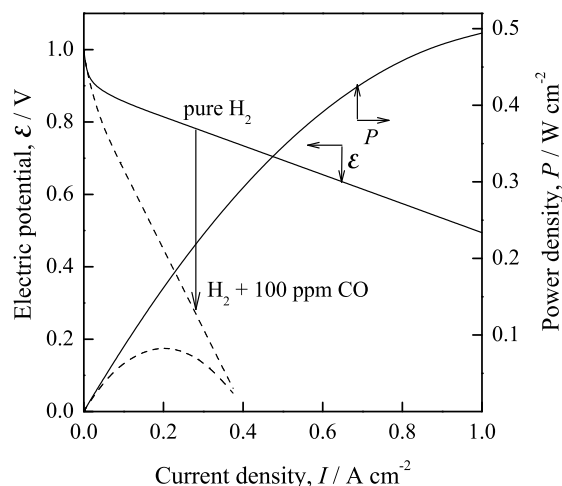


Figure 5.3: H₂/air fuel cell performance with a Nafion[®] polymer electrolyte membrane. Both the electric potentials (\mathcal{E}) and power densities (P) as a function of current density (i) measured on a cell operated at 80 °C under 2.4 atm H₂ and 4.1 atm air at the anode and cathode, respectively, and containing 0.13 mg Pt cm⁻². The solid line corresponds to the initial measurement, and the dashed line after 100 ppm CO was introduced to the anode. Reproduced from reference¹⁰.

to fuels, and (5) costly and inefficient waste heat management. To summarize, while polymeric electrolytes have exceptional laboratory performance, “real-world” limitations placed upon them are perhaps too great to overcome through engineering and design alone.

5.1.2 Solid Oxides

Fuel cells utilizing solid oxide electrolytes can operate, in principle, in the high temperature regime 500–1000 °C. Commercially available SOFCs can only operate efficiently at temperatures above 800 °C; however, significant effort has been put into bringing this temperature down to below 500 °C. Solid oxides have the advantage of no liquid electrolyte and the associated issues of electrolyte management and material corrosion, which limit design configurations. Moreover, operating at temperatures above 800 °C has the advantage of rapid reaction kinetics, without the need for expensive precious metal catalysts, as well as generating high quality heat for co-generation purposes. On the other hand, these high temperatures demand robust materials capable of high temperatures under demanding fuel cell environments. The development of suitable low-cost materials and ceramic fabrication techniques are presently the key technical challenge facing SOFCs¹³.

The all-solid-state nature of SOFC components allows for flexible cell design configurations. Currently, two primary cell configurations are being developed, tubular and bi-

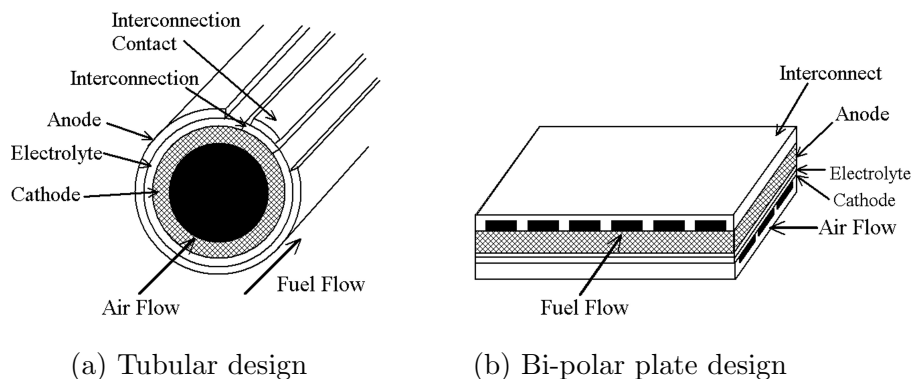


Figure 5.4: Solid oxide fuel cell configurations: (a) tubular design, and (b) bi-polar plate design.

polar plate designs, depicted in Figure 5.4. In the 90's, Siemens-Westinghouse Corporation introduced a 100 kW capacity solid oxide fuel cell generator, based upon a tubular design, Figure 5.4(a)—which avoids the issue of sealing. In this cell, a porous cathode of $\text{La}(\text{Sr})\text{MnO}_3$ is plasma sprayed with $\text{La}(\text{Sr})\text{CrO}_3$ for an interconnecting strip, then a thin (30–40 μm) YSZ electrolyte layer is deposited by electro-chemical vapor deposition, and finally a porous Ni-YSZ anode is slurry-spray deposited. Though technically successful, the cost of electrochemical vapor deposition of YSZ has inhibited these fuel cells from being competitive alternatives to gas-turbine generators. Furthermore, use of traditionally cost-effective ceramic processing techniques, such as sintering are prevented by the reaction of YSZ with the $\text{La}(\text{Sr})\text{MnO}_3$ cathode at temperatures above 1200 $^\circ\text{C}$ ³. Attempts at YSZ bipolar designs, Figure 5.4(b), have also been made through the use of compressive seals^{14,15}. However, gas leaks in this configuration have proven difficult to prevent, and high thermal stresses at the interfaces between dissimilar materials leads to mechanical degradation of the cell components upon thermal cycling.

As a result of temperature-imposed design constraints placed upon YSZ-based fuel cells, a concerted effort has been made to find intermediate-temperature (< 600 $^\circ\text{C}$) solid oxide electrolytes, in which more compliant high temperature gasket seals can be employed. One such electrolyte, CGO has sufficiently high ionic conductivity (see Figure 5.1) that it could be used at 500 $^\circ\text{C}$. However, at elevated temperatures (\sim 600 $^\circ\text{C}$), under the reducing conditions encountered at the anode, Ce^{4+} reduces to Ce^{3+} , causing electrical conduction in the electrolyte, and thereby shorting-circuiting the fuel cell. A further technological

challenge for these electrolytes is the development of cathodes that can operate at 500 °C, while simultaneously having good oxidation resistance and electrical conduction.

In summary, solid oxides electrolytes, opposite to that of polymer electrolytes, suffer issues arising from operating at too high of temperatures. At these temperatures, expensive processing techniques and thermal-mechanical toughness of materials still remain technical challenges to overcome—providing an impetus for research into intermediate temperature electrolytes.

5.2 Solid Acid Electrolytes

Issues encountered in state-of-the-art electrolytes make the operation of fuel cells in an intermediate temperature range, 100-500 °C, highly desirable. These temperatures are low enough that fuel cell component materials with appropriate properties can be chosen from a wide-range of inexpensive materials, yet high enough to allow for good catalytic activity and reaction kinetics. Fuel cells based on solid acid electrolytes, would operate in this highly sought after temperature range.

Prior to the research conducted here at Caltech^{16,17,18,19}, solid acids were known to exhibit high proton conductivity, but were not considered for fuel cell applications. The primary reason for this is the water-soluble nature of most solid acids. It was thought that H₂O generated at the cathode of a fuel cell would dissolve away the solid acid when employed as an electrolyte—eventually rendering the fuel cell useless. However, this issue is easily circumvented by simply operating above the boiling point of water (100 °C), at which point H₂O in gas phase has no effect on the solid acid.

5.2.1 CsHSO₄

In this work, we have selected the solid acid CsHSO₄ for “proof-of-principle” investigations in fuel cell applications. This particular acid has been chosen because it is relatively well-characterized and its superprotonic phase has a reasonably wide temperature range of stability, from the transition at 141 °C to decomposition/melting at ~ 200-230 °C^{5,20}. Here we demonstrate the feasibility of a solid acid based fuel cell. Although these initial results are quite promising, we show that the long-term viability of a fuel cell based on a CsHSO₄-electrolyte is precluded by the reduction of the solid acid under hydrogen atmospheres in

the presence of typical anode electrocatalysts.

5.2.1.1 H₂/O₂ Fuel Cell

Proof-of-Principle¹⁶

To demonstrate a fuel cell based on a solid acid electrolyte a membrane electrode assembly (MEA) was prepared as follows. A layer of the solid acid CsHSO₄ was sandwiched between two electrocatalysis layers comprised of CsHSO₄, Pt-black, C-black and Napthalene in a mass ratio of 6:10:1:1. These layers were, in turn, placed between two sheets of porous, graphite current collectors. The entire assembly was uniaxially pressed at 490 MPa, to yield a dense electrolyte membrane with good contact to the electrocatalyst layers. Fuel cell polarization curves were collected at 160 °C from the MEA placed in a standard graphite test station (Electrochem, Inc). Upon heating to the test temperature, the Naphthalene in the electrode presumably evaporated, leaving behind a porous electrode structure.

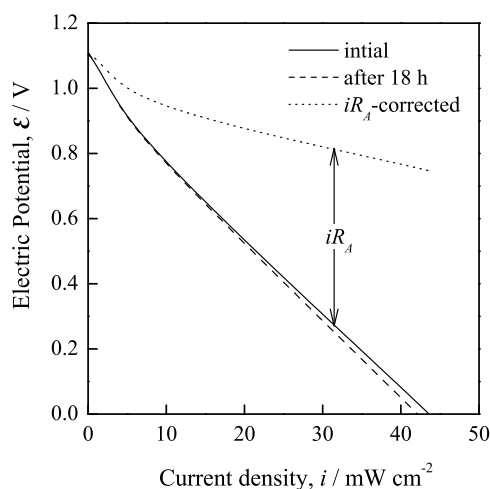


Figure 5.5: Performance (polarization curve) of an H₂/O₂ fuel cell based on a CsHSO₄ electrolyte. The electric potential (\mathcal{E}) is plotted versus current density (i) for a cell operated at 160 °C under humidified ($p_{\text{H}_2\text{O}} = 3.13 \times 10^{-2}$ atm) H₂ and O₂ gasses at the anode and cathode, respectively (total pressure of 1 atm). The solid line represents the initial measurement, the dotted-line—after 18 hrs of exposure to humidified air at both electrodes, and the dotted-line—the iR_A -corrected result for initial measurement. The cell was comprised of a 1.37 mm thick CsHSO₄ electrolyte layer and a catalyst loading of 18 mg Pt cm⁻².

The performance of this single cell fuel, characterized by the electric potential (\mathcal{E}) measured as a function of current density (i) while exposed to H₂O-saturated H₂ and O₂ at the anode and cathode, respectively, and held at 160 °C, is presented in Figure 5.5. The

electrocatalyst content or “loading” was 18 mg Pt cm⁻² at both the anode and cathode and the membrane thickness was 1.37 mm. The solid curve reflects the initial measurement and the dashed, the measurement after 18 hours of exposure to humid air. The anode and cathode gases were humidified during fuel cell operation only in order to explicitly establish the open circuit potential. Similar results were obtained for operation with dry gases. It is immediately apparent that despite the water solubility of CsHSO₄ and its ability to undergo extensive plastic deformation at high temperatures²¹, stable fuel cell performance is possible. The slight drop in performance with time is likely due to degradation at the anode, as a result of reduction by H₂, as described later, and not a result of interactions with H₂O or any lack of dimensional integrity.

The open circuit potential of the cell in Figure 5.5 is 1.11 V. This compares favorably with the theoretical value of 1.22 V, expected for the conditions $T = 160$ °C, $p_{\text{O}_2} \approx 1$ atm, $p_{\text{H}_2} \approx 1$ atm, and $p_{\text{H}_2\text{O}} = 3.13 \times 10^{-2}$ atm²². The difference between the measured and theoretical open circuit voltages (OCV) is likely due to gas permeation through residual pores within the polycrystalline electrolyte, or through leaks in the experimental apparatus. Nevertheless, the OCV obtained here is significantly higher than that typically observed in polymer based fuel cells, 0.9 - 1.0 V²³. The humidification requirements of the polymer, as well as its inherent permeability to H₂ and O₂ via molecular dissolution and transport, act to lower the maximum OCV achievable. In the case of the solid acid, improved processing will surely result in OCV values as high as theoretical, as has been reported, for example, for KH₂PO₄²⁴ and is routine for solid oxide fuel cells¹³.

The drop in fuel cell voltage with increasing current density, Figure 5.5, has many causes²³, the primary one being, for a relatively thick electrolyte as was used in this experiment the resistance of the membrane. This term is given by iR_A , where i is the current density, and R_A is the area specific resistance or t/σ , where t is the electrolyte thickness and σ is the conductivity. Thus, one expects a linear drop in voltage as a function of current density, the magnitude of which depends only on the properties and geometry of the electrolyte. While the characteristics of the superprotonic phase transition of CsHSO₄ are well-established, the reported conductivity at 160 °C varies from 3.70×10^{-3} Ω⁻¹cm⁻¹ to 2.08×10^{-2} Ω⁻¹cm⁻¹^{20,5}. However, our measurements of CsHSO₄ under H₂O-saturated air indicate a conductivity of $\sim 8 \times 10^{-3}$ Ω⁻¹cm⁻¹. Using this latter value and the electrolyte thickness of 1.37 mm, the expected slope in Figure 5.5 is -17.1 Ω cm², which is significantly

smaller than the measured value of $-22.7 \Omega \text{ cm}^2$. Additional resistance effects are likely due to slow charge transfer through the electrodes (also rather thick) and various contact resistances. The dotted curve ($\mathcal{E}_{meas} + iR_A$) in Figure 5.5 shows the magnitude of the losses due to all non-electrolyte factors.

In the present work, rather thick membranes were necessary to obtain impermeable MEAs and stable open circuit voltages. In order to achieve an area specific resistivity that is directly comparable to that of Nafion[®] membranes (typically 0.025 to $0.0875 \Omega \text{ cm}^2$ at $90 \text{ }^\circ\text{C}$ and under highly humidified atmospheres for membranes 50 - $175 \mu\text{m}$ in thickness²³) a dense CsHSO₄ membrane with a thickness on the order of 2 to $20 \mu\text{m}$ would be necessary. While such films may not be immediately achievable, routine fabrication of solid oxide electrolytes with comparable dimensions²⁵ renders this target quite realistic.

Performance Degradation¹⁹

The performance of a H₂/O₂ fuel cell based on a CsHSO₄ electrolyte is re-examined here under prolonged exposure to standard fuel cell gases (humidified H₂ and O₂ at the anode and cathode, respectively), as opposed to the previous measurement, in which, performance was measured both prior to and after 18 hours of exposure of the cell to humidified *air*. The performance of this second MEA, prepared in the same fashion as described in the previous section, is shown in Figure 5.6.

Upon initial examination, the peak power density was 12 mW cm^{-2} , and a maximum current density of 45 mA cm^{-2} . Damage to the fuel cell under operating conditions was rapid. After five hours of continuous operation, the performance fell to a peak power density of 6 mW cm^{-2} , and a maximum current density of 17 mA . After flushing both the anode and cathode with compressed air and then holding the system in stagnant air for 5 hours, the fuel cell performance recovered to a level close to that measured initially (peak power density of 10 mW cm^{-2} and maximum current density of 41 mA cm^{-2}). In some cases, the fuel cell recovery after flushing with air was such that the measured performance had peak power densities higher than initial values. These results indicate that the loss in performance cannot be associated with degradation of the membrane directly, which would be irreversible, but some other reversible process. Adsorption of small quantities of H₂S onto the surface of the Pt catalyst, and its desorption upon exposure of the anode to air, is consistent with the observed fuel cell behavior, although other possibilities cannot

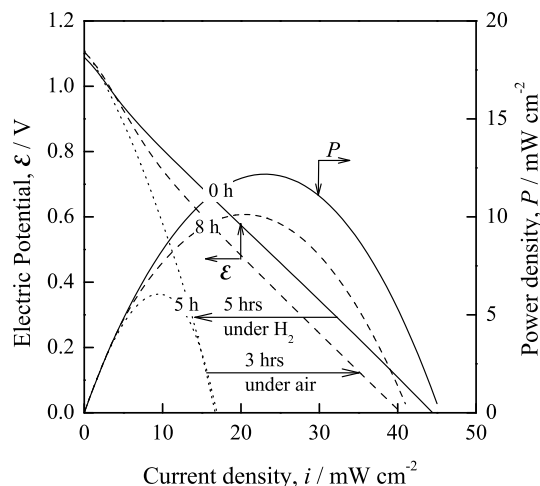


Figure 5.6: The degradation of H_2/O_2 fuel cell performance with CsHSO_4 -based electrolyte. Electric potential (\mathcal{E}) and power density (P) measured as a function of current density (i) for a CsHSO_4 -based single cell fuel cell operated at 154°C . Solid curves represent the initial measurement under humidified ($p_{\text{H}_2\text{O}} = 3.13 \times 10^{-2}$ atm) H_2 and O_2 gasses at the anode and cathode, respectively, the dashed curves after five hours of operation under these conditions, and the dotted curves after an additional three hours exposure to air.

be unequivocally ruled out. It has been established, in the case of phosphoric acid fuel cells, that as little as 50 ppm H_2S in the incoming fuel stream significantly degrades anode performance, and that this degradation is similarly reversible²⁶.

5.2.1.2 Chemical Stability under H_2

To identify the cause for the loss in performance observed in the H_2/O_2 fuel cell using a CsHSO_4 electrolyte from the previous section, thermal analysis of CsHSO_4 , alone and with various catalysts, under reducing H_2 atmospheres, as well as thermodynamic calculations of the stability of CsHSO_4 in H_2 gas were carried out and the results presented here.

Thermal Analysis¹⁹

Thermal analysis results upon slowly heating CsHSO_4 mixed with Pt catalyst while under flowing H_2/Ar gasses are presented in Figure 5.7. From the DSC results (top panel) a sharp endothermic peak is observed at 141°C , corresponding to the superprotonic phase transition in CsHSO_4 , and a second exothermic event at 201°C . From TG/DTG measurements (middle panel) slight weight loss is observed even before the superprotonic transition, with the maximum amount of weight-loss occurring at 147°C and 199°C . Mass spectroscopy analysis

of resulting evolved gas species (bottom panel) indicate that the weight-loss observed by TG/DTG correspond to H_2O and H_2S .

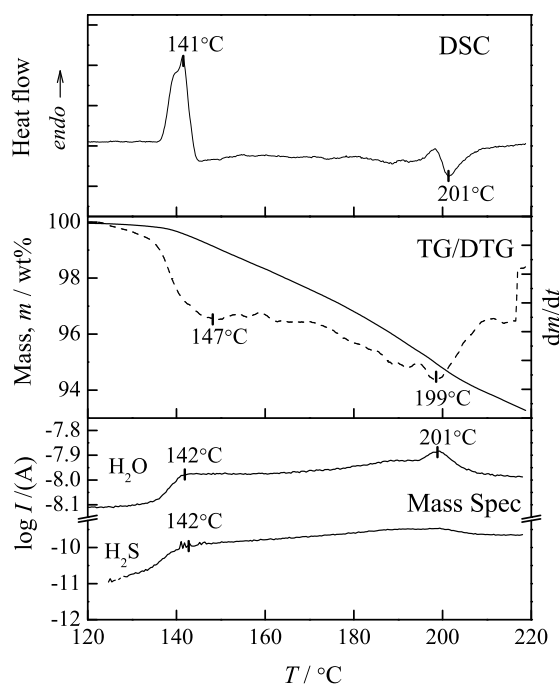
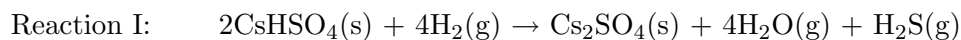


Figure 5.7: Combined differential scanning calorimetry (DSC—top panel), thermalgravimetry and differential thermalgravimetry (TG/DTG—middle panel), and evolved gas analysis by mass spectroscopy (Mass Spec—bottom panel) for gas species H_2O ($m_{18.00}$) and H_2S ($m_{34.00}$) while heating at $1\text{ }^\circ\text{C min}^{-1}$ CsHSO_4 mixed with 35 wt% Pt catalyst, under flowing 4% H_2 -Ar ($40\text{ cm}^3\text{min}^{-1}$).

A second sample of CsHSO_4 mixed with 35 wt% Pt catalyst was heated to and held at $160\text{ }^\circ\text{C}$ for ~ 15 hrs while exposed to H_2 gas. A powder X-ray diffraction pattern taken from the recovered sample is shown in Figure 5.8. The experimental diffraction pattern (solid-curve) corresponds well with the calculated patterns for Cs_2SO_4 plus Pt (dashed-curve).

The combination of these thermal analysis and diffraction results suggests the following decomposition reaction for CsHSO_4 in a H_2 atmosphere at elevated temperatures:



The onset of this reaction appears to be nearly simultaneous with the superprotonic phase transition at $141\text{ }^\circ\text{C}$. Therefore, the successful application of a CsHSO_4 -based H_2/O_2 fuel cell that uses Pt as a catalyst is prevented by this decomposition/dehydration reaction.

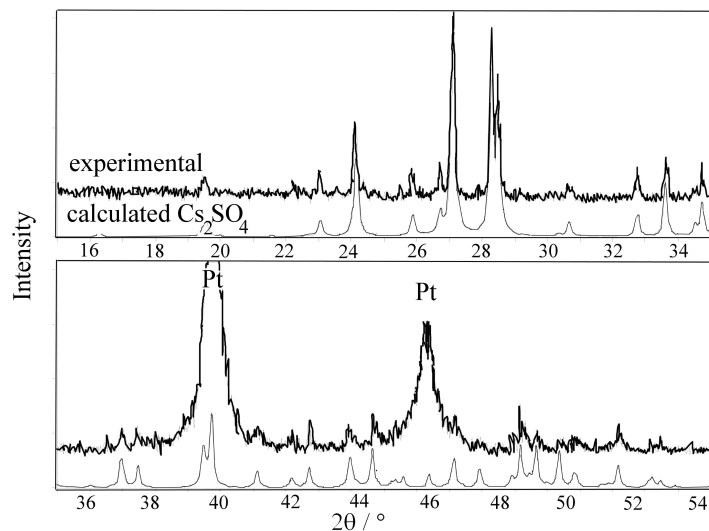


Figure 5.8: Powder X-ray diffraction pattern of the reaction by-product of $\text{H}_2(\text{g})$ with $\text{CsHSO}_4(\text{s})$ with 35 wt% Pt catalyst held at 160°C for ~ 15 hrs. *Top* curve represents the experimental diffraction pattern and the *bottom* the calculated pattern of Cs_2SO_4 .

Catalyst Effect

To establish the extent that catalysts promote the decomposition/dehydration reaction of CsHSO_4 under H_2 atmospheres, and to possibly identify an alternative catalyst to Pt that could be used in a CsHSO_4 -based fuel cell, isothermal thermalgravimetric analysis at 160°C was carried out on CsHSO_4 alone, and with the various catalysts listed in Table 5.1 below, under flowing H_2/Ar gasses.

Table 5.1: Physical characteristics of catalyst materials used in thermal stability investigation of CsHSO_4 under H_2 gas.

Catalyst	Source	Particle Size	Surface Area / $\text{m}^2 \text{g}^{-1}$
Pt black	Alfa Aesar	N/A	27
RuO (Ru)	Alfa Aesar	$< 1 \mu\text{m}$	45–65
Pd black	Aldrich	N/A	40
Au	Aldrich	100 nm (1–2 μm agglomerates)	N/A
Ir black	Alfa Aesar	N/A	30–60
Ni/Al “Raney Ni”	Alfa Aesar	200 mesh ($< 74 \mu\text{m}$)	N/A
WC	Alfa Aesar	$< 1 \mu\text{m}$	1.2–1.4

Here again, the results are undesirable for fuel cell applications. Even relatively inactive catalysts such as Au lead to a significant increase of the rate of Reaction I compared to its rate in the absence of catalysts. In general, the reaction rate increases according to the sequence $\text{Au} < \text{Ni/Al} < \text{RuO}_2 < \text{Pt} < \text{WC} < \text{Pd} < \text{Ir}$. Given the wide variation in specific surface areas of the catalyst materials employed, Table 5.1, it is impossible to establish whether this sequence is a direct consequence of catalyst chemistry. Nevertheless, it is surprising that WC, with a relatively low specific surface area, serves as a very effective catalyst for sulfur reduction.

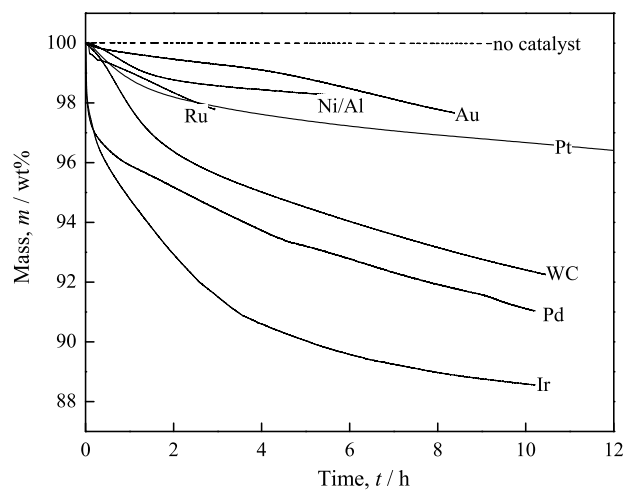


Figure 5.9: Weight loss isotherms at 160 °C of CsHSO₄ under flowing H₂ gas (20 cm³ min⁻¹) in the presence of various (potential) fuel cell catalysts (as indicated).

Thermodynamic Characterization¹⁸

In exploring alternatives to CsHSO_4 , a thorough investigation from a thermodynamic view point of the decomposition of CsHSO_4 could provide valuable insight into the thermochemical requirements necessary to create a stable solid acid-based electrolyte for fuel cell applications.

For the purpose of such an exploration, the following thermodynamic data are obtained from literature for each constitutive chemical species for the reaction of interest:

$$\begin{aligned} \Delta H_{f,298.15}^\circ & : \text{enthalpy of formation at 298.15 K and 1 bar} \\ S_{298.15}^\circ & : \text{standard entropy at 298.15 K and 1 bar} \\ C_p^\circ(T) & : \text{heat capacity function at 1 bar} \end{aligned}$$

where empirically

$$C_p^\circ(T) = A + B \cdot 10^{-3} T + C \cdot 10^5 T^{-2} + D \cdot 10^{-6} T^2 \quad (5.1)$$

and coefficients A, B, C , and D are obtained from reported literature values. Using these data, the standard enthalpy of formation $\Delta H_f^\circ(T)$ and standard entropy $S^\circ(T)$ functions for each chemical species are extrapolated to elevated temperatures using the equations

$$\Delta H_f^\circ(T) = \Delta H_{f,298.15}^\circ + \int_{298.15}^T C_p^\circ(T) dT + \sum_{tr} \Delta H_{tr} \quad (5.2)$$

and

$$S^\circ(T) = S_{298.15}^\circ + \int_{298.15}^T \frac{C_p^\circ(T)}{T} dT + \sum_{tr} \frac{\Delta H_{tr}}{T_c} \quad (5.3)$$

where ΔH_{tr} and T_c are the enthalpy and temperature of any relevant phase transitions. Now the reaction enthalpy $\Delta H_{rxn}^\circ(T)$ and entropy $\Delta S_{rxn}^\circ(T)$ functions can be calculated from the difference between the products and reactants of $\Delta H_{f,i}^\circ(T)$ and $S_i^\circ(T)$, respectively, of all chemical species i using

$$\Delta H_{rxn}^\circ(T) = \sum_i^{\text{products}} n_i \Delta H_{f,i}^\circ(T) - \sum_i^{\text{reactants}} n_i \Delta H_{f,i}^\circ(T) \quad (5.4)$$

and

$$\Delta S_{rxn}^\circ(T) = \sum_i^{\text{products}} n_i S_i^\circ(T) - \sum_i^{\text{reactants}} n_i S_i^\circ(T) \quad (5.5)$$

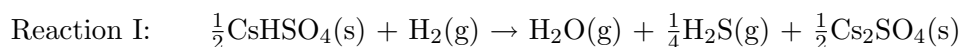
where n_i is the stoichiometric coefficient of chemical species i . Finally, the Gibbs free energy function for the reaction $\Delta G_{rxn}^\circ(T)$ can be obtained from

$$\Delta G_{rxn}^\circ(T) = \Delta H_{rxn}^\circ(T) - T\Delta S_{rxn}^\circ(T) \quad (5.6)$$

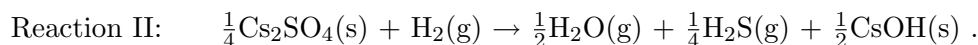
and then used to evaluate the equilibrium constant K_i for reaction i , where

$$\Delta G_{rxn}^\circ(T) = -RT \ln K_i. \quad (5.7)$$

For the reduction of CsHSO₄ in H₂ gas, thermal analysis from the previous section suggests the decomposition reaction



while the further reduction of Cs₂SO₄ to form CsOH would occur through



Thermodynamic data for each constitutive chemical species of the chemical reactions above are given in Table 5.2. Reported values are well-established for all chemical species, except for CsHSO₄, in which it was necessary to estimate its S° and $C_p^\circ(T)$, see Appendix for details. These estimates should be adequate given that accurate data for these values is not essential for obtaining rough *approximations* of thermodynamic behavior. Also, the transition enthalpies and temperatures of phase transitions in CsHSO₄ were taken into account. CsHSO₄ undergoes two relevant phase transitions, (1) a monoclinic ($P2_1/c$)-monoclinic ($P2_1/m$) transition at $T_c = 60$ °C, $\Delta H_{tr} = 0.53$ kJ mol⁻¹, and (2) a superprotonic transition at $T_c = 141$ °C, $\Delta H_{tr} = 6.13$ kJ mol⁻¹.²⁷

The equilibrium constants (K_i) for Reactions I and II can be written in terms of the partial pressures p_i 's of relevant gaseous species i , such that

$$K_{\text{I}} = \frac{p_{\text{H}_2\text{O}} \cdot p_{\text{H}_2\text{S}}^{1/4}}{p_{\text{H}_2}} \quad (5.8)$$

and

$$K_{\text{II}} = \frac{p_{\text{H}_2\text{O}}^{1/2} \cdot p_{\text{H}_2\text{S}}^{1/4}}{p_{\text{H}_2}}. \quad (5.9)$$

In Figure 5.10, K_{I} and K_{II} are plotted on a log scale in the temperature range 100-200 °C.

Table 5.2: Reported values for standard (1 bar) enthalpy of formation ΔH_f° ,_{298.15} and entropy S° ,_{298.15} at 298.15 K and the coefficients A, B, C , and D for the standard heat capacity function $C_p^\circ(T)$ of selected chemical species involved in the reduction of CsHSO₄ in the presence of H₂ gas. Empirically, $C_p^\circ(T) = A + B \cdot 10^{-3}T + C \cdot 10^5T^{-2} + D \cdot 10^{-6}T^2$.

Chemical Species	ΔH_f° , _{298.15}	S° , _{298.15}	$C_p^\circ(T)$ /J mol ⁻¹ K ⁻¹				Source
	/kJ mol ⁻¹	/J mol ⁻¹ K ⁻¹	A	B	C	D	
CsHSO ₄ (s)	-1158	189 [†]	141.5	0	0	0 [†]	NBS ²⁸
CsOH(s)	-416.2	104.2	-46.24	394.5	24.78	-330.0	Gurvich ²⁹
Cs ₂ SO ₄ (s)	-1442	211.8	99.72	113.4	-2.256	32.96	Barin ³⁰
H ₂ (g)	0	31.23	25.86	4.837	1.584	-0.037	JANAF ³¹
H ₂ O(g)	-241.8	188.8	28.41	12.48	1.284	0.360	JANAF ³¹
H ₂ S(g)	-4.900	49.18	25.35	24.52	1.735	-4.015	Gurvich ³²

[†]Estimated values, see Appendix for details.

It is evident from Figure 5.10 that the reaction constant K_I for the reduction of CsHSO₄ to Cs₂SO₄ is substantial. Even at moderately reducing conditions, $p_{H_2} = 0.001$ atm, suppression of the reduction of CsHSO₄ would require $p_{H_2O} \cdot p_{H_2S}^{1/4} > 10^5$ - 10^7 atm, a condition that is experimentally difficult, if not impossible, to achieve. Thus, the formation of Cs₂SO₄ is a thermodynamic expectation in almost any atmosphere which contains H₂ gas. However, the further reduction of Cs₂SO₄ is not expected in the presence of even modest amounts of H₂O and H₂S, because of the quite small equilibrium constant K_{II} for this reaction. Alternative reduction pathways of Cs₂SO₄ accompanied with formation of SO₂ were also considered, however these reactions were deemed insignificant compared to the reduction accompanied by the formation of H₂S. In conclusion, the reduction of CsHSO₄ by H₂ gas is expected to form the products Cs₂SO₄ and H₂S, which is in agreement with the previous experimental findings.

5.2.1.3 Chemical Stability under O₂

Thermodynamic characterization of CsHSO₄ in the presence of O₂ gas was carried out here, however these results would also be equally valid for the thermal stability of CsHSO₄ under inert atmospheres. Such characterization will help to confirm that the degradation in fuel cell performance observed when using a CsHSO₄ electrolyte from the previous sections is,

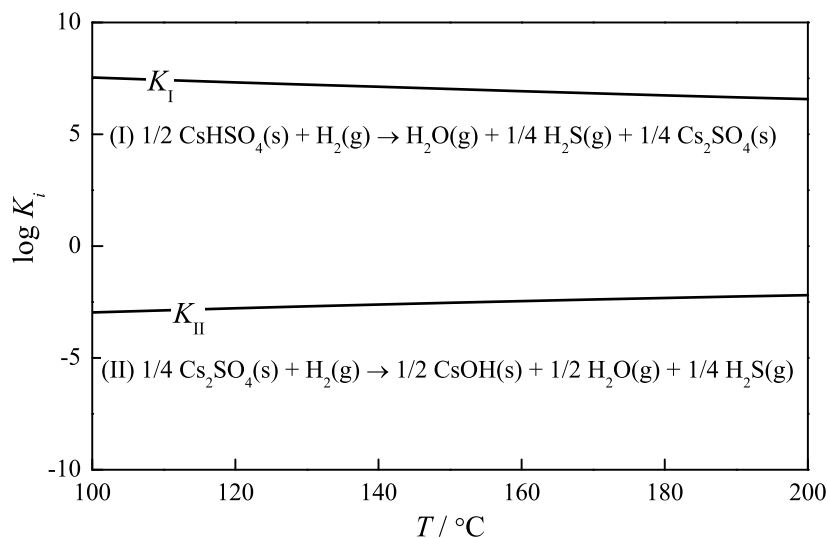


Figure 5.10: Reaction equilibrium constant (K_i) as a function of temperature (T) for the reduction of (I) CsHSO_4 to Cs_2SO_4 , and (II) Cs_2SO_4 to CsOH in H_2 gas.

in fact, solely the bi-product of an anode reaction with H_2 to form H_2S and *not* a result of any electrolyte instability at the cathode.

Thermodynamic Characterization¹⁸

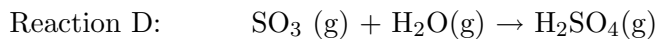
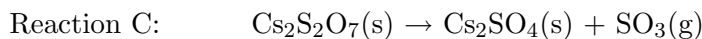
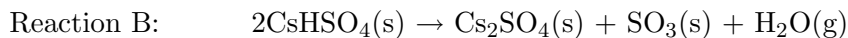
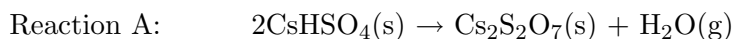
For this analysis of CsHSO_4 under oxidizing conditions, the oxygen partial pressure was assumed to be greater than 10^{-10} atm, at which all cations will remain in their maximum valence states (Cs^+ , H^+ and S^{+6}). That is, we can ignore species such as Cs , H_2 , SO_2 and other lower valence sulfur compounds. Consequently, degradation of CsHSO_4 can only take place via decomposition to compounds comprised of Cs_2O , SO_3 , and H_2O . Of these, Cs_2O and CsOH are unlikely products because of the strong chemical affinity of Cs_2O and SO_3 ($\text{Cs}_2\text{O}(\text{s}) + \text{SO}_3(\text{g}) \rightarrow \text{Cs}_2\text{SO}_4(\text{s})$, $\Delta G_f^\circ = -629 \text{ kJ mol}^{-1}$ at 100°C). If we then assume that there are no intermediate compounds between $\text{Cs}_2\text{S}_2\text{O}_7(\text{s})$ and $\text{CsHSO}_4(\text{s})$, and between $\text{Cs}_2\text{S}_2\text{O}_7(\text{s})$ and $\text{Cs}_2\text{SO}_4(\text{s})$, the by-products of the decomposition of CsHSO_4 in an oxidizing atmosphere are limited to $\text{H}_2\text{O}(\text{g})$, $\text{SO}_3(\text{g})$, $\text{H}_2\text{SO}_4(\text{g})$, $\text{Cs}_2\text{S}_2\text{O}_7(\text{s})$, and $\text{Cs}_2\text{SO}_4(\text{s})$. Thermodynamic data for these chemical species are given in Table 5.3. Due to a lack of reported data on $\text{Cs}_2\text{S}_2\text{O}_7$ it was necessary to estimate its thermodynamic data, as well as that of CsHSO_4 , as was mentioned in the previous section, see Appendix for details.

Table 5.3: Reported values for standard (1 bar) enthalpy of formation $\Delta H_{f,298.15}^\circ$ and entropy $S^\circ_{298.15}$ at 298.15 K and the coefficients A, B, C , and D for the standard heat capacity function $C_p^\circ(T)$ of selected chemical species involved in the decomposition of CsHSO_4 in the presence of O_2 gas. Empirically, $C_p^\circ(T) = A + B \cdot 10^{-3}T + C \cdot 10^5 T^{-2} + D \cdot 10^{-6}T^2$.

Chemical Species	$\Delta H_{f,298.15}^\circ$	$S^\circ_{298.15}$	$C_p^\circ(T) / \text{J mol}^{-1}\text{K}^{-1}$				Source
	/kJ mol ⁻¹	/J mol ⁻¹ K ⁻¹	A	B	C	D	
$\text{CsHSO}_4(\text{s})$	-1158	189 [†]	141.5	0	0	0 [†]	NBS ²⁸
$\text{Cs}_2\text{SO}_4(\text{s})$	-1442	211.8	99.72	113.4	-2.256	32.96	Barin ³⁰
$\text{Cs}_2\text{S}_2\text{O}_7(\text{s})$	-1990 [†]	265 [†]	105	0	0	0 [†]	NBS ²⁸
$\text{H}_2\text{O}(\text{g})$	-241.8	188.8	28.41	12.48	1.284	0.360	JANAF ³¹
$\text{H}_2\text{SO}_4(\text{g})$	-175.700	71.416	14.207	32.943	-2.316	-15.808	Barin ³⁰
$\text{SO}_3(\text{g})$	-94.590	61.370	4.826	29.879	0.042	-18.471	Barin ³⁰

[†]Estimated values, see Appendix for details.

The four relevant reactions inter-relating CsHSO_4 and its possible decomposition products are given as



For each of the above reactions, the corresponding equilibrium constant K_i for reaction i , given as a function of the relative partial pressures p_i of relevant gaseous species i are

$$K_A = p_{\text{H}_2\text{O}} \quad (5.10)$$

$$K_B = p_{\text{H}_2\text{O}} \cdot p_{\text{SO}_3} \quad (5.11)$$

$$K_C = p_{\text{SO}_3} \quad (5.12)$$

$$K_D = \frac{p_{\text{H}_2\text{O}} \cdot p_{\text{SO}_3}}{p_{\text{H}_2\text{SO}_4}} \quad (5.13)$$

Using equations 5.2 through 5.7, the data given in Table 5.3, and accounting for the phase transitions in CsHSO_4 , as in the previous section, the ΔG_{rxn}° was calculated at 100, 150, and 200 °C. From the ΔG_{rxn}° 's, the above K_i 's were used to generate stability domain diagrams (or chemical potential diagrams) for the decomposition of CsHSO_4 , shown as Figure 5.11 at (a) 100 °C, (b) 150 °C, and (c) 200 °C. The regions of stability of $\text{CsHSO}_4(\text{s})$, $\text{Cs}_2\text{S}_2\text{O}_7(\text{s})$, $\text{Cs}_2\text{SO}_4(\text{s})$, and H_2SO_4 - CsHSO_4 or $\text{Cs}_2\text{S}_2\text{O}_7$ solution are labeled. The region of H_2SO_4 - CsHSO_4 or $\text{Cs}_2\text{S}_2\text{O}_7$ solution is indicated as a gray area due to uncertainties in thermodynamic data with respect to the activity of H_2SO_4 and solubility of Cs compounds. The partial pressure of H_2SO_4 is indicated as dotted line at several different pressures ($p_{\text{H}_2\text{SO}_4} = 10^{-2}$, 10^{-3} and 10^{-4} atm). The equilibrium vapor pressures over liquid H_2SO_4 ($p_{\text{H}_2\text{SO}_4}$) at the temperatures of interest, 100, 150, and 200 °C are $10^{-3.7}$, $10^{-2.5}$, $10^{-1.6}$ atm, respectively. To suppress dehydration of CsHSO_4 , a $p_{\text{H}_2\text{O}}$ of greater than that indicated by the co-existence of CsHSO_4 with $\text{Cs}_2\text{S}_2\text{O}_7$ (Reaction A) is required, shown as line A in Figure 5.11. Similarly, to suppress the degradation of CsHSO_4 to form Cs_2SO_4 , a $p_{\text{H}_2\text{SO}_4} = 10^{-2}$ atm or greater than that indicated by the co-existence of CsHSO_4 with Cs_2SO_4 (Reactions B and C) is required, indicated line B. As temperature increases, the stability field of $\text{Cs}_2\text{S}_2\text{O}_7$ moves to higher p_{SO_3} and $p_{\text{H}_2\text{SO}_4}$, whereas that of CsHSO_4 moves to higher $p_{\text{H}_2\text{O}}$ —the stability field of CsHSO_4 becomes quite small at 200 °C. Given the direct

relationship between $p_{\text{H}_2\text{SO}_4}$ and those of p_{SO_3} and $p_{\text{H}_2\text{O}}$ (equation 5.13) for the sake of simplicity only the $p_{\text{H}_2\text{SO}_4}$ is considered, rather than p_{SO_3} in further analysis.

Plots of the co-existence curve of (a) $\text{CsHSO}_4\text{-Cs}_2\text{S}_2\text{O}_7\text{-H}_2\text{O}$ at a critical equilibrium $p_{\text{H}_2\text{SO}_4}$, and (b) $\text{CsHSO}_4\text{-Cs}_2\text{SO}_4\text{-H}_2\text{SO}_4$ at a critical equilibrium $p_{\text{H}_2\text{O}}$ as function of temperature are presented in Figure 5.12. The $\text{CsHSO}_4\text{-Cs}_2\text{S}_2\text{O}_7$ and $\text{CsHSO}_4\text{-Cs}_2\text{SO}_4$ co-existence lines, indicated by lines A and B, respectively, correspond to those indicated in Figure 5.11. For comparison, the liquid-vapor equilibrium pressure of H_2O liquid at 25 and 70 °C, $p_{\text{H}_2\text{O}} = 0.031$ and 0.31 atm, respectively, are also indicated in Figure 5.12(a). Under an equilibrium $p_{\text{H}_2\text{O}}$ of liquid H_2O at 70 °C, CsHSO_4 will not begin to dehydrate until temperatures greater than 200 °C, whereas an equilibrium $p_{\text{H}_2\text{O}}$ at 25 °C will retard dehydration up to ~ 170 °C. Thus, dehydration of CsHSO_4 can easily be suppressed by simply heating under humidified gasses. Heating under $p_{\text{H}_2\text{SO}_4}$ to suppress decomposition to Cs_2SO_4 is a more challenging prospect because of the corrosive nature of this gas, but would only be necessary at high temperatures. For example, at 170 °C, only about 1 ppm of H_2SO_4 in the atmosphere is necessary to suppress degradation. For a sample exposed to ambient atmospheres, a small amount of CsHSO_4 degradation and H_2SO_4 generation would easily prevent further degradation as a result of limited H_2SO_4 diffusion from the electrolyte surface to the atmosphere. At higher temperatures, however, careful control of $p_{\text{H}_2\text{SO}_4}$ would likely be necessary because of the exponential temperature dependence of the equilibrium $p_{\text{H}_2\text{SO}_4}$ and increased diffusion rates.

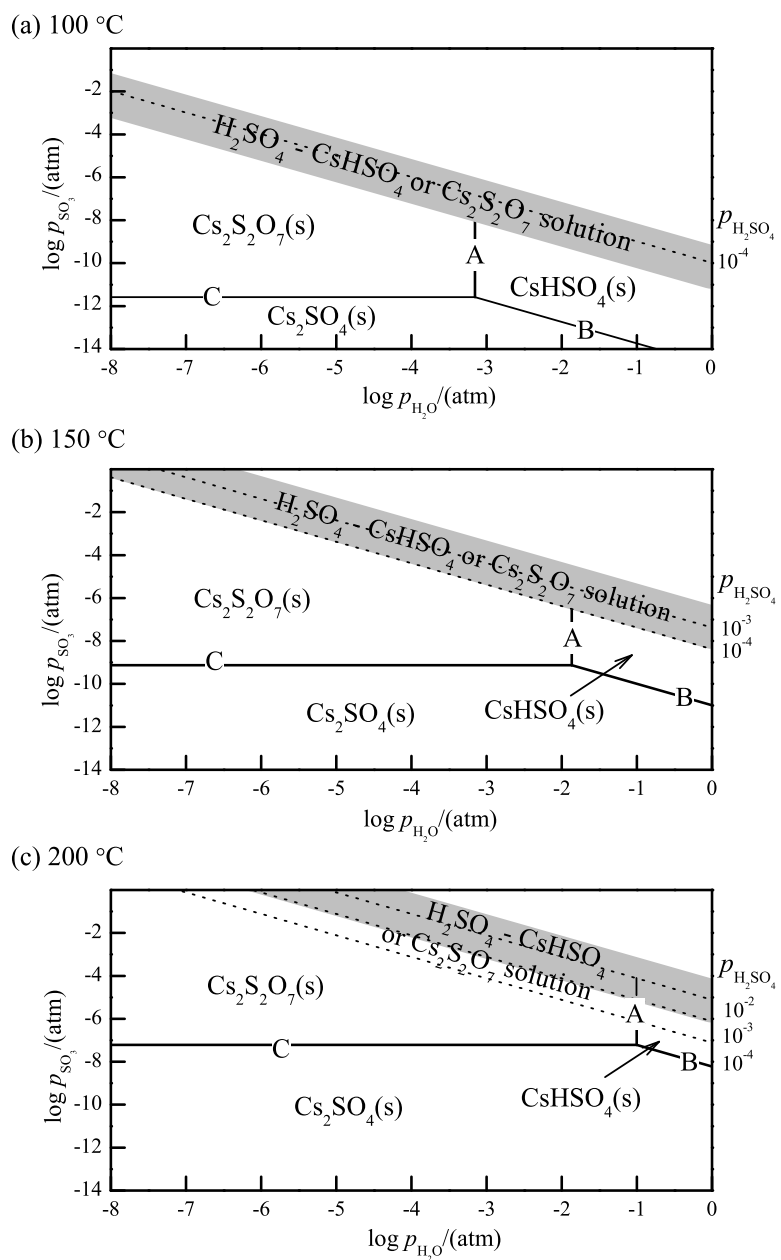
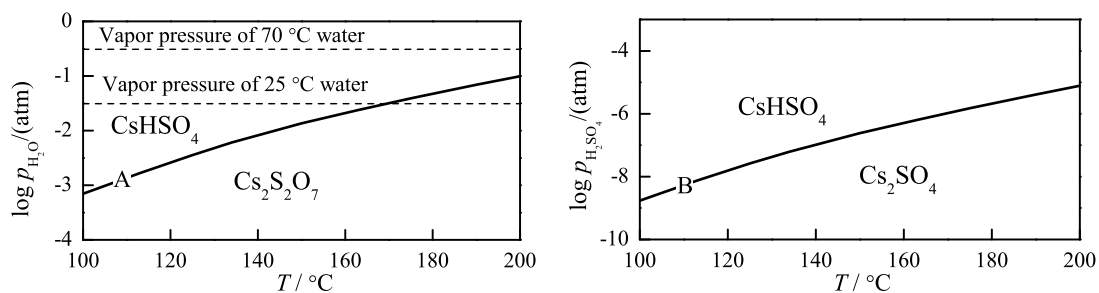


Figure 5.11: Chemical potential diagrams (or stability domain diagrams) for the Cs–H₂O–SO₃ system at temperatures (a) 100 °C, (b) 150 °C, and (c) 200 °C. The co-existence line with H₂SO₄ is shown as a dotted line at various H₂SO₄ partial pressures ($p_{\text{H}_2\text{SO}_4}$ s), as indicated on the right axis. The co-existence lines of CsHSO₄(s)–Cs₂S₂O₇(s) are indicated by line A, and CsHSO₄(s)–Cs₂SO₄(s) by line B.



(a) CsHSO_4 – $\text{Cs}_2\text{S}_2\text{O}_7$ co-existence curve (b) CsHSO_4 – Cs_2SO_4 co-existence curve

Figure 5.12: Co-existence curves as a function of temperature for (a) $\text{CsHSO}_4(\text{s})$ – $\text{Cs}_2\text{S}_2\text{O}_7(\text{s})$ and $p_{\text{H}_2\text{O}}$ at a critical equilibrium $p_{\text{H}_2\text{SO}_4}$ —line A, and (b) $\text{CsHSO}_4(\text{s})$ – $\text{Cs}_2\text{SO}_4(\text{s})$ and $p_{\text{H}_2\text{SO}_4}$ at a critical equilibrium $p_{\text{H}_2\text{O}}$ —line B as a function of temperature.

5.2.1.4 O₂ Concentration Cell

To experimentally verify the previous thermodynamic analysis of CsHSO₄ in an O₂ atmosphere, electromotive force (EMF) measurements were carried out on CsHSO₄ in an O₂ concentration cell. In addition to chemical stability, fuel cell electrolytes must also exhibit sufficient mechanical integrity so as to prevent the development of leaks across the membrane over long-term operation. The large volume change accompanying the superprotonic transition of solid acids, such as in CsHSO₄ (1-2 vol%), renders mechanical integrity a particular concern for these compounds. Furthermore, it is essential that electrolytes under consideration for fuel cell applications have an ionic (protonic) transference number close to one; that is, the entirety of the current should be carried by protons rather than electronic species, which would reduce fuel cell efficiencies. To address the issue of thermo-mechanical stability, measurements are carried out while thermal cycling through the phase transition, while the protonic transference number is determined by EMF measurements.

A schematic diagram of the experimental apparatus used is shown in Figure 5.13. Here CsHSO₄ powder was uniaxially pressed at 280 MPa into a pellet (2 mm thick by 19 mm in diameter). Both sides were sputter-coated with platinum and then lightly polished with fine sandpaper. Platinum gauze and leads were attached to both sides by applying moderate pressure. A fluorocarbon O-ring was used as a seal between both chambers. Flowing mixtures of Ar-O₂-3% H₂O gasses at 50 sccm were delivered to each chamber with different O₂ concentrations of 10 and 0.1% , respectively. The EMF across CsHSO₄ in an oxygen concentration cell was measured over several days, while the pellet was repeatedly cycled through the phase transition temperature (141 °C) between 129 (3 hrs) and 145 °C (14 hrs). The resultant voltage generated across the sample was measured using an Agilent 34970A digital multimeter and the H₂O vapor pressure was monitored using an EdgeTech 650 capacitance manometer.

The results of the EMF measurements are shown in Figure 5.14. At temperatures above the superprotonic phase transition (at 141 °C), the measured voltages were, after some equilibration period, consistent with the theoretical value of -41.5 mV within ± 2 mV. Thus, CsHSO₄ is a purely ionic conductor above the superprotonic phase transition. Furthermore, as expected on the basis of the thermodynamic analysis, the material was stabilized against dehydration as a result of the 3% H₂O in the atmosphere—there were no

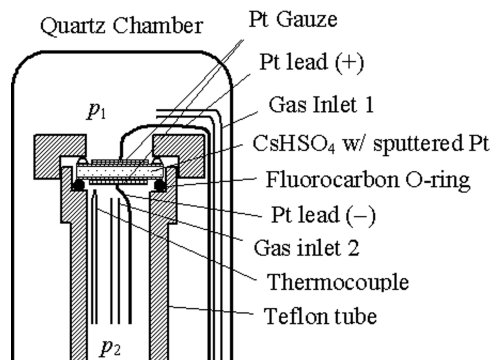


Figure 5.13: Schematic diagram of experimental apparatus used for electromotive force measurements of CsHSO_4 in an O_2 concentration cell, where p_1 and p_2 represent the different O_2 partial pressures.

signs of CsHSO_4 decomposition after 85 hrs of measurement. Rather unexpected is the drop in voltage at temperatures below the transition. Given the nature of the chemical bonding in CsHSO_4 , it is unlikely that this can be a result of high electronic conductivity at 129°C . It is instead believed that the low voltage is a result of microcracks which heal at elevated temperatures. The possibility that microcracks can heal at high temperatures is proposed on the basis of the reported “superplastic” behavior of CsHSO_4 in the superprotonic phase, in which it was observed that the mechanical properties were analogous to that of “clay or plasticine”²¹. Whatever the cause of the low voltage at low temperature, it is clear that it does not impact the high-temperature electrochemical behavior of CsHSO_4 , for which a large voltage is obtained in each thermal cycle. Furthermore, the unavoidable thermo-mechanical deformation of cesium hydrogen sulfate which occurs upon passing through the phase transition can be prevented from causing device damage with the appropriate experimental configuration.

These results demonstrate that CsHSO_4 can, with the use of humidified gasses, be used as an electrolyte in oxidizing atmospheres. Though it is clear that for fuel cell applications, CsHSO_4 is not an ideal candidate, this electrolyte could find its way into applications such as oxygen and sulfuric acid sensors.

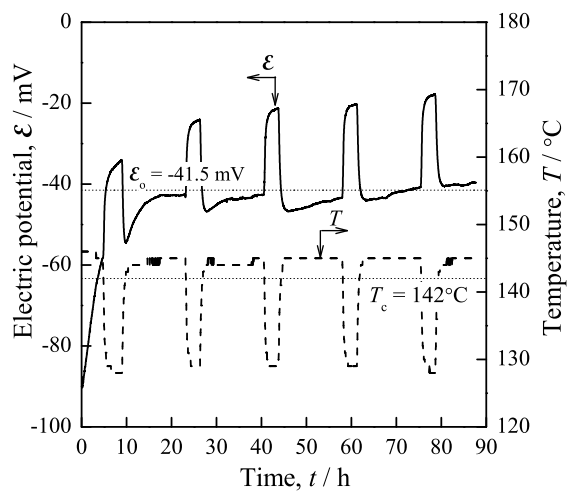


Figure 5.14: The electric potential as a function of time and temperature of a CsHSO_4 -electrolyte-based oxygen concentration cell. Flowing humidified gases ($p_{\text{H}_2\text{O}} = 0.3 \text{ atm}$) with O_2 concentrations of 10% and 0.1%, theoretical electric potential (\mathcal{E}_0) of -41.5 mV at $145 \text{ }^\circ\text{C}$, were used while cycling above and below the superprotonic phase transition temperature (T_c) of CsHSO_4 .

5.2.2 Sulfates and Selenates¹⁹

After the discovery of chemical instability of CsHSO_4 in H_2 containing atmospheres a concerted effort was made to identify a superprotonic solid acid which is stable in H_2 gas in the presence of a fuel cell catalyst. To accomplish this, rapid characterization of many known superprotonic solid acid sulfates and selenates by thermal analysis under H_2 in the presence of a Pt-catalyst was carried out. Isothermal gravimetric analysis studies at 160 °C under flowing H_2 gas in the presence of 35 wt% Pt on CsHSO_4 , $(\text{NH}_4)_3\text{H}(\text{SO}_4)_2$, $\text{Rb}_3\text{H}(\text{SeO}_4)_2$, $(\text{NH}_4)_3\text{H}(\text{SeO}_4)_2$, $\text{Cs}_2(\text{HSO}_4)(\text{H}_2\text{PO}_4)$, and Cs_2SO_4 (for reference), are presented in Figure 5.15. Each of the solid acid compounds undergoes a superprotonic transition at a temperature below the measurement temperature. It is apparent that the simple salt, Cs_2SO_4 , is stable under reducing conditions, despite the 6+ oxidation state of sulfur, and thus it is a likely final reaction product. Disappointingly, from an applications perspective, none of the sulfate or selenate solid acids are stable under these conditions. The rate of weight loss follows the sequence $(\text{NH}_4)_3\text{H}(\text{SO}_4)_2 > \text{CsHSO}_4 > \text{Rb}_3\text{H}(\text{SeO}_4)_2 > (\text{NH}_4)_3\text{H}(\text{SeO}_4)_2 > \text{Cs}_2(\text{HSO}_4)(\text{H}_2\text{PO}_4)$.

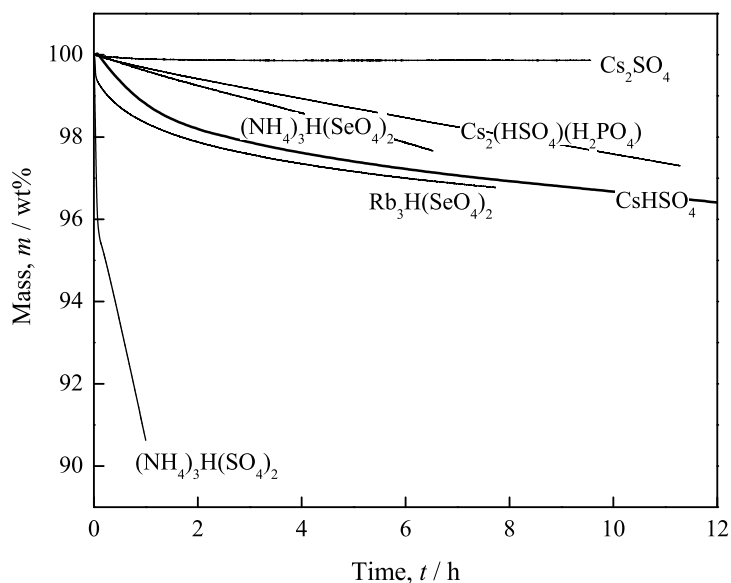
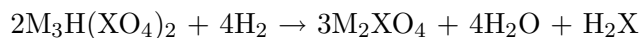
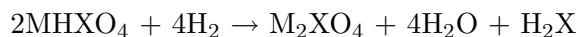


Figure 5.15: Weight loss isotherms at 160 °C of various superprotonic solid acid sulfates and selenates (as indicated) and Cs_2SO_4 (for comparison) under flowing H_2 gas ($20 \text{ cm}^3 \text{ min}^{-1}$) in the presence 35 wt% Pt catalyst.

The reduction reaction for CsHSO_4 in H_2 gas, Reaction I from the previous sections, can be expressed more generally to include all MHXO_4 and $\text{M}_3\text{H}(\text{XO}_4)_2$ compounds (where

M = monovalent cation, and X = S or Se):



Given the fractional weight change per formula unit reacted of the above reactions, one would expect weight loss to occur more quickly for MHXO_4 than $\text{M}_3\text{H}(\text{XO}_4)_2$ compounds. The rapid degradation of $(\text{NH}_4)_3\text{H}(\text{SO}_4)_2$ reveals that this material is particularly unsuitable for fuel cell applications. Indeed, attempts to demonstrate fuel cell performance using $(\text{NH}_4)_3\text{H}(\text{SO}_4)_2$ were uniformly unsuccessful³³. The lower reactivity of $\text{Cs}_2(\text{HSO}_4)(\text{H}_2\text{PO}_4)$ may be a result of the lesser tendency of phosphorous to form H_3P than sulfur to form H_2S and suggests that phosphate-based solid acids will likely have better chemical stability under fuel cell conditions.

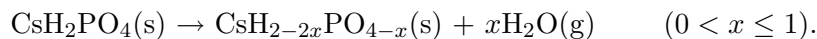
5.2.3 CsH_2PO_4 ¹⁷

In light of the chemical instability observed in solid acid sulphates and selenates under H_2 atmospheres, here we have investigated the viability of CsH_2PO_4 as an electrolyte in fuel cells. A phosphate-based compound is not expected to suffer a reduction reaction to form solid phosphorus or gaseous H_xP species, and therefore is a promising candidate for fuel cell applications. It is well-known that CsH_2PO_4 dehydrates in its superprotonic phase under ambient pressures, which, if employed in a fuel cell, would render it useless. This issue is addressed through (1) identifying the equilibrium partial pressure to suppress this dehydration, and then (2) employing this knowledge to the measurement of fuel cell performance under gasses, appropriately humidified so as to prevent dehydration.

5.2.3.1 Thermo-chemical Stability

First, to establish the stability of CsH_2PO_4 under fuel cell conditions, thermal analysis was carried out on CsH_2PO_4 mixed with Pt-catalyst (4:1 wt ratio) under H_2 and O_2 atmospheres, respectively, Figure 5.16. From these results it is clear that thermal decomposition of CsH_2PO_4 , even when combined with Pt catalyst, is independent of whether the atmosphere is reducing (left panel, flowing H_2) or oxidizing (right panel, flowing O_2). In both cases, weight loss begins at 223 °C, and, as evident from analysis of the evolved gasses, is

due entirely to dehydration, that is, no phosphate fragments were detected. It has been proposed³⁴ that the dehydration reaction proceeds via the formation of amorphous hydrogen pyrophosphate and polyphosphate intermediates until complete decomposition to CsPO_3 occurs according to the following reaction:



Regardless, what is clear from these results is that neither the presence of a Pt catalyst or reducing/oxidizing atmospheres affect the dehydration behavior of CsH_2PO_4 .

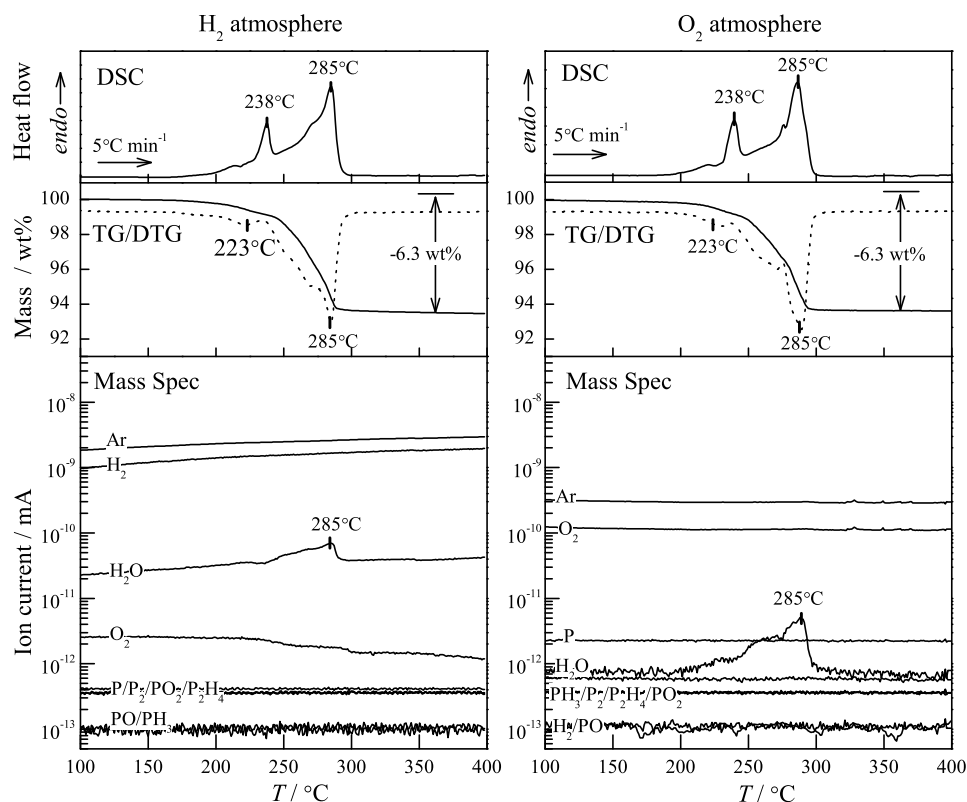


Figure 5.16: Thermal characterization of CsH_2PO_4 with Pt-black (4:1 wt ratio) powder upon heating to 400 °C at 5 °C min⁻¹ by simultaneous differential scanning calorimetry (top—DSC), thermogravimetry and differential thermogravimetry (middle—TG/DTG) with off-gasses analyzed by mass spectrometry (bottom—Mass Spec) under 4 vol% H_2 -Ar (left panel— H_2 atmosphere) and 15 vol% O_2 -Ar (right panel— O_2 atmosphere) gasses, each at a flow rate of 60 cm³ min⁻¹.

Though unaffected by reducing or oxidizing atmospheres, the issue of thermal dehydration of CsH_2PO_4 remains a barrier to its application as an electrolyte in fuel cells. However, it has been recently shown that, in addition to the application of pressure³⁵ (Chapter 3), the careful control of water partial pressure³⁶ can suppress the above dehydration reaction at

elevated temperatures. Thus, by retaining sufficient $p_{\text{H}_2\text{O}}$ in a CsH_2PO_4 -based fuel cell, the above reaction can be suppressed and, in principle, superprotonic behavior of the electrolyte accessed.

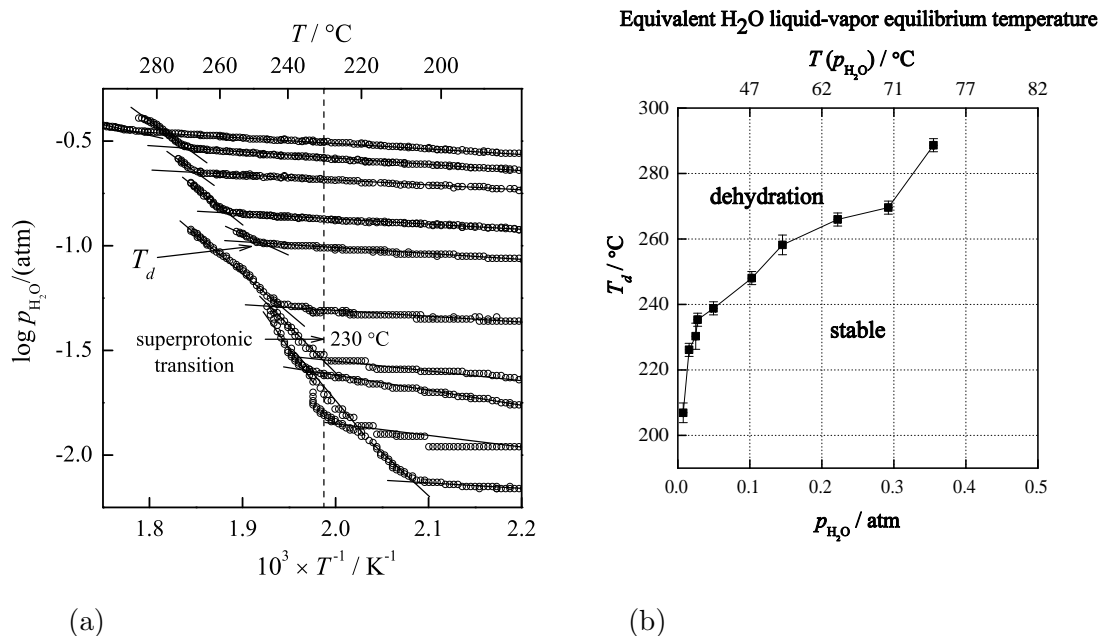


Figure 5.17: (a) Arrhenius plot of the measured water partial pressure, $p_{\text{H}_2\text{O}}$, as a function of temperature upon heating CsH_2PO_4 at $0.4^\circ\text{C min}^{-1}$ to 300°C under closed volume at several different initial water partial pressures. Here the onset of dehydration, T_d , is indicated by a change in slope. (b) Plot of the onset of dehydration temperatures as a function of water partial pressure. Here the top-axis corresponds to the equivalent H_2O equilibrium liquid-vapor temperature, $T(p_{\text{H}_2\text{O}})$, at each $p_{\text{H}_2\text{O}}$ given on the bottom-axis.

To this end powder samples of CsH_2PO_4 at ten different starting water partial pressures were slowly heated to $\sim 300^\circ\text{C}$ in a closed volume container. The onset of dehydration (T_d), indicated by a discontinuous change in the slope of $\log p_{\text{H}_2\text{O}}$ as a function of $1/T$, is shown in Figure 5.17(a). Here no clear Arrhenius behaviour was observed that would indicate a single dehydration reaction and corresponding Gibbs free energy (ΔG_{rxn}°) for the dehydration CsH_2PO_4 . In Figure 5.17(b), the onset of CsH_2PO_4 dehydration temperature (T_d) is plotted as a function $p_{\text{H}_2\text{O}}$. Here the top axis corresponds to the liquid-vapor equilibrium temperature, $T(p_{\text{H}_2\text{O}})$, at each water partial pressure, $p_{\text{H}_2\text{O}}$, indicated by the bottom axis. These data show that humidification of gases in liquid water at $\sim 70^\circ\text{C}$, with an equivalent $p_{\text{H}_2\text{O}}$ of ~ 0.30 atm, is sufficient to suppress CsH_2PO_4 dehydration up to a temperature of $\sim 270^\circ\text{C}$. Only slightly greater water partial pressures are required if dehydration is to be suppressed to temperatures as high as the melting point of CsH_2PO_4 , 346°C ³⁷. From

these results, we can see that the operation of a fuel cell utilizing a CsH_2PO_4 electrolyte without concern for dehydration is easily achievable by simply humidifying fuel cell gasses by passing through water maintained at a temperature of $70\text{ }^\circ\text{C}$ or greater.

5.2.3.2 H_2/O_2 Fuel Cell

To demonstrate the viability of using moderate water partial pressures to provide thermal stability to a chemically stable solid acid, a membrane electrode assembly (MEA) was prepared containing a $260\text{ }\mu\text{m}$ thick CsH_2PO_4 electrolyte and Pt electrocatalyst at both electrodes. The cell was operated under H_2/O_2 configuration at $235\text{ }^\circ\text{C}$, in which both anode and cathode gases were humidified ($p_{\text{H}_2\text{O}} = 0.3\text{ atm}$), where humidification was essential to prevent dehydration of the CsH_2PO_4 electrolyte. Electrical current (100 mA cm^{-2}) was drawn continuously for 35 hrs and polarization curves collected both before and after 35 hrs, Figure 5.18.

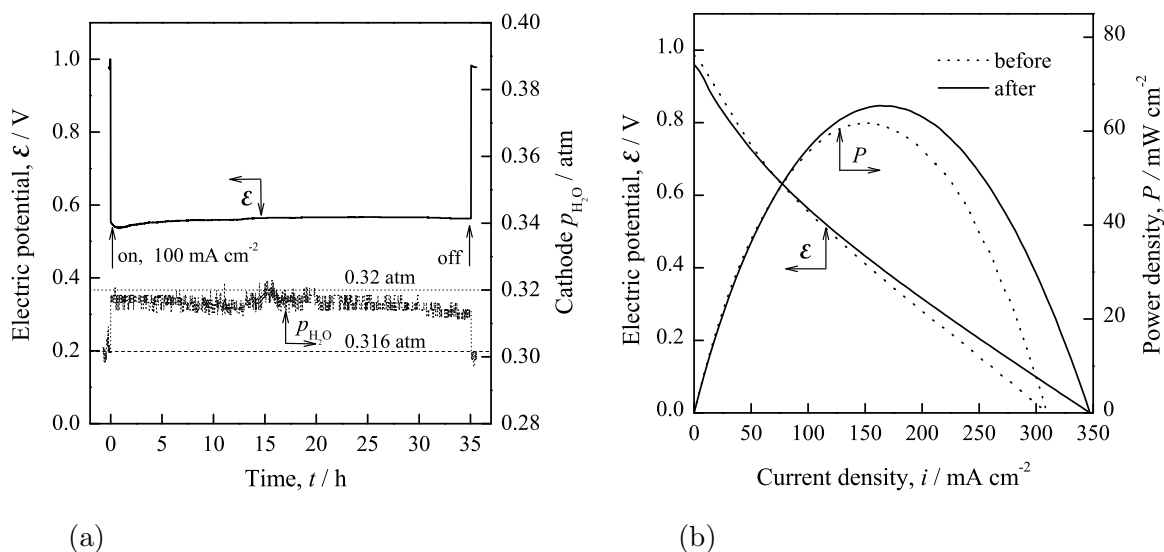


Figure 5.18: H_2/O_2 fuel cell performance with CsH_2PO_4 -based electrolyte. (a) Electric potential (ϵ) and water partial pressure ($p_{\text{H}_2\text{O}}$) as a function of time (t) while drawing 100 mA cm^{-2} continuous current for 35 hrs. (b) Electric potential and power density (P) versus current density (i) before and after 35 hr measurement. The cell was operated at $235\text{ }^\circ\text{C}$ under humidified ($p_{\text{H}_2\text{O}} = 0.3\text{ atm}$) 50 sccm flowing H_2 and O_2 gases at the anode and the cathode, respectively. Electrolyte thickness was $260\text{ }\mu\text{m}$ and catalyst loading 18 mg cm^{-2} Pt.

During the continuous measurement, the cell showed remarkable stability; the voltage very gradually increased from 0.538 to 0.567 V , with an average of 0.561 V . Water generated at the cathode was in correspondence with that expected from drawing 100 mA cm^{-2} current. The polarization curves obtained before and after the long-term evaluation were rather

similar to one another, although certainly not identical. The open cell voltage (OCV) was initially 0.986 and dropped to 0.960 V after 35 hrs measurement. Both values are somewhat lower than the theoretical open cell voltage (Nernst potential) of 1.15 V for this cell, and the difference is attributed to small leaks across the fuel cell seals and possibly micro-cracks within the electrolyte. The peak power and maximum current densities improved slightly over the 35 hrs stability test, from 61.7 to 65.4 mW cm⁻² and from 310 to 345 mA cm⁻², respectively. Performance limitations were primarily due to electrolyte resistance (Ohmic or iR_A losses), which can be reduced by up to a factor of ten by simply decreasing the electrolyte thickness. Nonetheless, these power and current density values are about five times those reported earlier for CsHSO₄ and represent a substantial breakthrough both in terms of electrolyte stability and fuel cell performance.

5.2.3.3 Direct Methanol Fuel Cell

Direct methanol fuel cells (DMFCs) based on a solid acid electrolyte are anticipated to provide significant advantages over current state-of-the-art polymeric electrolytes due to complete impermeability of the solid acids to methanol and elevated operating temperatures. These features, in turn, translate into higher power densities, higher CO tolerance and, ultimately, lower precious metal catalyst loadings.

In order to demonstrate the viability of a CsH₂PO₄ electrolyte in vapor-fed direct methanol fuel cells, a second MEA was constructed using PtRu (50:50 mol) as the anode electro-catalyst. Vapor-phase methanol and water (0.92:1 molar ratio), were fed into the anode compartment using argon as a carrier gas, and humidified oxygen fed into the cathode. The cell was operated at 243°C. Electrical current (80 mA cm⁻²) was drawn continuously for 35 hrs and polarization curves obtained both before and after the measurement, Figure 5.19. As in the case of the H₂/O₂ cell, the methanol cell showed remarkable stability, with the voltage decreasing slightly from an initial value of 0.441 V to a final value of 0.381 V, and the majority of that decrease occurring in the first few hours. Moreover, the two polarization curves are again quite similar. Peak power densities were 37.2 and 34.4 mW cm⁻², respectively, for the two measurements. Open circuit voltages, measured at 0.897 and 0.865 V, respectively, before and after stability examination, cannot be compared to a theoretical (Nernst) potential because, as is typical for DMFCs, the partial pressures of the product gas, CO₂, and possible intermediates, *e.g.* CH₄, were not controlled or monitored.

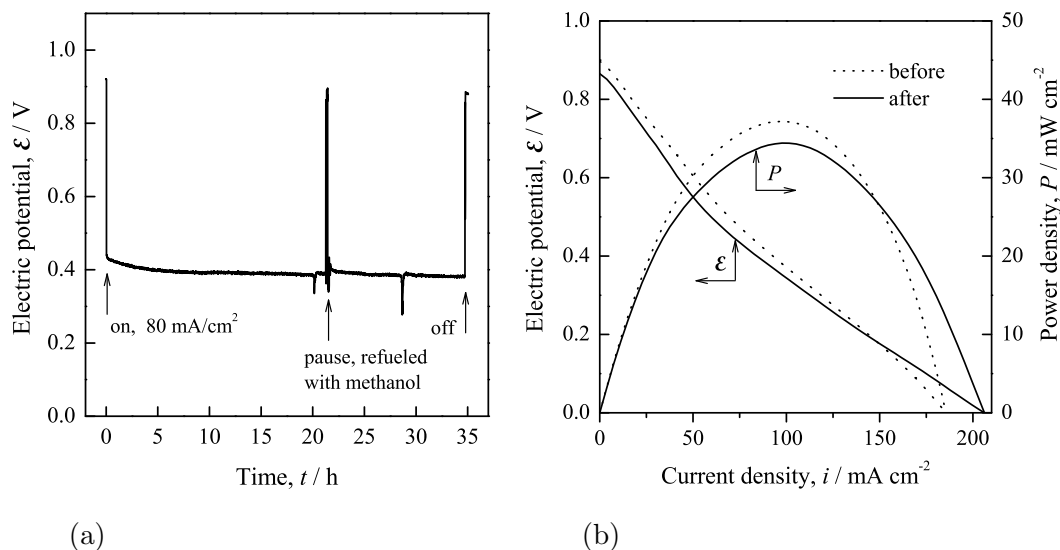


Figure 5.19: Direct methanol fuel cell performance with CsH_2PO_4 -based electrolyte. (a) Electric potential (\mathcal{E}) as a function of time (t) while drawing 80 mA cm^{-2} of current for 35 hrs. (b) Electric potential and power density (P) versus current density (i) before and after 35 hr measurement. The cell was operated at 243°C . Gasses fed to the anode and cathode were, respectively, $\text{CH}_3\text{OH-H}_2\text{O-Ar}$ (23:25:52 mol%) flowing at 97 sccm and $\text{O}_2\text{-H}_2\text{O}$ (67:33 mol%) flowing at 75 sccm. After 20 hrs, measurement was paused to replenish methanol supply. Electrolyte thickness was $260 \mu\text{m}$ and catalyst loadings were 13 mg cm^{-2} PtRu (50:50 mol%) at the anode and 15 mg cm^{-2} Pt at the cathode.

Nevertheless, the OCVs are greater than what is obtained from polymeric DMFCs ($\sim 0.8 \text{ V}$)^{38,39} presumably because of the higher methanol content utilized here and the lower membrane permeability. The power densities reached in this work are within about a factor of five of the most advanced DMFCs ($100\text{--}200 \text{ mW cm}^{-2}$).^{38,39}

5.3 Conclusions

Though initial results of solid acid fuel cells based on CsHSO_4 were quite poor, much was gained from these investigations including a “proof-of-principle” demonstration and the identification of the thermo-chemical requirements necessary for the application of solid acid in fuel cells. Thermodynamic characterization and stability studies of solid acid sulfates and selenates indicated that solid acid phosphates may have the thermo-chemical stability necessary for fuel cell applications. Further investigation into such compounds showed that despite the apparently poor thermal stability of CsH_2PO_4 in its superprotonic phase, both H_2/O_2 and direct methanol fuel cells based on this material have excellent long-term performance when stabilized with water partial pressures of $\sim 0.3 \text{ atm}$, depending on the

temperature of operation. These “humidity-stabilized” solid acid fuel cells exhibit higher open circuit voltages than polymer electrolyte fuel cells and thus may ultimately yield better overall system efficiencies. More importantly, high temperature operation and much less demanding humidification requirements lead to system simplifications. In conclusion, fuel cells based on solid acid phosphates operating in an intermediate temperature range ~ 230 - 300 °C, may offer significant advantages over current state-of-the-art electrolytes, and could significantly help to advance the current state of fuel cell technology.

Bibliography

1. EG&G Services, Parsons, Inc. *Fuel Cell Handbook*. National Energy Technology Laboratory, Office of Fossil Energy, U.S. Department of Energy, P.O. Box 880, Morgantown, West Virginia 26507-0880, 5th edition, October 2000.
2. K.-D. Kreuer. On solids with liquid-like properties and the challenge to develop new proton-conducting separator materials for intermediate-temperature fuel cells. *ChemPhysChem*, 3:771–775, 2002.
3. B.C.H. Steele and A. Heinzl. Materials for fuel-cell technologies. *Nature*, 414:345–352, 2001.
4. A.I. Baranov, V.P. Khiznichenko, V.A. Sandler, and L.A. Shuvalov. Frequency dielectric-dispersion in the ferroelectric and superionic phases of CsH_2PO_4 . *Ferroelectrics*, 81:1147–1150, 1988.
5. A.I. Baranov, L.A. Shuvalov, and N.M. Shchagina. Superior conductivity and phase-transitions in CsHSO_4 and CsHSeO_4 crystals. *JETP Letters*, 36(11):459–462, 1982.
6. A. Pawlowski, C. Pawlaczyk, and B. Hilczer. Electric-conductivity in crystal group $\text{Me}_3\text{H}(\text{SeO}_4)_2$ ($\text{Me} = \text{NH}_4^+, \text{Rb}^+, \text{Cs}^+$). *Solid State Ionics*, 44(1-2):17–19, 1990.
7. C.R.I. Chisholm and S.M. Haile. High-temperature phase transitions in $\text{K}_3\text{H}(\text{SO}_4)_2$. *Solid State Ionics*, 145(1-4):179–184, 2001.
8. C.R.I. Chisholm and S.M. Haile. Superprotonic behavior of $\text{Cs}_2(\text{HSO}_4)(\text{H}_2\text{PO}_4)$ - a new solid acid in the CsHSO_4 - CsH_2PO_4 system. *Solid State Ionics*, 136(SI):229–241, 2000.
9. C. Ramasastry and K.S. Ramaiah. Electrical-conduction in $(\text{NH}_4)_3\text{H}(\text{SO}_4)_2$ and $(\text{NH}_4)_3\text{H}(\text{SeO}_4)_2$ crystals. *Journal of Materials Science*, 16(7):2011–2016, 1981.
10. J.C. Amphlett, M. Farahani, R.F. Mann, B.A. Peppley, and P.R. Roberg. 26th energy conversion engineering conference. In *Proceedings of the 26th Energy Conversion Engineering Conference*, volume 3, page 624, La Grange, IL, USA, August 1991. Conversion Technologies/Electrochemical Conversion, American Nuclear Society.
11. H.P. Dhar, L.G. Christner, and A.K. Kush. Nature of CO adsorption during H_2 oxidation in relation to modeling for CO poisoning of a fuel-cell anode. *Journal of the Electrochemical Society*, 134(12):3021–3026, 1987.
12. H. Uchida, Y. Yamada, N. Asano, M. Watanabe, and M. Litt. Properties of AB-PBI membranes for fuel cells. *Electrochemistry*, 70(12):943–945, 2002.
13. N.Q. Minh. Ceramic fuel cells. *Journal of the American Ceramic Society*, 563-88(3):76, 1993.
14. M. Hsu. Zirconia fuel cell power systems. In *1985 Fuel Cell Seminar Abstracts*, Tucson, AZ, May 1985. 1985 Fuel Cell Seminar.

15. M. Hsu. Zirconia fuel cell power system planar stack development. In *1986 Fuel Cell Seminar Abstracts*, Tucson, AZ, October 1986. 1986 Fuel Cell Seminar.
16. S.M. Haile, D.A. Boysen, C.R.I. Chisholm, and R.B. Merle. Solid acids as fuel cell electrolytes. *Nature*, 410(6831):910–913, 2001.
17. D.A. Boysen, T. Uda, C.R.I. Chisholm, and S.M. Haile. High performance solid acid fuel cells through humidity stabilization. *Science*, in submitted, 2003.
18. T. Uda, D.A. Boysen, and S.M. Haile. Thermodynamic analysis and electrochemical evaluation of CsHSO₄. *Solid State Ionics*, submitted, 2003.
19. R.B. Merle, C.R.I. Chisholm, D.A. Boysen, and S.M. Haile. Instability of sulfate and selenate solid acids in fuel cell environments. *Energy & Fuels*, 17:210–215, 2003.
20. T. Norby, M. Friesel, and B.E. Mellander. Proton and deuteron conductivity in CsHSO₄ and CsDSO₄ by *in-situ* isotopic exchange. *Solid State Ionics*, 77:105–110, 1995.
21. L.F. Kirpichnikova, A.A. Urusovskaya, and V.I. Mozgovoi. Superplasticity of CsHSO₄ crystals in the superionic phase. *JETP Letters*, 62(8):638–641, 1995.
22. D.R. Gaskell. *Introduction to Metallurgical Thermodynamics*, page 574 and 586. McGraw-Hill, Washington, D.C., 2nd edition, 1981.
23. S. Srinivasan, O.A. Velev, A. Parthasarathy, D.J. Manko, and A.J. Appleby. High-energy efficiency and high-power density proton-exchange membrane fuel-cells – electrode-kinetics and mass-transport. *Journal of Power Sources*, 36(3):299–320, 1991.
24. F. Croce and G. Cigna. Determination of the protonic transference number for KH₂PO₄ by electromotive force measurements. *Solid State Ionics*, 6:201–202, 1982.
25. N.Q. Minh and C.R. Horne. Novel method for fabricating thin-film ionic and mixed conductors. In F.W. Poulsen, J.J. Bentzen, E. Jacobsen, T. Skou, and M.J.L. Østergård, editors, *Proceedings of the 14th Risø International Symposium on Materials Science: High Temperature Electrochemical Behaviour of Fast Ion and Mixed Conductors*, pages 563–588, Roskilde, Denmark, 1993. Risø National Laboratory.
26. D.T. Chin and P.D. Howard. Hydrogen-sulfide poisoning of platinum anode in phosphoric-acid fuel-cell electrolyte. *Journal of the Electrochemical Society*, 133(12):2447–2450, 1986.
27. Calum R. I. Chisholm. *Superprotonic Phase Transitions in Solid Acids: Parameters affecting the presence and stability of superprotonic transitions in MH_nXO₄ family of compounds (X = S, Se, P, As; M = Li, Na, K, NH₄, Rb, Cs)*. PhD thesis, California Institute of Technology, 2002.
28. Donald D. Wagman. *The NBS Tables of Chemical Thermodynamic Properties: selected values for inorganic and C1 and C2 organic substances in SI Units*. American Chemical Society, Washington, D.C., 1982.
29. L.V. Gurvich, G.A. Bergman, L.N. Gorokhov, V.S. Iorish, V.Y. Leonidov, and V.S. Yungman. Thermodynamic properties of alkali metal hydroxides. Part 2. Potassium, rubidium, and cesium hydroxides. *Journal of Physical and Chemical Reference Data*, 26(4):1031–1110, 1997.

30. Ihsan Barin. *Thermochemical Data of Pure Substances*. VCH, New York, NY, USA, c1989.
31. M.W. Chase. *JANAF Thermochemical Tables*, volume 14. American Chemical Society, Washington, D.C., c1986.
32. L.V. Gurvich, I.V. Veyts, and C.B. Alcocl, editors. *Thermodynamic Properties of Individual Substances*, volume 1 & 2. Hemisphere Pub. Corp., New York, NY, USA, 1989.
33. D.B. Boysen, C.R.I. Chisholm, C. Bielawski, S.M. Haile, and R. Grubbs. $(\text{NH}_4)_3\text{H}(\text{SO}_4)_2$ -based fuel cells. unpublished results, 2000.
34. B.M. Nirsha. *Russian Journal of Inorganic Chemistry*, 27:770, 1980.
35. D.A. Boysen, S.M. Haile, H. Liu, and R.A. Secco. High-temperature behavior of CsH_2PO_4 under both ambient and high pressure conditions. *Chemistry of Materials*, 15:727–736, 2003.
36. J. Otomo, N. Minagawa, C.J. Wen, K. Eguchi, and H. Takahashi. Protonic conduction of CsH_2PO_4 and its composite with silica in dry and humid atmospheres. *Solid State Ionics*, 156(3):357–369, 2003.
37. E. Rapoport, J.B. Clark, and P.W. Richter. High-pressure phase relations of RbH_2PO_4 , CsH_2PO_4 , and KD_2PO_4 . *Journal of Solid State Chemistry*, 24(3-4):423–433, 1978.
38. A.K. Shukla, C.L. Jackson, K. Scott, and R.K. Raman. *Electrochimica Acta*, 47:3401, 2002.
39. S.C. Thomas, X.M. Ren, S. Gottesfeld, and Zelenay P. *Electrochimica Acta*, 47:741, 2002.

Appendix

A.1 Solid Acid Synthesis Recipes

A.1.1 Cesium dihydrogen phosphate (CsH_2PO_4)

- (1) Weigh out 10.0 g of Cs_2CO_3 powder
- (2) Measure out 6.01 mL H_3PO_4 (phosphoric acid, 85% assay)
- (3) Slowly add (2) to (1)
- (4) Add DI- H_2O to (3) while stirring, until complete dissolution (~ 5 mL)
- (5) Add 50–100 mL methanol, until massive precipitation
- (6) Vacuum filter precipitate
- (7) Dry precipitate in an oven at 60 °C for several hours

→ theoretical yield = 14.1 g CsH_2PO_4

A.1.2 Cesium hydrogen sulfate (CsHSO_4)

- (1) Weigh out 10.0 g of Cs_2SO_4 powder
- (2) Measure out 3.10 mL H_2SO_4 (sulfuric acid, 85% assay)
- (3) Add DI- H_2O to (1) until completely dissolved (~ 5 mL)
- (4) Add (2) to (3)
- (5) Add 50–100 mL acetone, until massive precipitation
- (6) Vacuum filter precipitate

(7) Dry precipitate in an oven at 60 °C for several hours

→ theoretical yield = 12.7 g CsHSO₄

A.1.3 Potassium hydrogen selenate (KHSeO₄)

(1) Weigh out 1.00 g of K₂SeO₄ powder

(2) Weigh out 1.94 g H₂Se₄(60% aqueous solution)

(3) Add (1), (2), and 6 mL DI-H₂O

(4) Repeatedly heat and cool, until massive precipitation

(5) Vacuum filter precipitate

(6) Dry precipitate in an oven at 60 °C for several hours

→ theoretical yield = 1.65 g KHSeO₄

A.1.4 Rubidium dihydrogen phosphate (RbH₂PO₄)

(1) Weigh out 1.00 g of Rb₂CO₃ powder

(2) Add DI-H₂O to (1) until dissolution

(3) Weigh out 1.00 g H₃PO₄ (phosphoric acid, 85% assay)

(4) Slowly add (3) to (2)

(5) Add methanol, until massive precipitation

(6) Vacuum filter precipitate

(7) Dry precipitate in an oven at 60 °C for several hours

→ theoretical yield = 2.53 g RbH₂PO₄

A.1.5 Thallium dihydrogen phosphate (TlH_2PO_4)

- (1) Weigh out 1.00 g of Tl_2CO_3 powder
- (2) Add 20 mL DI- H_2O to (1)
- (3) Weigh out 0.492 g H_3PO_4 (phosphoric acid, 85% assay)
- (4) Slowly add (3) to (2)
- (5) Add 50 mL methanol, until massive precipitation
- (6) Vacuum filter precipitate
- (7) Dry precipitate in an oven at 60 °C for several hours

→ theoretical yield = 1.28 g TlH_2PO_4

A.1.6 Triammonium hydrogen disulfate ($(\text{NH}_4)_3\text{H}(\text{SO}_4)_2$)

- (1) Weigh out 5.0 g of $(\text{NH}_4)_2\text{SO}_4$ powder
- (2) Measure out 3.8 mL H_2SO_4 (sulfuric acid, 95% assay)
- (3) Add DI- H_2O to (1) until completely dissolved (~ 10 mL)
- (4) Add (2) to (3)
- (5) Add 150 mL acetone, until massive precipitation
- (6) Vacuum filter precipitate
- (7) Dry precipitate in an oven at 60 °C for several hours

→ theoretical yield = 6.23 g $(\text{NH}_4)_3\text{H}(\text{SO}_4)_2$

A.1.7 Tripotassium hydrogen diselenate ($\text{K}_3\text{H}(\text{SeO}_4)_2$)

- (1) Weigh out 1.0 g of KOH powder
- (2) Weigh out 12.9 g H_2Se_4 (60% aqueous solution)
- (3) Add (1) to (2)

- (4) Add 30 mL methanol, until massive precipitation
- (5) Vacuum filter precipitate
- (6) Dry precipitate in an oven at 60 °C for several hours

→ theoretical yield = 2.4 g $\text{K}_3\text{H}(\text{SeO}_4)_2$

A.1.8 Trirubidium hydrogen diselenate ($\text{Rb}_3\text{H}(\text{SeO}_4)_2$)

- (1) Weigh out 15.9 g of Rb_2CO_3 powder
- (2) Weigh out 100 g H_2Se_4 (60% aqueous solution)
- (3) Add (1) to (2)
- (4) Add 200 mL methanol, until massive precipitation
- (5) Vacuum filter precipitate
- (6) Dry precipitate in an oven at 60 °C for several hours

→ theoretical yield = 10.6 g $\text{Rb}_3\text{H}(\text{SeO}_4)_2$

A.2 Thermal Analysis Results

A.2.1 RbH_2PO_4

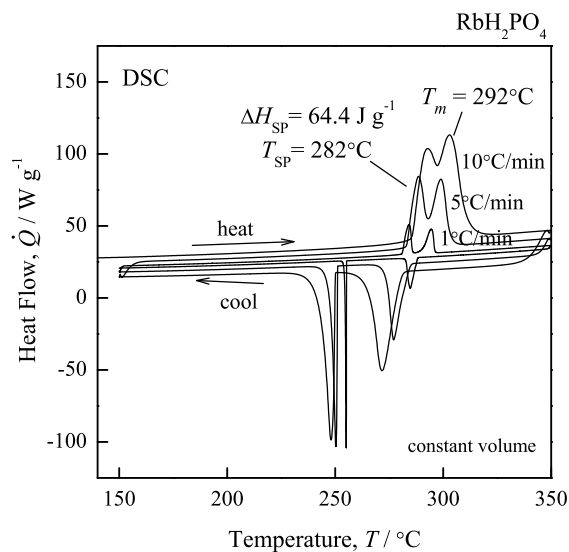


Figure A.1: Differential scanning calorimetry (DSC) data taken on RbH_2PO_4 powders in sealed-containers (constant volume) at heating rates of 1, 5, and 10 $^{\circ}\text{C min}^{-1}$ upon heating and cooling from 25 to 350 $^{\circ}\text{C}$. Both the melting (T_m) and the superprotonic transition (T_{SP}) temperatures are indicated.

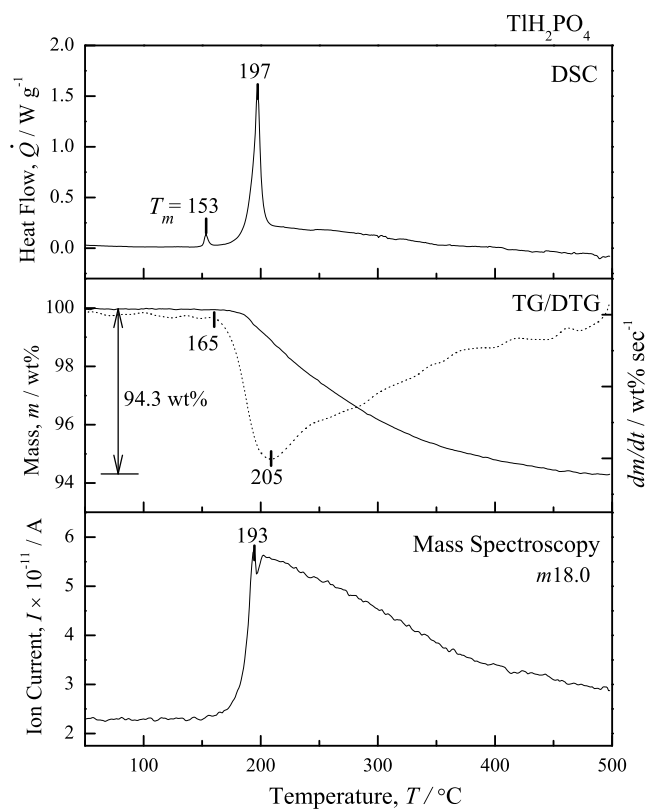
A.2.2 TiH_2PO_4 

Figure A.2: Simultaneous differential scanning calorimetry (DSC), thermal gravimetry (TG), and corresponding differential thermal gravimetry (DTG) of TiH_2PO_4 powder upon heating to 500 $^\circ\text{C}$ at 10 $^\circ\text{C min}^{-1}$ under flowing 40 $\text{cm}^3\text{min}^{-1}$ dry N_2 gas. H_2O in the evolved gas is identified by mass spectroscopy (Mass Spec), $m18.00$.

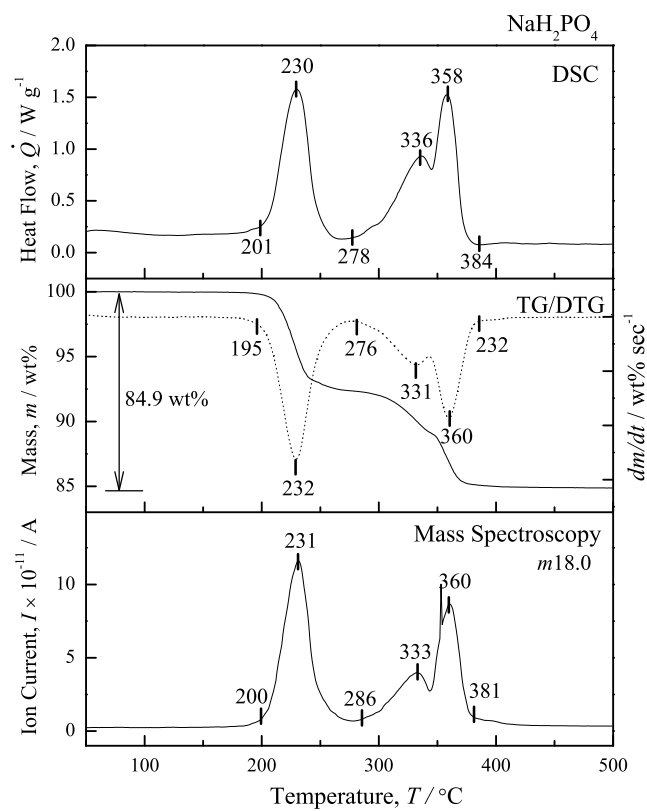
A.2.3 NaH_2PO_4 

Figure A.3: Simultaneous differential scanning calorimetry (DSC), thermal gravimetry (TG), and corresponding differential thermal gravimetry (DTG) of NaH_2PO_4 powder upon heating to 500 °C at 10 °C min⁻¹ under flowing 40 cm³min⁻¹ dry N₂ gas. H₂O in the evolved gas is identified by mass spectroscopy (Mass Spec), $m18.00$.

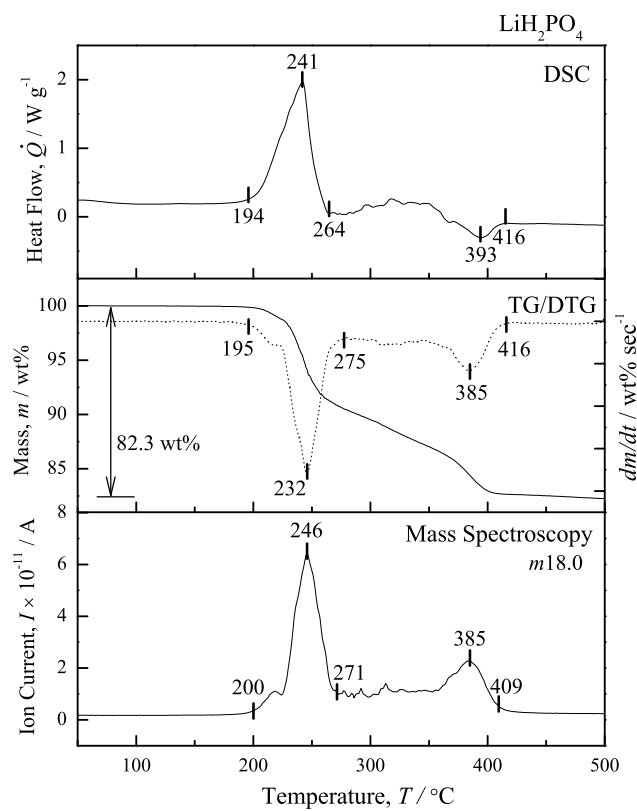
A.2.4 LiH_2PO_4 

Figure A.4: Simultaneous differential scanning calorimetry (DSC), thermal gravimetry (TG), and corresponding differential thermal gravimetry (DTG) of LiH_2PO_4 powder upon heating to 500 °C at 10 °C min⁻¹ under flowing 40 cm³min⁻¹ dry N₂ gas. H₂O in the evolved gas is identified by mass spectroscopy (Mass Spec), $m18.00$.

A.3 High Pressure Conductivity Results

A.3.1 NaH_2PO_4

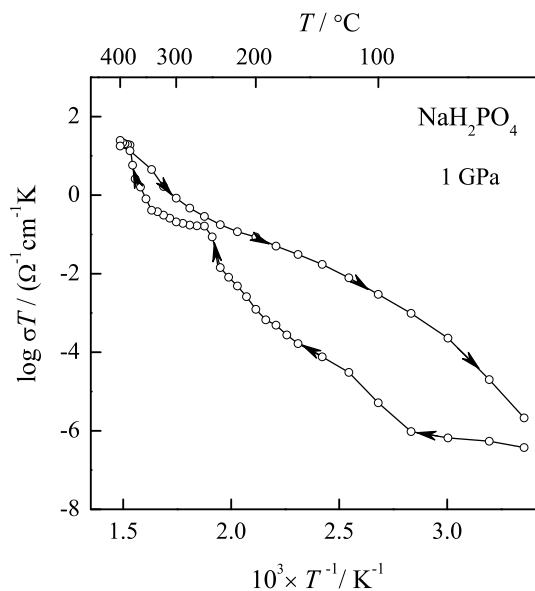


Figure A.5: Arrhenius plot of conductivity results from AC impedance measurements performed on NaH_2PO_4 powder upon heating and cooling (as indicated by direction of arrows) from 25 to 400 °C under 1.0 GPa of pressure.

A.3.2 LiH_2PO_4

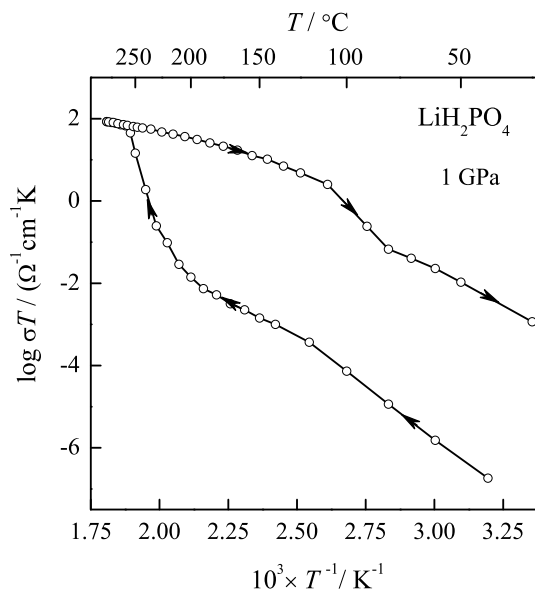


Figure A.6: Arrhenius plot of conductivity results from AC impedance measurements performed on LiH_2PO_4 powder upon heating and cooling (as indicated by direction of arrows) from 25 to 400 °C under 1.0 GPa of pressure.

A.4 MH_nXO_4 -type Solid Acid Phase Behavior

A.4.1 MH_2XO_4 Phase Behavior

Table A.1: Summary of phase transition temperatures (T_{tr}), entropies (ΔS_{tr}), and structures in MH_2XO_4 -type solid acids, where M = Li, Na, K, Rb, and Cs, and X = P, As. †Represents data obtained in this work.

Compound Phase	T_{tr} K	ΔS_{tr} J/mol·K	Crystal System	Space Group	Lattice Parameters							
					a	b	c /Å	α	β	γ /°	V /Å ³	Z
<u>CsH₂PO₄</u>												
IV ferroelectric ¹	154	1.05 ²	monoclinic ³	$P2_1$	7.870	6.320	4.890	90.0	108.3	90.0	230.9	2
III paraelectric	—	—	monoclinic ⁴	$P2_1/m$	7.912	6.383	4.880	90.0	107.7	90.0	234.8	2
II	380	1.18 ⁵										
I superprotonic ⁶	510	22.2†										
liq melt	619	25.2†	cubic ⁷	$Pm\bar{3}m$	4.961	4.961	4.961	90.0	90.0	90.0	122.1	1
<u>RbH₂PO₄</u>												
IV ferroelectric ⁸	77	2.86 ⁹	orthorhombic ¹⁰	$Fdd2$	10.800	10.672	7.242	90.0	90.0	90.0	834.7	8
III paraelectric	—	—	tetragonal ¹⁰	$I\bar{4}2d$	7.607	7.607	7.299	90.0	90.0	90.0	422.4	4
II	352	1.5 ⁵	monoclinic ¹¹	$P2_1/a$	9.606	6.236	7.738	90.0	109.1	90.0	438.1	4
I superprotonic†	553	21.3†	cubic†									
liq melt	563	22.7†										
<u>KH₂PO₄</u>												
III ferroelectric ¹	122	2.89	orthorhombic ¹²	$Fdd2$	10.530	10.440	6.900	90.0	90.0	90.0	758.5	8
II paraelectric	—	—	tetragonal ¹³	$I\bar{4}2d$	7.430	7.430	6.970	90.0	90.0	90.0	384.4	4
II'	453 ¹⁴		triclinic ¹⁵	$P\bar{1}$	7.438	7.393	7.200	88.5	86.9	87.8	394.9	4
I	506 ¹⁴		monoclinic ¹⁵	$P2_1/c$	6.141	4.499	8.966	90.0	91.6	90.0	394.2	4
liq melt	532 ¹⁴											
<u>NaH₂PO₄</u>												
I	—	—	monoclinic ¹⁶	$P2_1/c$	6.808	13.491	7.331	90.0	92.9	90.0	672.4	8
<u>LiH₂PO₄</u>												
I	—	—	orthorhombic ¹⁷	$Pna2_1$	6.253	7.656	6.881	90.0	90.0	90.0	329.4	4
<u>CsH₂AsO₄</u>												
IV ferroelectric ¹⁸	139	3.72 ¹⁹	orthorhombic ²⁰	$Fdd2$	11.516	11.103	7.870	90.0	90.0	90.0	1006.3	8
III paraelectric	—	—	tetragonal ²⁰	$I\bar{4}2d$	7.985	7.985	7.893	90.0	90.0	90.0	502.6	4
II	396	1.31 ²¹										
I superprotonic ²²	438	17.9 ²¹	cubic ²²									
liq melt	569 ²¹											
<u>RbH₂AsO₄</u>												
III ferroelectric ²³	110	4.17 ²⁴										
II paraelectric	—	—	tetragonal ²⁵	$I\bar{4}2d$	7.720	7.720	7.420	90.0	90.0	90.0	454.6	4
I	423 ²⁶											
<u>KH₂AsO₄</u>												
III ferroelectric	96	4.21 ²⁷										
II paraelectric	—	—	tetragonal ²⁸	$I\bar{4}2d$	7.623	7.623	7.155	90.0	90.0	90.0	415.7	4
I	403 ²⁹											
<u>NaH₂AsO₄</u>												
			<i>no information available</i>									
<u>LiH₂AsO₄</u>												
I	—	—	orthorhombic ³⁰	$Pna2_1$	6.416	7.727	7.298	90.0	90.0	90.0	361.8	4

A.4.2 MHXO₄ Phase Behavior

Table A.2: Summary of phase transition temperatures (T_{tr}), entropies (ΔS_{tr}), and structures in MHXO₄-type solid acids, where M = Li, Na, K, Rb, and Cs, and X = S, Se. †Represents data obtained in this work.

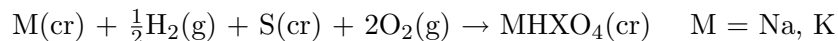
Compound Phase	T_{tr} K	ΔS_{tr} J/mol·K	Crystal System	Space Group	Lattice Parameters							
					a	b	c /Å	α	β	γ /°	V /Å ³	Z
<u>CsHSO₄</u>												
III	—	—	monoclinic ³¹	$P2_1/m$	7.304	5.810	5.491	90.0	101.5	90.0	228.3	2
II	330	0.10 ⁵	monoclinic ³²	$P2_1/c$	7.781	8.147	7.722	90.0	110.8	90.0	457.7	4
I superprotonic ³³	415	14.94 ³⁴	tetragonal ³⁵	$I4_1/amd$	5.718	5.718	14.232	90.0	90.0	90.0	465.3	4
liq melt	484	27.27 ⁵										
<u>RbHSO₄</u>												
IV ferroelectric ³⁶	263	—	monoclinic ³⁷	Pc	14.235	4.582	14.679	90.0	121.0	90.0	820.9	8
III paraelectric	—	—	monoclinic ³⁸	$P2_1/c$	14.360	4.636	14.814	90.0	120.9	90.0	844.5	8
II	439	0.50 ⁵										
I	455 ³⁹											
liq melt	481 ³⁹											
<u>KHSO₄</u>												
II	—	—	orthorhombic ⁴⁰	$Pbca$	8.429	9.807	18.976	90.0	90.0	90.0	1568.6	16
I	451	4.68 ⁴¹										
liq melt	488	34.02 ⁴¹										
<u>NaHSO₄</u>												
I	—	—	triclinic ⁴²	$P\bar{1}$	7.005	7.125	6.712	95.9	87.6	104.5	322.5	4
I'	—	—	monoclinic ⁴³	$P2_1/n$	8.759	7.500	5.147	90.0	99.5	90.0	333.5	4
<u>LiHSO₄</u>												
I	—	—	monoclinic ⁴⁴	$P2_1/c$	5.234	7.322	8.363	90	90.02	90	320.5	4
<u>CsHSeO₄</u>												
II	—	—	monoclinic ⁴⁵	$P2_1/c$	7.970	8.446	7.784	90.0	111.3	90.0	488.3	4
II'	355	0.61 ⁴⁶										
I superprotonic ⁴⁷	400	16.1 ⁴⁸	tetragonal ⁴⁵	$I4_1/amd$	5.880	5.880	14.415	90.0	90.0	90.0	498.5	4
<u>RbHSeO₄</u>												
III ferroelectric ⁴⁹	—	—	triclinic ⁵⁰	$P1$	10.622	4.622	7.575	89.4	110.8	102.1	339.0	3
II paraelectric	386	0.84 ⁵	monoclinic ⁵⁰	$I1$	19.443	4.629	7.635	90.0	90.0	90.8	687.1	6
I superprotonic [†]	446	19.2 [†]										
liq melt	474	12.8 [†]										
<u>KHSeO₄</u>												
I	—	—	orthorhombic ⁵¹	$Pbca$	8.690	10.053	19.470	90.0	90.0	90.0	1700.9	16
<u>NaHSeO₄</u>												
I	—	—	monoclinic ⁵²	$P2_1/n$	5.295	7.873	8.911	90.0	101.3	90.0	364.1	4
<u>LiHSeO₄</u>												
			<i>no information available</i>									

A.5 Estimated Thermodynamic Values

A.5.1 CsHSO₄

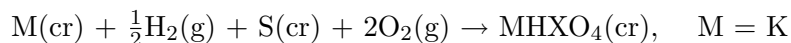
A.5.1.1 $S_{298.15}^{\circ}$ and C_p

The entropy of CsHSO₄ at 298.15 K ($S_{298.15}^{\circ}$) was estimated from the reported values for KHSO₄ and NaHSO₄ entropy of formation $\Delta S_f^{\circ}(298.15 \text{ K})$,



of -434 and -445 J mol⁻¹K⁻¹, respectively⁵³. Then the estimated $\Delta S_f^{\circ}(298.15 \text{ K})$ of CsHSO₄, by analogy to the previous compounds, is -439 J mol⁻¹K⁻¹ (average value) and $S_{298.15}^{\circ} = 189 \text{ J mol}^{-1}\text{K}^{-1}$.

For condensed phase reactions, such as those calculated in this work, it is often acceptable to neglect the heat capacity altogether, by employing the Neumann and Kopp rule⁵⁴. However, for completeness we have estimated the heat capacity of CsHSO₄. Therefore, in a similar fashion as with the entropy, the reported values for the heat capacity of formation of KHSO₄ ($\Delta_f C_p$),



of 13.567 J mol⁻¹K⁻¹⁵³ was used to estimate the heat capacity of CsHSO₄, $C_p = 141.5 \text{ J mol}^{-1}\text{K}^{-1}$.

A.5.2 Cs₂S₂O₇

A.5.2.1 ΔH_f° , $S_{298.15}^\circ$, and C_p

Since there are virtually no reported thermodynamic data for solid Cs₂S₂O₇, the enthalpy of the formation of Cs₂S₂O₇(s) ($\Delta H_f^\circ = -1990$ kJ mol⁻¹) was estimated from the reported formation enthalpy of aqueous Cs₂S₂O₇(aq) and from analogous reported values of other aqueous and solid M₂S₂O₇ (M = Na, K) compounds, given in Table A.3. Using reported values for the Gibbs energy of formation for these analogous compounds (also listed in Table A.3), the entropy of formation ($\Delta S_f^\circ(298.15 \text{ K}) = 536$ J mol⁻¹K⁻¹) was estimated for Cs₂S₂O₇(s), and finally the entropy $S_{298.15}^\circ = 265$ J mol⁻¹K⁻¹.

Table A.3: Thermodynamic data for M₂S₂O₇ compounds (M = Na, K, Cs) used to estimate the ΔH_f° and $S_{298.15}^\circ$ of Cs₂S₂O₇, from reference⁵⁵.

	ΔG_f°	ΔH_f°	/kJ mol ⁻¹
Cs ₂ S ₂ O ₇ (aq)	—	-1917.9	
K ₂ S ₂ O ₇ (aq)	—	-1914.6	
Na ₂ S ₂ O ₇ (aq)	—	-1888.2	
K ₂ S ₂ O ₇ (s)	-1791.5	-1986.6	
Na ₂ S ₂ O ₇ (s)	-1722.0	-1925.1	

Bibliography

1. G. Busch and P. Scherrer. Eine neue seignette-elektrische substanz. *Naturwissenschaften*, 23:737, 1935.
2. E. Kanda, M. Yoshizawa, T. Yamakami, and T. Fujimura. Specific-heat study of ferroelectric CsH_2PO_4 and CsD_2PO_4 . *Journal of Physics C-Solid State Physics*, 15(33):6823–6831, 1982.
3. Y. Uesu and J. Kobayashi. Crystal-structure and ferroelectricity af cesium dihydrogen phosphate CsH_2PO_4 . *Physica Status Solidi A-Applied Research*, 34(2):475–481, 1976.
4. H. Matsunaga, K. Itoh, and E. Nakamura. X-ray structural study of ferroelectric cesium dihydrogen phosphate at room-temperature. *Journal of the Physical Society of Japan*, 48(6):2011–2014, 1980.
5. B. Baranowski, M. Friesel, and A. Lundén. New phase-transitions in CsHSeO_4 , CsH_2PO_4 , RbHSO_4 , RbHSeO_4 , and RbH_2PO_4 . *Zeitschrift für Naturforschung Section A-A Journal of Physical Sciences*, 41(7):981–982, 1986.
6. A.I. Baranov, V.P. Khiznichenko, V.A. Sandler, and L.A. Shuvalov. Frequency dielectric-dispersion in the ferroelectric and superionic phases of CsH_2PO_4 . *Ferroelectrics*, 81:1147–1150, 1988.
7. A. Presinger, K. Mereiter, and W. Bronowska. The phase transition of CsH_2PO_4 (CDP) at 505 K. *Materials Science Forum*, 166:511–516, 1994.
8. P. Bärtschi, B. Matthias, W. Merz, and P. Scherrer. Eine neue, seignette-elektrische modifikation von rubidiumphosphat. *Helvetica Physica Acta*, 18(4):240–242, 1945.
9. M. Amin and B.A. Strukov. Specific heat of single-crystal RbH_2PO_4 . *Soviet Physics-Solid State, USSR*, 10(10):2498–2500, 1969.
10. N.S.J. Kennedy and R.J. Nelmes. Structural studies of RbH_2PO_4 in its paraelectric and ferroelectric phases. *Journal of Physics C-Solid State Physics*, 13(26):4841–4853, 1980.
11. M.T. Averbuch-Pouchot and A. Durif. Structure of a new form of rubidium dihydrogenphosphate, RbH_2PO_4 . *Acta Crystallographica Section C-Crystal Structure Communications*, 41(May):665–667, 1985.
12. B.C. Frazer and R. Pepinsky. X-ray analysis of the ferroelectric transition in KH_2PO_4 . *Acta Crystallographica*, 6(3):273–285, 1953.
13. J. West. A quantitative X-ray analysis of potassium dihydrogen phosphate (KH_2PO_4). *Zeitschrift für Kristallographie*, 74:306–332, 1930.
14. E. Rapoport. Phase transformations and melting in KH_2PO_4 to 40 kbar. *Journal of Chemical Physics*, 53(1):311–314, 1970.
15. J.A. Subramony, S. Lovell, and B. Kahr. Polymorphism of potassium dihydrogen phosphate. *Chemistry Of Materials*, 10(8):2053–2057, 1998.

16. M. Catti and G. Ferraris. Hydrogen-bonding in crystalline state – NaH_2PO_4 , a crystal-structure with a short asymmetrical hydrogen-bond. *Acta Crystallographica Section B–Structural Science*, B 30(Jan 15):1–6, 1974.
17. M. Catti and G. Ivaldi. Crystal-structure of LiH_2PO_4 , structural topology and hydrogen-bonding in alkaline dihydrogen ortho-phosphates. *Zeitschrift für Kristallographie*, 146(4–6):215–226, 1977.
18. B.C. Frazer and R. Pepinsky. A phase transition in CsH_2AsO_4 . *Physical Review*, 91(1):212–213, 1953.
19. B.A. Strukov, A. Baddur, V.I. Zinenko, Mikhailo.Vk, and V.A. Koptsik. Phase-transitions in CsH_2AsO_4 and CsD_2AsO_4 crystals. *Fizika Tverdogo Tela*, 15(7):2018–2023, 1973.
20. W.J. Hay and R.J. Nelmes. Structural studies of deuterated CsH_2AsO_4 in its paraelectric and ferroelectric phases. *Journal of Physics C–Solid State Physics*, 14(7):1043–1052, 1981.
21. S. Hart, P.W. Richter, J.B. Clark, and E. Rapoport. Phase-transitions in CsH_2AsO_4 at high-pressures and temperatures. *Journal of Solid State Chemistry*, 37(3):302–307, 1981.
22. A.I. Baranov, V.P. Khiznichenko, and L.A. Shuvalov. High-temperature phase-transitions and proton conductivity in some KDP-family crystals. *Ferroelectrics*, 100:135–141, 1989.
23. R. Blinc, M. Burgar, and A. Levstik. Order of phase-transition in KDA type ferroelectric crystals. *Solid State Communications*, 12(6):573–576, 1973.
24. C.W. Fairall and W. Reese. Thermodynamic properties of RbH_2AsO_4 . *Physical Review B*, 10(3):882–885, 1974.
25. R.M. Shklovskaya and S.M. Arkhipov. Rubidium and caesium dihydrogen arsenates. *Russian Journal of Inorganic Chemistry*, 12(9):1234–1237, 1967.
26. E. Torijano, R.A. Vargas, J.E. Diosa, R. Catano, and B.E. Mellander. Phase behaviour of RbH_2AsO_4 above room temperature. *Solid State Ionics*, 136:979–984, 2000.
27. C.W. Fairall and W. Reese. Electrical conductivity of KH_2AsO_4 and KD_2AsO_4 . *Physical Review B*, 8(7):3475–3478, 1973.
28. M. Ichikawa, D. Amasaki, T. Gustafsson, and I. Olovsson. X-ray structural study of ferroelectric KH_2AsO_4 and KD_2AsO_4 . *Journal of the Physical Society of Japan*, 70(8):2327–2332, 2001.
29. Y. Luspín, D.D. Meneses, P. Simon, and G. Hauret. Investigation of elastic properties of KH_2AsO_4 above room temperature by Brillouin scattering. *Physica B*, 253(1-2):56–60, 1998.
30. E. Fanchon, J. Vicat, D.T. Qui, and A. Boudjada. Absolute structure of LiH_2AsO_4 . *Acta Crystallographica Section C–Crystal Structure Communications*, 43(6):1022–1025, 1987.

31. K. Itoh, T. Ukeda, T. Ozaki, and E. Nakamura. Redetermination of the structure of cesium hydrogensulfate. *Acta Crystallographica Section C—Crystal Structure Communications*, 46(3):358–361, 1990.
32. C.R.I. Chisholm and S.M. Haile. X-ray structure refinement of CsHSO₄ in phase II. *Materials Research Bulletin*, 35(7):999–1005, 2000.
33. A.I. Baranov, L.A. Shuvalov, and N.M. Shchagina. Superior conductivity and phase-transitions in CsHSO₄ and CsHSeO₄ crystals. *JETP Letters*, 36(11):459–462, 1982.
34. Calum R. I. Chisholm. *Superprotonic Phase Transitions in Solid Acids: Parameters affecting the presence and stability of superprotonic transitions in MH_nXO₄ family of compounds (X = S, Se, P, As; M = Li, Na, K, NH₄, Rb, Cs)*. PhD thesis, California Institute of Technology, 2002.
35. Z. Jirak, M. Dlouha, S. Vratislav, A.M. Balagurov, A.I. Beskrovnyi, V.I. Gordelii, I.D. Datt, and L.A. Shuvalov. A neutron-diffraction study of the superionic phase in CsHSO₄. *Physica Status Solidi A—Applied Research*, 100(2):K117–K122, 1987.
36. R. Pepinsky and K. Vedam. Ferroelectric transition in rubidium bisulfate. *Physical Review*, 117(6):1502–1503, 1960.
37. K. Itoh and C. Moriyoshi. Structural study of phase transition in ferroelectric RbHSO₄. *Ferroelectrics*, 285:465–478, 2003.
38. K. Itoh, H. Ohno, and S. Kuragaki. Disordered structure of ferroelectric rubidium hydrogen sulfate in the paraelectric phase. *Journal of the Physical Society of Japan*, 64(2):479–484, 1995.
39. A.I. Baranov, V.V. Sinitsyn, E.G. Ponyatovskii, and L.A. Shuvalov. Phase-transitions in surface-layers of hydrosulfate crystals. *JETP Letters*, 44(4):237–240, 1986.
40. F. Payan and R. Haser. Hydrogen-bonding in potassium hydrogen sulfate – comparison with a previous crystal-structure determination. *Acta Crystallographica Section B—Structural Science*, 32(Jun15):1875–1879, 1976.
41. K.M. Eriksen, R. Fehrmann, G. Hatem, M. Gauneescard, O.B. Lapina, and V.M. Mastikhin. Conductivity, NMR, thermal measurements, and phase diagram of the K₂S₂O₇–KHSO₄ system. *Journal of Physical Chemistry*, 100(25):10771–10778, 1996.
42. E.J. Sonneveld and J.W. Visser. Structure and hydrogen-bonding of α-NaHSO₄. *Acta Crystallographica Section B—Structural Science*, 35(Sep):1975–1977, 1979.
43. E.J. Sonneveld and J.W. Visser. 2 crystal-structures of NaHSO₄. *Acta Crystallographica Section A*, 34(S):S159–S159, 1978.
44. E. Kemnitz, C. Werner, H. Worzala, S. Trojanov, and Y.T. Strutschkov. Synthesis and crystal-structure of LiHSO₄. *Zeitschrift für anorganische und allgemeine Chemie*, 621(4):675–678, 1995.
45. M.A. Zakharov, S.I. Troyanov, and E. Kemnitz. Superprotonic high temperature phase and refinement of the low temperature structure of CsHSeO₄. *Zeitschrift für Kristallographie*, 216(3):172–175, 2001.

46. M. Friesel, B. Baranowski, and A. Lunden. Pressure-dependence of the transition to the proton conducting phase of CsHSO_4 , CsHSeO_4 , and RbHSeO_4 studied by differential scanning calorimetry. *Solid State Ionics*, 35(1-2):85–89, 1989.
47. B. Hilczer, C. Pawlaczyk, and F.E. Salman. Superionic phase-transition in CsHSeO_4 and CsDSeO_4 single-crystal. *Ferroelectrics*, 81:1157–1160, 1988.
48. S. Yokota, N. Takanohashi, T. Osaka, and Y. Makita. Dielectric and thermal studies on new phase-transition of CsHSeO_4 . *Journal of the Physical Society of Japan*, 51(1):199–202, 1982.
49. R. Poprawski, J. Mroz, Z. Czapla, and L. Sobczyk. Ferroelectric properties and domain-structure in RbHSeO_4 crystals. *Acta Physica Polonica A*, 55(5):641, 1979.
50. I.P. Makarova, L.A. Muradyan, E.E. Rider, V.A. Sarin, I.P. Alexandrova, and V.I. Simonov. Neutron-diffraction study of RbHSeO_4 and NH_4HSeO_4 single-crystals. *Ferroelectrics*, 107:281–286, 1990.
51. J. Baran and T. Lis. Structure of potassium hydrogenselenate. *Acta Crystallographica Section C—Crystal Structure Communications*, 42(3):270–272, 1986.
52. M.A. Zakharov, S.I. Troyanov, V.B. Rybakov, L.A. Aslanov, and E. Kemnitz. Synthesis and crystal structure of sodium hydrogen selenates, NaHSeO_4 and $\text{Na}_3\text{H}(\text{HSeO}_4)_4$. *Crystallography Reports*, 44(3):408–413, 1999.
53. M.W. Chase. *JANAF Thermochemical Tables*, volume 14. American Chemical Society, Washington, D.C., c1986.
54. O. Kubaschewski and C.B. Alcock. *Metallurgical Thermochemistry*, page 184. Pergamon Press, 6th edition, 1979.
55. Donald D. Wagman. *The NBS Tables of Chemical Thermodynamic Properties: selected values for inorganic and C1 and C2 organic substances in SI Units*. American Chemical Society, Washington, D.C., 1982.